

Refinements of hybrid neurophysical volume conductor models and application to study epidural electrical stimulation of the cervical spinal cord

Présentée le 6 mars 2020

à la Faculté des sciences de la vie
Unité du Prof. Courtine
Programme doctoral en neurosciences

pour l'obtention du grade de Docteur ès Sciences

par

Nathan Antoine GREINER

Acceptée sur proposition du jury

Prof. R. Schneggenburger, président du jury
Prof. G. Courtine, Dr M. Capogrosso, directeurs de thèse
Dr E. Neufeld, rapporteur
Prof. S. Lempka, rapporteur
Prof. W. Gerstner, rapporteur

*Dans notre connaissance des choses de l'Univers (qu'elles soient mathématiques ou autres), le pouvoir rénovateur en nous n'est autre que **l'innocence**. C'est l'innocence originelle que nous avons tous reçue en partage à notre naissance et qui repose en chacun de nous, objet souvent de notre mépris, et de nos peurs les plus secrètes. Elle seule unit l'humilité et la hardiesse qui nous font pénétrer au cœur des choses, et qui nous permettent de laisser les choses pénétrer en nous et de nous en imprégner.*

Ce pouvoir-là n'est nullement le privilège de « dons » extraordinaires – d'une puissance cérébrale (disons) hors du commun pour assimiler et pour manier, avec dextérité et avec aisance, une masse impressionnante de faits, d'idées et de techniques connus. De tels dons sont certes précieux, dignes d'envie sûrement pour celui qui (comme moi) n'a pas été comblé ainsi à sa naissance, « au delà de toute mesure ».

Ce ne sont pas ces dons-là, pourtant, ni l'ambition même la plus ardente, servie par une volonté sans failles, qui font franchir ces « cercles invisibles et impérieux » qui enferment notre Univers. Seule l'innocence les franchit, sans le savoir ni s'en soucier, en les instants où nous nous retrouvons seul à l'écoute des choses, intensément absorbé dans un jeu d'enfant...

Alexandre GROTHENDIECK, *Récoltes et Semailles*.

ACKNOWLEDGEMENTS

I wish to thank Prof. Ralf SCHNEGGENBURGER, Prof. Wulfram GERSTNER, Dr. Esra NEUFELD, and Prof. Scott LEMPKA for having accepted to be part of my PhD jury and to review this thesis. Special thanks to Prof. SCHNEGGENBURGER for chairing this jury and to Prof. LEMPKA for having accepted to attend my PhD defense by videoconference in the middle of the night.

I wish to thank Prof. Grégoire COURTINE for having given me the opportunity to contribute to the research in spinal cord injury rehabilitation. I wish him success in developing therapeutic solutions for this painful medical condition.

I wish to thank Prof. Marco CAPOGROSSO, whom has supervised an important part of the work presented in this dissertation, and whom has introduced me to the fields of neurosciences, computational neurosciences, and spinal cord injury research. I wish him success in developing applications for the specific treatment of tetraplegia.

I warmly thank Dr. NEUFELD for his availability and for sharing his insights into the whys and wherefores of hybrid neurophysical volume conductor models, some of which resisted my most stubborn examinations.

Greetings to Théo LEMAIRE from the TNE-LAB and Andreas ROWALD from the GLAB.

Coco, Pierre, Lucas, Anthony, Kat: salut aux habitants de la Maison Vallaire...

Enfin, si cette thèse recèle quelque bien, je le dédie aux membres de ma famille, notamment mes parents, dont l'exemple me pousse à chercher, cultiver, et donner le meilleur de moi-même.

ABSTRACT

After spinal cord injury (SCI), the communication between the brain and spinal neural circuits below the lesion is disrupted, leading to paralysis. Epidural electrical stimulation (EES) of the lumbosacral spinal cord has been shown to restore locomotion and promote long-term recovery of voluntary leg control in individuals affected by SCI. EES predominantly engages sensory nerve fibers in dorsal roots and dorsal columns, modulating the motor output of lumbosacral spinal segments via mono- and poly-synaptic pathways.

Similar sensorimotor circuits involved in upper-limb motor control are located in the cervical segments, suggesting that EES could also be applied to promote arm and hand function in tetraplegic patients after SCI. However, the ability of EES to modulate specific cervical motor nuclei, likely essential to promote upper-limb function, remains largely unexplored.

Hybrid neurophysical volume conductor models have been valuable to unravel the mechanisms of lumbosacral EES and are still intensively used to design implantable electrode arrays and stimulation strategies. Via a two-steps computational scheme in which geometrical factors have a prominent importance, they allow to compute the tridimensional electric potential induced in biological tissues and assess the electrical response of neurons and nerve fibers.

In this thesis, I have conceived a new geometrical model to represent the spinal cord, including notably the spinal roots, I refined the geometry of spinal nerve fibers, and I have developed a software suite implementing these models and enabling the semi-automatic construction of detailed hybrid models from user configuration datasets.

I used this suite to build a hybrid model of EES of the macaque monkey cervical spinal cord to explore the potential targets of cervical EES and evaluate the recruitment selectivity of epidural electrode arrays specifically tailored to the cervical spinal cord. Electrophysiological experiments led on actual macaque monkeys overall corroborated the findings from the model: cervical EES can selectively modulate specific upper-limb motor nuclei via the direct recruitment of dorsal root primary afferents, but the specificity is limited notably by the mix of distinct afferent populations in the dorsal roots.

One way to increase this specificity might be to target individual rootlets, for which multipolar stimulation configurations could be decisive. I have reviewed the strategies employed to represent and search for optimal multipolar configurations using hybrid models, and I propose a new economic and versatile approach whose validity is proven on the theoretical ground.

KEYWORDS

Epidural electrical stimulation, cervical spinal cord, volume conductor models, neurophysiological models, multipolar stimulation configurations

RÉSUMÉ

Après une lésion de la moelle épinière (LME), la communication entre le cerveau et les circuits neuronaux spinaux situés sous la lésion est perturbée, entraînant la paralysie. La stimulation électrique épidurale (SEE) de la moelle épinière lombo-sacrée permet de restaurer la locomotion et favorise le rétablissement à long terme du contrôle volontaire des jambes chez des individus atteints de LME. La SEE engage principalement les fibres nerveuses sensorielles dans les racines et les colonnes dorsales, modulant les commandes motrices des segments spinaux lombo-sacrés par voies mono- et poly-synaptique.

Des circuits sensorimoteurs similaires impliqués dans le contrôle moteur des membres supérieurs sont situés dans les segments cervicaux, ce qui suggère que la SEE pourrait également être appliquée pour promouvoir la fonction du bras et de la main chez les patients tétraplégiques après une lésion médullaire. Cependant, la capacité de la SEE à moduler des noyaux moteurs cervicaux spécifiques, probablement essentielle pour promouvoir la fonction des membres supérieurs, demeure largement inexplorée.

Les modèles hybrides de conducteurs volumiques neurophysiques ont permis d'élucider des mécanismes importants de la SEE lombo-sacrée et sont encore utilisés intensivement pour concevoir des champs d'électrodes et des stratégies de stimulation. Ils permettent, par un schéma de calcul en deux étapes dans lequel les facteurs géométriques ont une importance de premier ordre, de calculer le potentiel électrique tridimensionnel induit dans les tissus biologiques et d'évaluer la réponse électrique de neurones et de fibres nerveuses.

Dans cette thèse, j'ai conçu un nouveau modèle géométrique pour représenter la moelle épinière incluant notamment les racines spinales, j'ai raffiné la géométrie de fibres nerveuses spinales, et j'ai développé une suite logicielle qui implémente ces modèles et permet la construction semi-automatique de modèles hybrides détaillés à partir de jeux de données de configuration.

J'ai utilisé cette suite pour construire un modèle hybride de SEE de la moelle épinière cervicale du singe macaque afin d'explorer les cibles potentielles de la SEE cervicale et d'évaluer la sélectivité du recrutement de champs d'électrodes épidurales adaptés. Des expériences électrophysiologiques menées sur des macaques ont globalement corroboré les prédictions du modèle : la SEE cervicale peut moduler des noyaux moteurs cervicaux spécifiques par le biais du recrutement direct d'afférents primaires dans les racines dorsales, mais la spécificité est limitée notamment par le mélange d'afférents de populations distinctes dans ces racines.

Une façon d'augmenter cette spécificité pourrait être de cibler des radicelles individuelles, ce pour quoi des configurations de stimulation multipolaire pourraient être décisives. J'ai

passé en revue les stratégies utilisées pour représenter et rechercher des configurations multipolaires optimales à l'aide de modèles hybrides, et je propose une nouvelle approche économique et polyvalente dont la validité est prouvée sur le plan théorique.

MOTS-CLÉS

Stimulation électrique épidurale, moelle épinière cervicale, volumes conducteurs, modèles neurophysiques, stimulation multipolaire

READING GUIDE

Chapter 1 – Introduction

The introduction of this dissertation contains a lengthy *Definitions and basic concepts* section which can be skipped, but which can be consulted when unknown expressions or concepts are encountered in the remaining of the text. In the *Problematic* section, the elements necessary to apprehend the main problem addressed by this thesis and the methods that were employed are exposed. The *Research objectives and dissertation outline* section summarizes the three main development lines of the thesis and their underlying motivations.

Chapter 2 – Bio-electromagnetism and hybrid neurophysical volume conductor models

This chapter is mainly a chapter of theory. In *Bio-electromagnetism*, the assumptions and approximations leading from Maxwell's equations to the computational scheme of hybrid neurophysical volume conductor models, are laid down. The *Volume conductor models* section is a brief and general presentation of volume conductor models. In *Neurophysical models*, I present the two models taken from the literature that I have used for the simulations presented in Chapters 3 and 4, as well as the minor modifications that I have made to them. The computer code that I have developed to use these models is available at https://bitbucket.org/ngreiner/biophy_smc_ees/src/master/.

Chapter 3 – Refinement of hybrid neurophysical volume conductor models of EES of the spinal cord

This chapter is about the new geometrical models of the spinal cord and of nerve fibers and motoneurons which I have developed. In *Hybrid models of EES of the spinal cord: literature review*, I present a brief review focused on the geometrical aspects of hybrid models, notably of the compartments represented in volume conductors and of dorsal root and dorsal column nerve fibers distributed within them. The next two sections, *Geometrical model of the spinal cord* and *Connectivity-based geometrical models of motoneurons and nerve fibers*, are technical sections. They can be seen as a conceptual documentation for the computer code implementing these models, available at https://bitbucket.org/ngreiner/fem_smc_ees/src/master/. In *Influence of anatomical elements in hybrid models*, I assess the influence of some of the refinements which I have introduced, namely the representation in the volume conductor of the spinal roots and of the paddle of epidural electrode arrays, and a refined dorsal root fiber geometry.

Chapter 4 – EES of the cervical spinal cord in monkeys and humans: computational and experimental analysis

This chapter is the core chapter of the thesis, addressing the questions about EES of the cervical spinal cord which motivated all the developments of the thesis. In *EES of the macaque monkey cervical spinal cord: theoretical analysis*, I report the computational investigations and findings which I have led. The *Material and methods* subsection describes the specifications and the construction steps of the presented hybrid model of EES of the macaque monkey cervical spinal cord. In *EES of the macaque monkey cervical spinal cord: experimental analysis*, I report the technological developments and experimental investigations which my collaborators and I have led to study cervical EES in actual macaque monkeys. In *EES of the cervical spinal cord in humans: applicability and limitations*, I report the findings of an analysis which we have led on clinical data acquired intra-operatively in human patients having received epidural stimulation of the cervical spinal cord.

Chapter 5 – Representation of multipolar stimulation configurations in hybrid neurophysical volume conductor models

This chapter presents a new approach to represent multipolar stimulation configurations in hybrid models. The approach itself is presented in *New versatile approach*, along with a demonstration of its theoretical soundness. The first two sections, *Position of the problem* and *State-of-the-art*, justify the need for the proposed new approach.

TABLE OF CONTENTS

ACKNOWLEDGEMENTS	vii
ABSTRACT	ix
RÉSUMÉ	xi
READING GUIDE	xiii
TABLE OF CONTENTS	xv
LIST OF TABLES	xix
LIST OF FIGURES	xxi
LIST OF ACRONYMS	xxv
CHAPTER 1 INTRODUCTION	1
1.1 Definitions and basic concepts	2
1.1.1 The nervous system	2
1.1.2 Anatomy of the spinal cord and vertebral canal	8
1.1.3 The neuro-muscular system	17
1.1.4 Electrical stimulation of the spinal cord	29
1.1.5 Hybrid neurophysical volume conductor models	32
1.2 Problematic	35
1.3 Research objectives and dissertation outline	41
CHAPTER 2 BIO-ELECTROMAGNETISM AND HYBRID NEUROPHYSICAL VOLUME CONDUCTOR MODELS	43
2.1 Bio-electromagnetism	44
2.1.1 Electromagnetic field and Maxwell's equations	44
2.1.2 Electric scalar potential, magnetic vector potential, Lorenz Gauge	45
2.1.3 Volume conduction and volume source	45
2.1.4 Case of the infinite, linear, homogeneous, isotropic medium	46
2.1.5 Quasi-stationarity	47
2.1.6 Poisson's equation	48
2.1.7 Non-linearity, inhomogeneity and anisotropy	49
2.1.8 Summary, conclusions, and computational strategy	50

2.2	Volume conductor models	51
2.2.1	Volume conductors	51
2.2.2	Boundary conditions	52
2.2.3	Geometry discretization and finite element method	56
2.3	Neurophysical models	57
2.3.1	Myelinated nerve fibers: MRG model	57
2.3.2	Motoneuron model	60

CHAPTER 3 REFINEMENT OF HYBRID NEUROPHYSICAL VOLUME CON-		
DUCTOR MODELS OF EES OF THE SPINAL CORD		65
3.1	Hybrid models of EES of the spinal cord: literature review	66
3.1.1	Coburn, 1980 [83]	66
3.1.2	Coburn and Sin, 1985 [58] – Coburn, 1985 [84]	67
3.1.3	Struijk et al., 1991 [87], 1992 [50], 1993 [88]	67
3.1.4	Rattay et al., 2000 [38]	68
3.1.5	Capogrosso et al., 2013 [42]	69
3.1.6	Howell et al., 2014 [90]	69
3.1.7	Lempka et al., 2015 [59]	70
3.1.8	Summary and conclusions	71
3.2	Geometrical model of the spinal cord	73
3.2.1	Generic representation	73
3.2.2	Spinal segments and cross-sections	73
3.2.3	Extensions, extended cross-sections	75
3.2.4	GM, WM, CSF, dura and fat	75
3.2.5	Inner compartments	78
3.2.6	Spinal roots	93
3.3	Connectivity-based geometrical models of motoneurons and nerve fibers . .	108
3.3.1	Geometrical model of motoneurons	108
3.3.2	Geometrical model of group-Ia fibers	112
3.3.3	Other nerve fibers	118
3.4	Influence of anatomical elements in hybrid models	120
3.4.1	Hybrid model specifications	120
3.4.2	Influence of spinal roots and electrode array paddle	122
3.4.3	Nerve fiber geometry and segmental selectivity	141

CHAPTER 4	EES OF THE CERVICAL SPINAL CORD IN MONKEYS AND HUMANS: COMPUTATIONAL AND EXPERIMENTAL ANALYSIS	149
4.1	Introduction	151
4.2	EES of the macaque monkey cervical spinal cord: theoretical analysis . . .	153
4.2.1	Model construction and anatomical findings	153
4.2.2	Primary direct targets of EES of the cervical spinal cord	155
4.2.3	Ia-mediated recruitment of upper-limb motoneurons	160
4.2.4	Material and methods	164
4.3	EES of the macaque monkey cervical spinal cord: experimental analysis . .	171
4.3.1	Design of tailored cervical epidural electrode arrays	171
4.3.2	Recruitment of upper-limb motoneurons with cervical EES	174
4.3.3	Electrophysiological assessment of the nature of the motoneuronal recruitment	176
4.3.4	Direct comparison between experimental and simulation results . .	180
4.3.5	Discussion	181
4.3.6	Material and methods	184
4.4	EES of the human cervical spinal cord: applicability and limitations	190
4.4.1	Nature of the motoneuronal recruitment	190
4.4.2	Recruitment selectivity	192
4.4.3	Summary and conclusions	192
4.4.4	Material and methods	193
CHAPTER 5	REPRESENTATION OF MULTIPOLAR STIMULATION CONFIGURATIONS IN HYBRID NEUROPHYSICAL VOLUME CONDUCTOR MODELS	195
5.1	Position of the problem	197
5.1.1	Computational cost	197
5.1.2	Superposition principle	199
5.1.3	Stimulation paradigms and boundary conditions	203
5.2	State-of-the-art	209
5.2.1	Butson and McIntyre, 2008 [61]	209
5.2.2	Capogrosso et al., 2011 [62]	209
5.2.3	Howell et al., 2015 [55]	210
5.2.4	Xiao et al., 2016 [63]	211
5.2.5	Pelot et al., 2018 [122]	211
5.2.6	Summary and conclusions	212
5.3	New versatile approach	213
5.3.1	Problem definition, basis solutions, and superposition	214
5.3.2	Neurophysical models and equivalent potential distributions	220

CHAPTER 6	CONCLUSION	229
6.1	Summary of works	229
6.2	Limitations and future research	231
6.2.1	Intrinsic limitations of hybrid models	231
6.2.2	Geometry meshing	231
6.2.3	Micro-anatomy of the cervical spinal cord	232
6.2.4	Experimental validation of simulation results	233
REFERENCES		235
CURRICULUM VITAE		249

LIST OF TABLES

4.1	Distribution of upper-limb motoneurons in the cervical segments of the macaque monkey spinal cord	156
4.2	Distribution of upper-limb Ia-fibers in the cervical dorsal roots of the macaque monkey spinal cord	156
4.3	Minimum synaptic conductances enabling the Ia-mediated recruitment of eight macaque monkey upper-limb muscles	163
4.4	Identification and licensing for animal experimentation	184
5.1	Typical computational costs of the different steps of the computational scheme of hybrid models	198

LIST OF FIGURES

1.1	Definitions and basic concepts: general structure of neurons	3
1.2	Definitions and basic concepts: various neuronal morphologies	5
1.3	Definitions and basic concepts: ion channels in cellular membrane	6
1.4	Definitions and basic concepts: ion pumps in cellular membrane	6
1.5	Definitions and basic concepts: synaptic transmission	7
1.6	Definitions and basic concepts: central nervous system	9
1.7	Definitions and basic concepts: anatomical terminology	11
1.8	Definitions and basic concepts: spinal cord in the human body	12
1.9	Definitions and basic concepts: organization of the human vertebral column and spinal cord	13
1.10	Definitions and basic concepts: vertebrae, spinal cord, spinal nerves	14
1.11	Definitions and basic concepts: transverse cross-section of the vertebral canal	16
1.12	Definitions and basic concepts: rootlets entering in the human spinal cord	16
1.13	Definitions and basic concepts: gray matter, white matter and spinal tracts	18
1.14	Definitions and basic concepts: muscle torques and movement	19
1.15	Definitions and basic concepts: internal structure of muscle fibers	19
1.16	Definitions and basic concepts: spatial arrangement of the motor nuclei in the spinal cord	21
1.17	Definitions and basic concepts: muscle spindles, γ -motor axons, group- Ia and group-II fibers	23
1.18	Definitions and basic concepts: morphology of group-Ia fibers	24
1.19	Definitions and basic concepts: group-Ia fiber collaterals in the trans- verse plane	25
1.20	Definitions and basic concepts: group-II fiber collaterals in the trans- verse plane	26
1.21	Definitions and basic concepts: Golgi tendon organs, group-Ib fibers	28
1.22	Definitions and basic concepts: group-Ib fiber collaterals in the trans- verse plane	28
1.23	Definitions and basic concepts: clinical epidural electrode arrays	33
2.1	Neurophysical models: electrical circuit of the MRG model.	58
2.2	Neurophysical models: modified P2 compartment	61
3.2	Spinal cord geometrical model: cross-sectional contour	73
3.1	Spinal cord geometrical model: overview	74

3.3	Spinal cord geometrical model: spinal segments and cross-sections . . .	76
3.4	Spinal cord geometrical model: extended cross-sections	77
3.5	Spinal cord geometrical model: GM, WM, CSF, dura and fat	79
3.6	Spinal cord geometrical model: inner compartments	79
3.7	Spinal cord geometrical model: DH	81
3.8	Spinal cord geometrical model: MGM	81
3.9	Spinal cord geometrical model: MR	83
3.10	Spinal cord geometrical model: VH	83
3.11	Spinal cord geometrical model: VQ	84
3.12	Spinal cord geometrical model: LT	84
3.13	Spinal cord geometrical model: ST	86
3.14	Spinal cord geometrical model: CT	86
3.15	Spinal cord geometrical model: DC	88
3.16	Spinal cord geometrical model: anatomical compartmentalization of the dorsal columns	88
3.17	Spinal cord geometrical model: DC compartments in $CS_{n_{seg}+1}$	90
3.18	Spinal cord geometrical model: DC compartments in $CS_{n_{seg}}$	90
3.19	Spinal cord geometrical model: DC compartments in $CS_{n_{seg}-1}$	91
3.20	Spinal cord geometrical model: DC compartments in multiple cross- sections	92
3.21	Spinal cord geometrical model: OD	93
3.22	Spinal cord geometrical model: roots and spinal segments definition .	94
3.23	Spinal cord geometrical model: dorsal root entry point	97
3.24	Spinal cord geometrical model: dorsal root guide curve and interpola- tion points	99
3.25	Spinal cord geometrical model: orthogonal $DR_{j,k}$	102
3.26	Spinal cord geometrical model: rectified $DR_{j,k}$	102
3.27	Spinal cord geometrical model: algorithm for $DR_{j,k}$ (1/5)	103
3.28	Spinal cord geometrical model: algorithm for $DR_{j,k}$ (2/5)	103
3.29	Spinal cord geometrical model: algorithm for $DR_{j,k}$ (3/5)	104
3.30	Spinal cord geometrical model: algorithm for $DR_{j,k}$ (4/5)	104
3.31	Spinal cord geometrical model: algorithm for $DR_{j,k}$ (5/5)	105
3.32	Spinal cord geometrical model: ventral root entry point	107
3.33	Influence of anatomical elements in hybrid models: hybrid model used for the sensitivity analysis.	121
3.34	Influence of anatomical elements in hybrid models: lateral and medial electrode positions.	124
3.35	Influence of spinal roots and electrode paddle: electric potential profile along a dorsal root fiber. Lateral electrode.	125

3.36	Influence of spinal roots and electrode paddle: electric potential profile along a dorsal root fiber. Medial electrode.	125
3.37	Influence of spinal roots and electrode paddle: profile of the second-order finite differences of the electric potential along a dorsal root fiber. Lateral electrode.	128
3.38	Influence of spinal roots and electrode paddle: profile of the second-order finite differences of the electric potential along a dorsal root fiber. Lateral electrode.	128
3.39	Influence of spinal roots and electrode paddle: electric potential profile along a dorsal column fiber. Lateral electrode.	129
3.40	Influence of spinal roots and electrode paddle: electric potential profile along a dorsal column fiber. Medial electrode.	129
3.41	Influence of spinal roots and electrode paddle: electric potential profile along a motor axon. Lateral electrode.	131
3.42	Influence of spinal roots and electrode paddle: electric potential profile along a motor axon. Medial electrode.	131
3.43	Influence of spinal roots and electrode paddle: profile of the second-order finite differences of the electric potential along a motor axon. Lateral electrode.	133
3.44	Influence of spinal roots and electrode paddle: recruitment curves of dorsal root fibers.	133
3.45	Influence of spinal roots and electrode paddle: threshold and saturation amplitudes of dorsal root fibers.	135
3.46	Influence of spinal roots and electrode paddle: recruitment curves of dorsal column fibers.	135
3.47	Influence of spinal roots and electrode paddle: threshold and saturation amplitudes of dorsal column fibers.	136
3.48	Influence of spinal roots and electrode paddle: recruitment curves of motor axons.	136
3.49	Influence of spinal roots and electrode paddle: threshold and saturation amplitudes of motor axons.	137
3.50	Influence of spinal roots and electrode paddle: selectivity curves of dorsal root fibers VS dorsal column fibers. Lateral stimulation. . . .	137
3.51	Influence of spinal roots and electrode paddle: selectivity curves of dorsal column fibers VS dorsal root fibers. Medial stimulation. . . .	138
3.52	Influence of spinal roots and electrode paddle: selectivity curves of dorsal root fibers VS motor axons. Lateral stimulation.	139
3.53	Influence of nerve fiber geometry: reference, unbranching, and OD ₃ geometries	142

3.54	Influence of nerve fiber geometry: targeted and non-targeted fibers . .	144
3.55	Influence of nerve fiber geometry: recruitment curves of fibers of targeted segment	145
3.56	Influence of nerve fiber geometry: threshold and saturation amplitudes of fibers of targeted segment	145
3.57	Influence of nerve fiber geometry: recruitment curves of fibers of non-targeted segments	146
3.58	Influence of nerve fiber geometry: threshold and saturation amplitudes of fibers of non-targeted segments	146
3.59	Influence of nerve fiber geometry: segmental selectivity	147
4.1	Cervical EES: morphology and hybrid model of EES of the macaque monkey cervical spinal cord	154
4.2	Cervical EES: computational analysis of the direct targets of cervical EES in macaque monkeys	159
4.3	Cervical EES: computational analysis of the Ia-mediated recruitment of motoneurons during cervical EES in macaque monkeys	162
4.4	Cervical EES: organization of the macaque monkey cervical spinal cord and custom epidural electrode array	172
4.5	Cervical EES: layouts of two custom epidural electrode arrays	173
4.6	Cervical EES: muscular recruitment induced by lateral cervical epidural electrodes in macaque monkeys	175
4.7	Cervical EES: muscular recruitment induced by medial cervical epidural electrodes in macaque monkeys, comparison with lateral electrodes	178
4.8	Cervical EES: patterns of muscular responses elicited during high-frequency cervical EES in macaque monkeys	179
4.9	Cervical EES: comparison between experimental muscular recruitment and simulated motoneuronal recruitment	180
4.10	Cervical EES: analysis of cervical EES in humans	191
5.1	Multipolar configurations: generic computational domain Ω	199
5.2	Multipolar configurations: implanted stimulation system with two electrodes: open-circuit situation	205
5.3	Multipolar configurations: implanted stimulation system with two electrodes: closed-circuit situation	205
5.4	Multipolar configurations: example of domain boundary partition . . .	216
5.5	Multipolar configurations: boundary conditions for basis solutions . .	216
5.6	Multipolar configurations: basis solutions and current fluxes	218
5.7	Multipolar configurations: generic compartmental model with extra-cellular mechanism in NEURON	221
5.8	Multipolar configurations: state variables in NEURON	223

LIST OF ACRONYMS

CMAP	Compound Muscle Action Potential
CNS	Central Nervous System
CS	Cross-Section
CSF	Cerebro-Spinal Fluid
DC	Dorsal Columns
DR	Dorsal Root
DRG	Dorsal Root Ganglion
EES	Epidural Electrical Stimulation
EEA	Epidural Electrical Array
EMG	Electromyography
FEM	Finite Element Method
GM	Gray Matter
ICC	Integrated Current Condition
IPG	Implantable Pulse Generator
MN	Motoneuron
PNS	Peripheral Nervous System
SCI	Spinal Cord Injury
VR	Ventral Root
WHO	World Health Organization
WM	White Matter

CHAPTER 1 INTRODUCTION

In 2011, around the world, the incidence-rate of traumatic spinal cord injury (SCI) was estimated to be approximately of 180 000 cases per year [1]. For those who survive the traumatic event, the clinical consequences are often severe, altering their independence, requiring extensive and continuous medical care all along their lives, and profoundly impacting their way of living. The consequences of SCI on individual lives and the cost it imposes on society require that intensive research be conducted to develop therapeutic strategies [2].

By damaging the central nervous system, SCI results in neurological disorders including paralysis, loss of sensation, chronic pain, loss of bladder and bowel control, and disrupted circulatory, respiratory and sexual functions [3, 4]. The nature and severity of the symptoms and the body parts which are affected vary greatly from individual to individual and are largely influenced by the level of the injury.

A significant fraction of SCIs occur at the cervical level (>50% of the cases reported in the USA [2]). This portion of the spinal cord contains neural circuits involved in the motor control of the upper-limb and is located above the lumbo-sacral portion, containing the circuits controlling the lower-limb. Thus, cervical SCIs often lead to tetraplegia, a paralysis of the four limbs which can be complete or incomplete.

Paralysis of the upper-limb is a major source of autonomy loss for affected individuals. It can cause the inability to participate in professional and social activities, but also of ensuring such elementary needs as feeding, dressing and cleaning oneself. Among all the disorders caused by cervical SCI, it is felt as the most burdening by tetraplegic patients [5]. For these reasons, the development of therapeutic strategies targeted to the recovery of upper-limb function is a priority objective for translational spinal cord injury research.

The work presented in this dissertation is a contribution to the development of epidural electrical stimulation (EES) of the cervical spinal cord, a promising technique to reanimate paralyzed upper-limbs after SCI.

1.1 Definitions and basic concepts

In this preliminary section, the very basic concepts necessary to apprehend the developments presented in this dissertation are laid down. These concepts should be familiar to most neuroscientists and electrophysiologists, but they may serve as a starting point for readers less experienced in these fields of study. One purpose of this section is to define the terminology that will be used throughout this document.

The covered elements are the general organization of the nervous system, the anatomy and organization of the spinal cord and vertebral canal, the neuro-muscular system, and the electrical stimulation of biological tissue and epidural electrical stimulation of the spinal cord in particular.

The material presented here is by no means exhaustive, but references have been provided for further reading. Much of it is taken from [6], and I have chosen not to notify this source each time a statement was stemming from it to avoid burdening the text unnecessarily.

1.1.1 The nervous system

I start by giving an overview of the nervous system, from the general structure and properties of neurons to the overall arrangement of the nervous system into central and peripheral nervous systems.

Neurons, axons, dendrites and synapses

Neurons are highly specialized cells constituting the primary functional units of the nervous system. The typical structure of neurons is depicted in Figure 1.1. It comprises three main components:

- the cellular body—or *soma* (plural *somata*)—, which contains the neuron’s nucleus and usual cytoplasmic organelles, such as the endoplasmic reticulum or mitochondria;
- the *axon*, which is a thin tubular structure projecting away from the soma (sometimes for very long distances, up to ~ 1 m in the human body) and which carries the output signals of the neuron to other neurons;
- the *dendrites*—or *dendritic tree*—, which is a network of thin ramifications and which receive the signals provided by other neurons.

At their distal end (*ie* away from the soma), neuronal axons ramify into so-called *terminal arborizations* and form *synaptic contacts*—or *synapses*—with the dendrites and somata of other neurons. Furthermore, many axons are *myelinated*, that is, they are wrapped by a

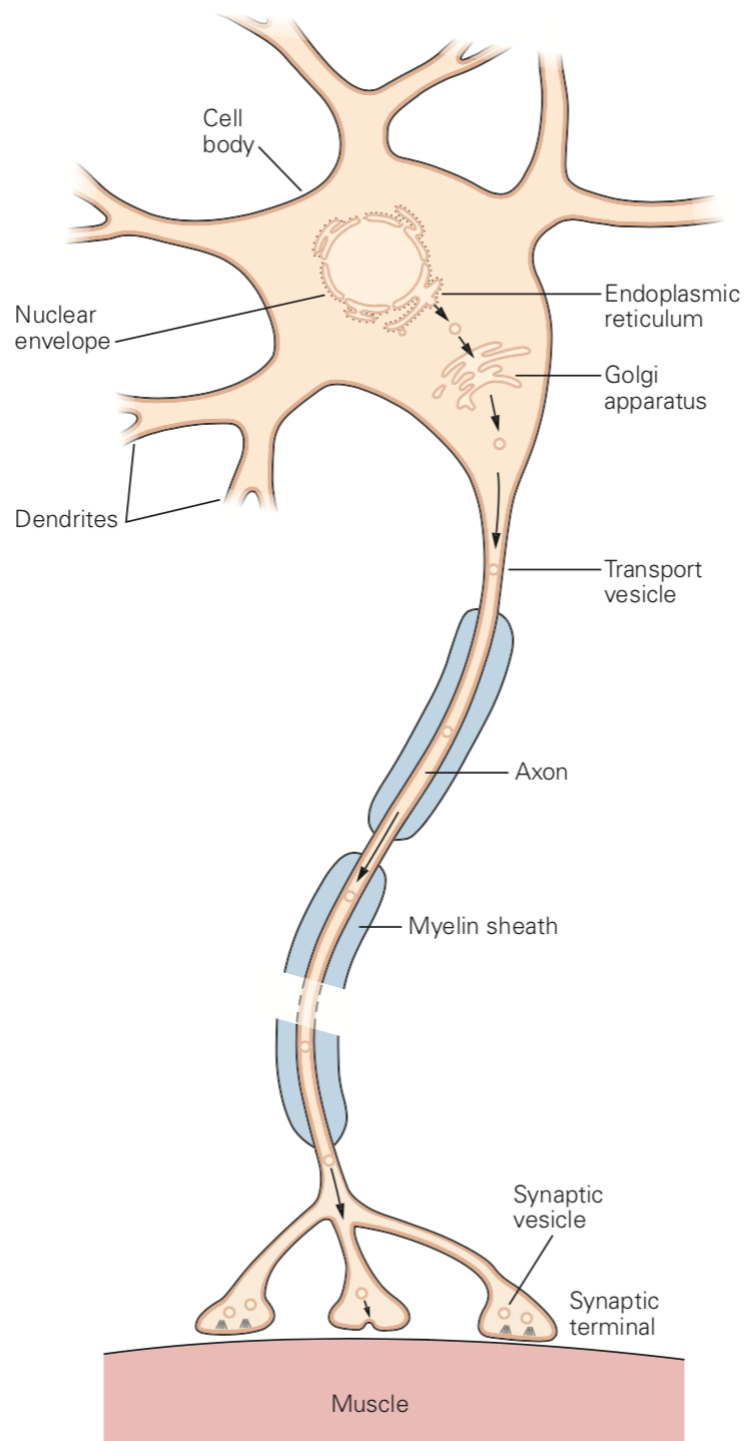


Figure 1.1 General structure of neurons. Here, the post-synaptic cell being labeled “muscle”, the represented neuron is a *motoneuron*. [Picture taken from [6].]

myelin sheath which speeds up the conduction of signals down their lengths (Figure 1.1). When present, the myelin sheath is regularly interrupted, leaving small portions of axon unmyelinated (about $1\text{ }\mu\text{m}$ long). These unmyelinated portions are known as *nodes of Ranvier*, and the myelinated portions between two consecutive nodes as *internodes*.

Typical dimensions for neurons are $10\text{ }\mu\text{m}$ to $60\text{ }\mu\text{m}$ for the soma diameters, $1\text{ }\mu\text{m}$ to $20\text{ }\mu\text{m}$ for axon diameters, and $1\text{ }\mu\text{m}$ to $10\text{ }\mu\text{m}$ for dendritic segments, with dendritic segments becoming thinner as the distance from the soma increases. There are about 100 different types of neurons, presenting a wide spectrum of morphologies (Figure 1.2).

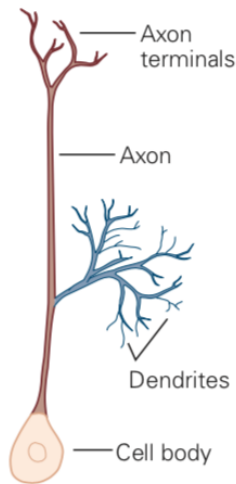
One of the main characteristics of neurons is that their membrane contains ion channels whose permeabilities depend upon various external stimuli and the internal state of the neurons. Moreover, the neuronal membrane also contains proteins that can actively pump specific ions against their concentration gradient across the membrane (see Figures 1.3 and 1.4). The pumps are responsible for maintaining a concentration disequilibrium between the intracellular and extracellular spaces for multiple ion species, creating a voltage drop across the membrane. The difference between the intracellular and extracellular potentials—which is not necessarily uniform throughout a neuron—is called the *membrane potential*. In resting conditions, a typical value for the membrane potential is -65 mV , though this value varies across and sometimes within neurons (the resting membrane potential of the soma may be different than that of the dendrites or of the axon for instance).

Incidentally, due to various external stimuli, the membrane potential of a neuron can be moved away from its resting level. When the membrane potential increases following such stimulus, the membrane is said to be *depolarized*. When the membrane potential decreases, it is said to be *hyperpolarized*. For instance, since sodium ions (Na^+) are positively charged, and since they are more concentrated outside the cell, the opening of channels permeable to sodium ions leads to an influx of positive charges inside the cell and depolarizes the membrane.

Due to such ion channels (and in particular to voltage-gated ion channels, *ie* ion channels whose opening probability depends upon the local membrane potential), the membrane of neurons are susceptible to undergo a very particular type of electrical event: the *action potential*. I will discuss later the mechanisms leading to their emergence. For now, suffice it to say that during an action potential, the membrane potential undergoes a very rapid and massive depolarization (passing from around -65 mV to around 40 mV) followed by an equally rapid fall back to the resting level, the whole event lasting approximately 1 ms.

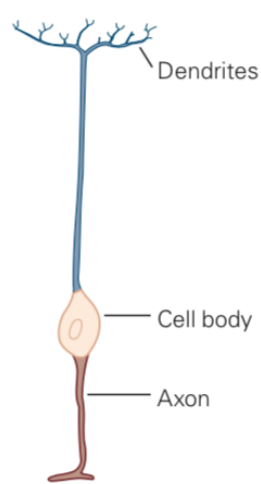
Furthermore, when an action potential is induced in the soma or the axon of a neuron, it is propagated down the axon via mechanisms of regeneration occurring at successive nodes of Ranvier. The time it takes for an action potential to be propagated from soma

A Unipolar cell



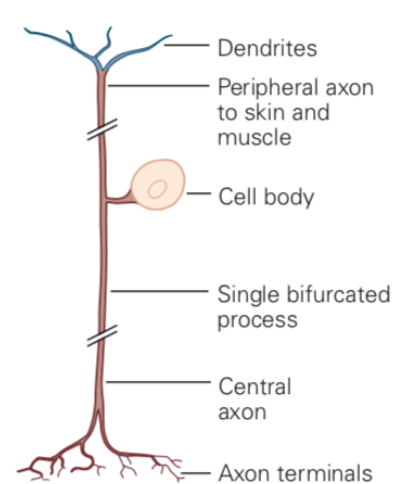
Invertebrate neuron

B Bipolar cell



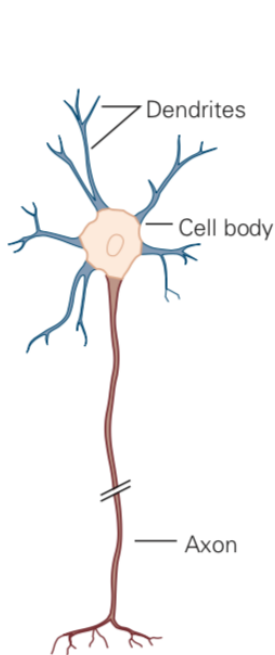
Bipolar cell of retina

C Pseudo-unipolar cell

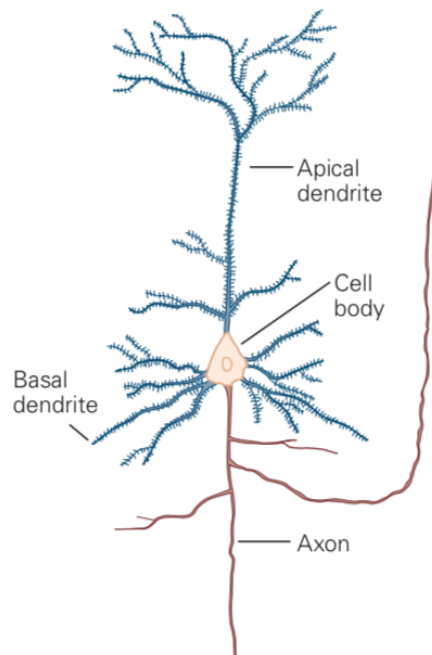


Ganglion cell of dorsal root

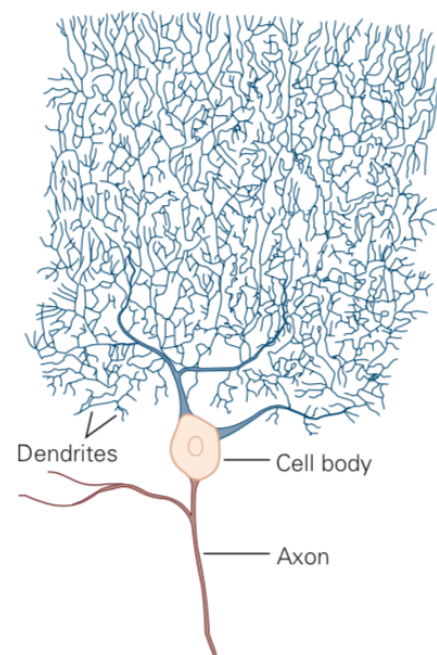
D Three types of multipolar cells



Motor neuron of spinal cord



Pyramidal cell of hippocampus



Purkinje cell of cerebellum

Figure 1.2 Various neuronal morphologies. *[Picture taken from [6].]*

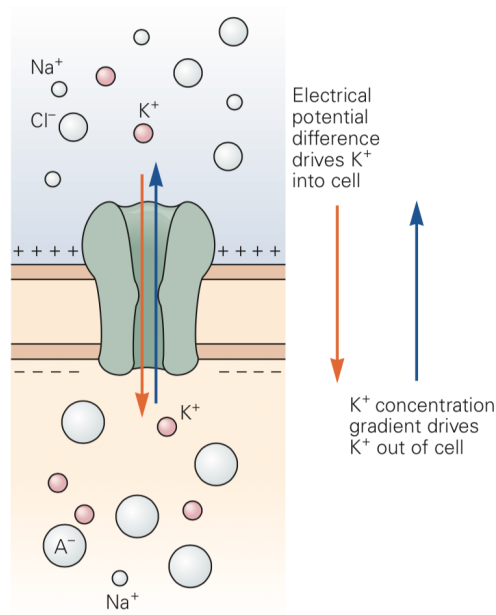


Figure 1.3 Ion channels in cellular membrane. Here, the represented channel is permeable to potassium ions (K^+). Na^+ : sodium ions. Cl^- : chloride ions. A^- : predominantly amino acids and proteins of negative polarity. [Picture taken from [6].]

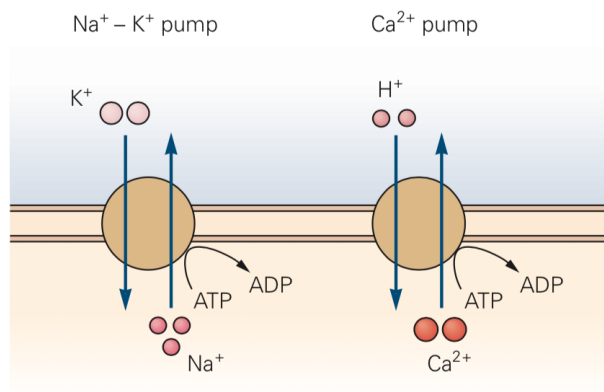


Figure 1.4 Ion pumps in cellular membrane. The transport of sodium, potassium and calcium ions (Ca^{2+}) against their concentration gradient requires energy expenditure: this is provided by the hydrolysis of adenosine triphosphate (ATP) into adenosine diphosphate (ADP). [Picture taken from [6].]

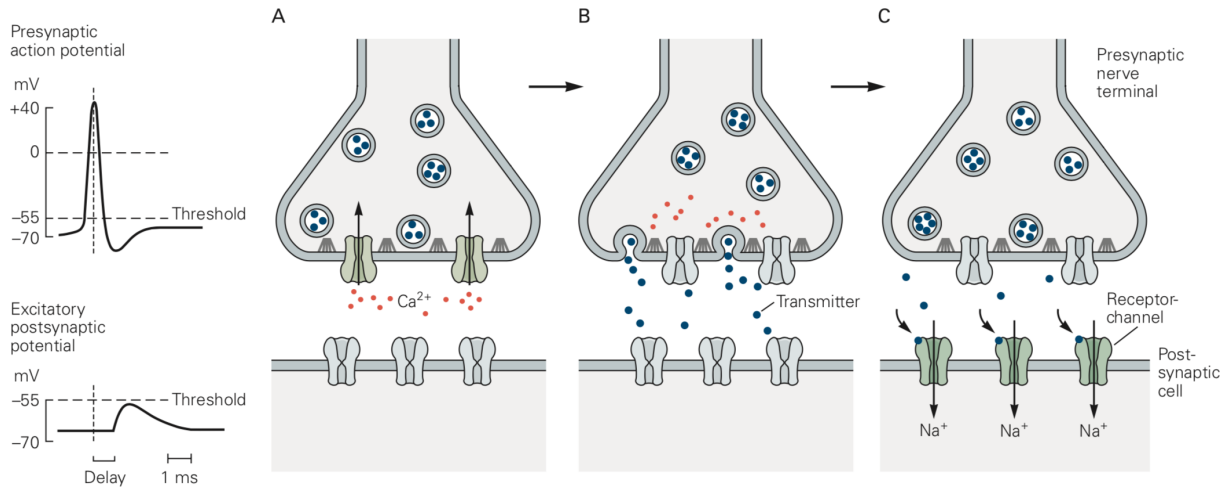


Figure 1.5 Synaptic transmission. **A.** An action potential invades the pre-synaptic terminal of an axon, causing the influx of Ca^{2+} ions inside the pre-synaptic terminal. **B.** The influx of Ca^{2+} causes the fusion of synaptic vesicles with the membrane of the pre-synaptic terminal, releasing neurotransmitters in the synapse. **C.** Neurotransmitters bind with receptor channels on the membrane of the post-synaptic cell, opening them and causing an influx of Na^{+} ions and a membrane depolarization in the post-synaptic cell. [Picture taken from [6].]

to axon terminals is referred to as *propagation delay* or *propagation duration*, and the velocity with which it travels along the axon, the *conduction velocity*.

When an action potential reaches the axon's synaptic terminals, it induces the release of specific molecules in the synapses: the *neurotransmitters* (there exists multiple species of neurotransmitter, and each neuron uses one specific type for all its synapses). In turn, these neurotransmitters bind to receptor channels on the post-synaptic membrane (that of dendrites or somata of post-synaptic cells), opening them and causing depolarization or hyperpolarization in the post-synaptic cells depending on the type of neurotransmitter and receptor channel. This is the process of *synaptic transmission* (Figure 1.5).

Central and peripheral nervous systems

Moving away from the microscopic structure of neurons, I here provide a few elements regarding the general organization of the nervous system, and notably its division into central and peripheral nervous systems.

The central nervous system (CNS) constitutes the main component of the nervous system, comprising the brain and the spinal cord. The CNS is commonly considered to be divided in seven compartments: the spinal cord, the medulla oblongata, the pons, the cerebellum, the midbrain, the diencephalon and the cerebrum (Figure 1.6). Together, the medulla oblongata, the pons, and the midbrain form the *brain stem*.

The cerebrum comprises the two cerebral hemispheres, whose outermost layers together constitute the *cerebral cortex*. Evidence suggests that the intent and planning of movements are elaborated in specific areas of the cerebral cortex (the pre-frontal area and the posterior parietal and pre-motor areas respectively), and that the coordinated neural signals effectively actuating the limbs are somehow subsequently elaborated by yet another cortical area (the primary motor cortex), the brain stem, and the spinal cord.

All the remaining neural tissue found in the body constitutes the peripheral nervous system (PNS), which comprises the peripheral nerves and the ganglia which are outside the brain and spinal cord.

In particular, the spinal roots—which emerge from the spinal cord and become peripheral nerves after they exit the vertebral canal (see Section 1.1.2)—are considered to be part of the PNS. In fact, it is not clear whether they should instead be considered to be part of the CNS, due to the fact that they lie within the dural sac (again, see Section 1.1.2), but I chose to follow the nomenclature used by Fabricius and colleagues [7] for consistency (see Section 2.3.2).

The role of the PNS is to ensure the communication between the CNS and the other organs of the body. Peripheral nerves are in fact bundles of axons¹ which can be *efferent* (when they convey signals from the CNS to the periphery) or *afferent* (when they convey signals from the periphery to the CNS).

Furthermore, nerve fibers are grouped into *fascicles* (groups of fibers isolated from one another by connective tissue) within the peripheral nerves, and efferent and afferent fibers innervating the same organs at the periphery (muscles, *dermatomes*², etc.) are clustered together in the same fascicles.

1.1.2 Anatomy of the spinal cord and vertebral canal

This section contains the essential elements of anatomy of the spinal cord and of the vertebral canal in relation with the developments presented in the following chapters. I begin by laying down the basic terminology to designate anatomical locations.

Anatomical planes, anatomical axes

I here below report the anatomical terminology used in [6], which will be used consistently throughout this document. For the most part, this terminology is illustrated by Figure 1.7.

The following points should be emphasized:

¹Axons are often called *nerve fibers*, or simply *fibers*.

²Dermatomes are areas of the skin innervated by sensory neurons of the same dorsal root ganglion (see Section 1.1.2).

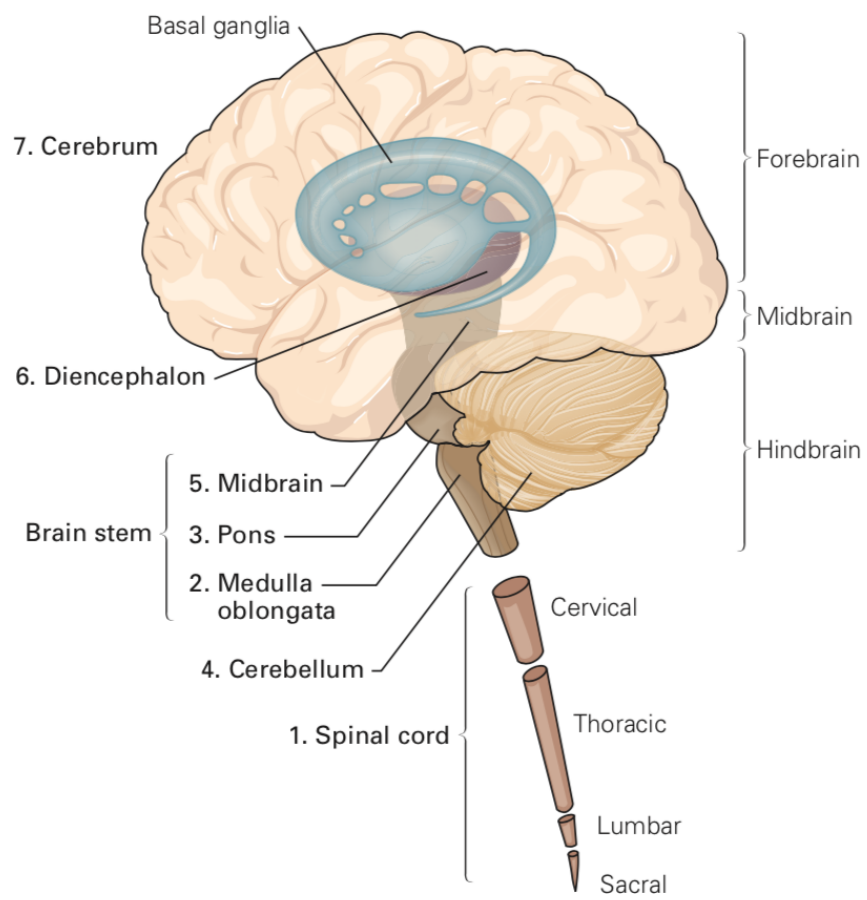


Figure 1.6 Central nervous system. *[Picture taken from [6].]*

- horizontal planes are sometimes referred to as *transversal* or *transverse* planes (Figure 1.7.c);
- in the following chapters, I will mostly focus on the spinal cord, and so it is best to keep in mind that *rostral* typically means “towards the head” while *caudal* means “towards the feet” (Figure 1.7.a);
- *medial* means “towards the sagittal plane” while *lateral* means “away from the sagittal plane” (Figure 1.7.b);
- *ventral* and *anterior* are synonymous, and *dorsal* and *posterior* as well.

I will also refer to:

- the *rostro-caudal axis*, whose direction is given by the intersection between sagittal and coronal planes, and which denotes the direction from head to feet;
- the *medio-lateral axis*, whose direction is given by the intersection between horizontal and coronal planes, or informally: the left-right direction;
- the *dorso-ventral axis*, whose direction is given by the intersection between horizontal and sagittal planes.

Spinal cord and vertebral column

As mentioned in Section 1.1.1, the spinal cord constitutes one of the compartments of the CNS. Prolonging the brain stem in the caudal direction, its morphology resembles that of a centipede (Figure 1.8).

The “body” of the centipede is enclosed in the *vertebral column*. The vertebral column—also referred to as the *spine*—is an essential part of the skeleton of all vertebrates. It consists in a chain of individual bones called *vertebrae*, connected pair-wisely by ligaments. The human vertebral column counts 7 cervical, 12 thoracic, 5 lumbar, and 5 sacral vertebrae (Figure 1.9).

Vertebrae are composed of a *vertebral body* on the anterior side and a *vertebral arch* on the posterior side, and they are pierced by a central hole. Furthermore, the central holes of the different vertebrae are somewhat aligned along the rostro-caudal axis, forming the *vertebral canal*, where the spinal cord resides (Figure 1.10).

Vertebral ligaments seal the anterior and posterior sides of the vertebral canal, and the vertebral arches also partially close its left and right sides. However, between two consecutive vertebrae, lateral openings are left clear of any bone or ligament: the *intervertebral foramina* (singular: *foramen*).

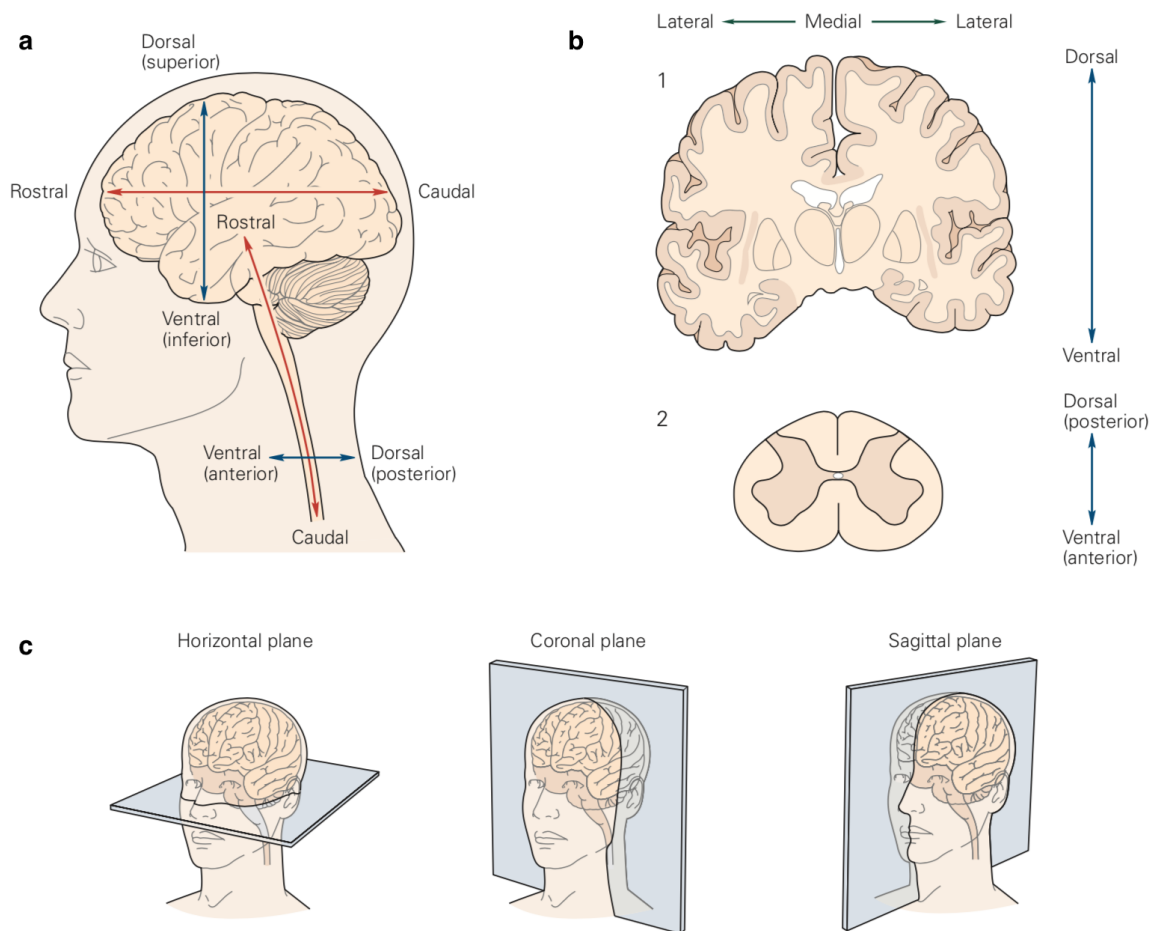


Figure 1.7 Anatomical terminology. [Picture adapted from [6].]

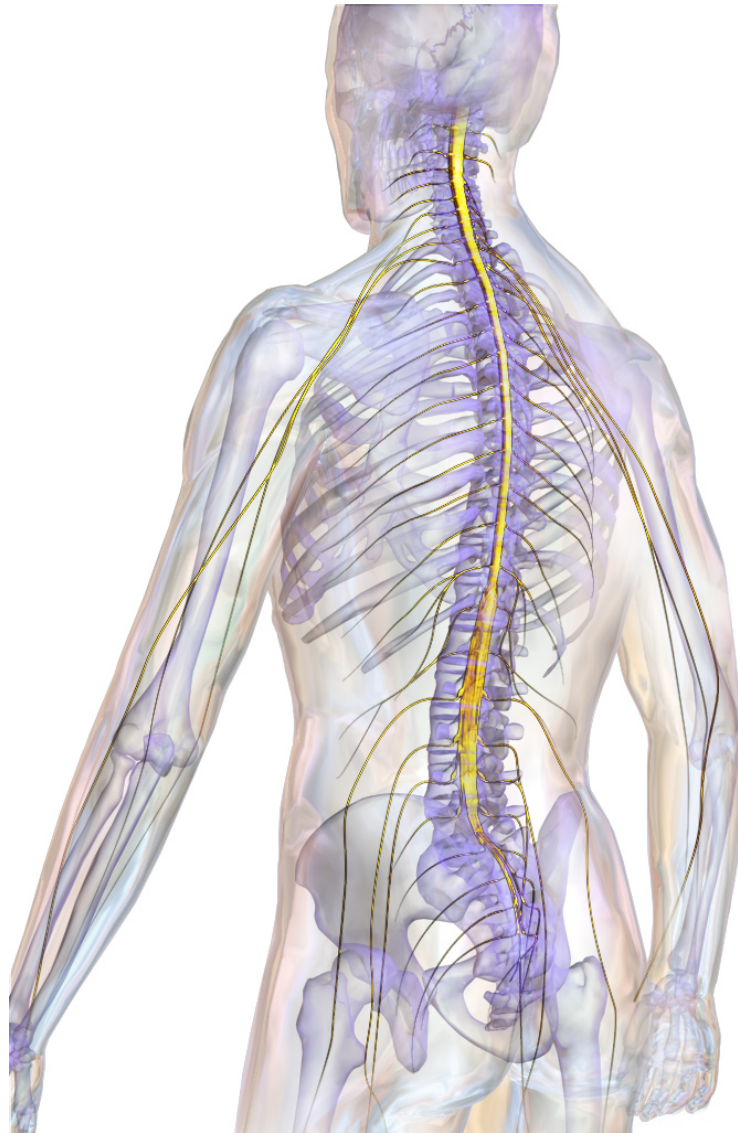




Figure 1.8 Tridimensional representation of the spinal cord in the human body. The central, yellow, elongated structure resembling a centipede represents the spinal cord. The thin yellow ramifications represent peripheral nerves. *[Picture by Bruce Blaus, Blausen Medical.  .*

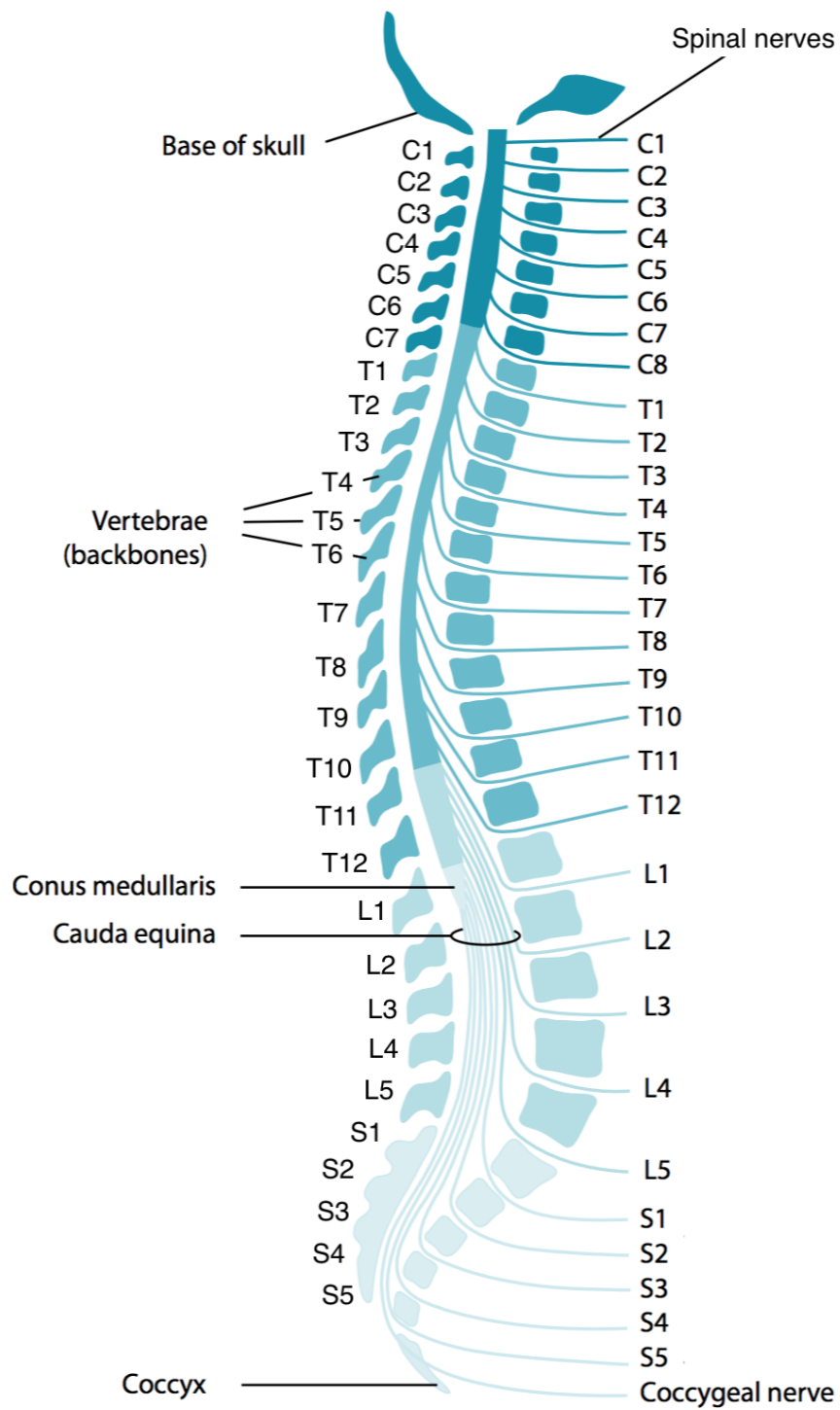


Figure 1.9 Organization of the human vertebral column and spinal cord. *[Picture adapted from [8].]*

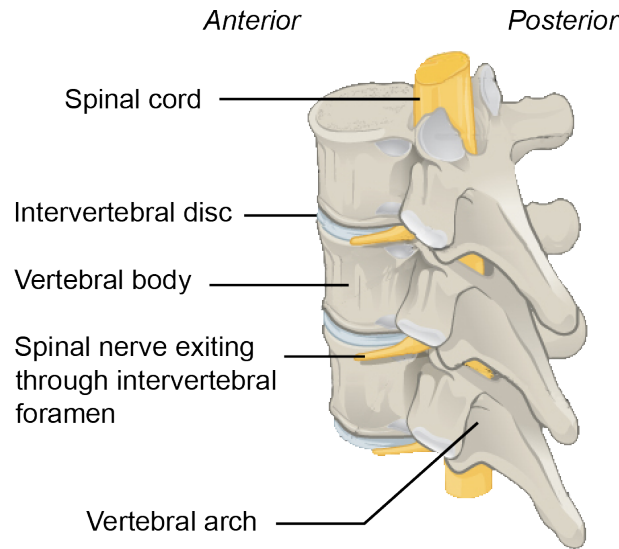


Figure 1.10 Vertebrae, spinal cord and spinal nerves. [Picture produced by Jordi March i Nogu , adapted with permission. .]

These openings allow the “legs” of the spinal-cord-centipede, the *spinal roots*, to exit the vertebral canal (Figure 1.10).

Spinal roots, spinal segments

Spinal roots go by groups of four: two ventral (one on the left side, one on the right side) and two dorsal (again, one on the left, one on the right) (Figure 1.11). The four spinal roots of a same group enter the spinal cord (or leave it, depending on how one looks at it) at nearly the same rostro-caudal level, defining a *spinal segment*.

There are almost as many spinal segments (*ie* groups of 4 spinal roots) as there are vertebrae in the vertebral column: just one more (Figure 1.9). The first and rostral-most group of spinal roots, the C1 roots (defining the C1 spinal segment), exits the vertebral canal above the C1 vertebra and below the skull. The second group, the C2 roots, exits through the left and right intervertebral foramina between the C1 and C2 vertebrae. And so on and so forth, until the junction between the C7 and T1 vertebrae: the roots exiting at that level are called the C8 roots, though there does not exist any C8 vertebra. Afterwards, the rule is simple: there is one group of spinal roots exiting the vertebral canal below each thoracic, lumbar, and sacral vertebra, and it takes the name of this vertebra. For instance, the roots exiting below the L4 vertebra (and above the L5 vertebra) are the L4 roots. But mind that the labeling is different in the cervical region: the roots exiting between the C5 and C6 vertebrae are the C6 roots for instance (Figure 1.9).

More precisely, after leaving the spinal cord, the *ipsilateral*³ ventral and dorsal roots of

³“of the same side” (left or right).

a spinal segment merge into *spinal nerves*. The merging itself takes place at the level of the intervertebral foramen, just after a protrusion presented by the dorsal root: the *dorsal root ganglion* (DRG). It is the spinal nerves which emerge out of the vertebral canal (Figure 1.11) and which subsequently become peripheral nerves (after eventual reorganization in the cervical or lumbo-sacral plexuses).

Furthermore, before entering in the the spinal cord, spinal roots split into small bundles arranged rostro-caudally: the *rootlets*, or *rootlet bundles*. In some regions of the spinal cord, the rootlets of consecutive roots form a pseudo-continuum of branches entering in the spinal cord, as depicted in Figure 1.12. In others, a gap exist between the rostral-most rootlet of a root and the caudal-most rootlet of the next rostral root.

Organization of the vertebral canal

Inside the vertebral canal, the spinal cord is protected by a series of *meninges* (Figure 1.11). The outermost meninge is the *dura*—or *dura mater*—, which constitutes an hermetic envelope around the entire CNS. It is filled with a liquid called *cerebro-spinal fluid*, in which the spinal cord and the brain are bathing. The dura is in fact composed of two layers: the outermost, called *periosteal layer*, which adheres to the inner surface of the skull and vertebral column (not represented in Figure 1.11); and the innermost, called *meningeal layer*, which is closer to the CNS. The space between these two layers is referred to as *epidural space*.

The remaining two meninges are the *arachnoid* and the *pia*—or *pia mater*. The former adheres to the inner surface of the meningeal layer of the dura, and the latter, which is a very thin membrane, adheres to the spinal cord and the brain (Figure 1.11). Due to this arrangement, the meningeal layer of the dura and the arachnoid can be seen as forming a single layer. In the remaining of the text, it is to this compound layer that *dura* will refer to.

In the vertebral canal, the dura (*ie* the compound layer) and everything it contains are known as the *dural sac*, and the space inside the dural sac, the *subdural space*. Surrounding the dural sac, filling the epidural space (*ie* the space between the inner surface of the vertebral column and the dura), one finds adipose tissue known as *epidural fat*, or simply *fat*.

Gray matter, white matter and spinal tracts

To conclude this brief anatomical description of the spinal cord and vertebral canal, I present the two compartments composing the spinal cord: the *gray matter* and the *white matter*.

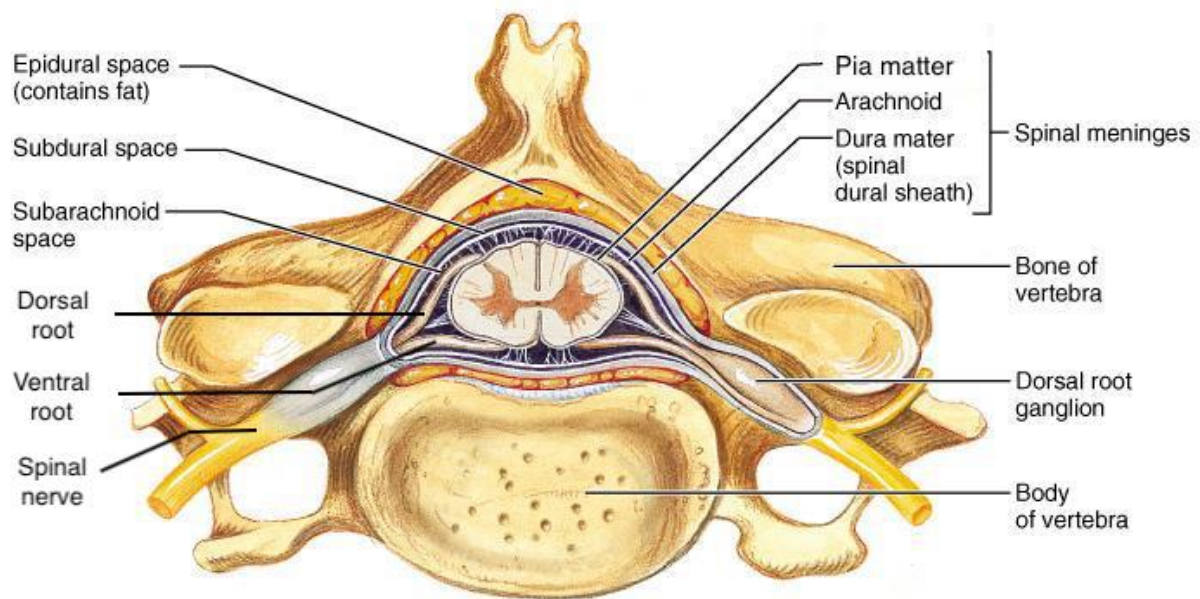


Figure 1.11 Transverse cross-section of the vertebral canal. *[Picture adapted from [9].]*

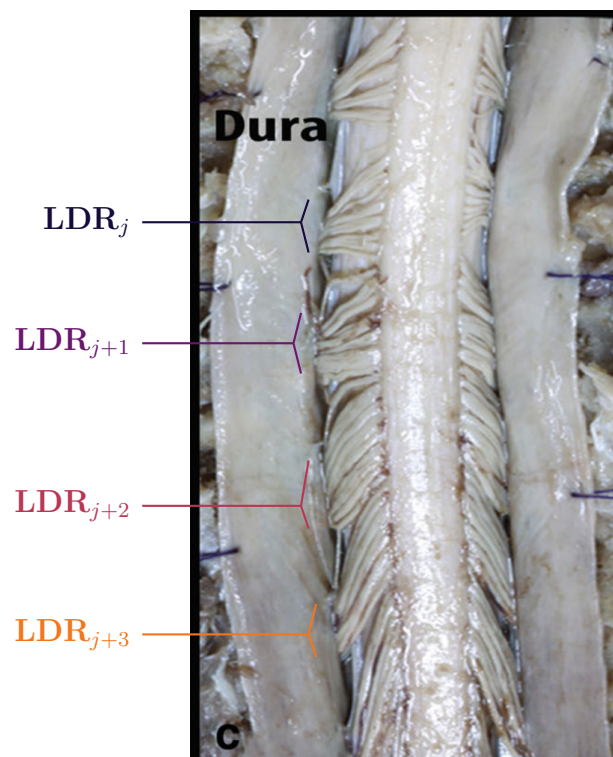


Figure 1.12 Pseudo-continuum of rootlets entering in the human spinal cord. The rootlet bundles of four consecutive left dorsal roots have been labeled. *LDR*: left dorsal root. *[Picture adapted from [10].]*

The gray matter (GM) occupies the central volume of the spinal cord: the white matter (WM) constitutes its outer shell (like the marrow and the bones). Cut in a transverse plane, the GM displays a characteristic shape reminding of a butterfly. Furthermore, two important regions distinguish themselves in the “wings” of the butterfly: the *dorsal horn* and the *ventral horn*, which are defined as their suggestive names indicate (see Figure 1.13). In between the two, one finds the *intermediate* or *middle region* of the gray matter.

On the other hand, the WM is somewhat cylindrical, but nonetheless present a thin but profound fissure on the anterior side: the *anterior median fissure*.

While the GM is essentially comprised of cellular bodies of neurons (with their dendritic trees and axons though), the WM is exclusively made of longitudinal nerve fibers running parallel along the rostro-caudal axis. WM nerve fibers can be split into two main categories: *descending* nerve fibers and *ascending* nerve fibers. As their names suggest, descending nerve fibers are axons of neurons located in the brain or in rostral spinal segments projecting caudally to innervate neurons in more caudal spinal segments. For ascending nerve fibers, the situation is reversed.

Furthermore, nerve fibers originating or projecting to the same brain areas are clustered together in the WM, forming so-called *spinal cord tracts*. The tracts most relevant to our study are represented in Figure 1.13.

1.1.3 The neuro-muscular system

I hereby denote *neuro-muscular system* the ensemble comprising the muscles, the motoneurons which actuate them, and the sensory neurons conveying signals about their state to the CNS. The focus is on skeletal muscles.

Muscles, muscle fibers

Skeletal muscles are the organs ultimately producing movement. Attached to bony segments via tendons, they can induce or oppose to rotations of these segments around their articulations by means of forcing contractions (Figure 1.14). To contract and exert torques on their bones of attachment, muscles rely on specialized cells called *muscle fibers*. Muscle fibers contain longitudinal structural elements—the *myofibrils*—which possess the faculty to contract under certain circumstances (Figure 1.15). Muscle fibers are the main constituents of skeletal muscles. They are arranged in parallel, and there may be from thousands to over a million of them in individual muscles.

Muscle fibers distinguish themselves by three important properties: *contraction speed*, *maximal force*, and *fatigability*. Contraction speed can be apprehended through the

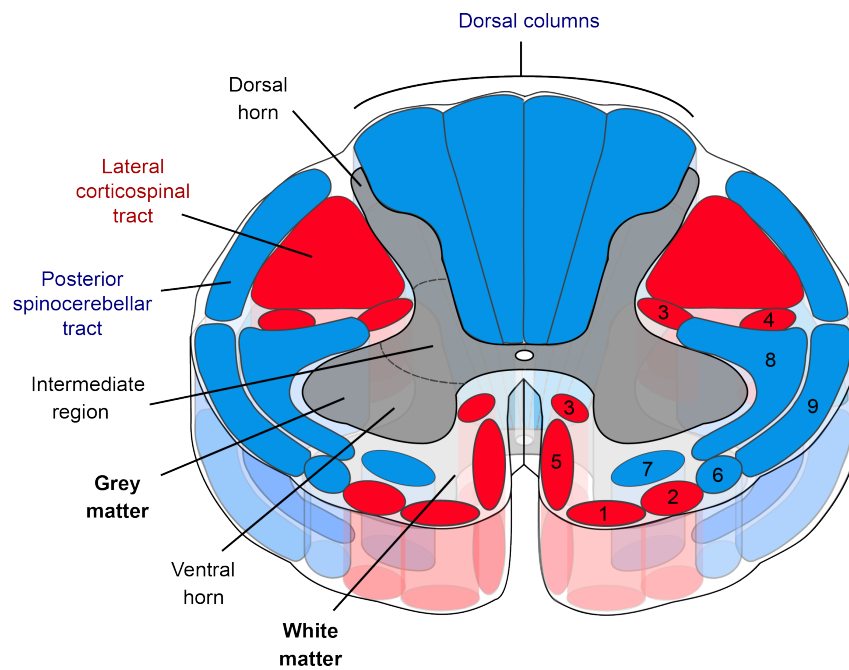


Figure 1.13 Gray matter, white matter and spinal tracts. *Blue*: spinal tracts comprised of ascending fibers. *Red*: spinal tracts comprised of descending fibers. 1: Vestibulospinal tract. 2: Olivospinal tract. 3: Reticulospinal tracts. 4: Rubrospinal tract. 5: Anterior corticospinal tract. 6: Spino-olivary tract. 7: Anterior spinothalamic tract. 8: Lateral spinothalamic tract. 9: Anterior spinocerebellar tract. [Picture produced by Mikael Häggström, adapted with permission. .]

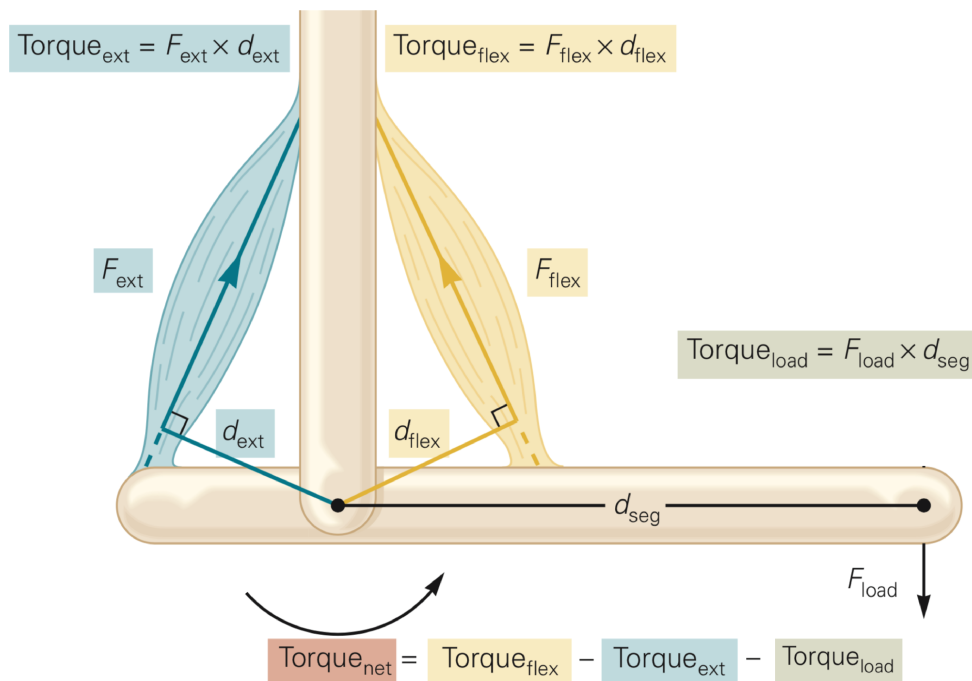


Figure 1.14 Muscle torques and movement. When the flexor muscle contracts (*flex*: flexor), an upward pulling force is exerted on the center of the right portion of the horizontal bone, resulting in a counterclockwise torque around the rotation axis articulating the two bones. If this torque exceeds the sum of the extensor torque (*ext*: extensor) and the load torque, the horizontal bone will effectively rotate in the counterclockwise direction around the axis. [Picture adapted from [6].]

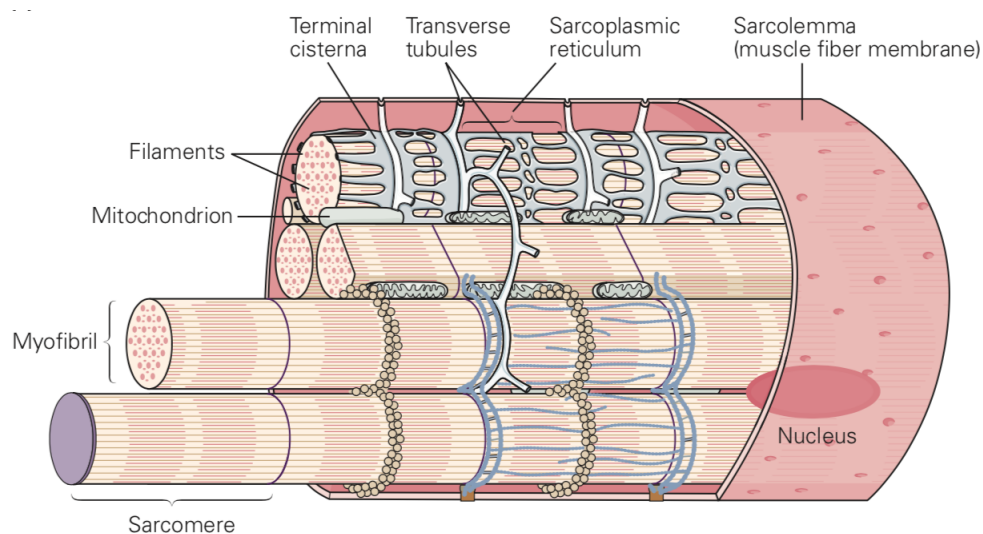


Figure 1.15 Internal structure of muscle fibers. [Picture taken from [6].]

contraction time, which is the duration needed by a muscle fiber to reach its maximal contraction force following the reception of a contraction signal. On the other hand, fatigability—or rather its opposite, *fatigue-resistance*—measures the ability of a muscle fiber to sustain contractions repeatedly and for long durations. Usually, muscle fibers with high contraction speeds and maximal forces are also highly fatigable, and vice-versa.

Furthermore, somewhat similarly to neurons, the membrane of muscle fibers contains ion channels and are subject to depolarizations and propagation of action potentials. When an action potential occurs in a muscle fiber, ion channels open and calcium ions (Ca^{2+}) invade the intracellular space of the muscle fiber. Calcium ions then bind to specific myofibril proteins, causing a cascade of molecular processes leading to their contractions.

Incidentally, it is the role of the nervous system to induce action potentials in muscle fibers, and more precisely, it is the role of spinal α -motoneurons.

Motoneurons, motor units and motor nuclei

Motoneurons are the final constituents of the neuro-motor system (the part of the nervous system dedicated to producing motor commands). Located in the ventral horn of the gray matter of the spinal cord, they are the only neurons to *send* signals to skeletal muscles.

There are essentially two types of motoneurons: the α -motoneurons and the γ -motoneurons. A major difference distinguishes them: the axons of γ -motoneurons innervate *intrafusal* muscle fibers (*ie* specialized muscle fibers located inside *muscle spindles*, a type of receptor found in skeletal muscles presented in Section 1.1.3), while the axons of α -motoneurons innervate *extrafusal* muscle fibers (those presented in the previous section).

Though the contraction of intrafusal muscle fibers contributes to the contractile force of muscles, this contribution is insignificant compared to that of the extrafusal muscle fibers⁴. Thus, the contraction of muscles is essentially due to α -motoneurons. For this reason, the developments reported in the following chapters have mostly focused on this latter class of motoneuron. Accordingly, unless stated otherwise, *motoneurons* will refer to α -motoneurons, *motor axons* to axons of α -motoneurons, and *muscle fibers* to extrafusal muscle fibers.

Individual motoneurons can innervate from a few muscle fibers to multiple thousands of them. However, any given motoneuron always innervates muscle fibers belonging to the same muscle, and usually of the same type (*ie* producing weak forces, slowly contracting and fatigue-resistant, or producing strong forces, rapidly contracting but highly fatigable). The ensemble formed by a motoneuron and the muscle fibers which it innervates is called a *motor unit*.

⁴The contraction of intrafusal muscle fibers play a different role, see [6].

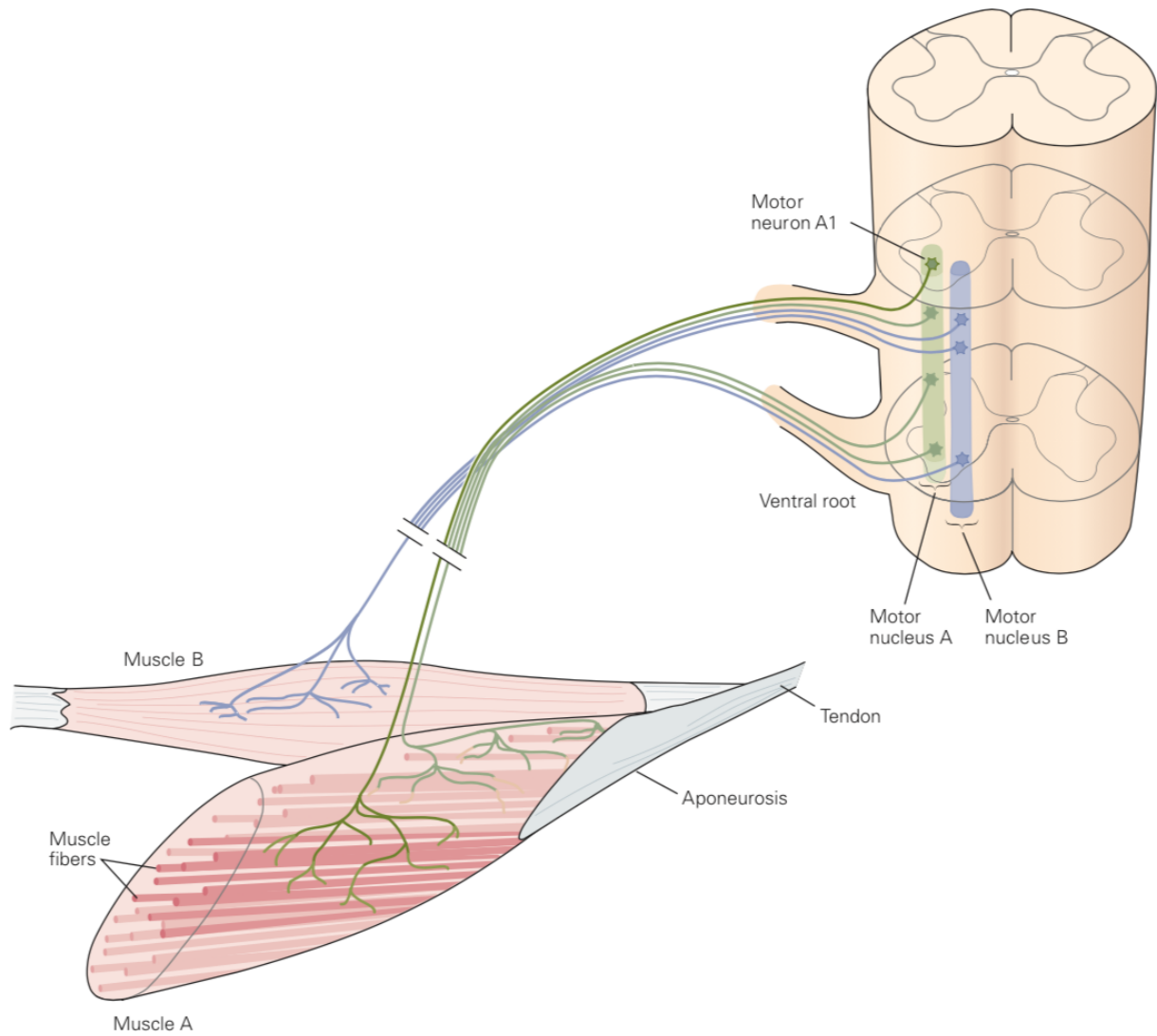


Figure 1.16 Spatial arrangement of the motor nuclei in the spinal cord. *[Picture taken from [6].]*

The innervation of muscle fibers by motor axons is of synaptic nature: the terminal ramifications of motor axons contact the membrane of muscle fibers via a synapse called the *neuromuscular junction*. As a matter of fact, the neuromuscular junction is a very efficient synapse: each action potential invading the synaptic terminals of a motor axon is sufficient to induce an action potential in the post-synaptic muscle fibers. Furthermore, due to the little influence of the terminal ramifications of a motor axon on the propagation delay from soma to synaptic terminals, an action potential generated in a motoneuron reaches all the synaptic terminals of its axon near-simultaneously. In turn, this results in synchronous action potentials in the innervated muscle fibers, giving rise to what is referred to as a *motor unit action potential* (MAP). However, when a stimulus induces a volley of action potentials in multiple motoneurons innervating the same muscle, a temporal dispersion will exist between the different MAPs that are elicited within that muscle, corresponding to the different propagation durations along the different motor axons involved. The temporally dispersed electrical activity arising during these events, which can last for as much as 20 ms, is referred to as a *compound muscle action potential* (CMAP). CMAPs are commonly referred to as *muscle responses* or *muscular responses*.

Finally, let us mention that the collection of all the motoneurons innervating a given muscle constitute the *motor nucleus* of the muscle, and that the motoneurons of a given motor nucleus are clustered together in the spinal cord, arranged along a column spanning one or more spinal segments (Figure 1.16).

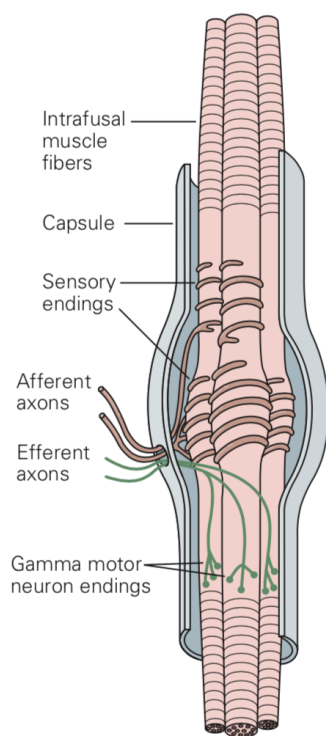
Muscle spindles, group-Ia fibers and group-II fibers

As mentioned in the previous section, apart from extrafusal muscle fibers, skeletal muscles contain *muscle spindles*. Muscle spindles are fusiform capsules lying among—and parallel to—the extrafusal muscle fibers, and enclosing specialized—intrafusal—muscle fibers (Figure 1.17).

In addition to being innervated by γ -motoneurons, intrafusal muscle fibers are also innervated by the peripheral endings of *group-Ia* and *group-II fibers*. Here the innervation is not of synaptic nature: it consists in the fibers' terminal ramifications being coiled around the intrafusal muscle fibers (Figure 1.17). When the muscle is stretched, the intrafusal muscle fibers are also stretched, and the terminal ramifications of group-Ia and group-II fibers themselves get stretched. This causes the opening of specialized ion channels in their membrane and leads to their depolarization and subsequent generation of action potentials.

Group-Ia and -II fibers (*ie* axons) belong to pseudo-unipolar neurons whose somata are located in the dorsal root ganglia (see **C** of Figure 1.2). After leaving the muscle spindle capsules and running through their dedicated peripheral nerve, these fibers keep on

A Muscle spindle



B Intrafusal fibers of the muscle spindle

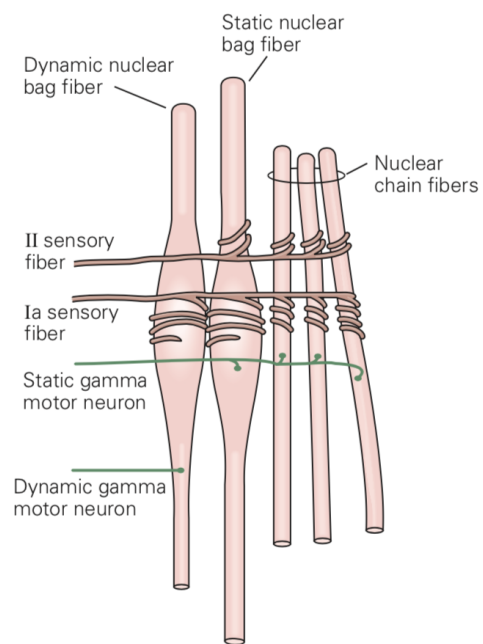


Figure 1.17 Muscle spindles, γ -motor axons, group-Ia and group-II fibers. [Picture taken from [6].]

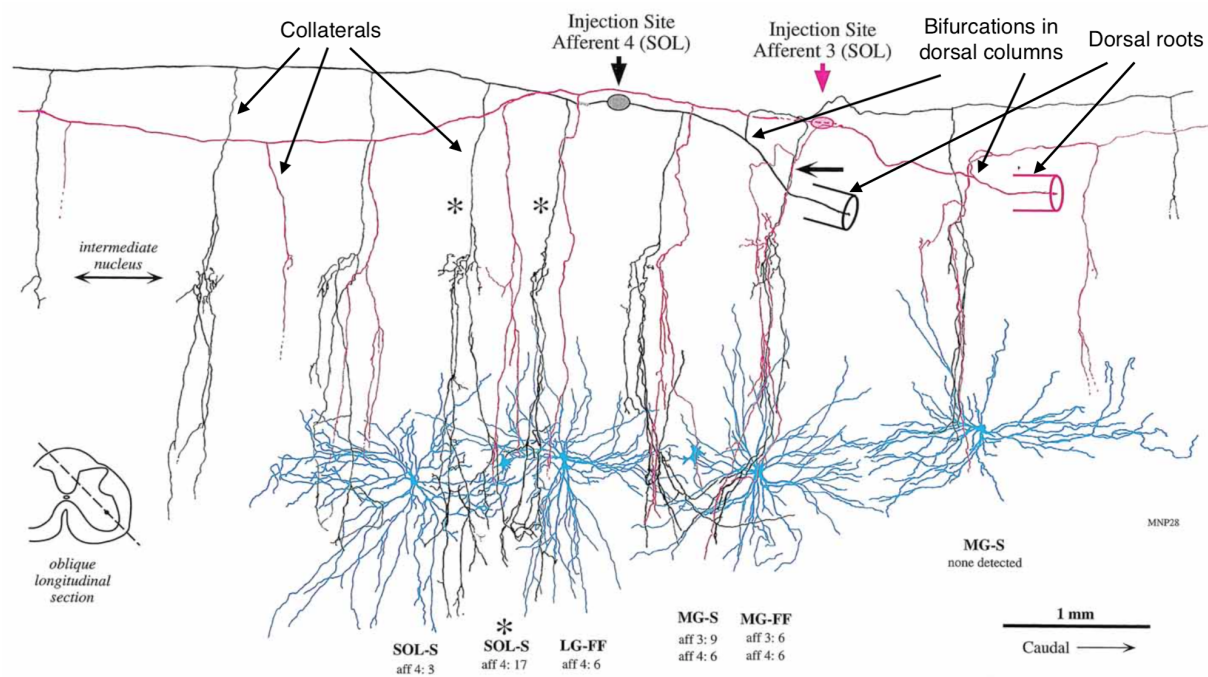


Figure 1.18 Morphology of group-Ia fibers. The trajectories of two group-Ia fibers originating from the soleus muscle (SOL) of a cat, stained with horseradish peroxidase, are represented in black and in pink. I have indicated the bifurcation points of their dorsal root branches. The dendritic trees of homonymous motoneurons (SOL-S) and heteronymous motoneurons (LG-FF, MG-S and MG-FF) innervated by these group-Ia fibers are represented in light blue. *S*: slow-contracting motoneuron. *FF*: fast-fatigue motoneuron. [Picture adapted from [11].]

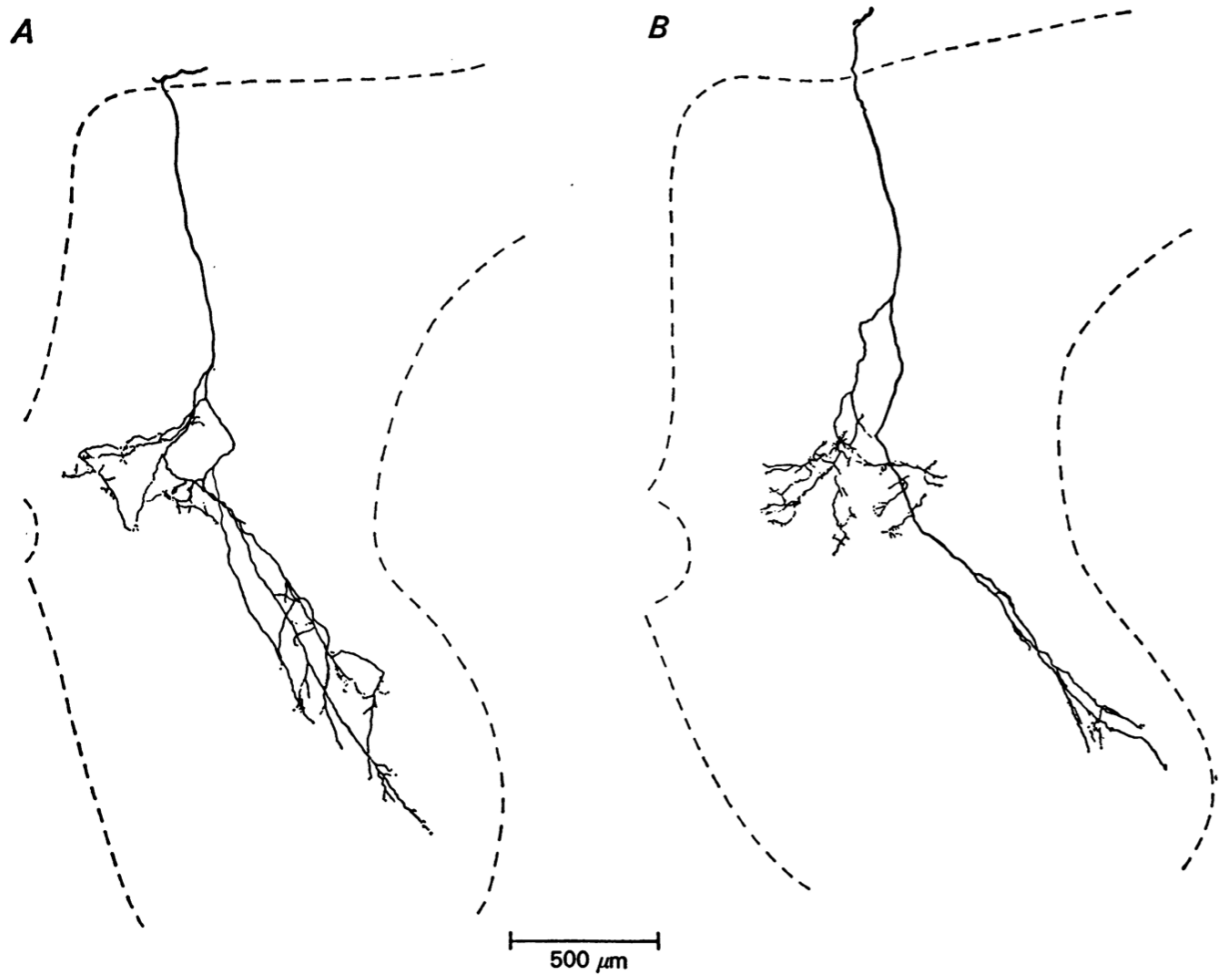


Figure 1.19 Group-Ia fiber collaterals in the transverse plane. The trajectories of two adjacent collaterals of the same group-Ia fiber from the gastrocnemius-soleus muscle of a cat, stained with horseradish peroxidase, are represented. In each of **A** and **B**, the solid line represents the collateral and the dashed line represents the border of the gray matter. *[Picture taken from [12].]*

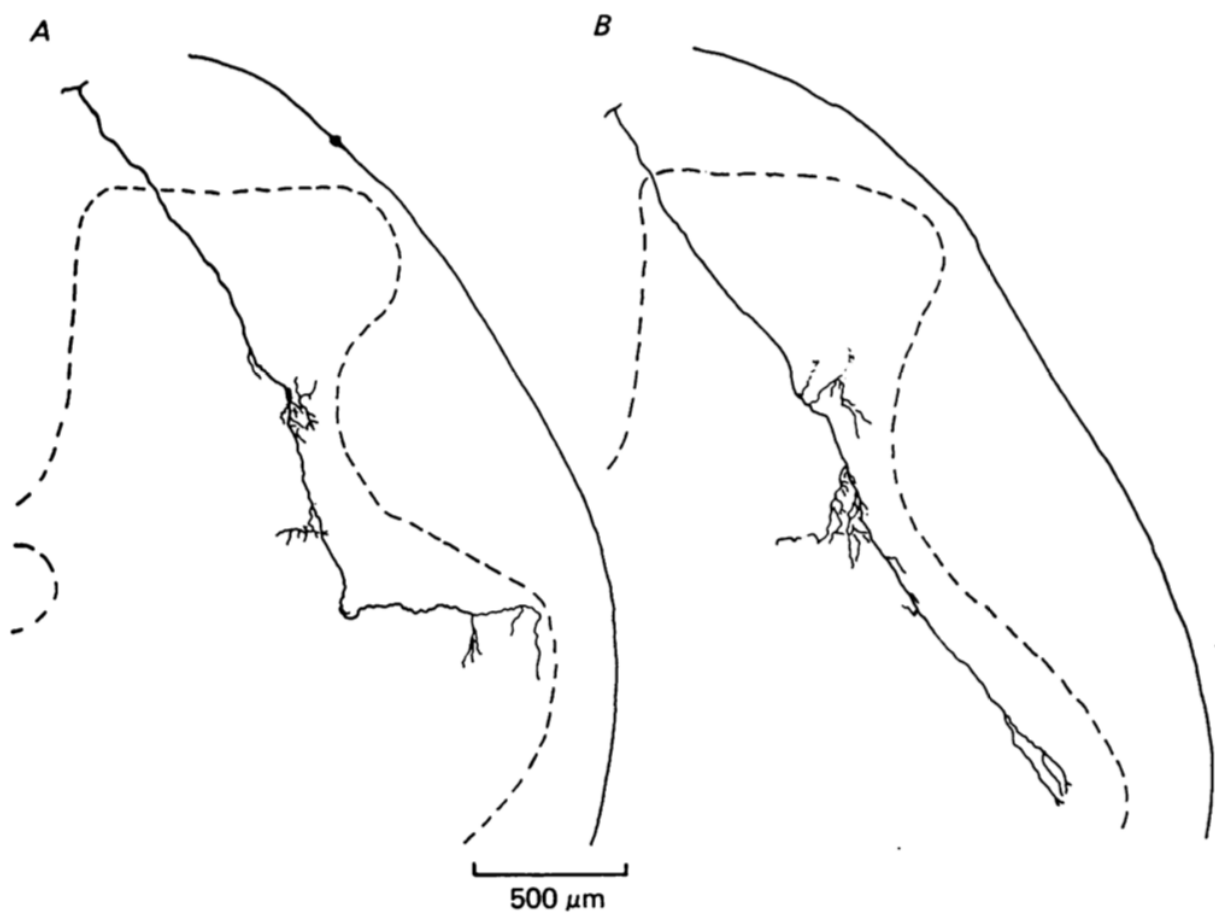


Figure 1.20 Group-II fiber collaterals in the transverse plane. The trajectories of two adjacent collaterals of the same group-II fiber from the gastrocnemius-soleus muscle of a cat, stained with horseradish peroxidase, are represented. In each of **A** and **B**, the jagged solid line represents the collateral, the dashed line represents the border of the gray matter, and the circular solid line represents the border of the white matter. *[Picture taken from [13].]*

running in the posterior spinal roots, beyond the dorsal root ganglia, until they reach the CNS. There, their central terminal endings innervate neurons in the spinal cord and up in the brain.

Because they convey signals from the periphery to the CNS, these fibers are referred to as *sensory afferents*—or *sensory fibers*, *afferent fibers*, or simply *afferents*. More specifically, since they relay information about the state of the body itself, they participate to the sense of *proprioception* and are referred to as *proprioceptive fibers*.

Importantly, they are relatively thick, and they are myelinated. As a matter of fact, group-Ia fibers belong to the $A\alpha$ diameter class: the thickest fibers of the nervous system (12 μm to 20 μm). On their part, group-II fibers belong to the $A\beta$ diameter class (8 μm to 12 μm), the second thickest after the $A\alpha$ class.

Furthermore, the CNS part of these fibers present a highly branching morphology. Upon entering the spinal cord, their dorsal root branch bifurcates into two branches running in the dorsal columns⁵: one ascending and one descending [11–14]. Moreover, new bifurcations—referred to as *collateral branches* or *collaterals*—depart from these dorsal column branches and project transversally towards the gray matter, where they further ramify to innervate various neuronal populations [15] (see Figures 1.18 to 1.20).

Importantly, the collaterals of group-Ia fibers are known to form excitatory synaptic contacts with *homonymous* and *heteronymous* motoneurons [11, 16]. For a given group-Ia fiber, homonymous motoneurons are motoneurons which innervate the very muscle from which the fiber originates, and conversely, heteronymous motoneurons are motoneurons innervating other muscles⁶.

I will often refer to group-Ia fibers and group-II fibers as *Ia-fibers* and *II-fibers* respectively.

Golgi tendon organs and group-Ib fibers

Another important type of muscular sensory organ is the *Golgi tendon organ* (Figure 1.21). Golgi tendon organs make the link between muscles and tendons. More specifically, each individual Golgi tendon organ is connected at one end to a few (10 to 20) muscle fibers, and at the other end to the tendon proper.

Furthermore, similarly to muscle spindles, Golgi tendon organs are innervated by the peripheral endings of sensory fibers: the *group-Ib fibers*. Here, the innervation consists in the intertwining of the terminal ramifications of group-Ib fibers in the collagen fibers composing the Golgi tendon organs (Figure 1.21). When muscles contract, the collagen fibers of Golgi tendon organs are stretched, compressing the Ib-fiber ramifications and caus-

⁵I will occasionally refer to these branches as *rostro-caudal branches* or *rostro-caudal bifurcations*.

⁶Usually, heteronymous motoneurons innervate muscles acting synergistically with the fiber's muscle of origin, *ie* which contract in synchrony with it and contribute to the same movements.

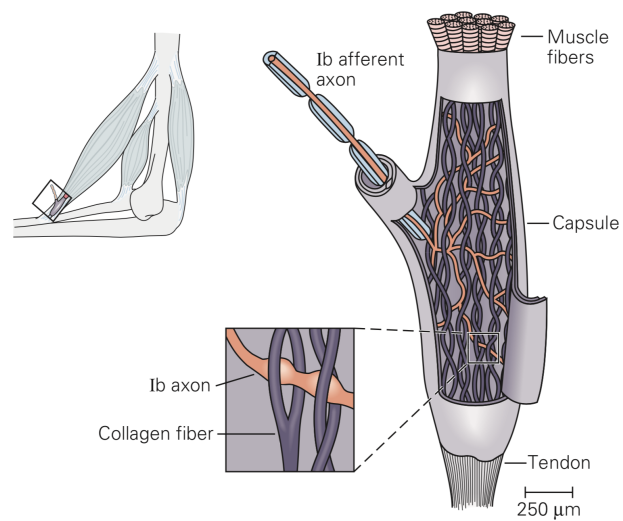


Figure 1.21 Golgi tendon organs and group-Ib fibers. *[Picture taken from [6].]*

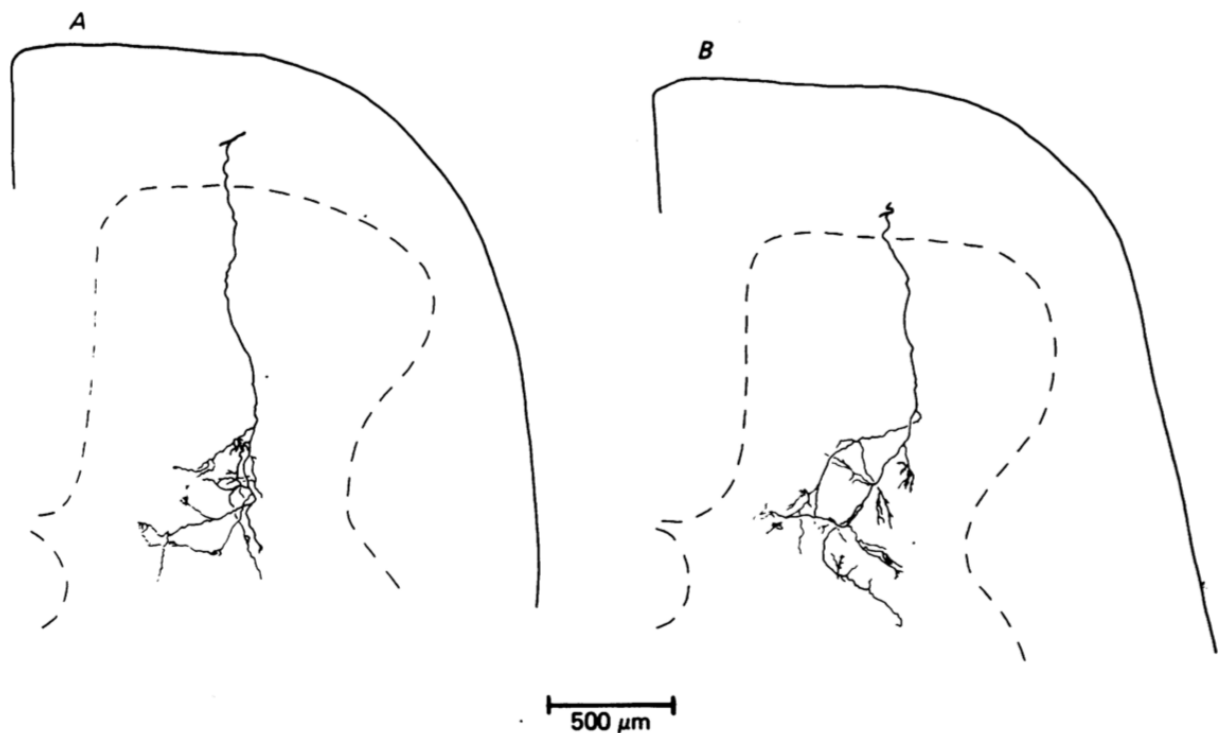


Figure 1.22 Group-Ib fiber collaterals in the transverse plane. The trajectories of two adjacent collaterals of the same group-Ib fiber from the gastrocnemius-soleus muscle of a cat, stained with horseradish peroxidase, are represented. In each of **A** and **B**, the jiggling solid line represents the collateral, the dashed line represents the border of the gray matter, and the circular solid line represents the border of the white matter. *[Picture taken from [13].]*

ing the opening of mechano-sensitive ion channels embedded in their membrane. Thus, muscle-contraction causes depolarization and subsequent generation of action potentials in group-Ib fibers.

The morphology of group-Ib fibers is similar to that of group-Ia and group-II fibers. They belong to pseudo-unipolar neurons whose somata are located in the dorsal root ganglia, and their dorsal root branch bifurcates into dorsal column branches from which transversal collaterals depart (see Figure 1.22). Moreover, they also are myelinated, and they belong to the A α diameter class.

Electromyography

I end this section dedicated to the neuro-muscular system by a short presentation of the *electromyography* technique. The purpose of electromyography (EMG) is to provide an indirect measure of the contractile activity of skeletal muscles via the recording of their electrical activity.

The principle at the core of electromyography is the following: since the contraction of muscle fibers is triggered by action potentials, by placing recording electrodes inside or in the vicinity of a muscle, it should be possible to measure electrical currents when the muscle contracts. Moreover, since the electrical currents generated by multiple muscle fibers should add (with both constructive and destructive spatiotemporal interferences), the intensity of the recorded electrical currents should reflect the total number of activated muscle fibers. In turn, this gives an indication of the proportion of motoneurons that were activated to induce the muscle contraction.

When the recording electrodes are directly inserted in the muscles (generally in the form of metallic needles or wires), we refer to them as *intramuscular* or *percutaneous EMG electrodes*, and the wires connecting the extra-corporal recording apparatus to the implanted electrodes are said to be *percutaneous*. When the electrodes are placed on the skin—which still allows to record currents whose sources are within specific muscles—we refer to them as *surface EMG electrodes*. Finally, the electrical activity recorded with EMG electrodes is often referred to as *EMG activity*, and muscular responses recorded with EMG electrodes sometimes called *EMG responses*.

1.1.4 Electrical stimulation of the spinal cord

This dissertation is predominantly concerned with a technique for stimulating the spinal cord termed *epidural electrical stimulation* (EES). Here, I lay down some terms and concepts regarding the electrical stimulation of the spinal cord that will be found throughout the dissertation. I also give a brief description of the typical hardware that is used to stimulate the spinal cord epidurally. For a thorough and illuminating presentation of the

physical processes underlying the electrical stimulation of biological tissues from the point of view of stimulating electrodes, the reader can consult [17].

Monopolar stimulation

The electrical stimulation of the spinal cord consists in using the body (and more specifically the spinal cord) to conduct electrical currents between two (or more) electrodes placed inside (or on the surface) of the body.

Monopolar stimulation is one of the simplest stimulation paradigm. It involves only two electrodes. The first electrode—termed *stimulating* or *active* electrode—is placed in the body region which is to be stimulated (for instance in the epidural space of the vertebral canal, to stimulate the spinal cord). Instead, the second electrode—termed *return* or *ground* electrode—is placed in a remote body region. The return electrode is generally of large dimensions and placed in a tissue weakly sensitive to electrical currents and electric potential fluctuations. It is sometimes placed on the skin. The injection or withdrawal of electrical current through this electrode should have no effect on the surrounding tissue: it should act as a mere return for the current injected through the active electrode. Instead, the active electrode is generally of small dimensions (although not too small for safety reasons), such that delivering electrical current through it induces important electric potential fluctuations in its vicinity, exciting the tissues (which can be neural, muscular, etc.) found there.

When positive current effectively flows from the active electrode to the return electrode (driving the electric potential of the active electrode positively, and the electric potential of the return electrode negatively), the stimulation is said to be *anodic*, and the active electrode to be an *anode*. In the reverse situation, the stimulation is said to be *cathodic*, and the active electrode to be a *cathode*.

Bipolar stimulation

Bipolar stimulation is the second simplest stimulation paradigm. Like monopolar stimulation it involves only two electrodes, but the two electrodes are placed together and close-by in the body region that is to be stimulated. In this situation the two electrodes are referred to as anode and cathode, similarly as in the monopolar paradigm.

Multipolar stimulation

As the name suggests, multipolar stimulation covers any paradigm where more than two electrodes are involved to inject and withdraw electrical current in the body. For safety reasons, all stimulation systems are built such that the currents injected through all the

electrodes sum up to zero. Generally, one electrode—again referred to as the *ground* or *return* electrode—is used to withdraw any excess current injected by the others.

Implanted stimulation systems

Recent technological advances have permitted the elaboration of stimulation systems fully-implanted in the body of patients or experimental animals. A fully-implanted stimulation system is generally comprised of:

- an implantable pulse generator (IPG);
- a series of electrodes, forming an *electrode array*, connected to the IPG via insulated wires running in the body.

The IPG contains a chemical battery and all the electronic equipment necessary to generate stimulation waveforms to be delivered in the body through the electrodes. It is controlled by ancillary extra-corporal devices communicating with it wirelessly. Depending on the IPG hardware, multiple stimulation paradigms may be available. Ideally, the electric current flowing through any electrode or the voltage between any electrodes could be prescribed, although in practice limitations exist. Furthermore, the enclosure of the IPG itself (often referred to as the *IPG case*) can be connected to the IPG electronic circuitry to serve as a return electrode.

Extra-corporal stimulation systems

For the purposes discussed in this dissertation, the notable difference between extra-corporal stimulation systems and implanted systems such as described above is that the former allow to apply electrodes on the surface of the skin. These can serve to really inject electrical current in the body—like in transcutaneous electrical stimulation [18]—or merely to withdraw eventual excess currents delivered by implanted electrodes connected to the extra-corporal stimulation system via percutaneous wires [19].

Epidural electrode arrays

To electrically stimulate the spinal cord from the epidural space in humans and experimental animals, three main types of electrodes have been or are being used:

- micro-wire electrodes, constituted by an insulated metallic wire whose tip is freed from insulation;

- cylindrical percutaneous electrode arrays, such as depicted on the left of Figure 1.23, in which cylindrical metallic contacts are distributed along a rod, separated from one another by insulating cylindrical portions;
- paddle electrode arrays, such as depicted on the right of Figure 1.23, in which small rectangular metallic contacts (with active area of typically few mm²) are distributed over a two-dimensional grid and embedded in a large rectangular matrix of insulating material.

One notable difference between percutaneous electrode arrays and paddle electrode arrays is that the active contacts of the former are free to inject current over 360°, while the insulating paddle of paddle electrode arrays forces the current to flow towards the non-insulated side of the active contacts.

1.1.5 Hybrid neurophysical volume conductor models

I end this quite lengthy introduction by giving a very brief and general description of hybrid neurophysical volume conductor models, whose underlying theory and computational scheme are presented in detail in Chapter 2.

One important purpose of hybrid models is to simulate the electrical behavior of neurons and nerve fibers in response to electrical stimulation. As their names indicate, they are based on two or more independent submodels: a volume conductor model, and one or several neurophysical models of neurons and nerve fibers.

Volume conductor models

Volume conductor models are idealized tridimensional representations of biological tissues in which each tissue is represented by a volume filled with a uniform material characterized by its electrical conductivity. Their purpose is to compute the tridimensional electric potential distribution elicited in the spinal cord by solving a variational formulation of Poisson's equation, complemented by appropriate boundary conditions, using the finite element method (FEM).

Neurophysical models

On the other hand, neurophysical models attempt to capture the electrical behavior of neurons and nerve fibers by means of electrical circuits in which the components (conductances, capacitances and batteries) represent the lumped electrical properties of neurons and nerve fibers. These models notably allow to estimate the spatiotemporal fluctuations of the membrane potential and thus the generation and propagation of action potentials along the represented entities.

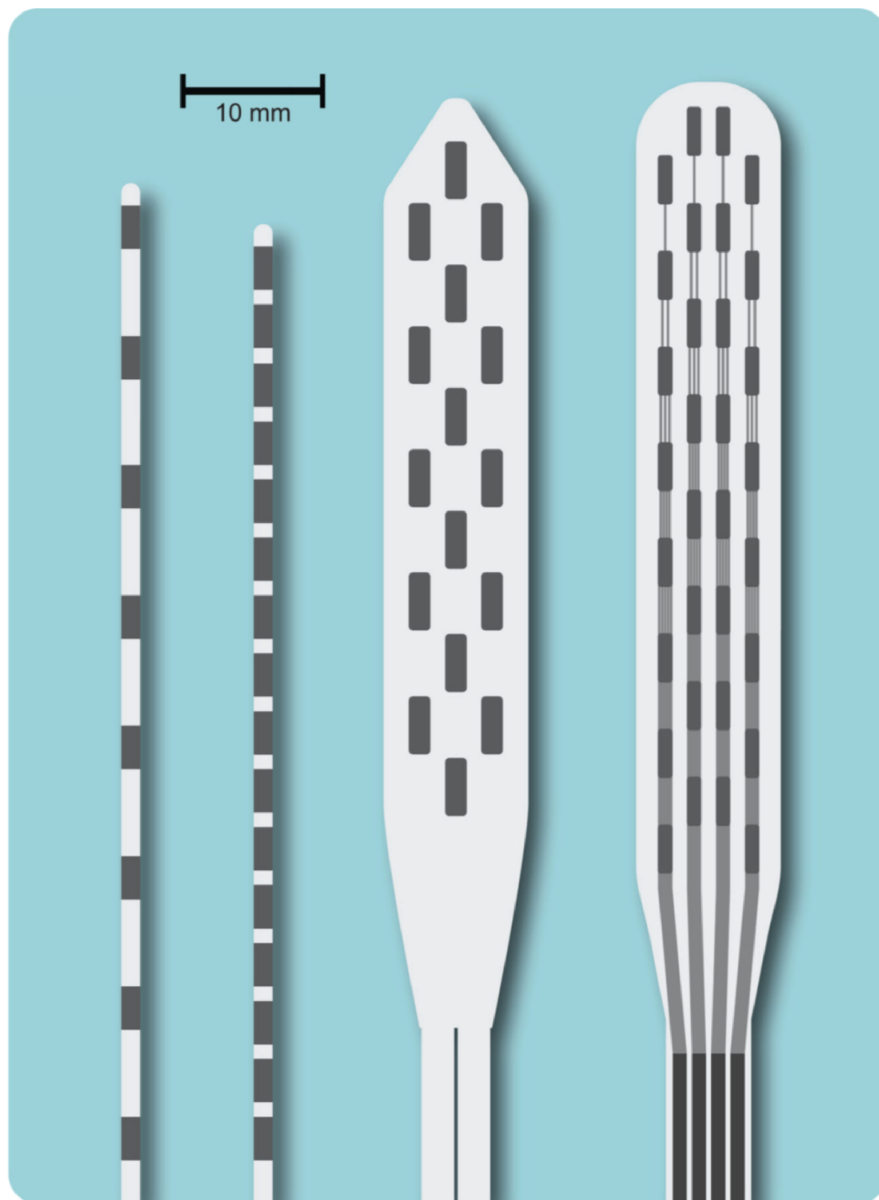


Figure 1.23 Clinical epidural electrode arrays. *Left:* two percutaneous electrode arrays. *Right:* two paddle electrode arrays.[Picture adapted from [20].]

Inter-model communication

The bridge between the two class of models is ensured by using the electric potential distribution calculated with the FEM in the volume conductor model as input to the extracellular electric potentials of neurophysical models. This procedure first requires interpolation of the electric potential along the trajectories of putative neurons and nerve fibers in the volume conductor model, at the central positions of their representative compartments in the neurophysical models.

1.2 Problematic

The motor disorders experienced by individuals affected by chronic SCI are of neurological nature. The limbs and muscles of these individuals remain functional⁷, but the commands issued by the nervous system to actuate them are disrupted.

Ultimately, it is via motoneurons located in the spinal cord that the nervous system issues its contraction commands to skeletal muscles. Under healthy conditions, spinal motoneurons integrate synaptic inputs from a wide range of sources to produce the firing patterns underlying motor behavior. These sources include supra-spinal neurons (notably from the motor cortex and the brain stem), proprio-spinal neurons, sensory neurons (from dorsal root ganglia), and a large variety of spinal interneurons, themselves integrating descending and sensory inputs to modulate the activity of motoneurons.

After SCI, this modulation is disrupted for motoneurons located either at the level, or below the level of the lesion. While in the first case the disruption is directly due to the damages undergone by the spinal circuits at the level of the lesion during or following the SCI event [22] (the motoneurons themselves may have been damaged and may no longer exist), in the second case, the spinal circuits remain intact and functional: it is their communication with supra-spinal centers which is compromised⁸. Either way, motor function in the limbs controlled by the affected circuits is impaired.

Over the last decades, EES of the spinal cord has emerged as a promising tool to restore functional activity in spared spinal circuits which are deprived of appropriate modulation after SCI. To phrase it in one sentence, the strategy pursued with EES is to apply electrical stimulation to the spinal cord to bring the spared but inactive sensorimotor circuits in a state of increased excitability so as to enable them to integrate residual descending commands and sensory inputs to produce coordinated, functional motoneuronal activity again.

Most studies involving EES have focused on the circuits controlling the lower-limbs, located in the lumbosacral spinal segments⁹. They have demonstrated that EES applied to the lumbosacral segments could mitigate a wide range of lower-limb motor deficits and promote long-term recovery of voluntary motor control after SCI [23–31]. Recently, the study of Wagner and colleagues even demonstrated restoration of voluntary locomotion in individuals who had been completely paralyzed for multiple years following SCI [30].

By contrast, there have been very few attempts to use EES to reactivate the circuits

⁷Though they are usually atrophied due to their prolonged disuse [21].

⁸Which is due to damages undergone by communication pathways, *ie* axons ensuring direct communication between the brain and the spinal circuits or proprio-spinal neurons in charge of integrating and relaying ascending or descending signals, at the level of the lesion.

⁹These circuits are often spared after SCI because many SCIs occur at the cervical and thoracic spinal levels, several segments rostral to the lumbosacral segments.

controlling the upper-limbs, located in the cervical segments. Yet, these circuits should be largely spared after high cervical SCI¹⁰, suggesting that EES may also be applicable in this context.

The first reported use of cervical EES to restore upper-limb function in humans is dated 2016, and remains the only one to date [32]. Searching the literature, one can also find two investigations about cervical EES conducted in rodents [33, 34] and one in monkeys [35], all dated later than 2014.

To summarize, what is stemming from these studies is (i) that EES applied to the cervical spinal cord can evoke contractions in upper-limb muscles, (ii) it can improve arm and hand function in humans with tetraplegia [32], but (iii) the observed improvements remained limited, and (iv) the specificity of the cervical spinal cord and its implications on the mechanisms by which EES engages upper-limb muscles remain largely unknown and unexplored. Importantly, a roadmap to guide the design of epidural electrode arrays tailored to the cervical spinal cord and of stimulation strategies exploiting cervical EES is still missing.

Incidentally, studies devoted to the lumbosacral segments have uncovered important mechanisms of action of EES, the understanding of which has played a significant role in the clinical achievements mentioned above. Besides, these mechanisms may also prevail when applying EES to the cervical segments.

Like any other paradigm of electrical stimulation of the nervous system, EES modulates the activity of spinal circuits via two basic mechanisms: (i) direct induction of action potentials in neurons and axons; and (ii) sub-threshold polarizations of neuron somata, dendrites and pre-synaptic terminals, which—though sub-threshold—influence the overall activity of the stimulated neural circuits [36].

While little is known about the second mechanism, numerous computational and experimental findings indicate that the direct induction of action potentials primarily takes place in large myelinated sensory fibers running in the posterior roots and in the dorsal columns of the spinal cord¹¹ [18, 38–42]. Furthermore, the direct recruitment of motoneurons in the gray matter or of their axons in the ventral roots should only occur at stimulation amplitudes significantly higher than necessary to recruit dorsal sensory fibers [18, 38, 39, 43].

As a matter of fact, this preferential recruitment of dorsal sensory fibers over ventral motor axons is a desirable characteristic of EES. The reason is that re-enabling motor tasks via the direct recruitment of motoneurons—or motor axons—poses two challenges which cannot be overcome satisfactorily even with state-of-the-art neuro-modulation technologies:

¹⁰The motor nuclei of upper-limb muscles are found in spinal segments C5 to T1, and high cervical SCI are located at or above the C4 level.

¹¹This is due both to the morphology (large diameters) and neurophysical properties (myelination) of these fibers [37], and to their spatial proximity to dorsal epidural electrodes [18, 38, 39].

(i) since any motor task involves the contraction of multiple muscles with independent timings, this approach requires (a) the ability to selectively induce action potentials in groups of motor axons innervating individual muscles, and (b) that the temporal profiles of muscular activation underlying the intended motor tasks be known¹²; and (ii) since thicker motor axons have lower excitation thresholds to extracellular stimulation [37], and since these same axons generally belong to fast-fatigue motor units [6], engaging muscles via extracellular recruitment of motor axons usually leads to rapid muscular fatigue¹³ [46].

By contrast, the action exerted on motoneurons following the recruitment of dorsal sensory fibers is indirect, mediated by synaptic transmission¹⁴. Large myelinated sensory fibers running in the posterior roots and in the dorsal columns include proprioceptive and cutaneous fibers which provide synaptic excitation both directly to motoneurons and to spinal interneurons [6]. For instance, muscle spindle group-Ia fibers provide monosynaptic excitation to homonymous and heteronymous motoneurons and connect to various interneuronal populations in different areas of the gray matter [11, 14]. Similarly, group-Ib fibers from Golgi tendon organs, muscle spindle group-II fibers, and class-A β fibers from low-threshold cutaneous mechanoreceptors connect to specific populations of interneurons, and sometimes directly to motoneurons [15, 47]. Thus, direct induction of action potentials in large dorsal sensory fibers supply excitatory inputs to widespread populations of neurons, thereby increasing the overall level of excitability of the spinal circuits.

Furthermore, since the nerve fibers found in the dorsal columns are for the most part the rostral-caudal bifurcations of posterior root fibers [12, 13, 48–52] (in fact, of fibers coming from *all* the posterior roots), electrical stimulation from the dorsal epidural space is likely to recruit sensory fibers coming from many posterior roots simultaneously. In turn, this is likely to spread the stimulation-induced synaptic inputs to a range of neuronal populations that is wide not only in terms of neuronal type, but also in terms of spatial localization and peripheral organs which they contribute to control¹⁵.

¹²One could argue that, to restore a 100% natural motor function, the ability to reproduce the natural firing patterns of each individual motor axon is in fact necessary, which in turn requires the ability to selectively induce action potentials in each of them—which is way out of reach.

¹³Though strategies exist to attenuate this effect [44, 45].

¹⁴Letting aside the sub-threshold polarizations mentioned previously.

¹⁵This is because fibers running in different roots are likely to originate from distinct peripheral organs (*ie* muscles, dermatomes, etc.)—especially if the roots are multiple spinal segments apart—and because sensory fibers predominantly modulate neurons involved in the control of their organs of origin [6]. However, it should be pointed out that the distribution of sensory fibers in the posterior roots remains largely undocumented to date, which is both surprising and unfortunate given the importance this distribution has on everything concerning EES (mechanisms, effects, design of electrodes, stimulation protocols, etc.). Nonetheless, there are convincing arguments to think that fibers originating from the same peripheral organs *are* clustered together in the posterior roots. For instance, since at their central end, group-Ia fibers innervate predominantly homonymous motoneurons, it seems logical that they enter the spinal cord at the segmental level where these motoneurons are located. Thus, the group-Ia fibers innervating a given muscle are likely to be clustered together in the few posterior roots whose corresponding segments

Conversely, the very same reasoning suggests that recruiting individual posterior roots may restrict the range of modulated neurons in the spinal cord, and targeting individual rootlets even more so. In particular, it may allow to modulate specific motor nuclei or groups of motor nuclei and their pre-motor proprioceptive circuits, which is likely desirable to restore motor function¹⁶. As a matter of fact, it has long been known that individual electric stimuli administered to a posterior root evokes efferent volleys in the corresponding ventral root¹⁷ [53], implying a restricted number of activated motor nuclei¹⁸. Furthermore, the primary discharge in these evoked volleys have been identified to be mediated by mono-synaptic pathways, *ie* essentially by group-Ia fibers [43].

How selectively EES is amenable to target posterior structures (*eg* roots vs. dorsal columns, or roots vs. other roots) and to modulate specific ensembles of motor nuclei are questions that have been addressed from multiple angles in the context of lumbo-sacral stimulation, yielding no definitive answer. Computational studies seem to indicate that appropriate electrode placements and stimulation amplitude ranges may allow to recruit individual posterior roots with high selectivity [38, 42], but no direct experimental evidence for this selectivity has been reported yet¹⁹. Nonetheless, a series of findings tend to corroborate this hypothesis [25, 30, 31, 43]. For instance, Minassian and colleagues [43] have observed that delivering EES at moderate stimulation amplitudes from electrodes located at the level of rostral lumbar segments evoked mono-synaptic responses in muscles whose motor nuclei were located in rostral segments, and similarly for the caudal lumbar and sacral segments²⁰. On the same note, the team led by Courtine has been quite successful at recruiting specific ensembles of motor nuclei by steering the stimulation towards the posterior roots of their host spinal segments [25, 30, 31].

contain the muscle's motor nucleus. Besides, it is known that sensory fibers from specific muscles, joints or dermatomes indeed aggregate into fascicles in the distal portions of peripheral nerves [6], and though peripheral nerves undergo important reorganizations at the brachial and lumbosacral plexuses (to form the posterior and anterior spinal roots), it can be hypothesized that fascicles are preserved across these plexuses, keeping sensory fibers of shared origin in the same posterior roots.

¹⁶This may seem contradictory to what I have stated previously regarding the direct recruitment of motor axons—namely that strategies attempting to directly reproduce motoneuronal firing patterns suffer from important intrinsic limitations—, but here the goal sought is not to directly activate motor axons or motoneurons: it is to raise the excitability of the motoneurons to help and let the nervous system activate them in a coordinated and functional manner.

¹⁷The author of [53] did not mention that these efferent volleys occurred *exclusively* in the corresponding ventral root, but I believe that this was implied in his statement.

¹⁸This is because the efferent volleys recorded in a ventral root are due to the activity of motoneurons located exclusively within its spinal segment, and there is only a limited number of motor nuclei represented in any given spinal segment.

¹⁹This would require to monitor the activity of dorsal root ganglia neurons of multiple posterior roots simultaneously while at the same time stimulating the spinal cord from the epidural space: it is in itself a very challenging experiment, and yet there is a more fundamental problem, which is that the necessary recording apparatus would likely interfere with the stimulation, compromising the relevance of the recorded signals.

²⁰Minassian and colleagues [43] also demonstrated that the specificity of the muscle recruitment can be lost at high stimulation amplitudes, and that in this case, the evoked responses are at least partly due to the direct recruitment of motor axons.

As a matter of fact, the objective underlying the latter investigations [25,30,31] was to deliver stimulation patterns modulating specific motor nuclei only at times when they should normally be active during motor behavior [54]. To this end, epidural electrode arrays have been specifically tailored to the lumbo-sacral spinal cord of rats and monkeys [25,31], and multipolar stimulation configurations—whereby the electrical current is injected through multiple contacts of an electrode array²¹—have been used in humans [30], increasing the selectivity with which muscles or groups of muscles could be engaged with current clinical epidural implants. As it turned out, these “spatiotemporal” patterns of EES revealed more efficacious to restore lower-limb function than conventional EES protocols.

All the above findings and clinical achievements suggest that a similar strategy might be employed to reactivate the cervical circuits after high cervical SCI, but the framework developed in the context of lumbo-sacral stimulation and sketched here above is missing for cervical stimulation. Important questions, such as whether the preferential recruitment of dorsal sensory fibers over ventral motor axons is preserved or not when stimulating the cervical segments, or how selectively the cervical posterior structures may be targeted and how this can translate into selective modulation of specific upper-limb motor nuclei, remain unelucidated to date.

To address these questions, numerical simulations seconded by animal experimentation constitute an appropriate entry point. Firstly because computational findings can guide the experimentation towards relevant directions; secondly because virtual environments allow to estimate quantities which are inaccessible to direct measurement in experimental or clinical settings; and thirdly because they enable to assess the influence of specific model parameters and to explore large parameter spaces beyond what is practically doable in experimental or clinical settings.

Nonetheless, they can not substitute themselves to physical world experimentation, especially in view of the development of actual clinical treatments. Moreover, new clinical treatments (or the novel use of already clinically-approved techniques and devices for new therapeutic targets) require that their efficacy and safety be first demonstrated in animal models. In the specific case of SCI treatments, and in particular for the restoration of upper-limb function, non-human primates provide unique advantages compared to other species [57]. For instance, the connection between the motor cortex and cervical motor circuits in humans present great similarities with that of monkeys (and important dissimilarities with that of rodents) [57]. An exclusive resemblance also prevail regarding their upper-limb musculature, suggesting that it might also be the case of their cervical proprioceptive circuits organization. Thus, a framework developed for cervical EES in monkeys may straightforwardly translate to humans.

²¹This technique allows to “steer” the electrical current within biological tissues and is often employed in the context of deep brain stimulation or cochlear stimulation [55,56].

On the modeling side, a widely used class of models to study the recruitment of neurons and nerve fibers induced by EES of the spinal cord is that of hybrid neurophysical volume conductor models [18,30,38,39,42,58,59]. As mentioned in the previous paragraphs, these models have proved valuable to understand the mechanisms of action of EES in the context of lumbo-sacral stimulation. Yet, previous realizations have entailed modeling options likely limiting the accuracy of the estimated recruitment of dorsal nerve fiber populations. For instance, spinal roots have seldom been represented by explicit material compartments in the volume conductor model, and posterior root fibers have been running in the cerebrospinal fluid (CSF) instead [18,38,39,42], although the difference in conductivity between spinal roots and CSF is substantial, likely impacting the electric potential along these fibers. Likewise, the dorsal column bifurcations of dorsal root fibers and the collaterals of dorsal column fibers have not been represented when evaluating the recruitment selectivity of individual dorsal roots [38,42]. Furthermore, few attempts have been made to use hybrid models to evaluate the indirect recruitment of motoneurons induced by pre-motor pathways, notably by group-Ia fibers [60]. In particular, the numbers of group-Ia fibers possessed by different muscles, which may have a significant influence on the Ia-mediated excitability of their motor nuclei (and thus on the ability of EES to engage them), have not yet been assessed.

Hybrid models can also be used to find multipolar stimulation configurations allowing to target specific neural structures more selectively [55,61–63]. In the context of spinal cord EES, this could be employed to find configurations targeting specific dorsal rootlets, which may refine the modulation exerted on spinal circuits. However, the configurations accessible to any multi-electrode array are theoretically countless and in practice, very numerous. The computational scheme of hybrid models may enable an efficient exploration of the configurations space, involving only a small number of FEM calculations and subsequent interpolations, which are highly computationally costly. Leveraging the superposition principle, the electric potential induced by arbitrary multipolar configurations can be obtained as a linear combination of a small set of basis solutions. However, uncertainties remain regarding the boundary conditions that shall be used to define the basis solutions.

1.3 Research objectives and dissertation outline

Given the problematic sketched above, the main objective of my thesis work was quite clear from the very beginning. It was to develop a hybrid neurophysical volume conductor model of EES specifically of the cervical spinal cord to address the following questions:

- When stimulating epidurally the cervical spinal cord, which are the primary neural targets of the stimulation? In particular, is it likely that cervical EES directly recruit motor axons? Or is it instead plausible that EES excite cervical motoneurons purely through pre-motor pathways, in particular via Ia-fibers?
- Can cervical EES modulate specific cervical motor nuclei? What are the implications of the cervical spinal cord anatomy on this ability? What are the implications of the distribution of afferent fibers in the dorsal roots and in the dorsal columns?
- How should we tailor epidural electrode arrays for the cervical spinal cord to maximize this specificity?

After reviewing the literature on hybrid models of EES of the spinal cord, it appeared that geometric and physical parameters, such as the dimensions and conductivity of the volume conductor compartments, or the position and trajectory of nerve fibers and neurons, had a significant influence on these models' predictions. Furthermore, it seemed that, although previous developers of hybrid models have benefited from the experience of their own predecessors, they all have had to build their own model from scratch. Being quite a lengthy exercise, I thus sought to develop a tool that could build such models as automatically as possible given a set of parameters specified by a user. For my own research, as I acquired more numerous and more precise information on the anatomy of the spinal cord and of spinal nerve fibers and neurons, to be able to update my model without having to build it from scratch each and every time was essential. To develop such a tool, which would build parameterized models quasi-automatically, I had to first devise an abstract geometrical model of the spinal cord and of the other constituents of the vertebral canal, including the spinal roots and epidural electrode arrays with their insulating paddle, as well as of trajectories of spinal nerve fibers and neurons in relation with the geometry of the spinal cord. This aspect of my work is presented in Chapter 3, where I also present the influence of some of the refinements which I introduced in my models.

Once my tool was ready, I could start building specific model instances to address the questions listed above regarding EES of the cervical spinal cord. These computational investigations were part of a broader collaborative effort at uncovering the mechanisms and the therapeutic potential of cervical EES, which also entailed a technological development

part and an experimental aspect involving non-human primates. Our team sought to develop epidural electrode arrays tailored to the cervical spinal cord, and the role of these experiments was to test for such arrays on macaque monkeys, as well as to test for hypotheses regarding cervical EES. For this reason, and to enable comparison between my model predictions and experimental data, I based my model on the anatomy of the macaque monkey, which required elaborating an anatomical database notably through in-house measurements and medical imaging techniques. These investigations are the object of Chapter 4.

One of the findings of our study was that the selectivity with which EES can modulate specific cervical motor nuclei is limited by the mix of different populations of afferent fibers in the dorsal spinal roots. Targeting individual rootlets may increase this specificity, for which multipolar stimulation configurations achieving appropriate current steering will certainly be required. I thus started questioning whether my hybrid model could be used to find optimal such configurations. I found that this had already been done by previous investigators, and that the approaches that have been employed were quite varied. I thus sought to understand what were the hypotheses underlying different approaches, and to propose a general and versatile approach which would be both numerically efficient and justified on the theoretical ground. These developments are reported in Chapter 5.

CHAPTER 2 BIO-ELECTROMAGNETISM AND HYBRID NEUROPHYSICAL VOLUME CONDUCTOR MODELS

In this chapter, I present the essential elements of theory underlying a class of computational models which may be called *hybrid neurophysical volume conductor models*, and which occupy a central place in the developments of this dissertation.

As the name indicates, hybrid neurophysical volume conductor models combine (i) a volume conductor model, and (ii) one or several neurophysical models of neurons and nerve fibers, which are conjugated in a multi-step computational scheme.

Hybrid models are commonly used for two main purposes:

- estimating the electrical behavior of neurons and nerve fibers in response to artificial electrical stimulation;
- estimating the electric potential resulting from the activity of neurons and nerve fibers that would be measured by hypothetical recording electrodes.

The modeling developments of this dissertation concern the hybrid models responding to the first use-case, and accordingly, the theoretical elements presented in the following sections are adapted to this specific context.

In Section 2.1, the assumptions and approximations leading to the multi-step computational scheme of hybrid models are laid down. In Section 2.2, a general presentation of volume conductor models is given. Finally, the specific neurophysical models which I have used, and the minor modifications that I have made to them, are exposed in Section 2.3. No general presentation of neurophysical models is included, since these models are barely affected by the developments of the thesis.

2.1 Bio-electromagnetism

By essence, the phenomena involved during electrical stimulation of the nervous system are of electromagnetic nature. Thus, the appropriate theoretical framework for their study is the theory of electromagnetism, of which the reader will find a good introduction in [64] and a more advanced presentation in [65].

In this section, I present the essential elements of this theory in relation to the electrical stimulation of biological tissues, the nervous system in particular. The aim is to spell out the main assumptions leading to the computational scheme of hybrid neurophysical volume conductor models. The development is inspired from that exposed in [66], which I have found illuminating.

2.1.1 Electromagnetic field and Maxwell's equations

The theory of electromagnetism stipulates the existence of a couple of vector fields (\mathbf{E}, \mathbf{B}), respectively termed the *electric* and *magnetic fields* and collectively referred to as the *electromagnetic field*, which are defined in every point of space and any instant in time, and which interact with the charged particles of matter.

The physical laws which govern the evolution of the electromagnetic field are classically described by four equations, referred to as *Maxwell's equations* after the physicist James Clerk Maxwell whom largely contributed to their establishment in the second half of the 19th-century. These are:

$$\left\{ \begin{array}{l} \nabla \cdot \mathbf{E}(\mathbf{x}, t) = \frac{\rho(\mathbf{x}, t)}{\epsilon(\mathbf{x}, t)} \\ \nabla \times \mathbf{E}(\mathbf{x}, t) = -\frac{\partial \mathbf{B}}{\partial t}(\mathbf{x}, t) \\ \nabla \cdot \mathbf{B}(\mathbf{x}, t) = 0 \\ \nabla \times \mathbf{B}(\mathbf{x}, t) = \mu(\mathbf{x}, t) \mathbf{j}(\mathbf{x}, t) + \mu(\mathbf{x}, t) \epsilon(\mathbf{x}, t) \frac{\partial \mathbf{E}}{\partial t}(\mathbf{x}, t) \end{array} \right. \quad \begin{array}{l} (2.1) \\ (2.2) \\ (2.3) \\ (2.4) \end{array}$$

The definitions and units of the symbols involved in these equations are the following:

- \mathbf{x} is the tridimensional space variable. Its magnitude is expressed in m.
- t is the time variable. It is expressed in s.
- \mathbf{E} is the electric field. Its magnitude is expressed in V m^{-1} .
- \mathbf{B} is the magnetic field. Its magnitude is expressed in T.
- ρ is the electric charge density. It is expressed in C m^{-3} .

- ϵ is the electric permittivity of the medium. It is expressed in $\text{C V}^{-1} \text{m}^{-1}$.
- \mathbf{j} is the electric current density. Its magnitude is expressed in A m^{-2} .
- μ is the magnetic permeability of the medium. It is expressed in T m A^{-1} .

2.1.2 Electric scalar potential, magnetic vector potential, Lorenz Gauge

Since \mathbf{B} is divergence-less according to Equation (2.3), it can be expressed as the curl of a vector field \mathbf{A} , ie $\mathbf{B} = \nabla \times \mathbf{A}$. Choosing any of the possible candidates for \mathbf{A} , we denote it as the *magnetic vector potential*.

Substituting $\nabla \times \mathbf{A}$ into Equation (2.2) and rearranging the terms, we obtain:

$$\nabla \times \left(\mathbf{E} + \frac{\partial \mathbf{A}}{\partial t} \right) = \mathbf{0}$$

Being irrotational, the vector field $\mathbf{E} + \frac{\partial \mathbf{A}}{\partial t}$ can be expressed as the gradient of a scalar field V (or better, as its opposite), ie:

$$\mathbf{E} + \frac{\partial \mathbf{A}}{\partial t} = -\nabla V$$

Defined within a constant, V is termed the *electric scalar potential* or simply *electric potential*.

Recall that since \mathbf{A} was chosen arbitrarily, it is always possible to change our choice, but that in so doing, V would also be modified.

Nonetheless, the \mathbf{E} and \mathbf{B} fields are insensitive to transformations of the form:

$$\begin{cases} \mathbf{A} \rightarrow \mathbf{A} - \nabla U \\ V \rightarrow V + \frac{\partial U}{\partial t} \end{cases}$$

where U is any scalar field.

These are called *gauge transforms*, and a most relevant one to obtain relevant expressions for the electromagnetic field is the *Lorenz gauge*, which is such that the chosen \mathbf{A} and V satisfy the requirement:

$$\nabla \cdot \mathbf{A} = -\epsilon\mu \frac{\partial V}{\partial t} \quad (2.5)$$

2.1.3 Volume conduction and volume source

In the case of biological tissue, it is possible to elaborate on Maxwell's equations due to two specificities of the medium:

1. it is conductive, characterized by a conductivity σ (expressed in S m^{-1});
2. it is filled with electric current sources.

These current sources can be of two origins:

- biological cells which convert chemical energy into electrical energy;
- artificial devices such as electrodes plugged to current generators or chemical batteries.

Taken together, these *primary* current sources can be described by an *impressed* current density $\mathbf{j}_i(\mathbf{x}, t)$. Furthermore, since the medium is conductive, the electric field induced by these primary sources give rise to a *conduction* current density $\mathbf{j}_c(\mathbf{x}, t) := \sigma(\mathbf{x}, t)\mathbf{E}(\mathbf{x}, t)$.

Thus, the current density in Equation (2.4) can be expressed as $\mathbf{j}(\mathbf{x}, t) = \mathbf{j}_i(\mathbf{x}, t) + \mathbf{j}_c(\mathbf{x}, t) = \mathbf{j}_i(\mathbf{x}, t) + \sigma(\mathbf{x}, t)\mathbf{E}(\mathbf{x}, t)$.

2.1.4 Case of the infinite, linear, homogeneous, isotropic medium

When the permittivity ϵ , permeability μ , and conductivity σ do not depend on the \mathbf{E} and \mathbf{B} fields, the medium is said to be *linear*.

Medium linearity implies Maxwell's equations' linearity, allowing to *superpose* (*ie* to add) the fields arising from different sources to obtain the field arising from the compound source, which is known as the *superposition principle*.

In particular, this allows to express the field arising from any source as a Fourier series or integral of the fields induced by mono-harmonic sources (*ie* oscillating at a single frequency ω).

Writing Maxwell's equations for such a mono-harmonic source, and adopting the Lorenz gauge, it is possible to derive the *inhomogeneous Helmholtz equation* for the electric potential [67]:

$$\nabla^2 V - \gamma^2 V = \frac{\nabla \cdot \mathbf{j}_i}{\sigma + j\omega\epsilon} \quad (2.6)$$

where j is the complex number such that $j^2 = -1$ and where $\gamma^2 := j\omega\mu\sigma - \omega^2\mu\epsilon$.

Note that in this equation, ϵ , μ and σ may depend on ω and that they are functions of the space variable, as well as \mathbf{j}_i and V .

If the medium is also assumed to be infinite, homogeneous (ϵ , μ , and σ independent of the space variable) and isotropic (ϵ , μ , and σ have the same value in all directions), Equation (2.6) can be solved analytically, yielding an integral expression for V [68]:

$$V(\mathbf{x}) = \frac{1}{4\pi(\sigma + j\omega\epsilon)} \int_{\mathcal{V}} \frac{\nabla \cdot \mathbf{j}_i(\mathbf{x}') e^{-\gamma R'}}{R'} d\mathcal{V} \quad (2.7)$$

where $R' := |\mathbf{x} - \mathbf{x}'|$ and where \mathcal{V} denotes the whole space.

If \mathbf{j}_i is concentrated at the origin, injecting isotropically a total amount of current I , the solution displays spherical symmetry and can be written:

$$V(R) = \frac{Ie^{-\gamma R}}{4\pi(\sigma + j\omega\epsilon)R} \quad (2.8)$$

where R denotes the distance to the origin.

2.1.5 Quasi-stationarity

Under certain circumstances, the electromagnetic field can be considered to be *quasi-static*, which means that it can be considered to be stationary at any instant in time, or said differently, that it is equal at any instant to the field that would be induced if the sources at that instant were stationary.

This is equivalent to say that any change in the sources is propagated infinitely rapidly, affecting the \mathbf{E} , \mathbf{B} , V and \mathbf{A} fields instantaneously everywhere in space.

In the case of the infinite, homogeneous, linear, isotropic medium, considering Equation (2.7), Plonsey and Heppner [68] have noted that this was the case when:

1. $|\gamma R'| \ll 1$ for all \mathbf{x}' where $\nabla \cdot \mathbf{j}_i(\mathbf{x}') \neq \mathbf{0}$, and for all ω ;
2. $\omega\epsilon \ll \sigma$ for all ω .

In this case, Equations (2.7) and (2.8) can be rewritten as:

$$V(\mathbf{x}) = \frac{1}{4\pi\sigma} \int_{\mathcal{V}} \frac{\nabla \cdot \mathbf{j}_i(\mathbf{x}')}{R'} d\mathcal{V} \quad (2.9)$$

and:

$$V(R) = \frac{I}{4\pi\sigma R} \quad (2.10)$$

indeed showing that once converted back to the time domain via Fourier integration, temporal variations of \mathbf{j}_i or I would be instantaneously transmitted to V .

Using experimentally-measured properties of biological tissues [69], Plonsey and Heppner [68] went on to demonstrate that given the size of biological systems ($R'_{\max} \leq 1$ m) and the frequency content of purely biological current sources (rarely exceeding 1 kHz), the two above conditions are fairly well met.

However, comparing the solutions of Equation (2.8) and Equation (2.10) for artificial current sources conventionally used in electrophysiology (with frequency-content extending

well beyond 1 kHz), Bossetti and colleagues [67] have found non-negligible discrepancies between them.

Still, they noted that the parameter most influencing the accuracy of the computed solutions was the medium conductivity σ , and they concluded that the quasi-static approximation could be employed to study most applications involving biological systems.

2.1.6 Poisson's equation

Embracing the quasi-static approximation, it is possible to derive a relatively simple equation for the electric potential from Maxwell's equations, known as *Poisson's equation*.

Taking the divergence of Equation (2.4), noting that the divergence of a curl is always zero, and assuming that the permeability μ is that of free-space [68], one obtains:

$$\nabla \cdot \left(\mathbf{j}(\mathbf{x}, t) + \epsilon(\mathbf{x}, t) \frac{\partial \mathbf{E}}{\partial t}(\mathbf{x}, t) \right) = 0$$

Expressing \mathbf{j} as the sum of the impressed and conduction currents yields:

$$\nabla \cdot \left(\epsilon(\mathbf{x}, t) \frac{\partial \mathbf{E}}{\partial t}(\mathbf{x}, t) + \sigma(\mathbf{x}, t) \mathbf{E}(\mathbf{x}, t) \right) = -\nabla \cdot \mathbf{j}_i(\mathbf{x}, t)$$

Assuming a mono-harmonic source:

$$\nabla \cdot \left(j\omega\epsilon(\mathbf{x}, \omega) \mathbf{E}(\mathbf{x}) + \sigma(\mathbf{x}, \omega) \mathbf{E}(\mathbf{x}) \right) = -\nabla \cdot \mathbf{j}_i(\mathbf{x})$$

Using the assumption that $\omega\epsilon \ll \sigma$ for any ω :

$$\nabla \cdot \left(\sigma(\mathbf{x}, \omega) \mathbf{E}(\mathbf{x}) \right) = -\nabla \cdot \mathbf{j}_i(\mathbf{x})$$

Finally, noting that the assumption $|\gamma R'_{\max}| \ll 1$ implies a negligible contribution of time-varying magnetic fields to \mathbf{E} [68], such that $\mathbf{E} = -\nabla V$, one obtains:

$$\nabla \cdot \left(\sigma(\mathbf{x}, \omega) \nabla V(\mathbf{x}) \right) = \nabla \cdot \mathbf{j}_i(\mathbf{x}) \quad (2.11)$$

which is Poisson's equation.

Now, recall that in the case of an infinite, linear, homogeneous, isotropic medium, the solution to Poisson's equation is given by Equation (2.9), and suppose that $\nabla \cdot \mathbf{j}_i(\mathbf{x})$ is much larger in a certain region of space \mathcal{V}_0 than anywhere else.

In this case, the integration domain in the integral of Equation (2.9) reduces to \mathcal{V}_0 , which is equivalent to neglecting the term $\nabla \cdot \mathbf{j}_i(\mathbf{x})$ in Equation (2.11) for all \mathbf{x} outside of \mathcal{V}_0 .

In fact, when artificial current sources are introduced in the medium, a much common assumption is to consider that biological current sources are comparatively negligible, and Equation (2.11) becomes:

$$\nabla \cdot (\sigma(\mathbf{x}, \omega) \nabla V(\mathbf{x})) = 0 \quad (2.12)$$

outside the regions where artificial current sources are found.

Moreover, as was done when passing from Equation (2.7) to Equation (2.8), volumetric current sources are often idealized as punctual or surface current sources by means of a passage to the limit.

In this case, Equation (2.12) is valid everywhere in space, except on a restricted set of points and surfaces.

2.1.7 Non-linearity, inhomogeneity and anisotropy

Though extremely instructive, the developments presented in Sections 2.1.4 and 2.1.5 were based on the assumptions of linearity, homogeneity and isotropy of the medium. Notably, the explicit expressions for the electric potential given by Equation (2.7) or Equation (2.9) were based on these assumptions.

Exploiting Poisson's equation also requires medium linearity, for Poisson's equation only allows to compute V for mono-harmonic sources, and estimating V for arbitrary sources necessitates superposition via Fourier integration.

Yet, biological tissues present non-linearity, inhomogeneity, and anisotropy by many aspects. For instance, the body of vertebrates are made of different tissues, presenting gross differences in their overall electrical properties [70, 71].

Moreover, when examined at the microscopic scale, individual tissues are themselves inhomogeneous and often comprise microscopic components with markedly distinct electrical properties. This is particularly true of neural tissue, in which the membrane of neurons has much stronger permittivity (leading to capacitive effects) than the cytoplasm or the extracellular milieu, and which also embeds non-linear elements (*eg* voltage-gated ion channels). Besides, these elements are crucial in the emergence and propagation of action potentials.

Finally, anisotropy may result from specific geometrical arrangements of such microscopic structures. This is for instance the case of the white matter and spinal roots of the spinal cord, where longitudinal fibers are running parallel, and where the longitudinal and transverse magnitudes of the electrical conductivity differ by as much as an order of magnitude [70].

2.1.8 Summary, conclusions, and computational strategy

Biological tissues are comprised of inhomogeneous materials with specific electrical properties affecting the electromagnetic field arising from stimulation current sources.

Experimental measurements suggest that these materials are overall linear, and predominantly conductive in the range of signal frequencies usually involved in electrophysiology [69–71]. This enables employing the quasi-static approximation and leads to Poisson’s equation for the electric potential.

Yet, by neglecting local non-linear and capacitive effects, this approach alone would not allow to represent the emergence and propagation of action potentials in neurons.

However, if the contribution of biological current sources to the electric potential is negligible compared to that of artificial sources, as discussed in Section 2.1.6, this implies that the electrical behaviors of individual neurons during electrical stimulation are independent from one another.

This leads us naturally towards the following computational scheme for estimating the electrical responses of neurons following electrical stimulation:

1. Computing the electric potential under quasi-stationarity conditions using Poisson’s equation, neglecting any non-linear and non-conductive properties of the medium.
2. Simulating the electrical behavior of putative neurons that would be plunged in this electric potential distribution, assuming that this latter distribution is left unaffected by the local phenomena (involving non-linear and capacitive effects) induced in these neurons.

This computational scheme is at the core of hybrid neurophysical volume conductor models.

2.2 Volume conductor models

Volume conductor models are idealized tridimensional representations of biological systems as comprised of purely conductive materials. They enable computing an approximation of the electric potential arising from biological or artificial current sources under quasi-stationarity conditions by means of Poisson's equation and appropriate numerical methods.

In this section, I give a general presentation of these models, insisting on two of their constituents: volume conductors and boundary conditions.

The main numerical method employed with volume conductor models, the finite element method (FEM), is only briefly sketched as it is not central to the work presented in this dissertation. The reader can consult [72] for a presentation of its theory and implementation details.

2.2.1 Volume conductors

To estimate the electric potential arising from current sources in biological systems, volume conductor models rely on a piecewise homogeneous representation of the studied systems. That is, a gross macroscopic distinction between different compartments of the system is made—*eg* between the gray and white matters of the spinal cord—and each of them is assumed to be homogeneous.

Let us denote $(\mathcal{C}_i)_i$ these compartments, $(\Omega_i)_i$ the volumes of space which they occupy, and $(\Sigma_i)_i$ the frontiers (*ie* the bounding surfaces) of these volumes. The volume occupied by the entire system is denoted Ω ($\Omega := \cup_i \Omega_i$) and its frontier $\partial\Omega$ (often referred to as the *border* of Ω).

Volume conductor models further assume that the materials composing the different compartments are linear and purely conductive, such that the material properties of each \mathcal{C}_i are fully characterized by a conductivity tensor σ_i , and $\sigma(\mathbf{x}) = \sigma_i \forall \mathbf{x} \in \Omega_i$.

The materials can be isotropic, in which case σ_i is a simple real scalar value, or anisotropic, in which case σ_i is described by a diagonal matrix:

$$\sigma_i = \begin{pmatrix} \sigma_{i,1} & 0 & 0 \\ 0 & \sigma_{i,2} & 0 \\ 0 & 0 & \sigma_{i,3} \end{pmatrix}$$

where $\sigma_{i,1}$, $\sigma_{i,2}$ and $\sigma_{i,3}$ are the magnitudes along $\mathbf{e}_1(\mathbf{x})$, $\mathbf{e}_2(\mathbf{x})$ and $\mathbf{e}_3(\mathbf{x})$ respectively, and where $(\mathbf{e}_1(\mathbf{x}), \mathbf{e}_2(\mathbf{x}), \mathbf{e}_3(\mathbf{x}))$ is an orthonormal basis of the local coordinates system at point \mathbf{x} .

Thus characterized by the σ_i 's, Ω is referred to as a *volume conductor*.

The materials being purely conductive, the quasi-static approximation is employed and Poisson's equation apply in the interior of each Ω_i :

$$\nabla \cdot (\sigma_i \nabla V(\mathbf{x})) = \nabla \cdot \mathbf{j}_i(\mathbf{x}) \quad \forall \mathbf{x} \in \Omega_i$$

where the subscript i of \mathbf{j}_i stands for *impressed* as in Section 2.1.3, while the subscript i of σ_i indicates that the considered conductivity tensor is that of Ω_i .

Recall from Section 2.1.6 that Poisson's equation is valid for mono-harmonic sources, and that the σ_i 's *a priori* depend upon the oscillation frequency ω of the source. For arbitrary sources whose temporal variations are not sinusoidal (for instance square pulses of electrical stimulation), two routes can be followed:

1. Assuming that the σ_i 's are frequency-independent (which option was retained in the developments presented in the subsequent chapters of this thesis, and which is fairly justified for the tissues which we have considered [73]).
2. Solving the problem for multiple values ω of the source's frequency-spectrum and superposing the obtained solutions via Fourier integration, as is done *eg* in [74].

Furthermore, when representing artificial current sources, these are usually concentrated on surfaces or points and represented by *boundary conditions* (see Section 2.2.2), and biological current sources are assumed to be comparatively negligible. As discussed in Section 2.1.6, in this case Poisson's equation becomes:

$$\nabla \cdot (\sigma_i \nabla V(\mathbf{x})) = 0 \quad \forall \mathbf{x} \in \Omega_i$$

for each Ω_i .

Lastly, the overall inhomogeneity and presumed arbitrary geometry of the studied system *a priori* prevents to derive an analytical expression for V . Thus, numerical methods are employed to approximate it. These methods are usually based on a discretized version of the system geometry, implying that the represented system must be of finite extent (*ie* we do not represent unbounded air or vacuum compartments). In particular, this requires that appropriate boundary conditions be specified on $\partial\Omega$.

2.2.2 Boundary conditions

As mentioned in the previous section, boundary conditions must be specified to estimate the electric potential in the volume conductor.

Firstly, because the volume conductor is of finite extent, which requires to specify what happens to the field at the frontier $\partial\Omega$ between the represented system and the outside *nothingness*.

Secondly, because these allow to represent the current sources (which are usually not represented as volumetric sources, as discussed in the previous sections).

And thirdly, because Poisson's equation is only valid in the interior of each Ω_i , which requires to specify what happens to the field at the interface between two of them.

Dirichlet and Neumann boundary conditions

Most of the time, the boundary conditions used in volume conductor models belong to one of two classes: *Dirichlet conditions* or *Neumann conditions*.

Dirichlet conditions take the form:

$$V(\mathbf{x}) = V_0 \quad \forall \mathbf{x} \in T \quad (2.13)$$

where T is any set of points (singleton, curve, surface or volume) and V_0 is any fixed real scalar value expressed in volts (V).

On the other hand, Neumann conditions write:

$$\left(\sigma_b \nabla V_b(\mathbf{x}) - \sigma_a \nabla V_a(\mathbf{x}) \right) \cdot \mathbf{n}_{a,b}(\mathbf{x}) = j_0 \quad \forall \mathbf{x} \in \Sigma \quad (2.14)$$

where:

- Σ is a surface separating two compartments \mathcal{C}_a and \mathcal{C}_b with respective conductivities σ_a and σ_b ;
- $\mathbf{n}_{a,b}(\mathbf{x})$ is the normal vector to Σ pointing from Ω_a to Ω_b at position \mathbf{x} ;
- $\nabla V_a(\mathbf{x})$ and $\nabla V_b(\mathbf{x})$ are the gradients of V evaluated in \mathbf{x} on the sides of Ω_a and Ω_b respectively;
- j_0 is any fixed real scalar value expressed in amperes per square meter (A m^{-2}).

In case where the surface Σ is part of $\partial\Omega$, one of the compartment \mathcal{C}_a or \mathcal{C}_b does not exist. This is equivalent to saying that the corresponding conductivity tensor is null, and the Neumann condition rewrites:

$$\sigma \nabla V(\mathbf{x}) \cdot \mathbf{n}(\mathbf{x}) = j_0 \quad \forall \mathbf{x} \in \Sigma$$

where $\mathbf{n}(\mathbf{x})$ is the normal vector pointing outwards of Ω and $\nabla V(\mathbf{x})$ is evaluated on the outside of $\partial\Omega$.

Recall from Section 2.1.3 that $\sigma \nabla V$ is the conduction current density, implying that the Neumann condition prescribes the normal component of the current density on the surface where it is applied.

Boundary condition on $\partial\Omega$

One instance of each class of conditions are most frequently employed for $\partial\Omega$: the *ground condition*, which is a Dirichlet condition with V_0 set to 0 V, and the *insulating condition* or *zero-flux condition*, which is a Neumann condition with j_0 set to 0 A m⁻².

The signification and implications of these boundary conditions is discussed in detail in Chapter 5, but let us mention that:

- A first interpretation for the ground condition on $\partial\Omega$ is that it represents an approximation to the ground condition at infinity. This latter condition stipulates that $V(\mathbf{r}) \rightarrow 0$ as $|\mathbf{r}| \rightarrow \infty$, which sets a convenient reference-level for V (recall from Section 2.1.2 that V is only defined within a constant) and which is always valid from the physics point of view (insofar as the prescription of V in other places of the geometry account for this reference level).
- Another widespread interpretation for the ground condition on $\partial\Omega$ is that $\partial\Omega$ acts as a *distributed return electrode*. This is further discussed in Chapter 5.
- On the other hand, as its name indicates, the insulating condition makes $\partial\Omega$ behave as a perfect insulator: no electric current flows out of the volume conductor through any part of its border. This is equivalent to assuming that the volume conductor is plunged in a non-conductive medium of infinite extent, and it is a good approximation of the insulation occurring at the skin-air interface when the volume conductor represents a whole body of a vertebrate that would be surrounded by air (not represented in the volume conductor).

If $(\Gamma_k)_k$ is a partition of $\partial\Omega$, it is also possible to specify a different condition on each Γ_k , as discussed in Chapter 5.

Boundary conditions representing current sources

In volume conductor models of electrical stimulation, current sources are commonly represented by punctual or surface current sources.

Punctual current sources Punctual current sources can formally be defined by introducing a Dirac distribution in Poisson's equation:

$$\nabla \cdot (\sigma(\mathbf{x}) \nabla V(\mathbf{x})) = I_0 \cdot \delta(\mathbf{x} - \mathbf{x}_0) \quad \forall \mathbf{x} \in \Omega$$

with I_0 the total amount of injected current and \mathbf{x}_0 the point at which it is injected.

This definition implies that the outgoing flux of the current density vector through any closed surface S enclosing \mathbf{x}_0 (and enclosing no other current source) will be equal to I_0 .

Surface current sources Surface current sources are usually represented by Neumann conditions with non-null values for j_0 . If Σ denotes the surface where the condition is applied, the total current I_0 injected at Σ can be calculated as the outgoing flux of the current density through any closed surface enclosing Σ (and enclosing no other current source). The smallest such surface (*ie* surrounding Σ as closely as possible) is constituted by the union of two copies of Σ itself: one copy on the side of Ω_a , one copy on the side of Ω_b . Evaluating the outgoing flux of the current density through this surface yields:

$$\begin{aligned} I_0 &= \int_{\Sigma} \mathbf{j}_a(\mathbf{x}) \cdot \mathbf{n}_{b,a}(\mathbf{x}) \, ds + \int_{\Sigma} \mathbf{j}_b(\mathbf{x}) \cdot \mathbf{n}_{a,b}(\mathbf{x}) \, ds \\ &= \int_{\Sigma} \sigma_a \nabla V_a(\mathbf{x}) \cdot \mathbf{n}_{b,a}(\mathbf{x}) \, ds + \int_{\Sigma} \sigma_b \nabla V_b(\mathbf{x}) \cdot \mathbf{n}_{a,b}(\mathbf{x}) \, ds = j_0 \times A_{\Sigma} \end{aligned}$$

where $\mathbf{n}_{b,a}(\mathbf{x}) = -\mathbf{n}_{a,b}(\mathbf{x})$ and A_{Σ} is the total area of Σ expressed in m^2 .

Boundary conditions at the interface between two media

At the interface Σ between two media, when no other condition applies, the continuity of the normal component of the current density must be respected. This is ensured by imposing the following Neumann condition:

$$(\sigma_b \nabla V_b(\mathbf{x}) - \sigma_a \nabla V_a(\mathbf{x})) \cdot \mathbf{n}_{a,b}(\mathbf{x}) = 0 \quad \forall \mathbf{x} \in \Sigma$$

Note that the continuity of the electric potential at Σ must also be respected at all times. However, this condition is automatically met due to the necessary geometry discretization mentioned in Section 2.2.1: there is only one single value that can be attributed to the electric potential at any point of Σ .

Boundary conditions representing voltage sources

Boundary conditions can also be specified to represent artificial voltage sources, whereby the voltage differences between specific electrodes is prescribed.

These can readily be represented by Dirichlet conditions applied to distinct surfaces or points with different prescribed values for V_0 . In particular, a *ground point* or *ground surface* is a point (resp. a surface) with $V_0 = 0$.

2.2.3 Geometry discretization and finite element method

Let us summarize the two previous sections. Volume conductor models comprise:

- a volume conductor, which is made of a series of compartments $(\mathcal{C}_i)_i$ with volumes $(\Omega_i)_i$ delimited by surface boundaries $(\Sigma_i)_i$ and characterized by conductivity tensors $(\sigma_i)_i$;
- a system of differential equations (Poisson's equations) and boundary conditions constraining the spatial distribution of the electric potential in this volume conductor.

Furthermore, as mentioned in Section 2.2.1, due to the inhomogeneity and irregular geometry of the volume conductor, analytical solving of this system of equations is usually impossible, requiring that numerical methods be employed to approximate the analytical solution. Multiple such methods are available, *eg* the finite differences method, the boundary element method, or the finite element method (FEM). Among them, the FEM is probably the most popular.

The FEM relies on a discretized version of the geometry on which it should operate. This discretization constitutes a *mesh*. It is made of simple elements (usually tetrahedron when treating tridimensional geometries) realizing a paving of the initial geometry.

Next, the FEM proceeds to approximate the analytical solution sought for by a linear combination of basis functions whose supports are restricted to individual elements of the mesh (*ie* these functions are null outside individual elements). The initial problem of solving a system of differential equations over a tridimensional domain is thus reduced to finding appropriate coefficients for the a linear combination of basis functions, which essentially amounts to assembling and inverting a matrix (see [72]).

The higher the number of elements composing the mesh, the more accurate the realized approximation, but also the more computationally costly. In the necessary arbitration between accuracy and computational economy, it is relevant to increase the number of elements where the computed field is likely to experience large variations, in our case, around the current sources. However, high number of elements may also be required to appropriately discretize the volume conductor geometry, notably in those places where it is highly curved or present sharp corners.

2.3 Neurophysical models

As mentioned in introduction of this chapter, this section does not contain a general presentation of neurophysical models, but a presentation of the specific models that were employed in the developments of this thesis. The reader can consult [66] for a brilliant summary of the history and theory of neurophysical models, and can refer to [75] or [76] for a more advanced presentation.

Let's simply mention that neurophysical models attempt to capture the electrical behavior of neurons and nerve fibers by means of electrical circuits in which the components (conductances, capacitances and batteries) represent the lumped electrical properties of these neurons and nerve fibers. By simulating the dynamics of these circuits in response to varying current or voltage sources (representing the application of electrical stimulation), one can thus estimate the spatiotemporal fluctuations of the membrane potential and thus the generation and propagation of action potentials along the represented entities.

2.3.1 Myelinated nerve fibers: MRG model

To simulate the electrical behavior of nerve fibers, I used the MRG model. The MRG model is a neurophysical model of mammalian myelinated motor nerve fiber developed by McIntyre, Richardson and Grill [77], which is recognized for faithfully reproducing salient experimental findings of electrophysiology, and which is widely used in the neuro-modeling community.

It is a multi-compartmental model consisting of the alternation of nodes of Ranvier embedding non-linear membrane ionic conductances, and passive internodal compartments wrapped by a myelin sheath. Each internodal section is made of multiple internodal compartments, with a finer discretization in the vicinity of the nodes of Ranvier.

An abstract representation of the model goes as follows:

-- **I** - **P2** - **P1** - **N** - **P1** - **P2** - **I** - **I** - **I** - **I** - **I** - **I** - **P2** - **P1** - **N** - **P1** - **P2** - **I** - --

where **N** stands for “Node”, **P1** stands for “Paranode1”, **P2** stands for “Paranode2”, and **I** stands for “Internode”.

This pattern is repeated a certain number of times until a terminal node is reached at both ends of the strand.

Electrical circuit

The lumped electrical components representing each of these compartments and their interconnections are depicted in Figure 2.1.

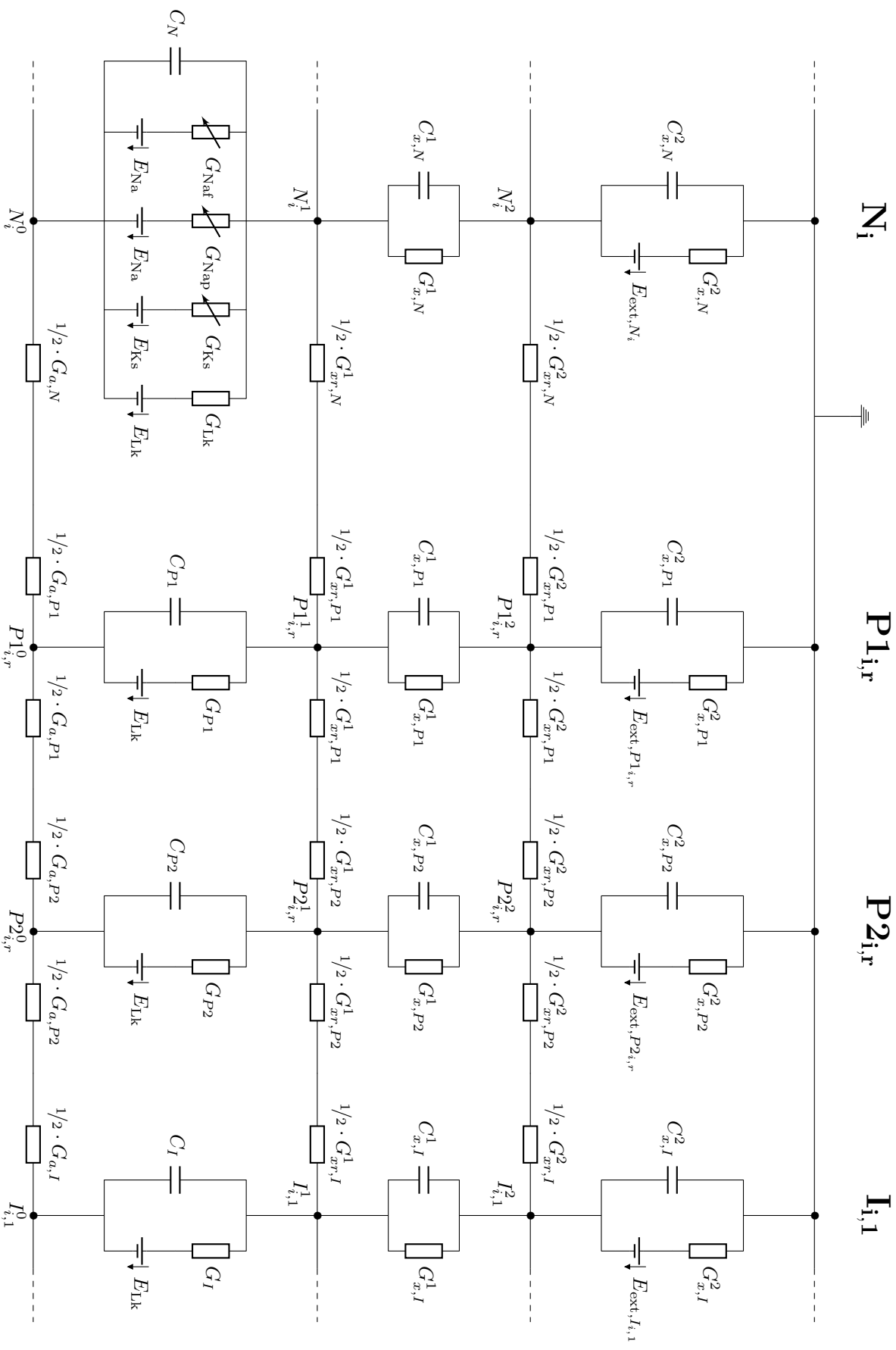


Figure 2.1 Electrical circuit of the MRC model.

On this diagram, one can distinguish 4 horizontal levels interconnected by parallel arrangements of electrical components, themselves distributed along 4 columns labeled \mathbf{N}_i (node $\#i$), $\mathbf{P1}_{i,r}$ (right paranode1 $\#i$), $\mathbf{P2}_{i,r}$ (right paranode2 $\#i$) and $\mathbf{I}_{i,1}$ (1st portion of internode $\#i$).

It should be understood that:

- on the right of column $\mathbf{I}_{i,1}$, one would find 5 replicas of the same column, labeled $\mathbf{I}_{i,2}$ (2nd portion of internode $\#i$) to $\mathbf{I}_{i,6}$ (6th portion of internode $\#i$);
- on the right of these five replicas, one would find, in this order, two columns labeled $\mathbf{P2}_{i,1}$ (left paranode2 $\#i$) and $\mathbf{P1}_{i,1}$ (left paranode1 $\#i$), being replicas of $\mathbf{P2}_{i,r}$ and $\mathbf{P1}_{i,r}$ respectively;
- the pattern $\mathbf{N}_i - \mathbf{P1}_{i,1}$ would repeat for as many internodes as the fiber possess.

Each of these columns, after the horizontal conductors directly surrounding them have been associated to them, represent a compartment of the fiber.

The lowermost horizontal level, on which one finds the $G_{a,X}$'s, represents the axoplasm, that is, the intracellular canal of the fiber.

The second horizontal level, on which one finds the $G_{xr,X}^1$'s, represents the external surface of the fiber membrane, such that the elements connecting the first to the second level represent the local membrane properties, which depend upon the compartment where it is considered. For instance, at the nodes (\mathbf{N}_i), one can find time-varying voltage-dependent conductances, each in series with an associated battery, which represent ion channels ("Naf" stands for *fast sodium* channels, "Nap" for *persistent sodium* channels, and "Ks" for *slow potassium* channels). The constant conductance and its associated battery represent the leakage conductance of the membrane ("Lk" stands for *leakage*). The capacitance stands for the membrane capacitance itself. At the internodal compartments, the membrane properties are purely passive (no voltage-gated conductances), but the values of the conductances and capacitances differ from that of the nodal compartments, both due to the different sizes of the compartments, and also to different specific membrane conductances [77].

The third horizontal level represents the external surface of the myelin sheath, and the elements joining the second to the third level, the myelin sheath itself. Thus the portion of myelin covering each compartment is represented by the parallel arrangement of a conductance and a capacitance. Note that the presence of these elements at the nodal compartments do not imply that the myelin is represented there, for the value of $C_{x,N}^1$ and $C_{g,N}^1$ can be chosen such that they behave as a short-circuit (infinite conductance, null capacitance).

Finally, the fourth level represents the electrical ground. In fact, this level is almost confounded with the third level, because of the values of the conductances $G_{x,X}^2$, $G_{xr,X}^2$, and capacitances $C_{x,X}^2$. The conductances $G_{x,X}^2$ are indeed based on a surfacic conductance of $1 \times 10^{10} \text{ S cm}^{-2}$ (making them act as short-circuits), the conductances $G_{xr,X}^2$ on a lineic resistance of $1 \times 10^{16} \Omega \text{ cm}^{-1}$ (making them act as open-circuits), and the capacitances $C_{x,X}^2$ on a surfacic capacitance of $0 \mu\text{F cm}^{-2}$ (also making them act as open-circuits). In the absence of extracellular electrical activity (and in particular in absence of external electrical stimulation), the batteries $E_{\text{ext},X}$ are set to 0 V, which finishes to confound the fourth and third levels, *ie* the electrical ground and the surface of the myelin sheath.

By setting $E_{\text{ext},X}$ to any non-null value V_X , one can impose the potential on the surface of the myelin of compartment X , and thus represent the application of external potential distributions. In the calculation chain of hybrid models, it is these batteries that are switched on and off (according to the temporal profiles of hypothetical stimulation pulses), using the electric potential values extracted from the volume conductor model.

Modified P2 compartments

In a later publication [78], McIntyre and colleagues have refined the MRG model to include a K^+ ion channel in the membrane of the **P2** compartments (called FLUT compartments in their original publication [77]), resulting in the electrical circuit depicted in Figure 2.2 for the **P2** compartments.

It is this modified MRG model which I have used for all the nerve fibers and motor axons in this thesis.

Extension to arbitrary fiber diameters

The authors of the MRG model have originally developed their model for a fixed ensemble of fiber diameters [77]. For each of these fiber diameters, the dimensions of the nodal, paranodal and internodal compartments were prescribed.

For the investigations presented in the next chapters, I have enabled to represent nerve fibers of arbitrary diameters by deriving the compartment dimensions using piecewise linear interpolation from the original dataset provided in [77].

2.3.2 Motoneuron model

The motoneuron model I have used to obtain the results presented in this dissertation is an extension of a model developed by McIntyre and colleagues [79]. The initial model of McIntyre and colleagues comprised:

- a multi-compartmental soma;

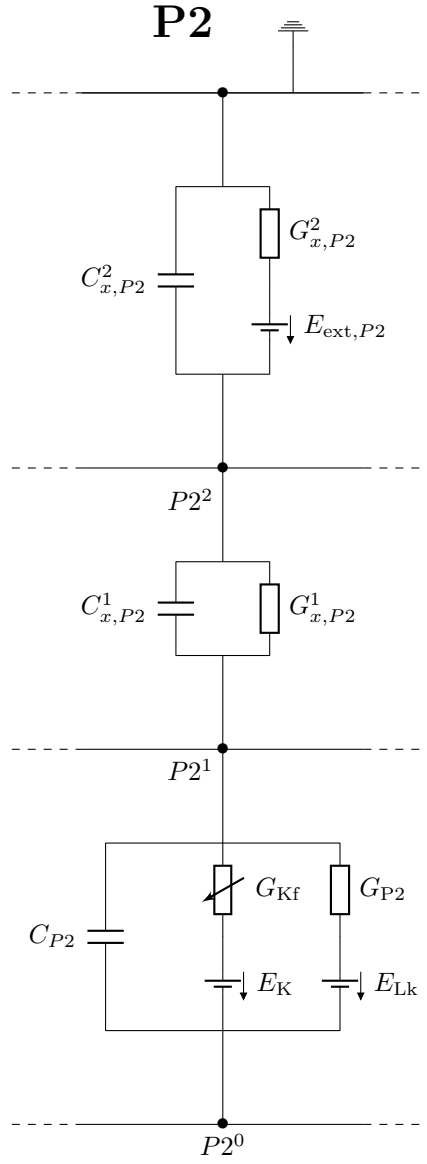


Figure 2.2 Extension of the MRG model with the inclusion of K^+ ion channels in **P2** compartments [78].

- a dendritic tree made of 5 identical multi-compartmental dendrites;
- a motor axon connected to the soma by a multi-compartmental axon initial segment.

The multi-compartmental soma was made of 6 tapered cylindrical compartments (denoted *frusta*, singular *frustum*), among which 5 were identical, connected at their small-diameter end to each of the 5 dendrites, and connected to one another at their large-diameter end. The 6-th frustum was connected to the other somatic frusta at its large-diameter end, and to the axon initial segment at its small-diameter end. The reader can refer to [79] for a description of the electrical components included in the somatic compartments, representing many various ion channels.

The 5 dendrites were each represented by binary trees of 107 interconnected compartments, based on the results of [80]. Like the somatic compartments, the dendritic compartments were most likely frusta, although this is not explicitly stated in [79]. The reason why this is likely the case is that the work presented in [80] resulted in digital reconstructions of motoneuron dendritic trees in the form of *SWC-files*¹, which are freely available on the online open-access library NeuroMorpho.org under references NMO_00604 to NMO_00609, are commonly used for neurophysical simulations of motoneurons, and which describe the dendritic compartments as frusta.

The axon initial segment was made of 3 linearly-connected cylindrical compartments, connected at one end to the 6-th somatic frustum, and at the other end to an MRG nerve fiber model as described in the previous section. The first node of the MRG nerve fiber was likely discarded, replaced by the axon initial segment (although, here again, this is not explicitly stated in [79]). In addition, the four first internodal portions of the fiber were 3× shorter than the subsequent internodal portions, which was based after observations made by Fabricius and colleagues [7]. The reader can refer to [79] for a description of the electrical components included in the compartments of the axon initial segment.

Extension to arbitrary diameters and dendritic trees

The original model exposed in [79] prescribed the dimensions of every compartment of the soma, dendrites and axon. Yet, the size of motoneurons (specifically the surface area of their somata and dendritic trees [81]) greatly influence their synaptic excitability, and motor axons with large diameters are more excitable by extracellular stimulation than small-diameter motor axons [37].

For these reasons, I have enabled to represent motoneurons of arbitrary sizes and possessing arbitrary dendritic trees (as described by SWC-files). In practice, I have used only the

¹See SWC format specifications at: <http://www.neuronland.org/NLMorphologyConverter/MorphologyFormats/SWC/Spec.html>.

six SWC-files mentioned above (references NMO_00604 to NMO_00609 on NeuroMorpho.org), but the collection of usable files can be extended *ad libitum*. For instance, for the investigations reported in Chapter 4, any given motoneuron was attributed a diameter sampled uniformly from a given range (see Section 4.2.4) and a SWC-file chosen among the six available, from which the dimensions of all the compartments of the model could be derived. The algorithm which I conceived is as follows:

1. The diameter of the axon is scaled linearly from the motoneuron diameter (see Section 4.2.4).
2. The dimensions of the axon compartments, including those of the axon initial segment, are derived from the axon diameter by piecewise linear interpolation.
3. Since SWC-files indicate the diameters of the motoneurons which they describe, the coordinates of the selected SWC-file are scaled according to the diameter randomly selected for the motoneuron. By so doing, the electrotonic structure of the motoneuron originally described by the SWC-file is compromised [82], but this allows to increase the variability of the properties of the motoneurons that can be simulated.
4. The dendrites (binary trees of interconnected frusta) are reconstituted from the scaled SWC-file, and the initial diameters of the stems of each dendrite are retrieved (the stem of a dendrite is the compartment by which it is attached to the soma).
5. If the number of stems is N , the soma possesses $N + 1$ compartments, one for each stem and one for the axon initial segment.
6. The $N + 1$ somatic frusta share the same diameter at one of their ends, by which they are connected to one another. At their other end, they share the initial diameter of the stem or of the axon initial segment to which they are connected. Their lengths are adjusted so as to yield a total somatic surface area equal to that of a spherical soma with the same diameter.

This and other algorithms are implemented in a software suite which I have developed and which is hosted on an open-access online repository at https://bitbucket.org/ngreiner/biophy_smc_ees/src/master/.

CHAPTER 3 REFINEMENT OF HYBRID NEUROPHYSICAL VOLUME CONDUCTOR MODELS OF EES OF THE SPINAL CORD

Hybrid neurophysical volume conductor models have been valuable to uncover mechanisms of EES of the lumbo-sacral spinal cord [38, 42]. Moreover, they keep on being used for various purposes, for instance exploring new mechanisms [59] or finding optimal patient-specific stimulation configurations for clinical applications [30].

However, previous hybrid model realizations have entailed modelling options that likely limit the accuracy of the estimated recruitment of dorsal nerve fiber populations. For instance, the spinal roots or the insulating paddle of epidural electrode arrays have seldom been represented in the volume conductor model. Furthermore, the influence exerted by the dorsal column and collateral bifurcations of dorsal root fibers on the recruitment selectivity of specific dorsal roots have not yet been assessed.

In this chapter, I present refinements of hybrid neurophysical volume conductor models of EES of the spinal cord. First, a brief literature review focusing on the geometrical aspects of these models is given in Section 3.1, justifying the subsequent developments. Then, in Section 3.2, a new geometrical model of the spinal cord and its surrounding tissues, enabling to build more realistic volume conductor models, is presented. In Section 3.3, new geometrical models for the trajectories of nerve fibers populating the spinal cord and spinal roots, based on the connectivity between nerve fibers and motoneurons, and relying on the previous spinal cord geometrical model, are exposed. Finally, in Section 3.4, I assess the influence of the introduced novelties on the estimation of relative and absolute recruitments of nerve fibers using hybrid models.

3.1 Hybrid models of EES of the spinal cord: literature review

In this section, I present a brief review of the available literature on hybrid models of EES of the spinal cord. I have focused this review on the nature and the geometry of the compartments represented in the volume conductor models, and on the type and morphology of the neurons and nerve fibers whose electrical behavior have been simulated with neurophysical models. Little will be found in this review about the employed neurophysical models themselves, for the developments that I have led and reported in this dissertation predominantly concern the two former aspects of hybrid models.

3.1.1 Coburn, 1980 [83]

To my knowledge, Coburn is the first investigator whom has used the finite element method (FEM) to study the electric potential distribution elicited in the spinal cord during epidural electrical stimulation. He built two two-dimensional volume conductor models: one of a transverse cross-section of the human thorax, and one of a sagittal cross-section of the same thorax. These models were already pretty detailed with respect to the compartments of the vertebral canal that were represented. They comprised distinct compartments for the gray matter (GM), the white matter (WM), the spinal roots, the cerebro-spinal fluid (CSF), the epidural fat, the vertebral column and one compartment to represent all the surrounding tissues of the thorax. In particular, it is remarkable that spinal roots were represented by specific compartments, as they have been absent of most subsequent volume conductor models reported in the literature. Stimulation electrodes were not explicitly represented by specific compartments, but Coburn reported that at the time, epidural stimulation was delivered through the tip of metallic wires inserted percutaneously into the epidural space, for which punctual current sources seemed appropriate representations.

He represented the anisotropic conductivity of the white matter by specifying a tensor with two distinct values: one for the two directions of the transverse plane, and one for the rostro-caudal direction. For the spinal roots conductivity, Coburn used the mean between the two previous values, motivated by the fact that their orientation is neither transversal nor sagittal, but somewhat *in between*. In fact, the difficulty of specifying an appropriately oriented anisotropic conductivity tensor for the spinal roots may be one reason for their seldom representation in the subsequent tridimensional volume conductor models found in the literature.

Coburn's models provided first theoretical insights into the propagation of electric currents in the spinal tissues, and although they were not coupled with neurophysical models of nerve fibers, they already hinted that dorsal root and dorsal column fibers were likely the primary neural targets of epidural stimulation of the spinal cord.

3.1.2 Coburn and Sin, 1985 [58] – Coburn, 1985 [84]

Five years later, Coburn and Sin published new results stemming from a volume conductor model elaborating on Coburn’s previous developments [58]. The new model was a tridimensional extrusion of Coburn’s two-dimensional transverse model, which thus featured the same compartments assigned with the same electrical conductivities. In particular, this tridimensional model did include the spinal roots, but the latter were represented by a single continuous domain and was assigned with an isotropic conductivity tensor. On another note, the authors mentioned that they chose not to represent the meninges (dura mater and arachnoid in particular) to avoid computational complexity, and because previous findings [85] indicated that only when assuming extreme values for the conductivity of these tissues were the electric potentials in the spinal cord significantly influenced by their presence.

The advantage of a tridimensional model was that it offered the possibility to interpolate the electric potential all along realistic trajectories of nerve fibers. In a companion publication [84], Coburn proceeded to interpolate the potential along dorsal column, dorsal root, and corticospinal tract fiber trajectories which he used to excite neurophysical models of myelinated nerve fibers (specifically, he used McNeal’s model [86]). The dorsal root fiber trajectories were pretty basic in that they did not present any rostro-caudal bifurcations nor transverse collateral branches. Similarly, dorsal column and corticospinal tract fibers were represented as straight lines and did not possess transversal collaterals.

Using this model, Coburn found that the required stimulus amplitude to excite corticospinal fibers was much higher than that required for dorsal column fibers (more than $3\times$ higher) and conversely that dorsal root fibers exhibited lower threshold amplitudes than dorsal column fibers. Importantly, this was the case despite the modeled stimulation was delivered from an electrode positioned on the midline of the spinal cord, and Coburn identified the strong curvature of dorsal root fibers upon entering in the spinal cord as a determining factor explaining this recruitment order.

3.1.3 Struijk et al., 1991 [87], 1992 [50], 1993 [88]

Struijk and colleagues further investigated the relative recruitment of dorsal column and dorsal root fibers. In a first paper [87], they presented a tridimensional volume conductor model of the spinal cord which comprised distinct compartments for the GM, the WM, the CSF, the epidural fat, and a surrounding layer of unspecified tissue. The electrodes were represented as punctual voltage sources. They found that the electrical conductivity of the CSF and of the WM significantly influenced the magnitude of the electric potentials elicited in the dorsal columns, in turn likely impacting the selectivity of the recruitment of nerve fibers. They also noted, that the thickness of the dorsal CSF layer (separating

the dorsal columns from the stimulating epidural electrodes), which is subject to great variability, also had a great influence.

In a second paper [50], they investigated the influence of the branching morphology of dorsal column fibers on their excitation thresholds. They interpolated the electric potential along putative collaterals of dorsal column fibers, and compared the excitation of neurophysical models of branching and unbranching fibers. Overall they found that the presence of collaterals could decrease the excitation threshold of these fibers by up to 50%, but noted that some characteristics of the collateral branching (*eg* the increased area of the branching nodes) could have converse effects (increasing the excitation threshold).

Following-up on these developments, they compared the recruitment of dorsal root and dorsal column fibers [88] and concluded like Coburn that under many circumstances, dorsal root fibers had lower excitation thresholds than dorsal column fibers. In addition to their curvature when entering the cord, they noted that the increased diameter of dorsal root fibers (compared to dorsal column fibers) as well as their passage from the highly conductive CSF to the more resistive WM contributed significantly to their reduced thresholds, and that recruitment likelihood was highest at the dorsal root entry zone. Importantly, they mentioned that the thinness of dorsal rootlets is such that their representation with specific compartments in the volume conductor should be of very limited influence, and therefore unnecessary.

3.1.4 Rattay et al., 2000 [38]

Later, Rattay and colleagues developed a geometrically realistic hybrid model of the lumbosacral spinal cord to assess the influence of the rostral-caudal position of epidural electrodes. Their model comprised compartments for the GM, the WM, the CSF, the epidural fat, the vertebral column, a surrounding layer of unspecified tissue, and also the dura mater. The electrodes were represented by cylindrical elements, emulating a cylindrical electrode array. Importantly, they represented dorsal root fibers and ventral motor axons whose trajectories in the vertebral canal were based on a realistic positioning of the lumbosacral spinal cord with respect to the vertebrae. For instance, the trajectory representing a dorsal fiber running in the L4 root entered the spinal cord at the level of the L4 segment and exited the vertebral canal at the level of the L4-L5 intervertebral foramina, as it is supposed to. However, the spinal roots were not represented, and dorsal root fibers did not bifurcate in the dorsal columns nor possessed collateral branches.

Using this model, Rattay and colleagues were able to explain to some extent the relationship between the rostral-caudal position of epidural electrodes and the recruitment of lower-limb muscles observed in human patients during epidural electrical stimulation. In particular, their model suggested that epidural electrodes located at the level of rostral

segments predominantly engaged rostrally-innervated muscles via the selective recruitment of rostral dorsal roots (*ie* of the primary afferents, notably group-Ia fibers, which they contain), while more caudal positions for the electrodes induced recruitment of many muscles simultaneously due to the simultaneous presence of both rostral and caudal dorsal roots.

They noted that the excitation threshold of dorsal root fibers was lowest when the cathode was placed at the level of their entrance in the spinal cord, which could partly be attributed to the geometrical curvature of the fibers upon entering the cord, as already noted by Coburn and Sin [58], but also to the conductivity discontinuity at the WM-CSF interface, also significantly influencing the electric potential profile along the fibers' course.

3.1.5 Capogrosso et al., 2013 [42]

On their part, Capogrosso and colleagues have developed a hybrid model of the rat lumbosacral spinal cord notably to assess the implications of the specific dimensions of the spinal cord of these small mammals. Their model comprised compartments for the GM, the WM, the CSF, the epidural fat, the vertebral column and a surrounding layer of unspecified tissue. They represented stimulation delivered via the tips of micro-wire electrodes with punctual current sources. As was done by Rattay and colleagues [38], they modeled dorsal root fibers and ventral motor axons with realistic trajectories in the dural sac, but the spinal roots and the dorsal column bifurcations of dorsal root fibers were also missing from their model. Furthermore, they investigated the direct recruitment of motoneurons and interneurons positioned in the gray matter, for which they interpolated the electric potential along collections of interconnected segments representing the dendritic trees of these neurons.

Their study revealed that the direct recruitment of motor axons in rats was not as unlikely as in humans, most probably due to the reduced size of the rat spinal cord. Moreover, their simulations indicated a virtually inexistent direct influence of epidural stimulation on interneurons and motoneurons in the gray matter, partly due to the weak electric potentials induced inside the gray matter, and partly to the spatial compactness of neuronal somata and dendritic trees, making these neural elements less excitable by external electrical stimuli than longitudinal nerve fibers [89].

3.1.6 Howell et al., 2014 [90]

Howell and colleagues have developed a hybrid model of the lower thoracic human spinal cord with the aim to compare the therapeutic potentials of intradural and epidural stimulations to alleviate chronic back pain. Their model comprised compartments for the GM, the WM, the CSF, the epidural fat, the vertebrae and for the dura mater and interver-

tebral disks. They used a standard shape of the spinal cord at the T8 segmental level prolonged rostro-caudally. They modeled a cylindrical electrode array with three contacts whose material properties were not specified.

They represented dorsal column fiber trajectories as straight lines regularly distributed in the dorsal columns according to a segmental medio-lateral lamination pattern suggested by previous investigations [51]. They also represented dorsal root fibers with realistic trajectories in the spinal canal as in [38, 42], and with straight rostro-caudal bifurcations positioned in the lateral-most lamina of the dorsal columns. The diameters of the dorsal column bifurcations and the dorsal root branches were assumed to be equal. They concluded that medial placement of electrodes could selectively activate dorsal column fibers, but that electrode lateral displacements progressively targeted more lateral dorsal column fibers until targeting dorsal root fibers.

As Rattay and colleagues [38], they reported an abrupt change of the spatial second-order finite difference of the electric potential along dorsal root fiber trajectories at the level of the WM-CSF interface, attributed to the discontinuity of the conductivity between the two media, which might have caused an overestimation of the recruitment of dorsal root fibers.

3.1.7 Lempka et al., 2015 [59]

Lempka and colleagues also developed a hybrid model of the lower thoracic human spinal cord to study mechanisms of spinal cord stimulation to alleviate chronic back pain, but this time to investigate the possible mechanisms of kilohertz frequency spinal cord stimulation (KHFSCS). Their model comprised compartments for the GM, the WM, the CSF, the dura mater, the epidural fat, the vertebral column, and a compartment for all the tissues composing the thorax. A cylindrical electrode array was explicitly represented, with cylindrical active contacts made of highly conductive material separated by cylindrical portions of highly insulating material. They used their model to assess the influence of a great number of parameters on the effects of KHFSCS on dorsal column and dorsal root fibers: stimulation waveform shape, CSF dorsal layer thickness, electrode array location, fiber collateralization, and fiber size. In particular, their dorsal column and dorsal root fiber trajectories were somehow similar to those of Howell and colleagues [90], but they additionally provided them with straight transversal collaterals projecting in the ventral direction.

Interestingly, their results indicated that collaterals of realistic size had insignificant influence on the excitation threshold of dorsal column and dorsal root fibers, contrasting the results obtained by Struijk and colleagues two decades earlier [50].

3.1.8 Summary and conclusions

An important finding stemming from the above review is that hybrid models have rarely included specific compartments to represent the spinal roots. Yet, despite the fact that rootlets are pretty thin with regard to the large volume of the CSF (as pointed out by Struijk and colleagues [88]), some rootlets may nonetheless contain up to several hundreds of fibers, and fibers located at the center are likely to be less excitable than those at the periphery due to an electrical shielding exerted by the latter. Moreover, the diameter of the roots when the rootlets are bundled together may reach up to 3 mm [91], for which the size argument to justify neglecting the resistive properties of the roots becomes irrelevant. Furthermore, representing the roots with fully-fledged compartments seems all the more important given the observations made by Rattay [38] and Howell [90] whom reported that the abrupt change of conductivity at the CSF-WM interface tended to favor the recruitment of dorsal root fibers at their entrance in the spinal cord, which may in fact be a modeling artifact.

The silicone paddles embedding the active contacts of paddle epidural electrode arrays have also rarely been represented in hybrid models. Yet, their strong electrical insulation properties are likely to affect both the absolute stimulation amplitudes necessary to excite spinal nerve fibers, and, by modifying the electric potential distribution at large, also the selectivity of the recruitment.

Another important point concerns the representation of the branching structure of dorsal column and dorsal root fibers. First, contradictory results have been reported by different investigators regarding the influence of collaterals on the excitation threshold of dorsal column and dorsal root fibers, such that it is not clear whether they should be represented or not. Second, since dorsal column fibers are quite subject to excitation during epidural stimulation, this means that sensory nerve fibers coming from dorsal roots that are remote from the stimulating electrode are likely to get recruited via their dorsal column bifurcations, although this likelihood strongly depends on the depth of these bifurcations in the dorsal columns. This suggests that appropriate representation of these bifurcations is of great importance if one seeks to assess the selectivity of the recruitment of nerve fibers of different dorsal roots.

Finally, it should be noted that the previous volume conductor models all seem to have been built somewhat *from scratch*. In particular, although the more recent models have benefited from the feedback gained from the more ancient models, the previous investigators have had to invent new strategies and perhaps develop new computer programs to represent and build the compartments of their volume conductor or to distribute trajectories of neurons or nerve fibers within it. As of today, this would also be the case of future researchers seeking to lead new investigations using hybrid models of the spinal cord.

Yet, although the dimensions and shape of the different compartments of the spinal cord and vertebral canal are subject to great variability across species and subjects, they nonetheless present characteristic features that could be described on a somewhat abstract level, allowing to establish a sort of class template from which model instances could easily be built, and this holds true for neuron and nerve fiber trajectories.

3.2 Geometrical model of the spinal cord

To address the limitations highlighted in the previous section, I have developed a new geometrical model for the spinal cord and its surrounding tissues in the vertebral canal. In this model, compartments are included to represent the GM, the WM, the spinal roots $(R_x)_{x=1\dots n_{\text{roots}}}$, the CSF, the dura mater, and the epidural fat. I present it in its most general form (applicable to any animal species, and any portion of the spinal cord), and I illustrate it with the example of the cervical spinal cord of the macaque monkey.

3.2.1 Generic representation

Each of the previous structures is ultimately described by a collection of 1d-planar cross-sectional contours. As their names indicate, the cross-sectional contours are 1d-planar closed-curves delimiting cross-sections of the structure they describe. For instance, in the case of the GM, assuming that the volume representing it is aligned with the z -axis, we find that the intersection of this volume with horizontal planes consist in 2d-planar bounded surfaces (well-known to be butterfly-shaped). These constitute cross-sections, and a cross-sectional contour is simply the border of one such cross-section.

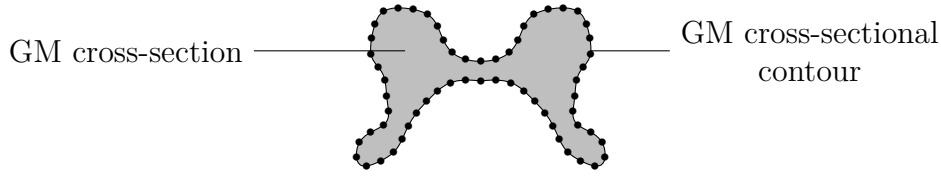


Figure 3.2 Cross-section and cross-sectional contour of the GM in the C5 cross-section of the non-human primate cervical spinal cord.

By interpolation, such collections of 1d-planar cross-sectional contours can form 3D volumes realizing a good approximation of the original volumes from which they were drawn. If X denotes a structure, the model thus provides a family $(X_j)_{j=1\dots n_X}$ of cross-sectional contours. Each cross-sectional contour X_j is a $n_{X_j} \times 3$ matrix of coordinates, where n_{X_j} is the number of points composing X_j , and where the i -th row of X_j contains the triplet of coordinates (x_i, y_i, z_i) of the i -th point of X_j .

3.2.2 Spinal segments and cross-sections

The model can represent an arbitrary number of spinal segments, n_{seg} , which are delimited by horizontal cross-sections defining them implicitly: the upper and lower cross-sections of segment S_j are denoted CS_j and CS_{j+1} respectively. The total number of cross-sections (CS) is thus $n_{\text{CS}} := n_{\text{seg}} + 1$.

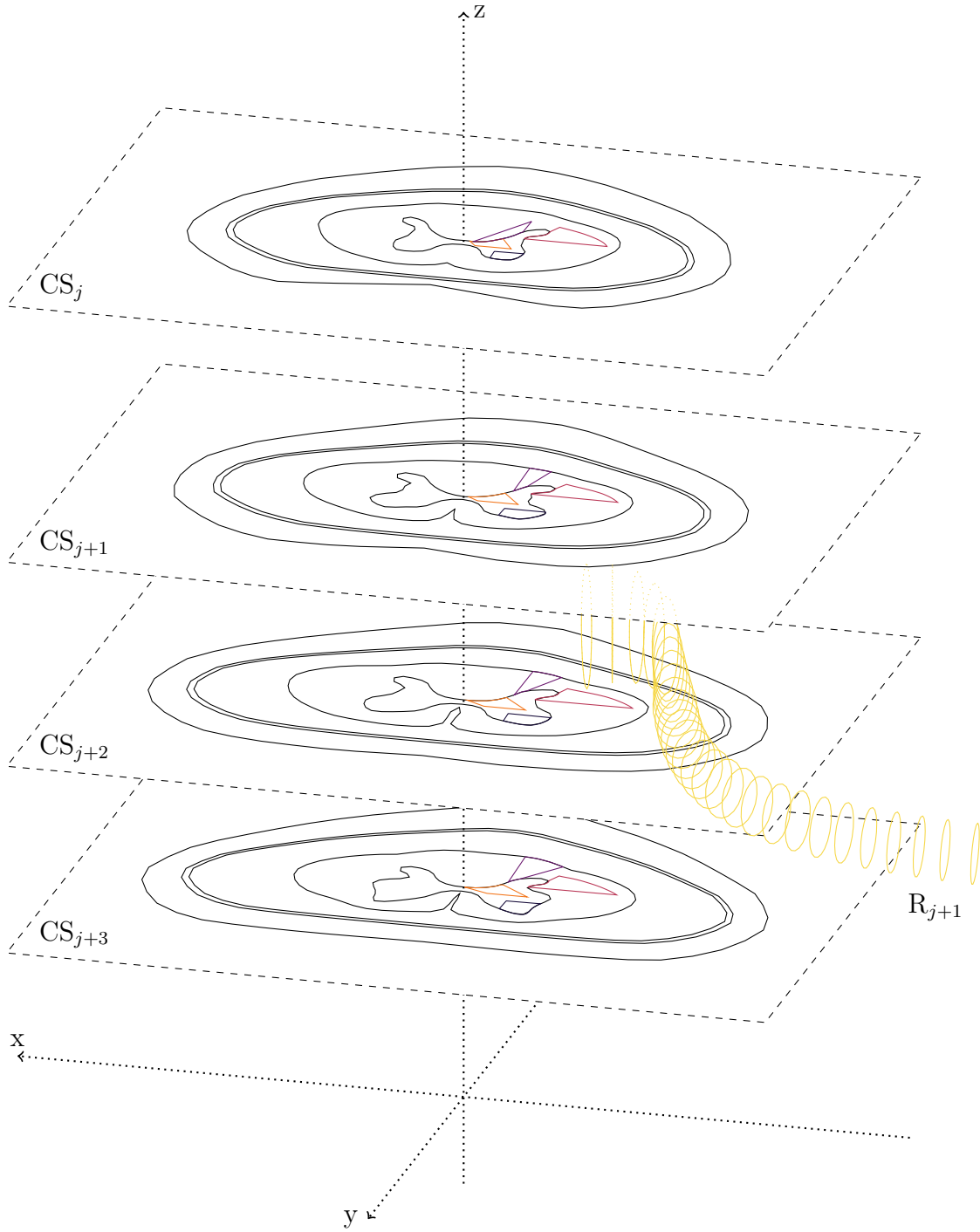


Figure 3.1 Overview of the spinal cord geometrical model. Three spinal segments S^j to S^{j+2} , delimited by the cross-sections CS_j to CS_{j+3} , and the dorsal spinal root R_{j+1} are represented. The black cross-sectional contours in each cross-section, from innermost to outermost, belong respectively to the GM, the WM, the CSF, the dura and the fat. The cortico-spinal tract (CT) is in red. The ventro-lateral quarter (VQ) of the ventral horn of the GM is in dark blue. The middle region (MR) of the middle area of the GM is in orange. DC_j , the dorsal columns compartment corresponding to R_j , is represented in purple.

The elevations (z -coordinates) of the cross-sections are given by the variable z_{CS} , *ie* $z_{CS}(j)$ is the elevation of CS_j . It follows that the rostro-caudal length of spinal segment S_j (*ie* its extent along the z -axis) is given by $L_j := z_{CS}(j) - z_{CS}(j+1)$. The cumulated length of the spinal segments, L_{seg} , is given by $L_{seg} := z_{CS}(1) - z_{CS}(n_{CS}) = z_{CS}(1) - z_{CS}(n_{seg} + 1)$. By convention, we set $z_{CS}(n_{seg} + 1) := 0$.

Notice the difference between the cross-sections mentioned in Section 3.2.1 and the cross-sections described here-above. In Section 3.2.1, a cross-section was defined as a 2d-planar bounded surface while here and in the following, a cross-section essentially denotes a horizontal plane. The organization of the spinal segments and cross-sections is depicted in Figure 3.3.

3.2.3 Extensions, extended cross-sections

The model additionally provides a collection of *extended* cross-sections. These extended cross-sections (eCS) can be split in two subgroups: a first subgroup made of cross-sections above the upper-most *regular* cross-section, *ie* above CS_1 ; and a second subgroup made of cross-sections below the lower-most regular cross-section, *ie* below $CS_{n_{seg}+1}$.

The eCS extend upwards and downwards the volumes representing the GM, WM, CSF, dura and fat, as described by the regular cross-sections CS. The length of these extensions, L_{ext} , is a multiple integer of the cumulated length of the spinal segments, that is, $L_{ext} := r_{ext} \cdot L_{seg}$, with $r_{ext} \in \mathbb{N}^*$. The number of upwards-extended cross-sections (ueCS), which is the same for the downwards-extended cross-sections (deCS), is $r_{ext} + 1$.

For the upwards-extended cross-sections, the first of them, counting from bottom to top, is at the elevation $z_{ueCS_1} := z_{CS}(1) + \frac{1}{10} \cdot L_{seg}$, while the subsequent ones are at the elevations $z_{ueCS_j} := z_{CS}(1) + (j-1) \cdot L_{seg}$, $j = 2 \dots r_{ext} + 1$. For the downwards-extended cross-sections, the first of them, counting from top to bottom, is at the elevation $z_{deCS_1} := z_{CS}(n_{seg} + 1) - \frac{1}{10} \cdot L_{seg}$, while the subsequent ones are at the elevations $z_{deCS_j} := z_{CS}(n_{seg} + 1) - (j-1) \cdot L_{seg}$, $j = 2 \dots r_{ext} + 1$.

The organization of the extended cross-sections with respect to the main cross-sections is depicted in Figure 3.4.

3.2.4 GM, WM, CSF, dura and fat

As mentioned previously, the GM, WM, CSF, dura and fat are each represented by a collection of cross-sectional contours. More specifically, each of them possess exactly one cross-sectional contour in each cross-section and extended cross-sections described in the previous paragraphs.

For each of them, the upwards-extended cross-sectional contours are replicas of the cross-

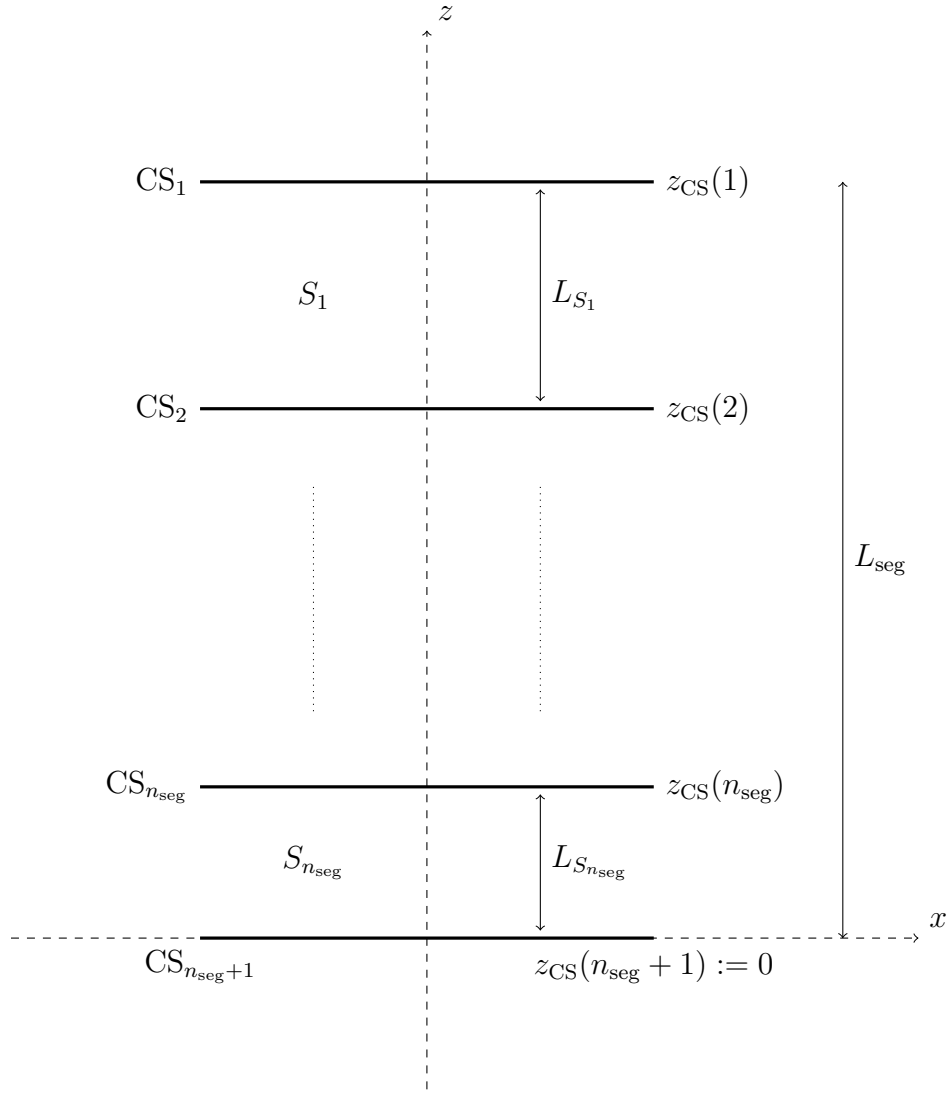


Figure 3.3 Spinal segments and cross-sections.

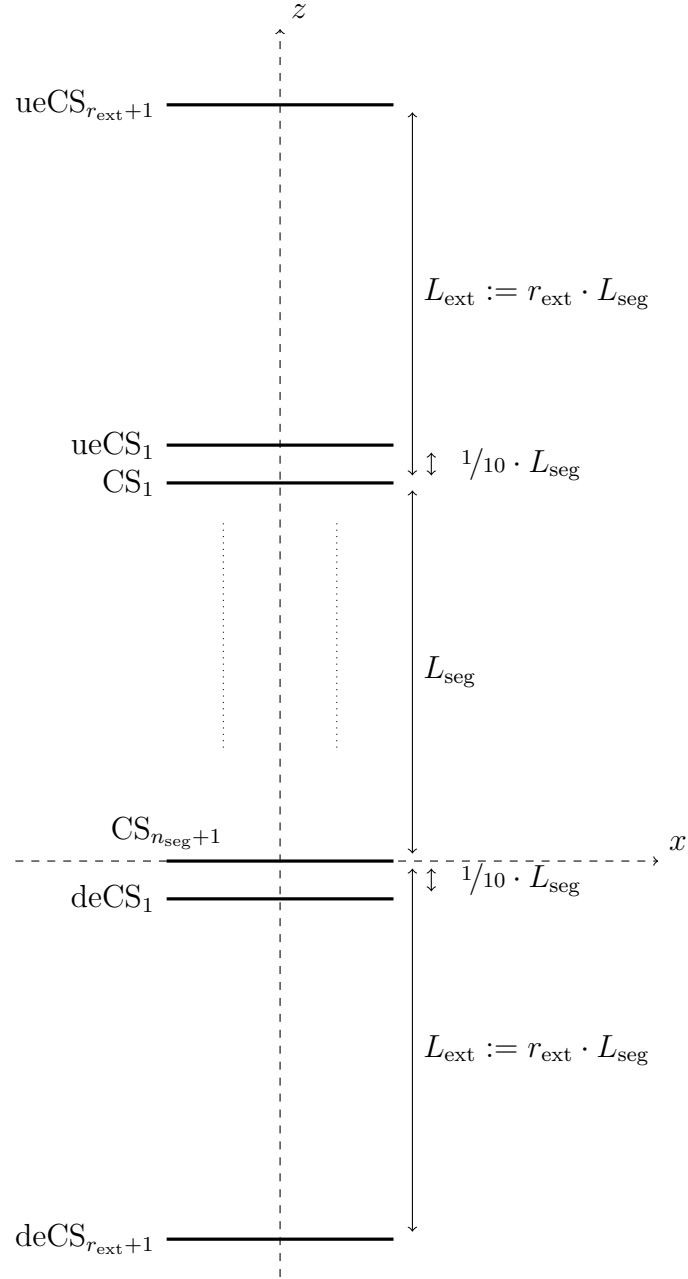


Figure 3.4 Extended cross-sections ($r_{\text{ext}} = 1$).

sectional contour in the first regular cross-section CS_1 , differing only by their z -coordinates. Similarly, the downwards-extended cross-sectional contours are replicas of the cross-sectional contour in the last regular cross-section $CS_{n_{seg}+1}$. Accordingly, the upwards-extended cross-sections themselves are replicas of the first regular cross-section CS_1 while the downwards-extended cross-sections are replicas of the last regular cross-section $CS_{n_{seg}+1}$, all differing by their z -coordinates.

Importantly, the cross-sectional contours of the GM, WM, CSF, dura and fat are symmetrical with respect to the xz -plane, and they are centered around the z -axis in the sense highlighted by Figure 3.5 (the z -axis is inside the cross-sectional contours).

3.2.5 Inner compartments

The model also includes features to describe various inner compartments of the gray matter and white matter. These are:

- the dorsal horn of the gray matter (DH);
- the middle area of the gray matter (MGM), between the ventral and dorsal horns;
- the middle region of the MGM (MR);
- the ventral horn of the gray matter (VH);
- the ventro-lateral quarter of the VH (VQ);
- the Lissauer tract (LT), which is the column-like tract located between the dorsal root entry zone and the dorsal horn of the gray matter;
- the spinocerebellar tract (ST);
- the corticospinal tract (CT);
- the dorsal columns (DC), which are further compartmentalized into several compartments;
- and the outermost layers of the dorsal columns (OD), also compartmentalized into 6 sub-compartments.

Once again, these inner compartments are represented by cross-sectional contours, which are, similarly to the GM and WM, lying in the regular and extended cross-sections of the model. The most useful of these inner compartments in the C5 cross-section of the same model instance as used for Figure 3.5 are depicted in Figure 3.6.

The paragraphs below describe how the inner compartments are defined. Because the cross-sectional contours of the GM and of the WM are symmetrical, we discuss only the

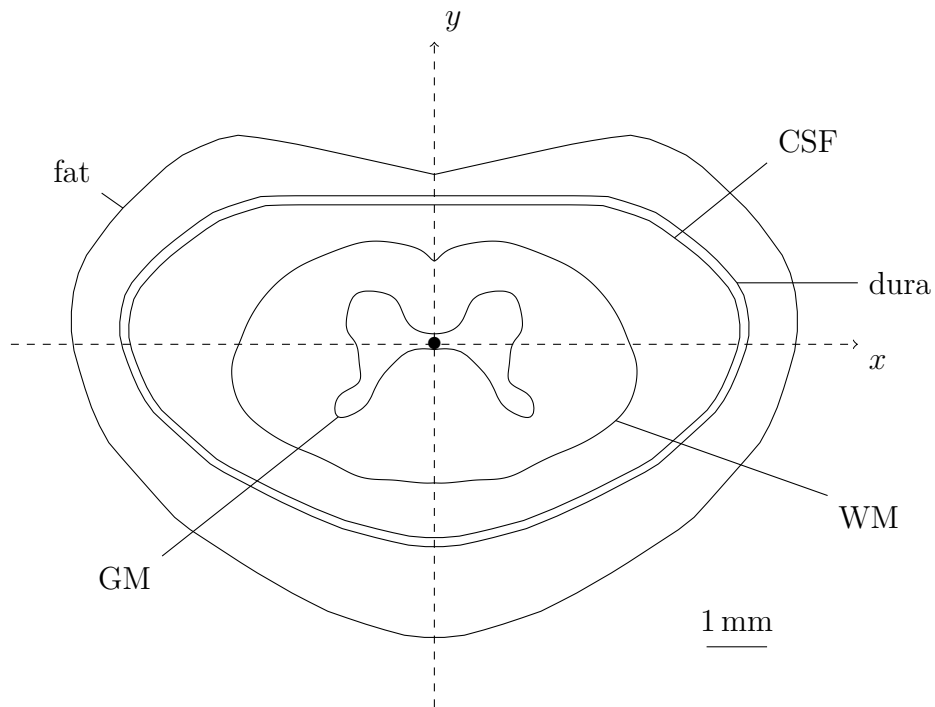


Figure 3.5 Cross-sectional contours of the GM, WM, CSF, dura and fat in the C5 cross-section of the macaque monkey cervical spinal cord.

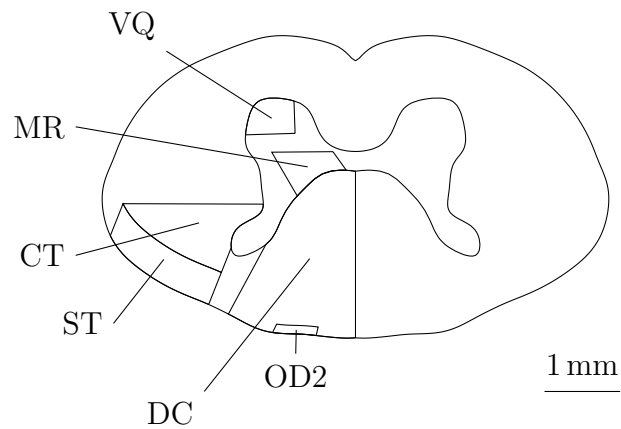


Figure 3.6 Cross-sectional contours of the VQ, MR, CT, DC and OD2 in the C5 cross-section of the macaque monkey cervical spinal cord. *Note: OD2 is one out of six similar compartments forming the outermost layers of the dorsal columns OD.*

definition of the left specimens of each inner compartment, keeping in mind that they have a right symmetrical counterpart.

Dorsal horn of the gray matter (DH)

The DH cross-sectional contour is made of a portion of the GM cross-sectional contour, and a segment joining the points P_1 and P_2 as depicted in Figure 3.7.

In this figure, P_0 is the point of the GM cross-sectional contour satisfying the requirements $x == 0$ and $y < 0$, and P_{\min} and P_{\max} are the points with minimal and maximal y -coordinates respectively.

To determine P_1 we proceed as follows:

1. We extract the lateral portion of the GM cross-sectional contour (which is the portion between points P_{\min} and P_{\max} as depicted in Figure 3.7).
2. We divide this portion in 3 regions of equal extent along the y -axis, and we look for points in the middle region where the slope of the curve changes sign (from positive to negative whilst running from P_{\min} to P_{\max}).
3. If there are such points (*ie* if there are such slope sign inversion events in the middle region), we let P_1 be the lowermost (minimal y -coordinate) of these points.
4. Otherwise, we let P_1 be the point of the lateral portion at the limit between the lower and middle regions, as defined during steps 1 and 2 above.

The definition of P_2 follows that of P_1 : it is the point of the dorso-medial portion of the GM cross-sectional contour (which is the portion between points P_0 and P_{\min} as depicted in Figure 3.7) which has y -coordinate closest to that of P_1 .

Middle area of the gray matter (MGM)

The MGM cross-sectional contour is made of 2 portions of the GM cross-sectional contour, and the three segments joining respectively points P_1 and P_2 , P_3 and P_{end} , and P_{end} and P_0 , as depicted in Figure 3.8.

Here P_0 and P_{end} are the points of the GM cross-sectional contour satisfying the requirements $x == 0$ and $y > 0$, and $x == 0$ and $y < 0$ respectively.

P_1 and P_2 are the same points that together define the DH (see Section 3.2.5).

Finally, P_3 is the point of the lateral portion of the GM cross-sectional contour which has closest y -coordinate to that of P_{end} .

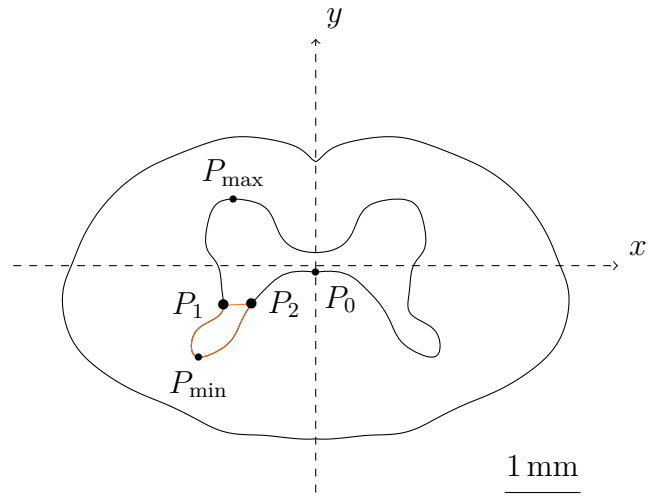


Figure 3.7 Cross-sectional contour of the DH in the C5 cross-section of the non-human primate cervical spinal cord.

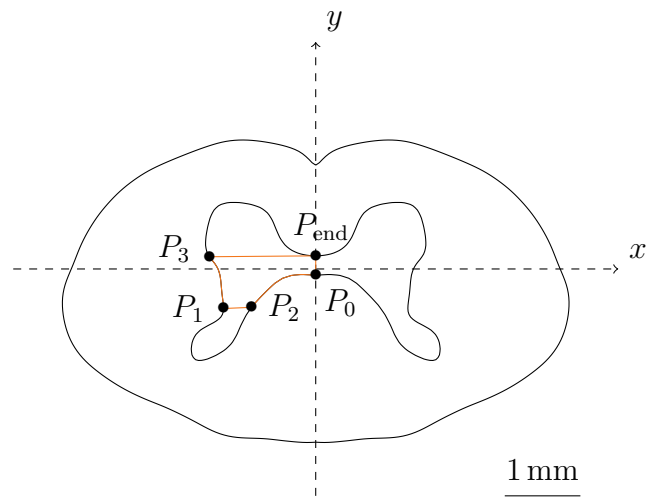


Figure 3.8 Cross-sectional contour of the MGM in the C5 cross-section of the non-human primate cervical spinal cord.

Middle region of the middle area of the gray matter (MR)

The MR cross-sectional contour is defined algorithmically after the MGM cross-sectional contour. Overall, it is a contour of area half that of the MGM cross-sectional contour and somewhat cropping the right and left extremities out of the MGM cross-sectional contour.

First, the points $P_{m,1}$ and $P_{m,2}$ are retrieved from the MGM cross-sectional contour as the mid-points of its dorso-medial portion (portion between P_0 and P_2 in Figure 3.8) and its upper portion (segment between P_3 and P_{end} in Figure 3.8) respectively.

Then, starting from $P_{m,1}$ for points P_1 and P_2 , and from $P_{m,2}$ for points P_3 and P_4 , P_1 , P_2 , P_3 and P_4 are alternatively and consecutively advanced along the MGM cross-sectional contour (in the anti-clockwise, clockwise, anti-clockwise and clockwise directions, respectively) until the area of the contour they form reaches half the area of the MGM cross-sectional contour itself.

Ventral horn of the gray matter (VH)

The VH cross-sectional contour is made of a portion of the GM cross-sectional contour and of the segment joining points P_3 and P_{end} , as depicted in Figure 3.10.

P_3 and P_{end} are defined just as in the case of the MGM.

Ventro-lateral quarter of the ventral horn of the gray matter (VQ)

The VQ cross-sectional contour is made of a portion of the GM cross-sectional contour, of the horizontal segment joining P_c and P_1 , and of the vertical segment joining P_c and P_2 , as depicted in Figure 3.11.

First, P_c is obtained as the center of mass of the VH cross-sectional contour. Then, P_1 and P_2 are obtained as those points of the VH cross-sectional contour having respectively closest y -coordinate and closest x -coordinate to those of P_c .

More precisely, the search for P_1 is restricted to those points of the VH cross-sectional contour whose x -coordinates are smaller than that of P_c , while the search for P_2 is restricted to the points whose y -coordinates are higher than that of P_c .

Lissaeur tract (LT)

The LT cross-sectional contour is made of a portion of the GM cross-sectional contour, a portion of the WM cross-sectional contour, and the two segments joining respectively points P_1 and P_2 , and P_3 and P_4 , as depicted in Figure 3.12.

To determine P_1 we proceed somewhat similarly as for the DH : we extract the lateral portion of the GM cross-sectional contour, and we look for the first point (whilst running

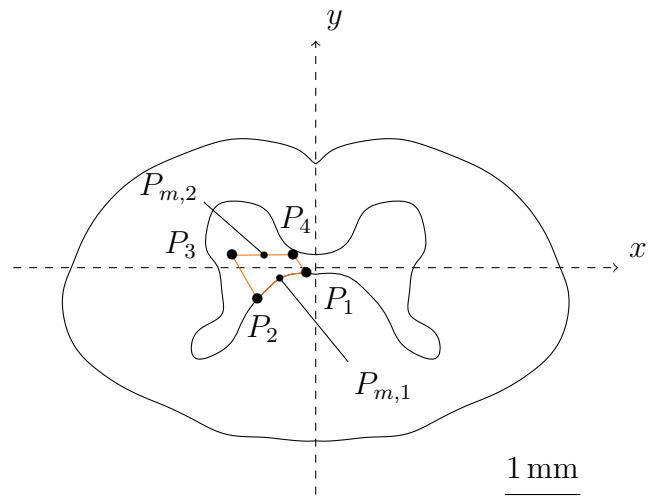


Figure 3.9 Cross-sectional contour of the MR in the C5 cross-section of the non-human primate cervical spinal cord.

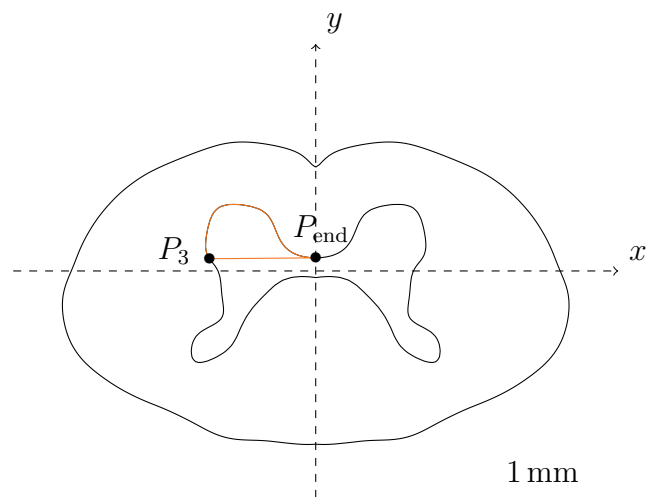


Figure 3.10 Cross-sectional contour of the VH in the C5 cross-section of the non-human primate cervical spinal cord.

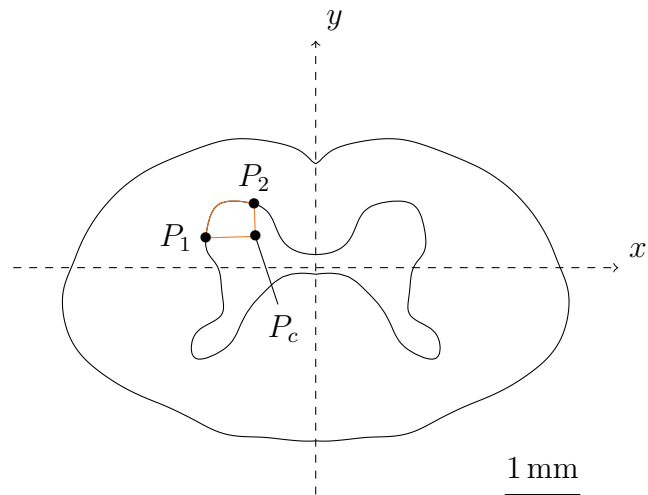


Figure 3.11 Cross-sectional contour of the VQ in the C5 cross-section of the non-human primate cervical spinal cord.

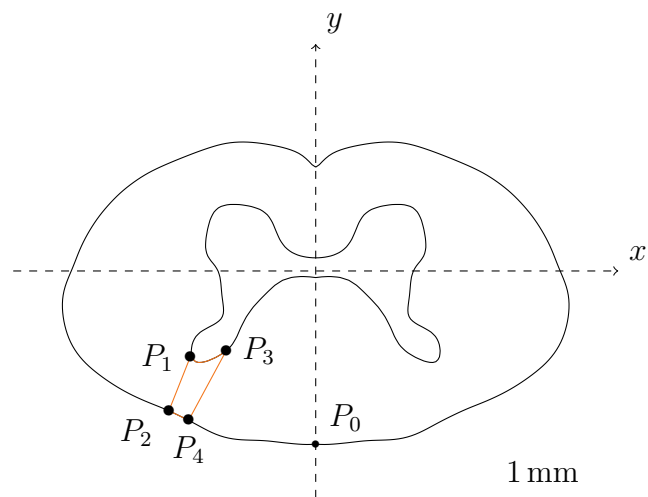


Figure 3.12 Cross-sectional contour of the LT in the C5 cross-section of the non-human primate cervical spinal cord.

from P_{\min} to P_{\max}) where the slope of the curve changes sign, this time from negative to positive.

The definition of P_2 follows that of P_1 : it is the point of the WM cross-sectional contour that is closest to P_1 .

Next, we determine P_3 as the point of the GM cross-sectional contour that is closest to P_0 , as depicted in Figure 3.12, where P_0 is the point of the WM cross-sectional contour satisfying the requirements $x == 0$ and $y < 0$.

Finally, P_4 is the point of the WM cross-sectional contour that is closest to P_3 .

Spinocerebellar tract (ST)

The ST cross-sectional contour is made of a portion of the WM cross-sectional contour, of a translated copy of this portion of contour, and of the two segments P_1P_2 and P_3P_4 joining two by two the tips of these portions of contour, as depicted in Figure 3.13.

First, the point P_1 is obtained after the LT cross-sectional contour. It is the mid-point of the segment of the LT cross-sectional contour joining points P_1 and P_2 in Figure 3.12.

Then, the y -coordinate of the point P_4 is set to be equal to the y -coordinate of the horizontal segment separating the DH from the MGM (specifically, it is the y -coordinate of point P_1 in Figure 3.7).

But in fact, P_4 is simply defined to be $P_4 := P_3 + \overrightarrow{P_3P_4}$ where we impose $\overrightarrow{P_3P_4} = \overrightarrow{P_2P_1}$.

Thus, we finally define P_3 to be the point of the WM cross-sectional contour which makes the criteria on the y -coordinate of P_4 best fulfilled.

Corticospinal tract (CT)

The CT cross-sectional contour is made of a portion of the GM cross-sectional contour, of a translated copy of a portion of the WM cross-sectional contour, and of the two segments joining P_1 and P_2 , and P_3 and P_4 , as depicted in Figure 3.14.

All the previous points have already been defined:

- P_1 , P_2 and P_3 coincide with P_0 , P_1 and P_4 in Figure 3.13.
- P_4 coincides with P_1 in Figure 3.7.

Dorsal columns (DC)

The DC cross-sectional contour is made of a portion of the GM cross-sectional contour, of a portion of the WM cross-sectional contour, and of the two segments joining $P_{0,1}$ and $P_{0,2}$, and P_1 and P_2 , as depicted in Figure 3.15.

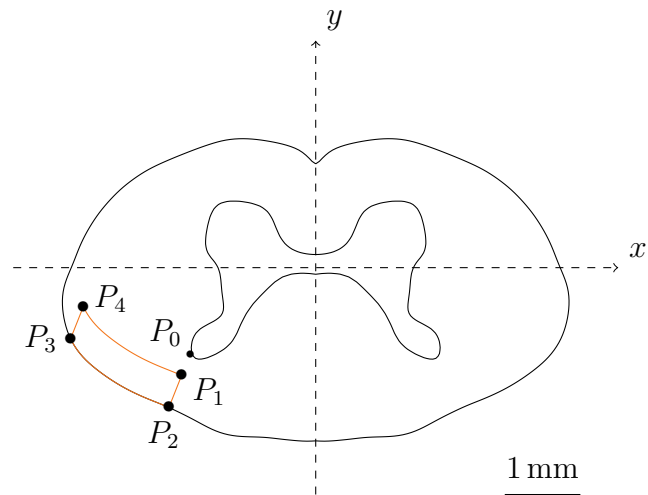


Figure 3.13 Cross-sectional contour of the ST in the C5 cross-section of the non-human primate cervical spinal cord.

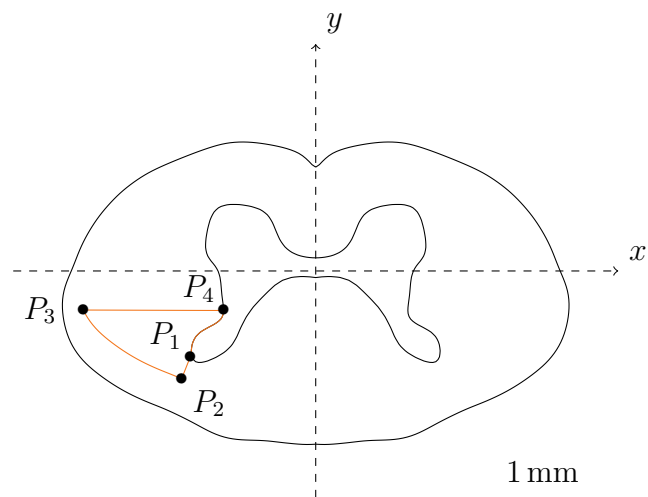


Figure 3.14 Cross-sectional contour of the CT in the C5 cross-section of the non-human primate cervical spinal cord.

All the previous points have already been defined:

- $P_{0,1}$ and $P_{0,2}$ are the points respectively of the GM cross-sectional contour and of the WM cross-sectional contour and satisfying the requirements $x == 0$ and $y < 0$.
- P_1 and P_2 coincide with P_3 and P_4 in the definition of the LT (see Figure 3.12).

In each cross-section of the model, the DC cross-sectional contour is further split into multiple cross-sectional contours.

This compartmentalization was implemented after principles regarding the organization of the dorsal columns reported by [51]. These principles state that fibers in the dorsal columns are subject to a medio-lateral segmental lamination, as illustrated by the sketch reproduced in Figure 3.16.

In the sketch of Figure 3.16, which represents a cross-section of the dorsal columns at the T11 segmental level, we see that the space allocated to the fibers of the T11 dorsal root—which just joined the spinal cord—is lateral to the space allocated to the fibers of the T12 dorsal root, which is lateral to the space of L1, and so on and so forth. In summary: the fibers of more caudal roots are clustered in more medial layers in the dorsal columns.

In fact, more recent investigations suggest a different organization of the dorsal columns, based on the fiber type rather than the fibers' segment of origin [52]. However, the compartmentalization implemented in the model presented here is based after the work of Feirabend and colleagues [51]: modifications to take into account the findings of [52] should be considered in the future.

Since in our model n_{seg} contiguous spinal segments are represented, we split the dorsal columns into $n_{\text{seg}} + 1$ compartments.

The first compartment, $\text{DCC}_{n_{\text{seg}}+1}$, accounts for all the spinal segments that would be caudal to the caudal-most segment represented in the model. For instance, suppose that we use the model to represent segments T5 to L3, then $\text{DCC}_{n_{\text{seg}}+1}$ would account for all the spinal segments L4 to S5, and it would be represented by the union of the compartments labeled S4-5 to L4 in Figure 3.16.

For the model, this means two things for $\text{DCC}_{n_{\text{seg}}+1}$:

1. It will be the only one to be represented in the caudal-most cross-section of the model ($\text{CS}_{n_{\text{seg}}+1}$), as illustrated by Figure 3.17.
2. It will be represented in every cross-section of the model—and its cross-sectional contours in successively more rostral cross-sections will be more and more medial, as

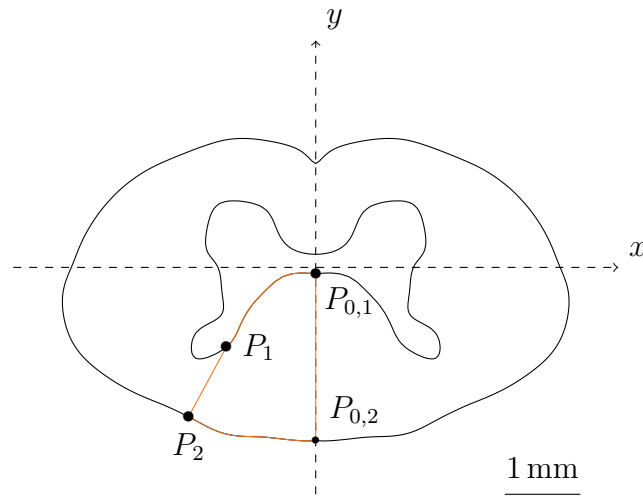


Figure 3.15 Cross-sectional contour of the DC in the C5 cross-section of the non-human primate cervical spinal cord.

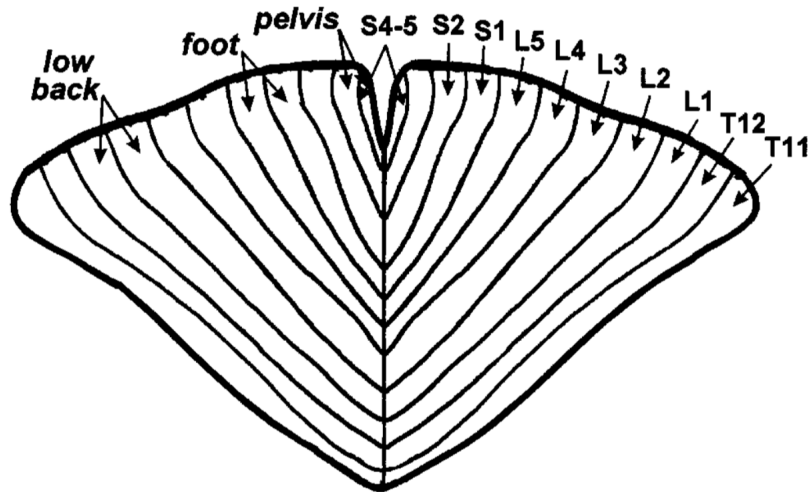


Figure 3.16 Topographical representation of the dermatomes in the dorsal columns of the Th11 segment. Adapted from Smith and Deacon (1984). L = lumbar; S = sacral; T = thoracic. *[Picture and caption taken from [51].]*

illustrated by Figures 3.17 to 3.19. (*Notation:* the name taken by the cross-sectional contour of DCC_k in cross-section CS_j , which exists only if $k \geq j$, is DCC_k^j .)

In the next rostral cross-section, $CS_{n_{\text{seg}}}$, a new DC compartment, $DCC_{n_{\text{seg}}}$, corresponding to the spinal root of spinal segment $S_{n_{\text{seg}}}$, gets a space allocated next to the space allocated to the previous and first compartment $DCC_{n_{\text{seg}}+1}$. This space is lateral compared to the space allocated to $DCC_{n_{\text{seg}}+1}$. The policy to determine how the DC cross-sectional contour gets split between the two compartments is as follows:

- The area of $DCC_{n_{\text{seg}}+1}^{n_{\text{seg}}}$ should be equal to the area of $DCC_{n_{\text{seg}}+1}^{n_{\text{seg}}+1}$.
- A vertical line splits $DCC_{n_{\text{seg}}+1}^{n_{\text{seg}}}$ and $DCC_{n_{\text{seg}}}^{n_{\text{seg}}}$. $DCC_{n_{\text{seg}}+1}^{n_{\text{seg}}}$ should be medial; $DCC_{n_{\text{seg}}}^{n_{\text{seg}}}$ should be lateral.
- Algorithmically: starting from P_0 , the points P_1 and P_2 are alternatively and consecutively advanced along the DC cross-sectional contour (respectively in the anti-clockwise and clockwise directions and while preserving the verticality of $\overrightarrow{P_1P_2}$ at best) until the contour complementary to that formed by P_0 , P_1 and P_2 reaches the area of $DCC_{n_{\text{seg}}+1}^{n_{\text{seg}}+1}$.

If the area of the DC cross-sectional contour in $CS_{n_{\text{seg}}}$ is lower than $(1 + \epsilon)$ times its area in $CS_{n_{\text{seg}}+1}$ (where $\epsilon > 0$ is a model parameter), the available area in $CS_{n_{\text{seg}}}$ is shared evenly between $DCC_{n_{\text{seg}}+1}^{n_{\text{seg}}}$ and $DCC_{n_{\text{seg}}}^{n_{\text{seg}}}$.

Similarly, in each subsequent cross-section $CS_{n_{\text{seg}}-1}$, $CS_{n_{\text{seg}}-2}$, \dots , a new DC compartment gets a lateral space allocated in the DC cross-sectional contour, and the complementary space is split among the previous DC compartments. The splitting is done according to the following rules:

- The cumulated area occupied by the previous DC compartments in CS_i should be equal to that which they occupy in CS_{i+1} (which is the area of the entire DC cross-sectional contour in this cross-section).
- The new DC compartment should be allocated the remaining lateral area enclosed by the DC cross-sectional contour of CS_i , separated by a vertical line from the medial area occupied by the previous DC compartments.
- If the area A_i available in CS_i is lower than $(1 + \epsilon)$ times the area occupied by the previous DC compartments in CS_{i+1} , the areas occupied by the previous DC compartments in CS_i are redefined. If n_{DCC} is the number of previous DC compartments plus one (to account for the new DC compartment), the area allocated to each previous DC compartment and also to the new DC compartment in CS_i is set to be A_i/n_{DCC} .

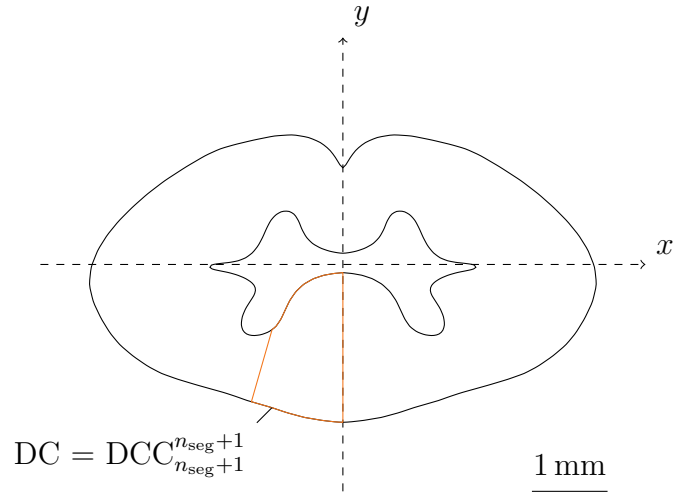


Figure 3.17 Cross-sectional contours of the DC compartments in $CS_{n_{seg}+1}$. There is only one DC compartment represented in this cross-section: $DCC_{n_{seg}+1}^{n_{seg}+1}$. The whole DC cross-sectional contour coincides with $DCC_{n_{seg}+1}^{n_{seg}+1}$.

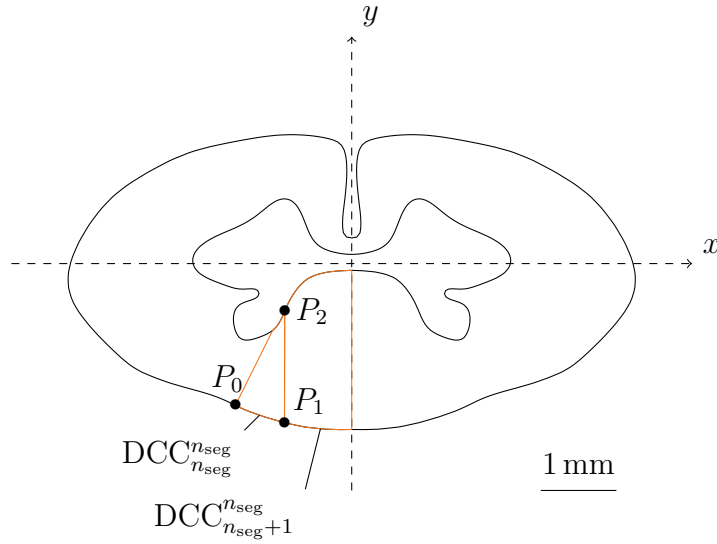


Figure 3.18 Cross-sectional contours of the DC compartments in $CS_{n_{seg}}$. There are two DC compartments represented in this cross-section: $DCC_{n_{seg}+1}^{n_{seg}+1}$ and $DCC_{n_{seg}}^{n_{seg}}$.

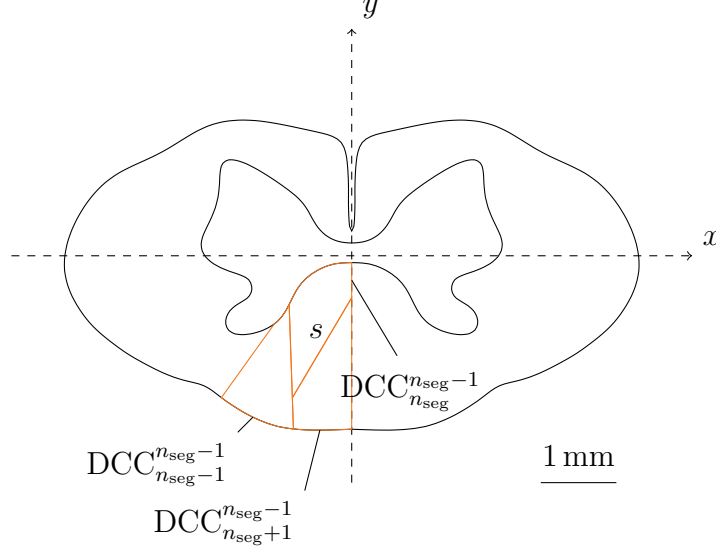


Figure 3.19 Cross-sectional contours of the DC compartments in $CS_{n_{seg}-1}$. There are three DC compartments represented in this cross-section: $DCC_{n_{seg}+1}$, $DCC_{n_{seg}}$ and $DCC_{n_{seg}-1}$.

- The medial area occupied by the previous DC compartments should be split among the previous DC compartments by oblique lines with a specified and fixed slope s .

This splitting in $CS_{n_{seg}-1}$ is represented in Figure 3.19, and a tridimensional representation of the overall dorsal columns compartmentalization is given in Figure 3.20.

Outermost layer of the dorsal columns (OD)

The OD comprises the OD_1 , OD_2 , OD_3 , OD_4 , OD_5 and OD_6 , which together compartmentalize the outermost layer of the dorsal columns. The OD is defined by the region delimited by the portion of WM cross-sectional contour between $P_{0,0}$ and $P_{1,0}$, the copy of this curve dilated by factor $\epsilon < 1$ joining points $P_{0,1}$ and $P_{1,1}$, and the segments joining $P_{0,0}$ and $P_{0,1}$, and $P_{1,0}$ and $P_{1,1}$, as depicted in Figure 3.21.

In Figure 3.21, OD_1 is the lower-right compartment of OD, OD_2 the lower-central compartment, OD_3 the lower-left compartment, and OD_4 , OD_5 and OD_6 the upper-right, upper-central, and upper-left compartments.

The curve separating the two bands comprising respectively OD_1 , OD_2 and OD_3 , and OD_4 , OD_5 and OD_6 , is a copy of the WM cross-sectional contour between $P_{0,0}$ and $P_{1,0}$ dilated by the factor $1+\epsilon/2$. It is thus the “mean” between the curves joining $P_{0,0}$ and $P_{1,0}$, and $P_{0,1}$ and $P_{1,1}$). Each OD_i occupies one third of the area of the band in which it is embedded.

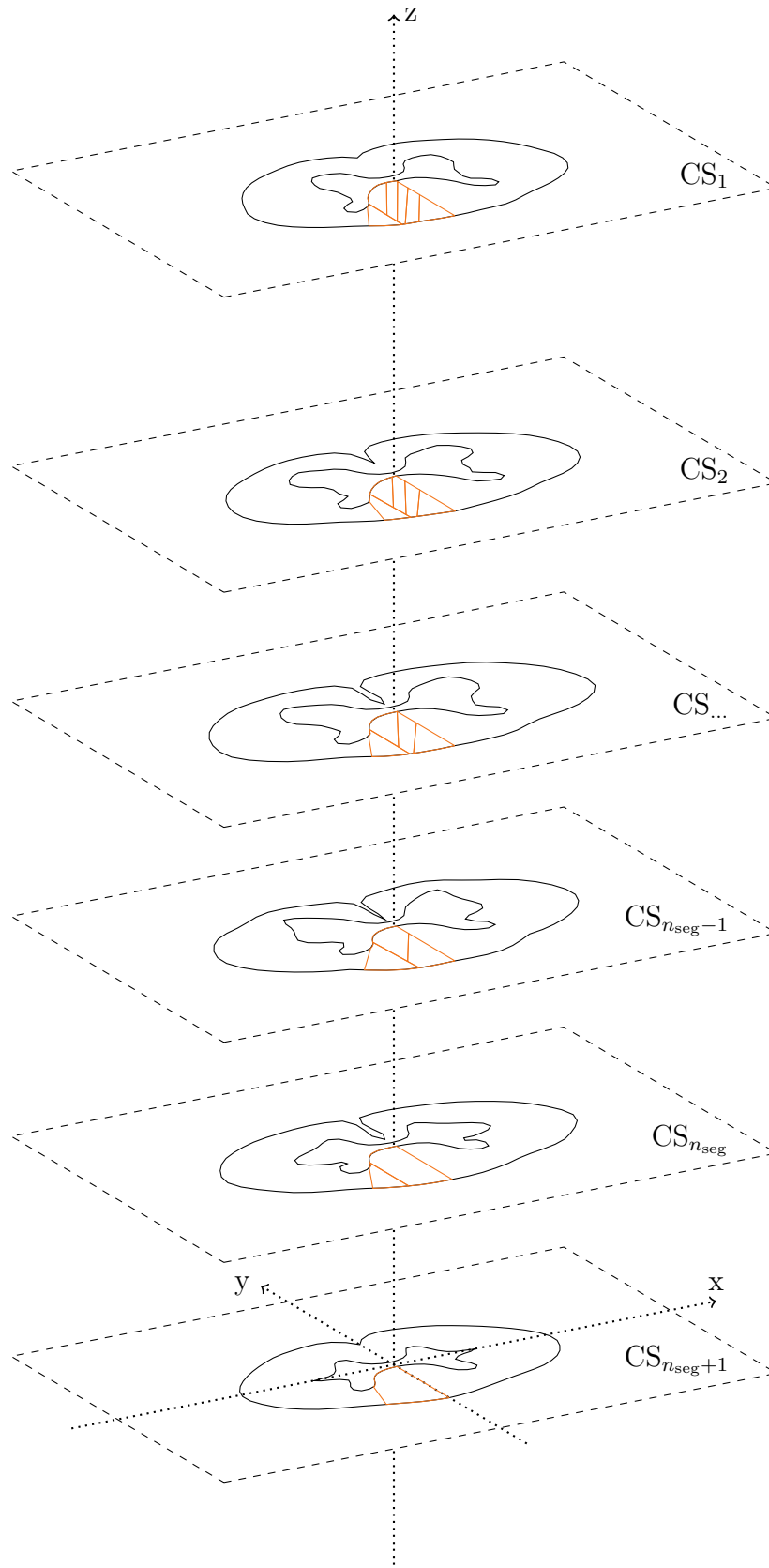


Figure 3.20 Tridimensional representation of the cross-sectional contours of the dorsal columns compartments in each cross-section of the geometrical model.

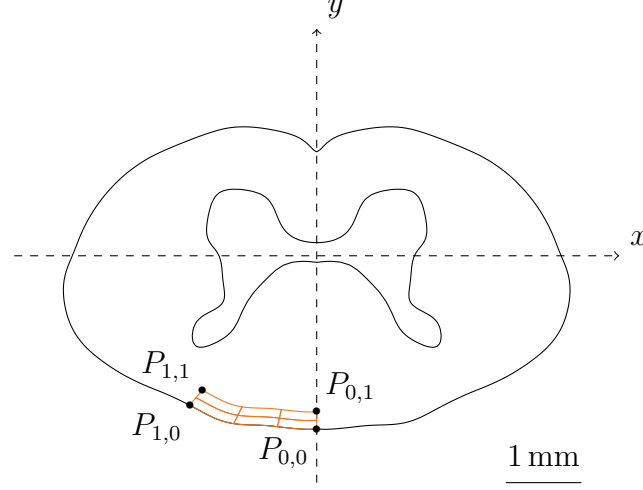


Figure 3.21 Cross-sectional contour of the OD compartments in the C5 cross-section of the non-human primate cervical spinal cord.

3.2.6 Spinal roots

The geometrical model offers the possibility to represent the spinal roots of the represented spinal segments. Each spinal segment whose roots are represented possess one pair of ventral roots and one pair of dorsal roots: one of each on the left side, and one of each on the right side.

As discussed in Section 1.1.2, the spinal segments are in fact anatomically defined by their spinal roots. One definition, yet incomplete, comes from [92]: “*The length of each [spinal] segment was defined as the root attachment length plus the upper inter-root length.*” Based on this, I opted to define spinal segment S_j as the portion of spinal cord extending rostro-caudally from the entry point of the lowermost rootlet of spinal root R_j to the entry point of the lowermost rootlet of spinal root R_{j-1} (recall that the numbering is such that the uppermost spinal segment is S_1). Yet this definition is still incomplete, for it does not specify whether the lowermost rootlets considered should be those of the dorsal roots or of the ventral roots, and of which side, all of which may be at distinct rostro-caudal levels.

An example delimitation between consecutive spinal segments based on the left dorsal roots is illustrated by Figure 3.22. In this picture, it can be appreciated that the lowermost rootlet of a left dorsal root may not be precisely at the same rostro-caudal level than that of the corresponding right dorsal root (as is the case *eg* of LDR_j , for which the lowermost rootlet of the left dorsal root is more caudal than that of the right dorsal root). In the model, this variability is neglected, and it is assumed that the lowermost rootlets of both ventral and both dorsal roots of the same spinal segment enter in the spinal cord at the same rostro-caudal level.

I developed two models for the spinal roots: one in which the rootlets are explicitly rep-

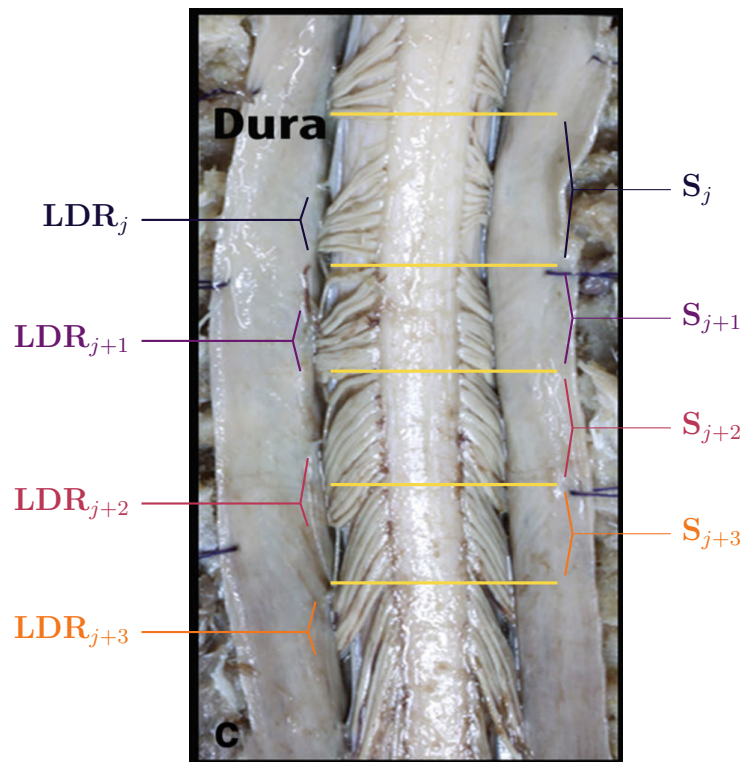


Figure 3.22 Rootlet bundles and delimitations between consecutive spinal segments. *Left:* generic labels of left dorsal roots. *Right:* generic labels of spinal segments. [Picture adapted from [10].]

resented as distinct entities, and one in which the rootlets are not represented as distinct entities, but in which the shape of the roots emulates the rootlet bundles. However, I encountered difficulties later on in building and meshing the volumes meant to represent the rootlets. I thus couldn't make use of the model with rootlets to build actual volume conductor models, and this model is therefore not presented here.

On the other hand, the merging of the ipsilateral ventral and dorsal roots of a same segment into a spinal nerve can also optionally be represented. In this case, the spinal nerve prolong the ventral and dorsal roots beyond the vertebral column. In the converse case, the ventral and dorsal roots are represented as reaching the intervertebral foramina and ending there.

Similarly to the other structures represented in the model, the roots—prolonged or not by the spinal nerve—, are ultimately represented by series of cross-sectional contours. However, the first step in the definition of these contours is the definition of the guide curves along which they are distributed. These guide curves are 3D open curves materializing the trajectories of the roots from the WM to their respective intervertebral foramina (or beyond if the spinal nerve is included). The cross-sectional contours are then defined as ellipses lying in planes orthogonal to the guide curves, and centered around them.

In the following, the definitions of the left ventral and dorsal roots ($x < 0$) are exposed, and the left ventral and dorsal roots of spinal segment S_j will be denoted as VR_j and DR_j . The right ventral and dorsal roots are assumed to be defined similarly, though distinct definitions or parameterizations could be envisaged. There are slight differences between the ventral and dorsal roots, and I start by exposing the case of the dorsal roots.

Dorsal roots

The definition of the cross-sectional contours of dorsal root DR_j starts with that of its guide curve. The latter was established so as to respect the following criteria, based upon anatomical observations:

1. The lowermost point of DR_j at its entrance into the spinal cord should be at the elevation of the lower cross-section of segment S_j , that is, at the elevation $z_{CS}(j+1)$. This ensues from the definition of the spinal segments given here above.
2. The entrance of DR_j into the spinal cord should be in the direction of the dorsal horn (DH) in S_j .
3. DR_j should exit the spine (*ie* the vertebral column) through its dedicated intervertebral foramen, whose center-point coordinates, which constitute a parameter of the model, are given by the variable P_{IF} .

4. Along the first half of its trajectory (from entrance in the spinal cord to exit from the spine through the intervertebral foramen), DR_j should run closely to the spinal cord (*ie* closely to the white matter). Along the second half, DR_j should run straight towards P_{IF} .

The strategy adopted to define the guide curve consists in defining a series of interpolation points, to interpolate them with a cubic spline, and to sample a collection of uniformly spaced points along that spline. This is explained below.

Entry point The first interpolation point defining the guide curve is called the entry point of DR_j (in the sense of the entrance of the root into the spinal cord). It is the first point of the guide curve and we denote it by P_E . It is defined such that the first two requirements here above be respected.

To further spell out the first of these requirements, let us clarify the meaning of “the lowermost point of DR_j at its entrance into the spinal cord”. For this, let us anticipate and say a few words about the cross-sectional contours of DR_j . As mentioned before, the cross-sectional contours of DR_j are defined as ellipses orthogonal to its guide curve. These ellipses all have the same diameter D (mean between major-axis and minor-axis lengths), but different eccentricities. By definition, the first of these ellipses, $DR_{j,1}$, is centered around the first point of the guide curve—*ie* centered around P_E —, is vertically-oriented (major-axis parallel to z -axis), and has eccentricity ecc_{REZ} ($\text{REZ} = \text{Root Entry Zone}$). The lowermost point of DR_j at its entrance into the spinal cord is simply the lowermost point P_{low} (minimal z -coordinate) of $DR_{j,1}$.

Thus, P_E , which shall be the center of the ellipse $DR_{j,1}$, is defined as follows:

1. Let z_E be defined as $z_E = z_{\text{CS}}(j+1) + \text{ecc}_{\text{REZ}} \cdot D/2$: the elevation of P_E is z_E .
2. Let α_E be the angular direction of the DH at the elevation z_E .

Since there is no cross-sectional contour to define the DH at z_E , we set α_E to be the weighted average of α_{up} and α_{down} , the angular directions of the DH in the upper and lower cross-sections of segment S_j respectively (these are CS_j and CS_{j+1}). More specifically, α_{up} (resp. α_{down}) is the angular direction of point $P_{\text{DH,up}}$ (resp. $P_{\text{DH,down}}$) as depicted in Figure 3.23, and $P_{\text{DH,up}}$ (resp. $P_{\text{DH,down}}$) is defined as the point of the DH cross-sectional contour in CS_j (resp. CS_{j+1}) which is farthest from the z -axis.

We let $\alpha_E := \omega_{\text{up}} \cdot \alpha_{\text{up}} + \omega_{\text{down}} \cdot \alpha_{\text{down}}$ with $\omega_{\text{up}} := (z_E - z_{\text{CS}}(j+1)) / (z_{\text{CS}}(j) - z_{\text{CS}}(j+1))$ and $\omega_{\text{down}} := 1 - \omega_{\text{up}}$.

3. Let $P_{\text{WM,up}}$ and $P_{\text{WM,down}}$ be the points of the cross-sectional contours of the WM respectively in CS_j and CS_{j+1} which are lying in the angular direction α_E .

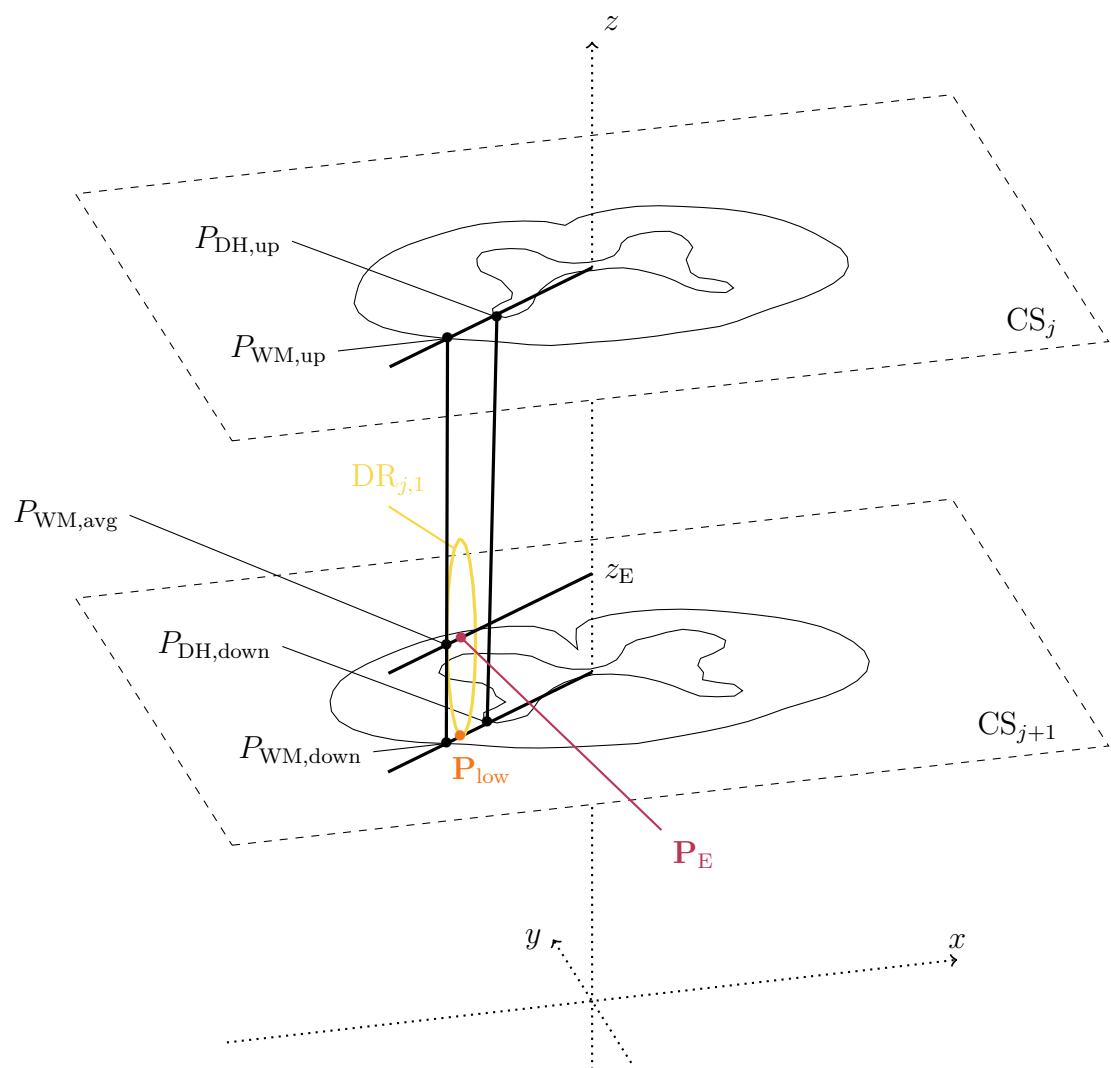


Figure 3.23 Definition of the entry point P_E of dorsal root DR_j .

Let $P_{\text{WM,avg}}$ be the weighted average of these points: $P_{\text{WM,avg}} = \omega_{\text{up}} \cdot P_{\text{WM,up}} + \omega_{\text{down}} \cdot P_{\text{WM,down}}$ where ω_{up} and ω_{down} are defined as in step 2 above.

4. We finally let P_E be the point lying in angular direction α_E , at the elevation z_E , and whose distance to the z -axis is ϵ_E times that of $P_{\text{WM,avg}}$, with $\epsilon_E < 1$.

This way, the requirements on the direction and elevation of $\text{DR}_{j,1}$ are fulfilled. Furthermore, the condition $\epsilon_E < 1$ ensures that $\text{DR}_{j,1}$ is completely enclosed within the volume formed by interpolation of the cross-sectional contours of the WM (hereafter referred to as the volume of the WM), provided ϵ_E is chosen sufficiently small. Thus, the volume formed by interpolation of the cross-sectional contours of DR_j penetrates into the volume of the WM.

Subsequent interpolation points Let us denote by n_P the total number of interpolation points, including P_E and P_{IF} , and by α_{IF} and z_{IF} the angular direction and elevation of P_{IF} .

For each $i \in \{2, \dots, n_P - 1\}$, we define:

$$\begin{aligned} z_i &:= z_E + \frac{i-1}{n_P-1} \cdot (z_{\text{IF}} - z_E) \\ \alpha_i &:= \alpha_E + \frac{i-1}{n_P-1} \cdot (\alpha_{\text{IF}} - \alpha_E) \end{aligned}$$

To comply with the 4th requirement introduced in the beginning of this section, we use two different modalities to define the interpolation points P_i , $i \in \{2, \dots, n_P - 1\}$. For the first “half” of them, the definition is such as for these points to stay close to the WM, while for the second “half”, the definition makes these points go straight to P_{IF} . The two “halves” may in fact be unbalanced, as will appear clearer below.

The point starting from which the modality changes is the point with index i_0 such that the angular direction α_{i_0} is just $< \pi$ and α_{i_0-1} still $> \pi$. This corresponds to the passage of the root from the dorsal region ($y < 0$) to the ventral region ($y > 0$). Note that we always have $\alpha_E \in]\pi, 3\pi/2[$ and $\alpha_{\text{IF}} \in]\pi/2, \pi[$ (as illustrated in Figure 3.24) so the sequence $(\alpha_i)_i$ does indeed cross the level π while decreasing.

The points are thus split in two groups: $\{P_2, \dots, P_{i_0-1}\}$ on one hand, and $\{P_{i_0}, \dots, P_{n_P-1}\}$ on the other hand. For each point P_i of the first group (which shall stay close to the WM), P_i is defined in terms of its angular direction α_i , elevation z_i , and its distance from the z -axis d_i . α_i and z_i being already defined, there simply remains to define d_i .

d_i is defined in terms of the distance from the z -axis of the point of the WM cross-sectional contour lying in the same angular direction α_i and elevation z_i . We note this distance $d_{\text{WM},i}$.

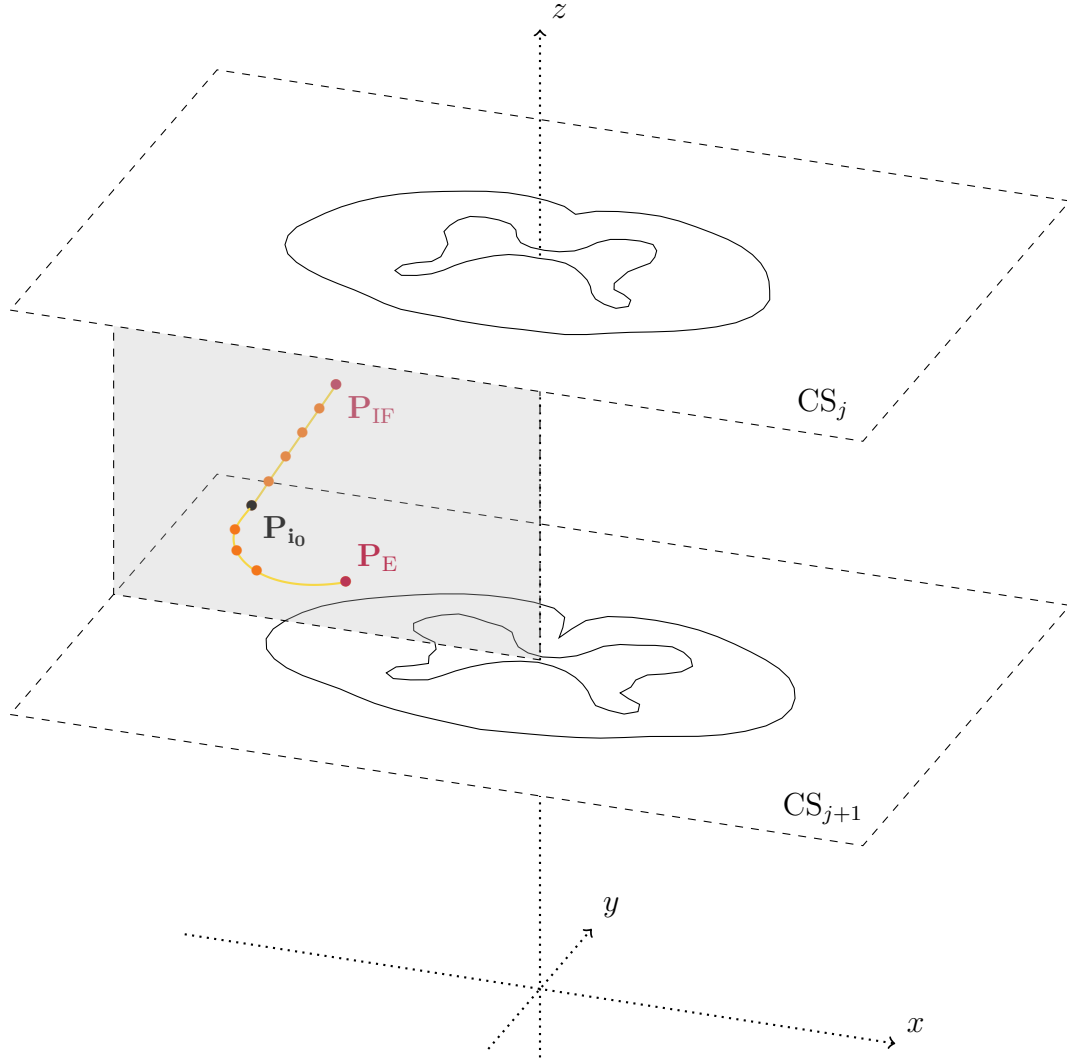


Figure 3.24 Guide curve and interpolation points of dorsal root DR_j . From P_E to P_{i_0-1} : points of the first group. From P_{i_0} to P_{IF} : points of the second group. *Shaded gray area:* vertical half-plane with angular direction equal to π .

Yet, since z_i may not coincide with one of the z_{CS} 's, there may not be any cross-sectional contour of the WM at the elevation z_i . Thus, to define $d_{WM,i}$, we proceed as for P_E , ie by averaging the points of the WM cross-sectional contours in the cross-sections just above and just below the concerned z_i .

Once done and $d_{WM,i}$ defined, we let $d_i := d_{WM,i} + \text{gap}_{GC}$, where gap_{GC} is a fixed constant, parameter of the model.

For the second group, the points P_i are straightforwardly defined as:

$$P_i := (1 - \omega_i) \cdot P_{i_0-1} + \omega_i \cdot P_{IF}$$

where $\omega_i = \frac{i-i_0+1}{n_P-i_0+1}$, thus making them uniformly-spaced along the straight segment joining P_{i_0} and P_{IF} .

Guide curve The guide curve of DR_j is defined after the previous interpolation points. It is a collection of points sampled with uniform spacing along a spline interpolating these interpolation points. The spline used is a cubic spline satisfying not-a-knot end conditions, as implemented by the *interparc* program [93].

Cross-sectional contours The last step is to define the cross-sectional contours of DR_j . Let n_C be the total number of them (which is determined based on a density of cross-sectional contours per unit length of guide curve and the total length of the guide curve).

As mentioned previously, each cross-sectional contour is an ellipse centered around one point of the guide curve. Let $\{i_1, i_2, \dots, i_{n_C}\}$ be the indices of these points. We have $i_1 = 1$ (ie $P_{i_1} = P_E$) and $i_{n_C} = n_{GC}$ where n_{GC} is the total number of points of the guide curve ($P_{i_{n_C}} = P_{IF}$). The other indices are such that the points $P_{i_1}, P_{i_2}, \dots, P_{i_{n_C}}$ are uniformly-spaced along the guide curve.

Next, we need to define the eccentricities and the major-axis directions of the ellipses. In fact we already defined them for the first cross-sectional contour $DR_{j,1}$ when we defined the guide curve entry point. For the subsequent cross-sectional contours, we proceed as follows.

The eccentricity ecc_k of $DR_{j,k}$ is defined as a weighted average between the eccentricity at the root entry zone ecc_{REZ} and a lower eccentricity ecc_{root} , reflecting the fact that the root is less and less flat and elongated as we move away from the REZ:

$$\text{ecc}_k := \text{ecc}_{REZ} + \frac{k-1}{n_C-1} \cdot (\text{ecc}_{root} - \text{ecc}_{REZ})$$

Notice that this yields $\text{ecc}_1 = \text{ecc}_{\text{REZ}}$ and $\text{ecc}_{n_C} = \text{ecc}_{\text{root}}$.

On the other hand, the vector v_k directing the major-axis of $\text{DR}_{j,k}$ is defined to be orthogonal to the local direction of the guide curve at P_{i_k} .

For $k \neq 1$ and $k \neq n_C$, this local direction is given by $u_k = \overrightarrow{P_{i_k-1}P_{i_k+1}} / \|\overrightarrow{P_{i_k-1}P_{i_k+1}}\|$.

For $k = n_C$, we let $u_{n_C} = \overrightarrow{P_{n_{GC}-1}P_{n_{GC}}} / \|\overrightarrow{P_{n_{GC}-1}P_{n_{GC}}}\|$.

We further impose that v_k lie in the vertical plane containing the direction u_k . In other words, the projections $p(v_k)$ and $p(u_k)$ of v_k and u_k in the horizontal plane should be collinear.

The previous requirements are readily obtained by defining v_k as the rotation of vector u_k by angle $\pm \frac{\pi}{2}$ around the axis directed by the normalized cross-product $n_k = \pi(u_k) \wedge u_k / \|\pi(u_k) \wedge u_k\|$. The sign of the rotation angle is chosen such that the resulting vector v_k be pointing upwards (its z -coordinate ≥ 0).

For high densities of ellipses per unit length of guide curve (which increase the success rate of the interpolation process to form 3D volumes), and at places where the guide curve is highly curved, consecutive ellipses defined with the previous approach often tend to intersect each other, which is not acceptable for subsequent interpolation.

This situation is particularly frequent at the root entry zone for a root exiting the spine at a rostro-caudal level far from its entrance in the spinal cord. Indeed in this case, the guide curve of the root adopts a course almost purely vertical as soon as it exits the WM. It thus defines close-to-horizontal cross-sectional contours which end-up intersecting the vertically oriented first cross-sectional contour $\text{DR}_{j,1}$.

To cope with this, we relax the condition of strict orthogonality of the vectors v_k with the local guide curve direction. Instead, we make the v_k 's progressively switch from being vertical (condition satisfied by v_1) to satisfying the orthogonality condition.

To do so, note that rotating u_k by angle $\pm \frac{\pi}{2}$ around the axis directed by n_k is equivalent to rotating $\pi(u_k)$ by angle $\alpha_k \pm \frac{\pi}{2}$ around this axis, where α_k is the angle between $\pi(u_k)$ and u_k (see Figure 3.25). Also note that if $\alpha_k \sim 0$, the resulting v_k is close to being vertical.

These observations suggest to replace α_k in the previous definition by $\alpha'_k := k^{-1}/n_C - 1 \cdot \alpha_k$ as depicted in Figure 3.26.

Algorithmically, the ellipse $\text{DR}_{j,k}$ can be defined as follows:

1. Let \mathcal{C} be the circle with diameter D lying in the horizontal plane, centered on the origin O . Let P_0 be the point of \mathcal{C} such that $P_0 = (D, 0, 0)$.
2. Let \mathcal{E} be the ellipse obtained by dilating \mathcal{C} by ecc_k in the x -direction and by ecc_k^{-1} in the y -direction.

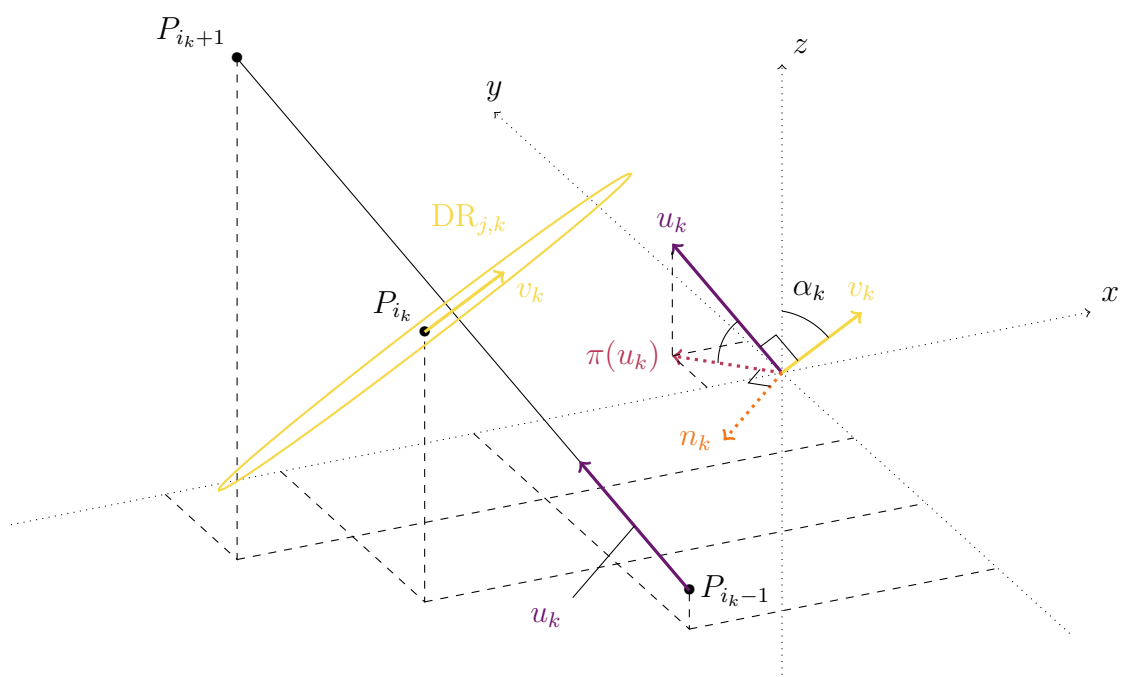


Figure 3.25 Orthogonal $DR_{j,k}$.

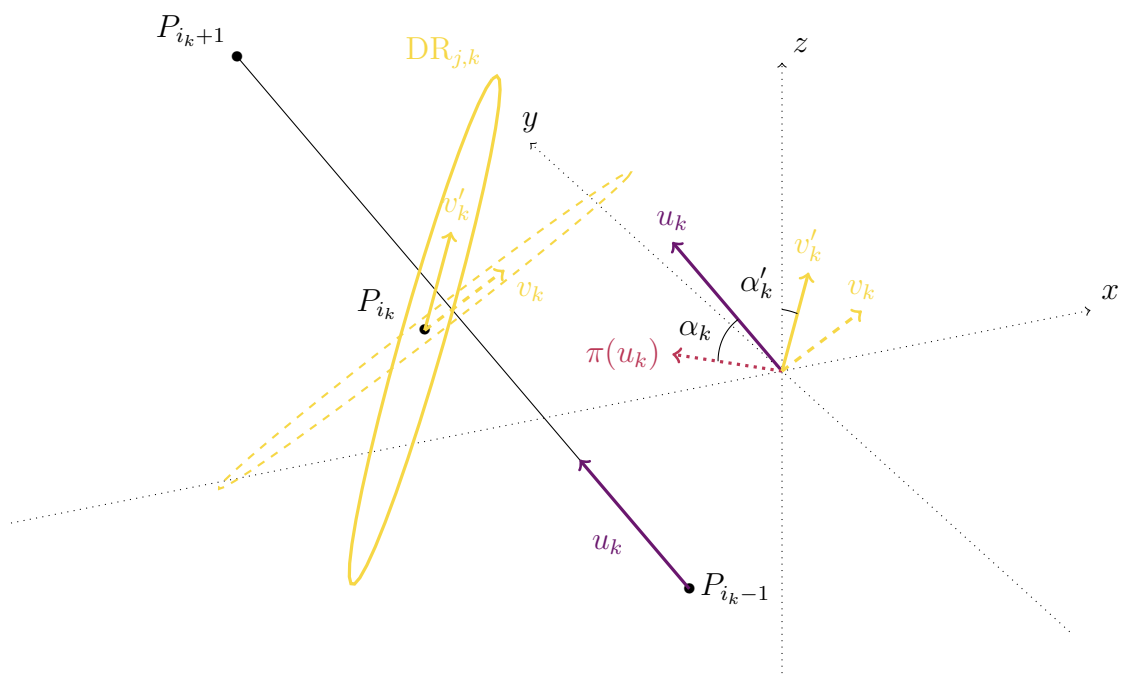


Figure 3.26 Rectified $DR_{j,k}$.

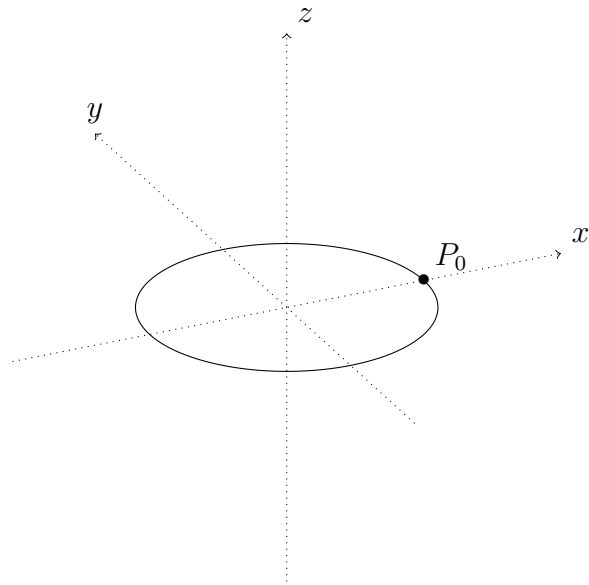


Figure 3.27 Algorithm for $\text{DR}_{j,k}$ (1/5).

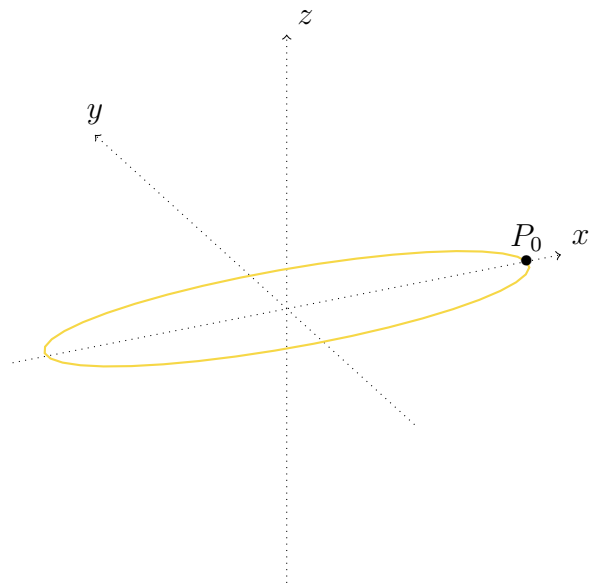


Figure 3.28 Algorithm for $\text{DR}_{j,k}$ (2/5).

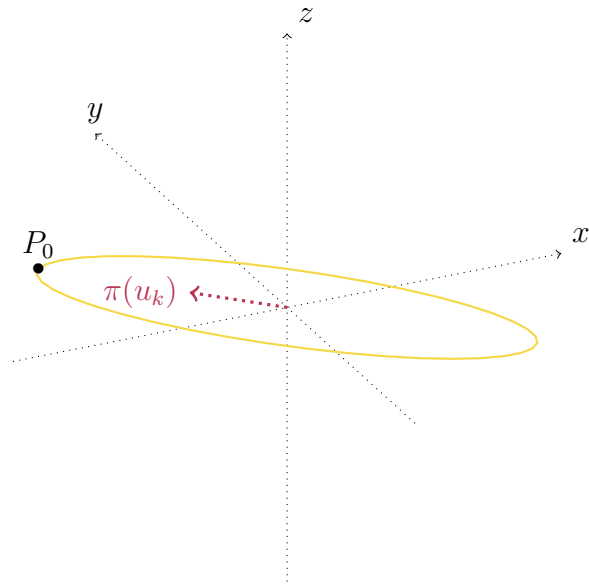


Figure 3.29 Algorithm for $\text{DR}_{j,k}$ (3/5).

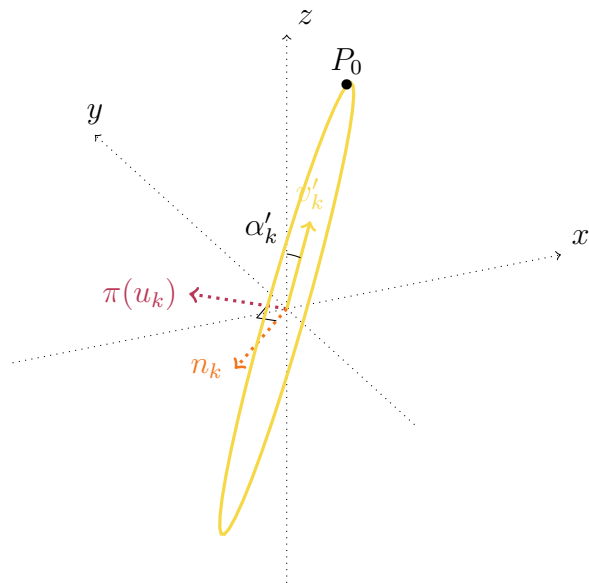
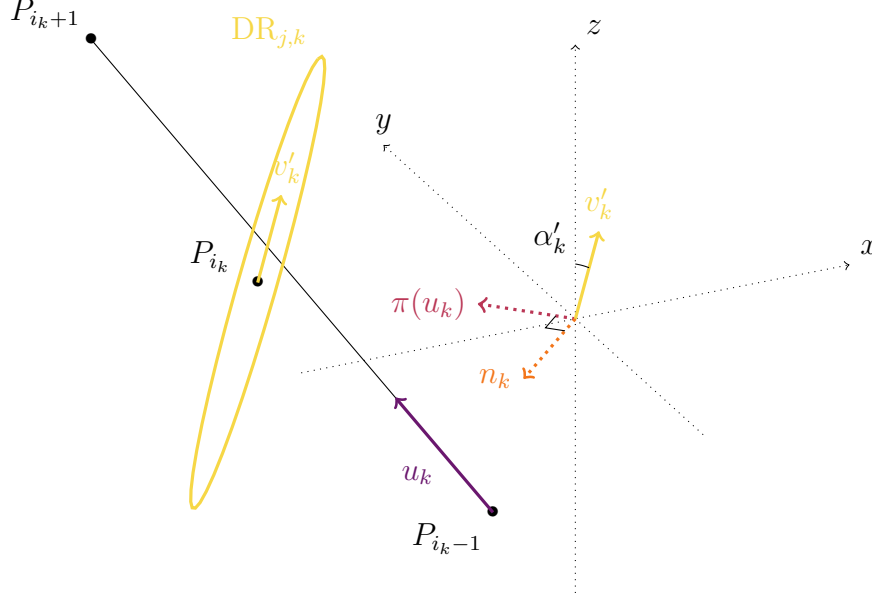


Figure 3.30 Algorithm for $\text{DR}_{j,k}$ (4/5).


 Figure 3.31 Algorithm for $DR_{j,k}$ (5/5).

3. Let \mathcal{E}_r be the rotation of \mathcal{E} around the z -axis such that P_0 points in the same direction as $\pi(u_k)$.
4. Let \mathcal{E}_b be the rotation of \mathcal{E}_r around the axis directed by n_k by angle $\alpha'_k \pm \pi/2$.
5. Let $DR_{j,k}$ be the translation of \mathcal{E}_b by vector $\overrightarrow{OP_{i_k}}$.

Recall that the $DR_{j,k}$'s actually constitute finite collections of points. This is readily achieved by using the same and unique collection of points for the initial circle \mathcal{C} . By so doing, the $DR_{j,k}$'s share the same number of points, and points with equal indexes on different $DR_{j,k}$'s are isomorphic (by construction). This is important as it will allow appropriate definition of dorsal root fiber pathways, as discussed in Section 3.3.

Ventral roots

The strategy to define the cross-sectional contours of ventral root VR_j is very similar to that employed for the dorsal root DR_j . It again relies on the definition of a guide curve, itself relying on the definition of a series of interpolation points.

These are based on the following requirements:

1. The lowermost point of VR_j at its entrance into the spinal cord should be at the elevation of the lower cross-section of segment S_j , that is, at the elevation $z_{CS}(j+1)$.
2. The entrance of VR_j into the spinal cord should be either in the direction of the ventro-lateral quarter of the ventral horn (VQ) in S_j , or in the direction of the

intervertebral foramen through which VR_j exits the spine (whichever of the two is most ventral).

3. VR_j should exit the spine through its dedicated intervertebral foramen, which is the same as that dedicated to DR_j , and whose center-point coordinates are given by the variable P_{IF} .
4. Along the first half of its trajectory (from entrance in the spinal cord to exit from the spine through the intervertebral foramen), VR_j should run closely to the spinal cord (*ie* closely to the white matter). Along the second half, VR_j should run straight towards P_{IF} .

Entry point The entry point P_E of the ventral root VR_j is defined in a similar way than that of the dorsal root DR_j , with differences in the definition of its angular direction. This time α_E is defined as the minimum between:

- a weighted average of the angular directions of the center of masses of the VQs of the cross-sections CS_j and CS_{j+1} , denoted α_1 on Figure 3.32;
- a little less than the angular direction α_{IF} of the intervertebral foramina through which the root exits, denoted α_2 on Figure 3.32 (“a little less” means that $\alpha_2 = \epsilon \times \alpha_{IF}$ with $\epsilon < 1$, $\epsilon \simeq 1$, parameter of the model).

Guide curve and cross-sectional contours The guide curve and cross-sectional contours are defined similarly for the ventral as for the dorsal root. Importantly, the different $VR_{j,k}$ ’s are also obtained from the same and unique collection of points sampling the initial circle \mathcal{C} . They thus share the same number of points, and points with equal indexes on different $VR_{j,k}$ ’s are isomorphic.

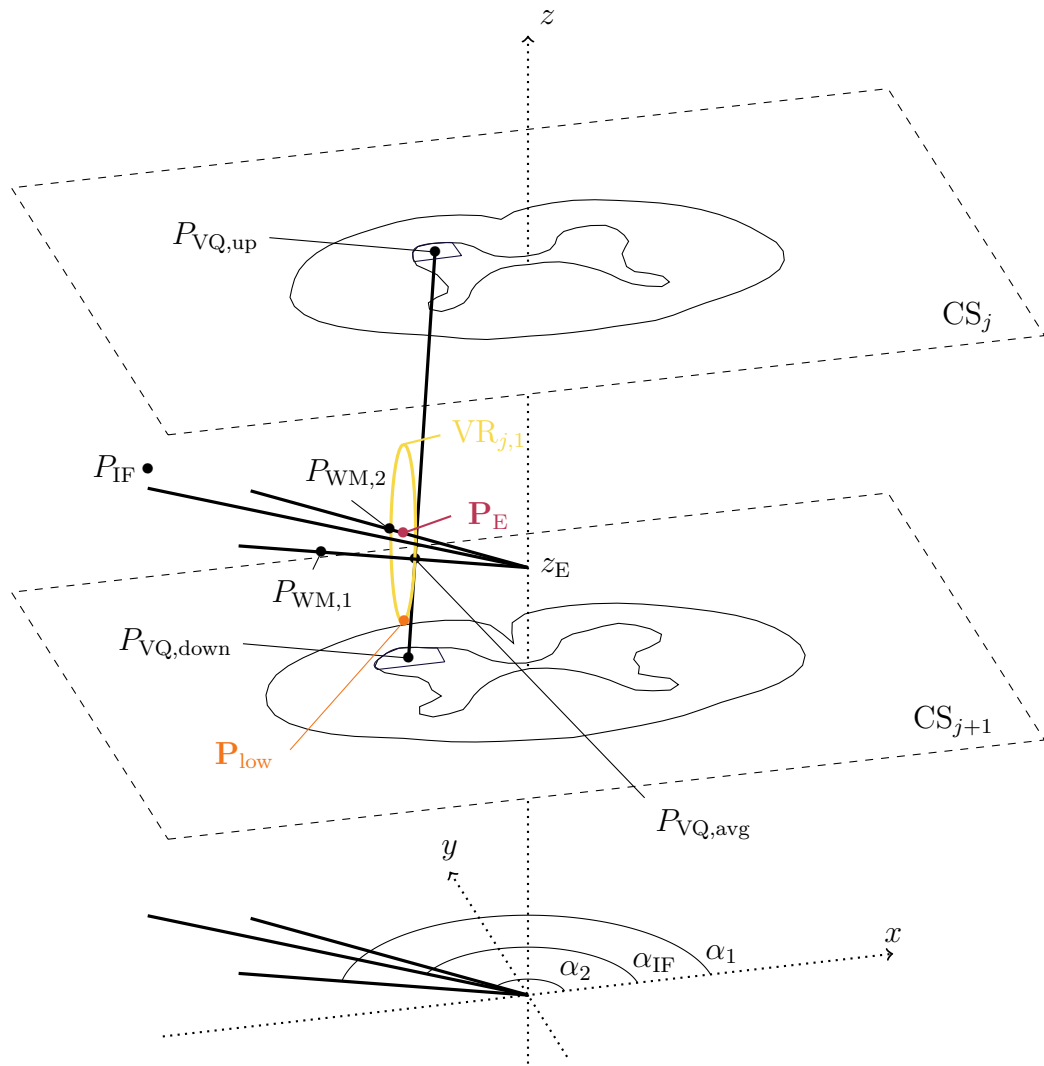


Figure 3.32 Definition of the entry point P_E of ventral root VR_j .

3.3 Connectivity-based geometrical models of motoneurons and nerve fibers

Along with the geometrical model of the spinal cord presented in the previous section, I have developed new geometrical models to represent the trajectories of motoneurons and nerve fibers in the spinal cord and in the spinal roots. In particular, the geometrical model of dorsal root primary afferents capture the relationship between fiber morphology and connectivity with motoneurons.

3.3.1 Geometrical model of motoneurons

For the purpose of interpolating the extracellular electric potential along motoneurons in volume conductor models of the spinal cord, and in view of passing these potentials as input to neurophysical models of motoneurons as described in Section 2.3.2, I propose to describe their geometry by the following elements:

- a point giving the position of the soma center;
- a pathway for the motoneuron's axon;
- a series of binary trees of segments describing the motoneuron's dendrites (one binary tree per dendrite).

One point for the soma (*ie* one interpolated electric potential value) should be sufficient for the different somatic compartments due to their close proximity; the motor axon pathway should allow to interpolate a value for each axon and axon initial segment compartment (they are distributed along that pathway); the binary trees of segments should allow to interpolate one value for each dendritic compartment (in the middle of each segment).

This representation is similar to that employed *eg* by McIntyre and Grill [79] and Capogrosso and colleagues [42]. The advantages of the model described hereafter is that it enables the automatic generation of random distributions of motoneuron somata in the ventral horn of the gray matter together with their dendritic trees and their axons running in the appropriate ventral roots.

Distribution of motoneurons in the spinal cord

In the model, each motoneuron is identified as belonging to the motor nucleus of a given muscle M_i . Let us define:

- N_i^{MN} : the cardinality of the i -th motor nucleus.
- $MN_{i,k}$: the k -th motoneuron of the i -th motor nucleus.

- $N_{i,j}^{\text{MN}}$: the number of motoneurons of the i -th motor nucleus located in spinal segment S_j .
- $\text{MN}_{i,j,k}$: the k -th motoneuron of the subset of the i -th motor nucleus located in spinal segment S_j .
- $\omega_{i,j} := N_{i,j}^{\text{MN}}/N_i^{\text{MN}}$: the proportion of motoneurons of the i -th motor nucleus located in spinal segment S_j .

Motoneuron somata centers

We consider the motoneurons of muscle M_i located in spinal segment S_j , $\text{MN}_{i,j,k}$, $1 \leq k \leq N_{i,j}^{\text{MN}}$. We denote by $C_{i,j,k} := (x_{i,j,k}, y_{i,j,k}, z_{i,j,k})$, $1 \leq k \leq N_{i,j}^{\text{MN}}$, the coordinates of their somata centers. Our aim is to distribute the $C_{i,j,k}$'s uniformly at random in the ventro-lateral quarter of the ventral horn (VQ) of segment S_j (see Section 3.2.5).

z-coordinates We start by sampling uniformly at random a family of weights $(\lambda_{i,j,k})_{k=1 \dots N_{i,j}^{\text{MN}}}$ in the interval $[0, 1]$. The $z_{i,j,k}$'s are readily defined as:

$$z_{i,j,k} = \lambda_{i,j,k} \cdot z_{\text{CS}}(j) + (1 - \lambda_{i,j,k}) \cdot z_{\text{CS}}(j + 1)$$

where $z_{\text{CS}}(j)$ and $z_{\text{CS}}(j + 1)$ are the z -coordinates of the cross-sections delimiting segment S_j , namely CS_j and CS_{j+1} (see Section 3.2.2).

(x, y)-coordinates The coordinates $(x_{i,j,k}, y_{i,j,k})$'s are then obtained in order for the $C_{i,j,k}$'s to be uniformly distributed in the transverse cross-section of the VQ of S_j . The strategy is to generate two points—one denoted $P_{i,j,k}^0$ lying in the convex hull of cross-sectional contour VQ_j , and one denoted $P_{i,j,k}^1$ lying in the convex hull of cross-sectional contour VQ_{j+1} —and to select the point at level $z_{i,j,k}$ on the segment joining these two points.

Let us describe the algorithm to generate $P_{i,j,k}^0 := (x_{i,j,k}^0, y_{i,j,k}^0, z_{\text{CS}}(j))$ in the convex hull of VQ_j . $P_{i,j,k}^0$ is obtained as a weighted sum of the N_p points composing VQ_j , whose x - and y -coordinates we denote $(X_l^0)_{l=1 \dots N_p}$ and $(Y_l^0)_{l=1 \dots N_p}$. The weights are obtained as follows.

First, a collection $(\bar{\omega}_l)_{l=1 \dots N_p}$ is sampled uniformly at random in the unit simplex of \mathbb{R}^{N_p} :

$$\left\{ \begin{array}{l} \bar{\omega}_l \geq 0, \ l = 1 \dots N_p \\ \sum_{l=1}^{N_p} \bar{\omega}_l = 1 \end{array} \right.$$

This is achieved by the following algorithm, taken from [94]:

- Sample N_p values $(\hat{\omega}_l)_{l=1\dots N_p}$ uniformly at random in the interval $[0, 1]$.
- Sort them such that $0 \leq \hat{\omega}_{i_1} \leq \dots \leq \hat{\omega}_{i_l} \leq \dots \leq \hat{\omega}_{i_{N_p}} \leq 1$.
- Introduce an $(N_p + 1)$ -th point $\hat{\omega}_{i_{N_p+1}} = 1$.
- Let $\bar{\omega}_l = \hat{\omega}_{i_{l+1}} - \hat{\omega}_{i_l}$, $l = 1 \dots N_p$.

When the previous weights are directly used to form $(x_{i,j,k}^0, y_{i,j,k}^0)$ from the $(X_l^0, Y_l^0)_{l=1\dots N_p}$, the resulting $P_{i,j,k}^0$ ends up located very close to the center of mass of VQ_j , compromising the randomness of its position. This is due to the fact that weights of equal magnitude often affect points somewhat diametrically opposed on VQ_j . In order for $P_{i,j,k}^0$ to occasionally be eccentric with appreciable likelihood, the previous weights need be modified. One approach is to ensure that only the weights of a small group of consecutive points are appreciably large, so that the weighted sum tend to be positioned near this small group of points. To achieve this, the $(\bar{\omega}_l)_{l=1\dots N_p}$ are exponentiated to the fourth-power and renormalized.

Thus we define:

$$\omega_l = \frac{\bar{\omega}_l^4}{\sum_{l'=1}^{N_p} \bar{\omega}_{l'}^4}$$

and we simply let:

$$\begin{cases} x_{i,j,k}^0 = \sum_{l=1}^{N_p} \omega_l \cdot X_l^0 \\ y_{i,j,k}^0 = \sum_{l=1}^{N_p} \omega_l \cdot Y_l^0 \end{cases}$$

We proceed identically to generate $P_{i,j,k}^1 := (x_{i,j,k}^1, y_{i,j,k}^1, z_{\text{CS}}(j+1))$ in the convex hull of VQ_{j+1} . Finally, the coordinates $(x_{i,j,k}, y_{i,j,k})$ are defined as:

$$\begin{cases} x_{i,j,k} = \lambda_{i,j,k} \cdot x_{i,j,k}^0 + (1 - \lambda_{i,j,k}) \cdot x_{i,j,k}^1 \\ y_{i,j,k} = \lambda_{i,j,k} \cdot y_{i,j,k}^0 + (1 - \lambda_{i,j,k}) \cdot y_{i,j,k}^1 \end{cases}$$

In summary, we have:

$$C_{i,j,k} = \begin{pmatrix} x_{i,j,k} \\ y_{i,j,k} \\ z_{i,j,k} \end{pmatrix} = \lambda_{i,j,k} \cdot \begin{pmatrix} x_{i,j,k}^0 \\ y_{i,j,k}^0 \\ z_{\text{CS}}(j) \end{pmatrix} + (1 - \lambda_{i,j,k}) \cdot \begin{pmatrix} x_{i,j,k}^1 \\ y_{i,j,k}^1 \\ z_{\text{CS}}(j+1) \end{pmatrix}$$

Motor axon trajectories

For the motor axon of $MN_{i,j,k}$, the aim is to define a pathway originating at the soma center $C_{i,j,k}$ and running in the ventral root of segment S_j . Recall from Section 3.2.6 that this ventral root is denoted VR_j , and that it is described by a series of cross-sectional contours denoted $(VR_{j,n})_{n=1\dots N_j}$. The strategy is the following:

1. Define one interpolation point $P_{i,j,k,n}^{\text{int}}$ in each $VR_{j,n}$, $1 \leq n \leq N_j$;
2. Let $P_{i,j,k,0}^{\text{int}} := C_{i,j,k}$;
3. Fit a spline interpolating the collection $(P_{i,j,k,n}^{\text{int}})_{n=0\dots N_j}$;
4. Sample N_{tot} points $(P_{i,j,k,n})_{n=1\dots N_{\text{tot}}}$ along the spline to represent the motor axon pathway.

To generate the interpolation points, a similar approach to that employed to obtain the (x, y) -coordinates of the motoneuron somata centers is used. An additional requirement compared to the motoneuron somata centers is that the $P_{i,j,k,n}^{\text{int}}$'s should be positioned somewhat similarly in their respective $VR_{j,n}$. This is necessary if one wishes to represent the fact that nerve fibers remain similarly positioned relative to each other inside spinal roots. In particular, their pathways should not jump from side to sides within a short extent of longitudinal distance, which could happen if interpolation points in two consecutive $VR_{j,n}$'s were generated without correlation.

To fulfill this requirement, recall from Section 3.2.6 that the $VR_{j,n}$'s were defined with similar topologies. Namely, they possess the same number of points N_p , and points with equal indexes are isomorphic. Such that it is possible to use a single set of weights $(\omega_l)_{l=1\dots N_p}$ to define:

$$P_{i,j,k,n}^{\text{int}} = \sum_{l=1}^{N_p} \omega_l \cdot \begin{pmatrix} X_{j,n,l} \\ Y_{j,n,l} \\ Z_{j,n,l} \end{pmatrix}, \quad \forall n = 1 \dots N_j$$

where $(X_{j,n,l}, Y_{j,n,l}, Z_{j,n,l})_{l=1\dots N_p}$ are the coordinates of the points composing $VR_{j,n}$. Like in the previous section, the weights $(\omega_l)_{l=1\dots N_p}$ are sampled uniformly at random in the unit simplex of \mathbb{R}^{N_p} , followed by exponentiation to the third-power and renormalization.

The algorithm to fit the bicubic spline and sample the points $(P_{i,j,k,n})_{n=1\dots N_{\text{tot}}}$ uniformly along its path is that employed by the *interparc* program [93]. In particular, this algorithm ensures that $P_{i,j,k,1} = P_{i,j,k,0}^{\text{int}} := C_{i,j,k}$ and that $P_{i,j,k,N_{\text{tot}}} = P_{i,j,k,N_j}^{\text{int}}$.

Dendritic tree geometry

As mentioned previously, I propose to describe the geometry of motoneuron dendrites as binary trees of segments. For a given motoneuron, these binary trees of segments are derived from the SWC-file attributed to the motoneuron, as mentioned in Section 2.3.2. More precisely, they are derived from the scaled version of the motoneuron's SWC-file (accounting for the motoneuron diameter), and they are rotated at random around the soma center to introduce further variability of the dendritic tree positioning across motoneurons.

3.3.2 Geometrical model of group-Ia fibers

I sought to develop a geometrical model of group-Ia fibers accounting for their branching morphology and for the spatial distribution of the motor nuclei which they innervate. This model thus relies on the prior definition of the geometry of the innervated motoneurons, and in particular on the position of their somata centers, as described in the previous section.

Morphology of group-Ia fibers

Let us first recall the essential features of the morphology of group-Ia fibers. After running straightforwardly in the dorsal spinal roots, Ia-fibers bifurcate into two branches running in the dorsal columns: one ascending and one descending [11, 12, 14, 95]. Burke and colleagues [11] additionally report that the descending branch usually has a diameter about half that of the ascending branch.

Furthermore, as they ascend or descend, these rostro-caudal branches further bifurcate into collateral branches projecting ventro-laterally towards the gray matter (see Figures 1.18 and 1.19). Brown and Fyffe [12] have noted that collaterals depart from rostro-caudal branches somewhat irregularly: the inter-distance between their points of origin on the rostro-caudal branches ranging from 100 μm to 2600 μm and averaging around 1000 μm .

Moreover, collaterals abundantly ramify to form synaptic contacts with spinal interneurons and motoneurons in the gray matter (Figure 1.19). Finally, in their course towards the ventral horn, collaterals tend to slightly deviate rostrally, such that their ramifications in the intermediate region are 100 μm to 300 μm caudal to those in the ventral horn.

Innervated motoneurons

As mentioned in Section 1.1.3, each Ia-fiber innervates mono-synaptically a certain collection of MNs via its collaterals. Those MNs are either homonymous (when they innervate

the very muscle from which the Ia-fiber originates) or heteronymous (when they innervate synergistic muscles of this muscle). Previous investigations have reported that the proportions of homonymous and heteronymous MNs contacted by a single Ia-fiber are on the order of 90% (p_{homo}) and 65% (p_{hete}) respectively [14].

For a given Ia-fiber originating from muscle M_i , those MNs can be defined as follows:

- Compute the number of homonymous innervated by the Ia-fiber as:

$$N_{\text{homo}} := \text{ROUND} \left(p_{\text{homo}} \cdot N_i^{\text{MN}} \right).$$

- Select at random N_{homo} motoneurons among the $\text{MN}_{i,k}$'s.
- Repeat the above two operations for each heteronymous motor nucleus (which depends on the number of synergistic muscles possessed by M_i) and using p_{hete} instead of p_{homo} .

Taken together, the homonymous and heteronymous MNs innervated by a given Ia-fiber denoted Iaf are denoted MN_k^{Iaf} , $1 \leq k \leq N_{\text{MN}}^{\text{Iaf}}$. Considering the rostral-most and caudal-most of them, we can find out which segments of the spinal cord they are spanning. There is some j_0 and some n such that these segments are the segments S^{j_0} to S^{j_0+n} . This information is important to derive the trajectory of the Ia-fiber, as described below.

Distribution of group-Ia fibers in the spinal roots

Let us introduce:

- N_i^{Iaf} : the total number of Ia-fibers of muscle M_i .
- $\text{Iaf}_{i,k}$: the k -th Ia-fiber of muscle M_i .
- $N_{i,j}^{\text{Iaf}}$: the total number of Ia-fibers of muscle M_i running in dorsal root DR_j .
- $\text{Iaf}_{i,j,k}$: the k -th Ia-fiber of the subset of Ia-fibers of muscle M_i running in DR_j .

Contrary to motor nuclei, whose distributions in the spinal segments are fairly well characterized in monkeys and humans [96,97], little is known about the distributions of group-Ia fibers innervating individual muscles in the spinal roots. Nonetheless, since group-Ia fibers innervate predominantly homonymous motoneurons, it seems logical that they enter the spinal cord at the segmental level where these motoneurons are located. Thus, the group-Ia fibers innervating a given muscle are likely to be clustered together in the few posterior roots whose corresponding segments contain the muscle's motor nucleus.

Formally, the model assumes that the number of Ia-fibers of muscle M_i running in dorsal root DR_j can be estimated as:

$$N_{i,j}^{\text{Iaf}} = \omega_{i,j} \cdot N_i^{\text{Iaf}}$$

where $\omega_{i,j}$ is the proportion of MNs innervating muscle M_i located in spinal segment S_j , as defined in Section 3.3.1.

Geometrical model

The proposed geometry for Ia-fibers constitutes a simplified summary of the features reported in the previous sections. It comprises:

- a dorsal root branch;
- an ascending branch in the dorsal columns;
- a descending branch in the dorsal columns;
- a series of collaterals originating from the ascending and descending branches.

Each of these branches is made of a series of points defining a pathway. In the following paragraphs, I describe these pathways and how to obtain them. I consider a Ia-fiber originating from muscle M_i and running in dorsal root DR_j .

Branch diameters The diameter D of the Ia-fiber is a parameter of the model. Once set, the diameter of the dorsal root branch is readily given by D . The diameters of the ascending and descending branches are respectively set to $2/\sqrt{5} \cdot D$ and $1/\sqrt{5} \cdot D$, which ensures that the ascending branch has a diameter twice as large as the descending branch, and that the total cross-sectional area is preserved upon bifurcation. The diameters of the collaterals are also parameters of the models (they should be drawn from a statistical distribution, see Section 4.2.4).

Dorsal root branch The dorsal root branch of the Ia-fiber is defined similarly to the motor axon of a motoneuron lying in segment S_j (see Section 3.3.1), with the two following noteworthy differences:

1. There is no soma center to serve as initial interpolation point.
2. The cross-sectional contours used to define the interpolation points are those of DR_j , not VR_j (see Section 3.2.6).

In the following paragraphs, the points composing the dorsal root branch of the Ia-fiber are denoted P_n^{DR} , $1 \leq n \leq N_{\text{DR}}$.

Ascending branch Similarly to the dorsal root branch, the ascending branch is represented by a series of points denoted P_n^A , $1 \leq n \leq N_A$. Again, those are defined by sampling a spline fitting a series of interpolation points P_m^{int} , $1 \leq m \leq N_{\text{int}}$.

The first of these points is readily given by the first point of the dorsal root branch: P_1^{DR} . Recall from the algorithm presented in Section 3.3.1 that P_1^{DR} is lying in the first cross-sectional contour $\text{DR}_{j,1}$ of DR_j , and that this cross-sectional contour is the one “penetrating” the spinal cord in the direction of the dorsal horn (see Figure 3.23). As a matter of fact, this point will also serve as the first point defining the descending branch: it is in fact the bifurcation point of the Ia-fiber.

The strategy for defining the subsequent interpolation points is motivated by the considerations already evoked in Section 3.2.5. Namely, that the ascending branches of fibers running in specific dorsal roots are clustered in specific dorsal column compartments, which were defined in Section 3.2.5. For a fiber running in DR_j , this dorsal column compartment is DCC_j , and it is described by a series of cross-sectional contours labeled DCC_j^j to DCC_j^1 .

If the ascending branch of a fiber was to run up until the rostral-most cross-section of the model (CS_1), we would generate an interpolation in each of DCC_j^j to DCC_j^1 . But how rostral should the ascending branch of a Ia-fiber be running? In all the publications cited in Section 3.3.2, the authors have reported that the staining techniques employed to trace and reconstruct the Ia-fiber trajectories did not ensure that the entirety of the Ia-fiber was well-stained. In particular, the staining was more and more faint as the distance from the injection site increased. Therefore, the authors could not exclude that the disappearance of the stained Ia-fibers from rostral and caudal cross-sections was due to a lack of staining rather than to the actual ending of the rostro-caudal branches of the Ia-fibers.

Given the absence of indication regarding the real extent of the rostro-caudal branches of Ia-fibers, I retained the following option: the ascending branch of any Ia-fiber should run only until it reaches the rostral cross-section of the rostral-most segment where it innervates MNs, which we labeled S_{j_0} in Section 3.3.2. Therefore, we shall generate an interpolation point in each of DCC_j^j to $\text{DCC}_j^{j_0}$. To do so, we form weighted sums of points as described in Section 3.3.1.

Descending branch The strategy to define the descending branch is very similar to that employed for the ascending branch, with minor differences. First, a symmetrical issue to that encountered with the ascending branch had to be addressed: how caudal should the descending branch of a Ia-fiber be running? The same considerations as mentioned above led me to retain a symmetrical option: it should run only until it reaches the caudal cross-section of the caudal-most segment where the Ia-fiber innervates MNs, which we labeled S_{j_0+n} in Section 3.3.2.

Second, while it was relatively straightforward to define the dorsal column compartments into which the ascending branch had to run (see Section 3.2.5), this was not the case for the descending branch. Nonetheless, the observation that the rostro-caudal branches of Ia-fibers tend to stay in the dorso-lateral region of the dorsal columns—as shown for instance in Figure 1.19 but also in other pictures from [12]—led me to retain the following option: the descending branch should run in the dorso-lateral-most compartment of the dorsal columns in each segment S_j to S_{j_0+n} .

Thus, in addition to using P_1^{DR} as first interpolation point as mentioned in the previous paragraph, interpolation points should be generated in each of DCC_{j+1}^{j+1} to $\text{DCC}_{j_0+n+1}^{j_0+n+1}$. The points of the descending branch are denoted P_n^{D} , $1 \leq n \leq N_{\text{D}}$.

Collaterals Three steps are necessary to define the collaterals of the Ia-fiber: determining their number, determining the families of motoneurons innervated by each of them, and determining their trajectories.

Number Their number, denoted N_{col} , is obtained as:

$$N_{\text{col}} = \text{ROUND}(0.75 \cdot L) + \epsilon$$

where:

- L is the rostro-caudal extent of the fiber expressed in mm. Specifically, it is the difference $z_{\text{CS}}(j_0) - z_{\text{CS}}(j_0 + n + 1)$.
- $\epsilon = \eta \cdot (2b - 1)$.
- η is a Poisson distribution with parameter $\lambda = 0.7$.
- b is a Bernoulli distribution with parameter $p = 1/2$.

The previous definition is based on the following:

1. I estimated the best fit for the relation $N_{\text{col}} = a \cdot L$ from the data reported by [12] using the least squares method, which yielded a parameter $a = 0.75$.
2. Since the number of collaterals can only be an integer, I opted for a contribution of this linear fit to N_{col} in the form of $\text{ROUND}(0.75 \cdot L)$.
3. Since the data reported by [12] presented deviations in both the positive and negative directions from this rounded linear fit, I added a deviation decomposed into its amplitude—represented by the parameter η taking integer values—and its sign—represented by the factor $(2b - 1)$, taking values 1 and -1 with equal probabilities.

In so doing, the mean number of collaterals of fibers with rostro-caudal extent equal to L is $\text{ROUND}(0.75 \cdot L)$ —since $\mathbb{E}(\epsilon) = \mathbb{E}(\eta)\mathbb{E}(2b-1) = 0.7 \times 0 = 0$ —and the standard deviation is the standard deviation of η , which was so defined to fit the deviation amplitudes distribution at best (maximum likelihood estimator).

Innervated motoneuron families The next step is to determine which MNs are innervated by each of the N_{col} collaterals of the fiber. We do so by splitting the MN_k^{Iaf} 's into N_{col} families as follows:

1. We sort the MNs by decreasing order of their z -coordinates, keeping on denoting MN_k^{Iaf} , $1 \leq k \leq N_{\text{MN}}^{\text{Iaf}}$, the sorted list of MNs.
2. We split the MNs into N_{col} families of similar sizes but subject to variability (with a variation coefficient arbitrarily fixed *eg* at $\text{cv} = 0.1$). This is done by first determining the cardinality of each family, and by then selecting the MNs in order from the list.

Notice that the second point above implies that the families of MNs innervated by different collaterals don't overlap. While it is likely that such two families are largely segregated, it is also very likely that some MNs are innervated by two (or more) collaterals.

Let us denote $N_{\text{MN},j}$, $1 \leq j \leq N_{\text{col}}$, the cardinalities of the families. The mean number of MNs in each family is:

$$\mu = \frac{N_{\text{MN}}^{\text{Iaf}}}{N_{\text{col}}} = \frac{1}{N_{\text{col}}} \sum_{j=1}^{N_{\text{col},\text{Iaf}}} N_{\text{MN},j}$$

The standard deviation writes:

$$\sigma = \frac{1}{N_{\text{col}}} \sum_{j=1}^{N_{\text{col}}} (N_{\text{MN},j} - \mu)^2$$

To obtain a variation coefficient σ/μ of 0.1, we proceed as follows:

- Sample $(\epsilon_j)_{j=1 \dots N_{\text{col}}}$ in the unit simplex of dimension N_{col} .
- Let $\tilde{\epsilon}_j = \epsilon_j - 1/N_{\text{col}}$ for $j = 1 \dots N_{\text{col}}$ such that we have $\sum_j \tilde{\epsilon}_j = 0$.
- Let $N_{\text{MN},j} = \mu + \lambda \tilde{\epsilon}_j$, such that $\sum_j N_{\text{MN},j} = N_{\text{MN}}^{\text{Iaf}}$.
- Let $\lambda = \left(N_{\text{MN}}^{\text{Iaf}} \cdot 0.1 / \sum_j \epsilon_j^2 \right)^{1/2}$, such that $\text{cv} = 0.1$.

Finally, since the $N_{\text{MN},j}$'s need be integers, we let $N_{\text{MN},j} = \text{ROUND}(\mu + \lambda \tilde{\epsilon}_j)$ for $j = 1 \dots N_{\text{col}} - 1$ and we let the last one $N_{\text{MN},N_{\text{col}}} = N_{\text{MN}}^{\text{Iaf}} - \sum_{j=1}^{N_{\text{col}}-1} N_{\text{MN},j}$ so that the numbers of MNs in each group sum up to $N_{\text{MN}}^{\text{Iaf}}$.

Trajectories Once the groups of MNs are formed, we derive the trajectories of the collaterals as follows. Let us consider collateral number h which innervates the MNs of group number h . Like the dorsal root, ascending and descending branches, collateral h is comprised of a series of points P_h^n , $1 \leq n \leq N_h$, which are derived by interpolation from another series P_m , $1 \leq m \leq N_{\text{int}}$. We use only 3 interpolation points.

P_1 , is defined as the center of mass of the somata centers of the MNs of group h . P_2 shall sit in the middle area of the central region of the gray matter (MR). Moreover, it shall be at a z -level smaller than the z -level of P_3 by an amount Δz between 100 μm and 300 μm , so as to take into account the observation of [12] about the rostral deviation of the collaterals. This is done by sampling uniformly at random Δz in the interval [100 μm , 300 μm] and letting $z_{P_2} = z_{P_3} - \Delta z$. The (x, y) -coordinates are obtained similarly as the (x, y) -coordinates of the MNs somata centers in the VQ, described in Section 3.3.1. P_3 is defined as the closest node of Ranvier of the rostro-caudal bifurcations with z -level just smaller than that of P_2 . This requires that the positions of the nodes of Ranvier be known, which is straightforward since the fiber compartments are distributed linearly along the branches, and their lengths are known as soon as the branch diameters are known.

Finally, a cubic spline is fitted to P_1 , P_2 and P_3 and the P_h^n 's are sampled uniformly along this spline.

3.3.3 Other nerve fibers

Based on the model of group-Ia fibers described above, I developed models for other spinal nerve fibers. First the very same model allows to represent any other $A\alpha$ or $A\beta$ dorsal root fibers, such as group-Ib fibers, muscle spindle group-II fibers or low-threshold mechanoreceptor fibers, although the definition of the collaterals based on the connectivity with motoneurons is not relevant for these other fibers.

Dorsal column fibers

The model of dorsal column fibers comprises a single dorsal column branch and a series of collaterals. The dorsal column branches can be made to run in specific OD compartments, or unspecifically in the whole DC compartment (see Section 3.2.5). The interpolation points defining their pathways are obtained as random weighted sums of the appropriate cross-sectional contours, as described in Section 3.3.1.

Dorsal column fibers are not associated with specific MNs. To define their collaterals, the steps are carried out in the inverted order. First the nodes of Ranvier of the dorsal column branch where the collaterals are attached are chosen at random. Then random points in the MR and in the VQ are generated slightly rostrally to these nodes of Ranvier for subsequent interpolation.

Spinocerebellar tract fibers

The model of spinocerebellar tract fibers is very similar to the model of dorsal column fibers. Instead of a dorsal column, it comprises a spinocerebellar tract branch. Furthermore, the formula to define the number of their collaterals is $N_{\text{col}} = \text{ROUND}(0.2 \cdot L) \pm \eta'$, with η' obeying a Poisson distribution with parameter 0.5 instead of 0.7. These adaptations imply a lower number of collaterals for ST-fibers than for DC-fibers. Also, instead of sitting in the MR, the second interpolation point P_2 of their collaterals is more lateral, obtained as a weighted sum between an MR point and a point on the segment joining P_1 and P_3 .

Corticospinal tract fibers

Finally, the model of corticospinal tract fibers is similar to the model of spinocerebellar tract fibers. However, CT-fibers are associated with motoneurons, and their collaterals are thus defined as for group-Ia fibers, with the difference that they deviate caudally instead of rostrally from the corticospinal branch to the ventral horn [98].

These nerve fiber geometrical models and the spinal cord geometrical model of Section 3.3 are implemented in a software suite, written in the Matlab programming language (Matlab, The Mathworks, Inc.), available at https://bitbucket.org/ngreiner/fem_smc_ees/src/master/.

3.4 Influence of anatomical elements in hybrid models

In this section, I examine the influence of some of the features that I have developed and described in the previous sections of this chapter. The analysis is led with a hybrid model of EES of the macaque monkey cervical spinal cord which I have developed in the context of a broader study, presented in detail in Chapter 4. The first subsection hereafter summarizes the specifications of this model. In the second subsection, I examine the influence of the presence of fully-fledged compartments representing the spinal roots and the silicone paddle of an epidural implant in the volume conductor model. In the third subsection, I examine the influence of the representation of the branching structure of dorsal root fibers for the assessment of the recruitment selectivity of different dorsal roots.

3.4.1 Hybrid model specifications

As mentioned, this subsection summarizes the main specifications of the hybrid model used to lead the sensitivity analysis. The reader can refer to Section 4.2.4 for a more detailed description and for a description of the construction process of this model.

The model is illustrated in Figure 3.33. The volume conductor comprised compartments for the gray matter, the white matter with the spinal roots, the cerebro-spinal fluid, the dura mater, the epidural fat, the vertebrae, the silicone paddle of a paddle electrode array, the active sites of the array, and a large cylinder wrapping all the previous compartments (not represented in Figure 3.33).

Each compartment was assigned with a scalar isotropic electrical conductivity, except for the white matter and the spinal roots (constituting a single computational domain Ω_i), which possessed an anisotropic conductivity tensor, with a higher value along the longitudinal than along the transversal directions. To orient this anisotropic conductivity tensor, curvilinear coordinates were generated within their volume.

The finite element mesh comprised approximately ten million tetrahedral elements, with smaller and more numerous elements near the stimulating electrodes, in the spinal roots and the spinal cord, and in the dorsal space between the spinal cord and the electrodes.

To represent the delivery of monopolar stimulation through any given electrode (geometrically represented by parallelepipeds), the boundary conditions were as follows:

- a Neumann boundary condition with $j_0 = 1 \text{ A m}^{-2}$ was assigned on the electrode surface which was facing the spinal cord;
- the outer surface of the volume conductor's wrapping cylinder was assigned with an insulating boundary condition (*ie* a zero current-flux condition);

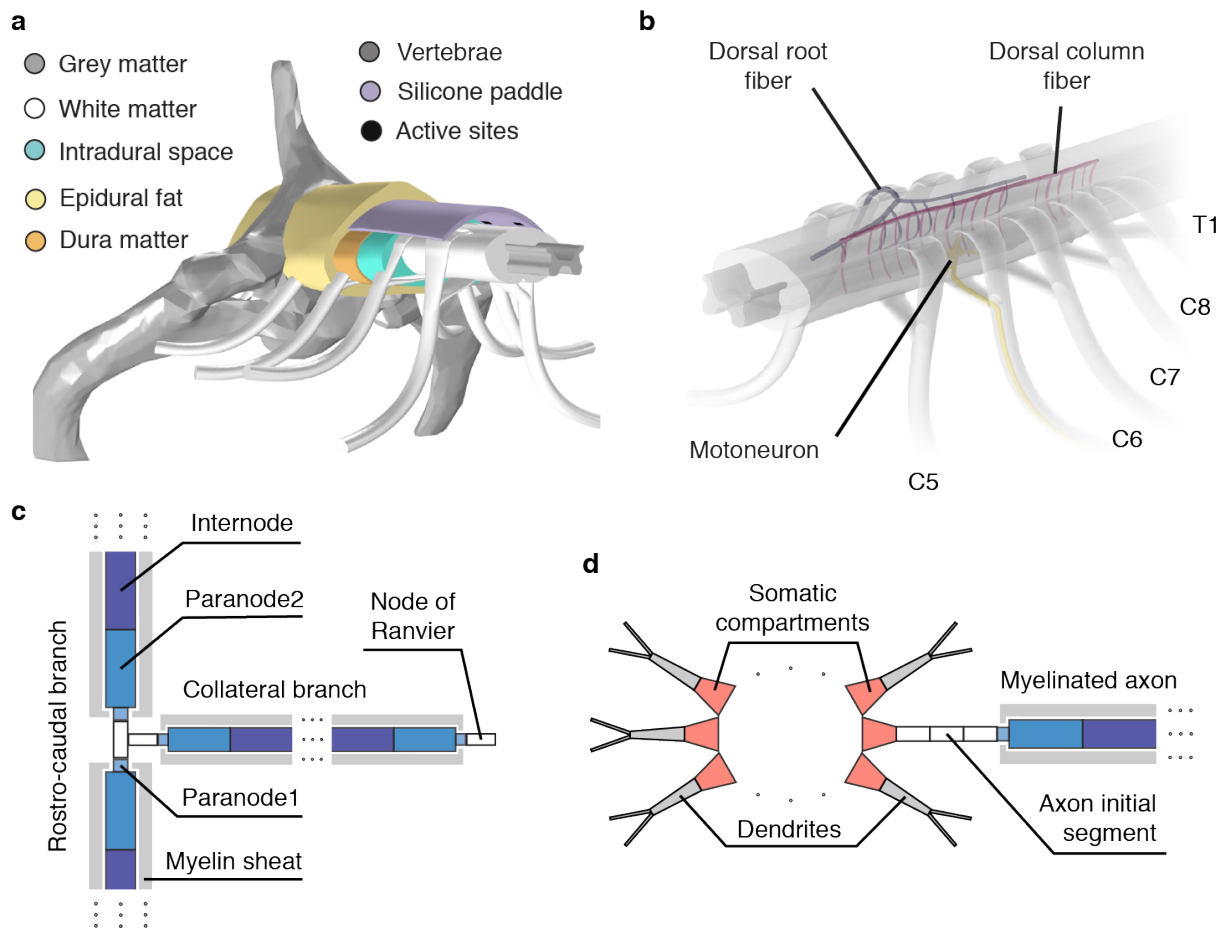


Figure 3.33 Hybrid model used for the sensitivity analysis. **a** Volume conductor model. **b** Representative trajectories of dorsal root fibers, dorsal column fibers, and motoneurons with their dendritic trees and motor axons. **c** Compartmentalization of dorsal root and dorsal column fibers for neurophysical simulations. **d** Compartmentalization of motoneurons and motor axons for neurophysical simulations. For details, see Section 4.2.4.

- a ground point ($V = 0$ V) was placed in the ventral region of the wrapping cylinder, far from the spinal cord.

Continuity of the normal current density was enforced at the interfaces between the different media. The resulting potential distribution was then divided by the area of the active surface of the electrode, and then divided by 1×10^3 . By considering that it was expressed in millivolts instead of volts, it thus corresponded to a total injected current of 1 μ A.

The morphologies of dorsal root and dorsal column fibers and of motoneurons and motor axons were based on the models described in Section 3.3. The dorsal root branches of dorsal root fibers had diameters of $14 \mu\text{m} \pm 3 \mu\text{m}$ (mean \pm standard deviation, log-normally distributed). The diameters of the ascending and descending branches were obtained by multiplication of the dorsal root branch diameters respectively by $\sqrt{4/5}$ and $\sqrt{1/5}$. The dorsal column branches of dorsal column fibers had diameters of $9 \mu\text{m} \pm 2 \mu\text{m}$. The collaterals had diameters of $2.5 \mu\text{m} \pm 1 \mu\text{m}$. Motor axons had diameters uniformly distributed in the range from 10 μm to 18 μm . The neurophysical models of dorsal root and dorsal column fibers and of motoneurons and motor axons were based on refs. [77, 79], described in Section 2.3. More details are provided in Section 4.2.4.

3.4.2 Influence of spinal roots and electrode array paddle

To phrase it one more time, the representation of the spinal roots in the volume conductor model is likely to have a significant influence on model predictions, especially on the estimated excitation threshold of dorsal root fibers, but also on the estimated recruitment selectivity of dorsal root or dorsal column fibers.

Similarly, the insulation provided by the electrode paddle is likely to diminish the estimated excitation threshold of dorsal root and dorsal column fibers, and potentially also affect the recruitment order of different fiber populations.

To verify these hypotheses, I compared the predictions of three different volume conductor models:

- a *reference* model, comprising compartments for the spinal roots and the electrode paddle (depicted in Figure 3.33);
- the same model but without the compartments representing the roots (referred to as *without roots*);
- the reference model without the compartment representing the paddle (referred to as *without paddle*).

Note: Due to the representation of the different compartments in the finite element modelling software, a specific finite element mesh had to be generated for each of the three models. For this reason, and because the curvilinear coordinates depended on the finite element mesh, specific curvilinear coordinates for the white matter and the spinal roots also had to be generated for each model (for the model without roots, the curvilinear coordinates were evidently generated exclusively in the white matter). Finally, in the model without paddle, the surfaces of the stimulating electrode which were not used as boundary current source (all but the one facing the spinal cord) were made insulating.

Electric potential distribution

As a first step, I compared the electric potential profiles induced by each model along the trajectories of dorsal root fibers, dorsal column fibers, and motor axons. I used two electrode positions: one lateral, with the electrode facing a dorsal root; and one medial, with the electrode on the midline of the spinal cord, facing the dorsal columns, as depicted in Figure 3.34.

The dorsal root fibers and the motor axons were running in the dorsal and ventral roots of the spinal segment at the rostro-caudal level of the stimulating electrode. The dorsal column fibers were running in the OD₂ compartment, as defined in Section 3.2.5 and illustrated in Figure 3.33.

In particular, I have examined two characteristics of the potential profiles: the peak potential; and the potential's second-order finite differences along the fibers, which I hereafter abbreviate Δ^2V . The negative peaks of Δ^2V , which become positive for cathodic stimulation (*ie* for negative stimulation currents), determine the peaks of the activating function along the fibers. To ease the reading, I will refer to the peaks of $-\Delta^2V$ instead of the negative peaks of Δ^2V . Higher peak potentials are likely to cause higher peaks of $-\Delta^2V$, but this is not necessary the case.

Dorsal root fibers On Figures 3.35 and 3.36, I have plotted the profile of the electric potential along a dorsal root fiber for the three models and for the lateral and medial electrodes respectively.

Peak potential: On Figure 3.35, it can be appreciated that the peak of the potential profile induced by the lateral electrode (which occurs at the point of the dorsal root branch closest to the electrode), is significantly influenced by the presence of the root compartments or the paddle. Specifically, the peak without the roots was 12% lower than the reference peak, and the peak without the paddle, 21.5% lower.

It was somewhat surprising for the peak potential without the roots to be lower than the

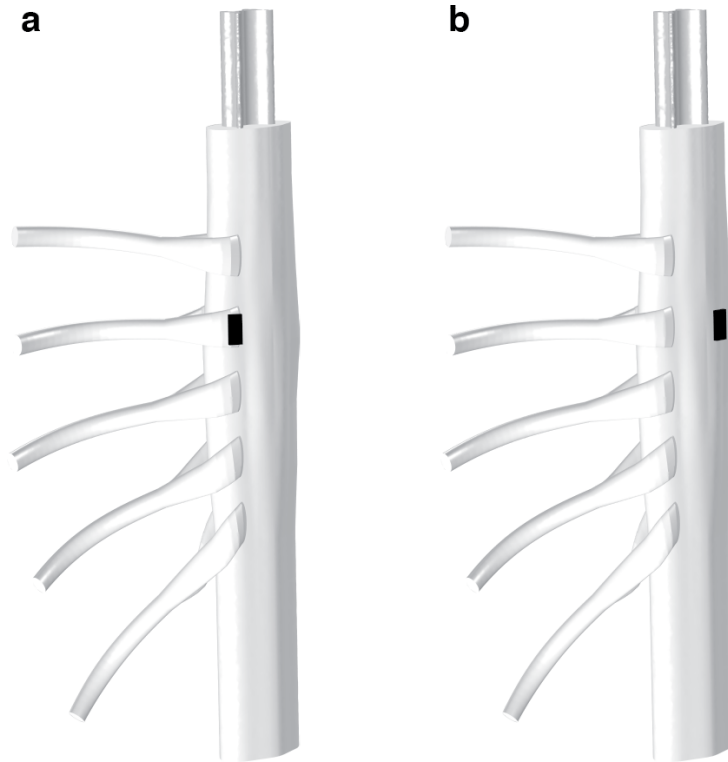


Figure 3.34 Lateral and medial electrode positions. The electrodes are magnified for better visualization (scale factor = 2). **a.** Lateral. **b.** Medial.

reference peak. One could indeed expect that the higher resistivity of the roots (compared to the CSF) would cause higher voltage drops in the volumes which they occupy, which should lower the peak potential along the fiber. A likely reason for the observed ranking could have been that the total impedance between the stimulating electrode and the return electrode (measured as the average potential of the stimulating electrode divided by the injected current of $1\text{ }\mu\text{A}$) were increased when the roots were included (the roots indeed occupy the space normally occupied by the lowly resistive CSF). In this case, despite a higher voltage drop occurring in the roots, the “starting” potential—*ie* the potential of the stimulating electrode—would also have been higher, and the cumulative effect could have been an increased peak potential along the fiber. But comparing the voltages of the electrode for both models showed a decrease of only 2% when the roots were not included, contrasting the 12% decrease of peak potential.

I thus extended the analysis to a population of 50 dorsal root fibers. As it turned out, the profiles shown in Figure 3.35 did not constitute an isolated case, but there were also cases where the profiles with or without roots were very close, and even some where the order was reversed. Overall, the average peak potential was 6% lower when the roots were not included, with a standard deviation of 9%. A possible reason for this variance across fibers might come from the finite element mesh, which was likely coarser in the model without roots (precisely because the roots didn’t have to be meshed), implying poorly

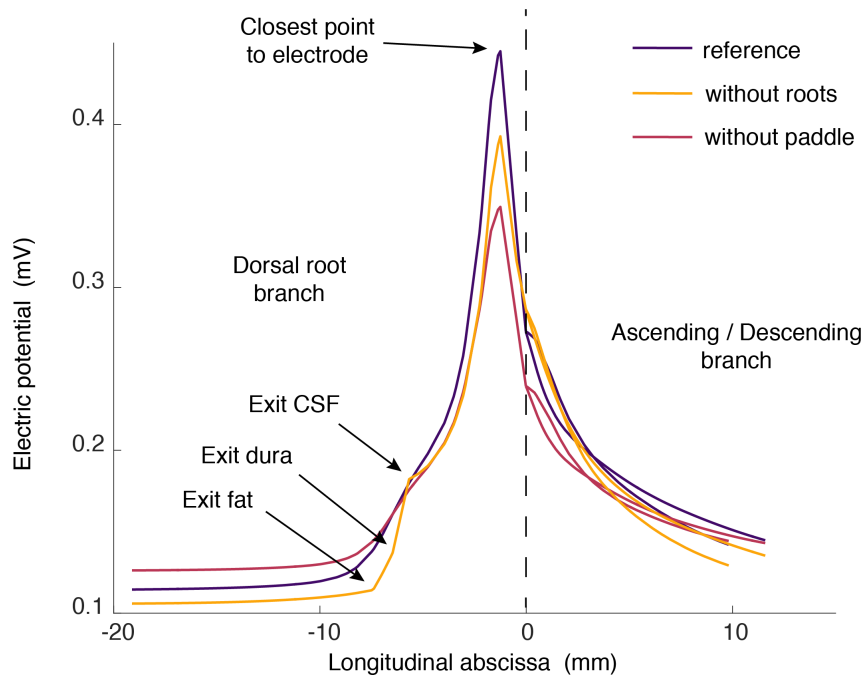


Figure 3.35 Electric potential profile along a dorsal root fiber for a unitary stimulation current of $1\text{ }\mu\text{A}$ delivered from an electrode facing the root. *Horizontal axis*: longitudinal abscissa along the dorsal root fiber, starting from the tip of the dorsal root branch (on the left) until the tips of the dorsal column bifurcations (on the right). The dashed line at $x = 0\text{ mm}$ indicates the bifurcation point of the fiber. *Reference*: volume conductor model including compartments for the spinal roots and for the electrode paddle. *Without roots*: same as reference but without the spinal roots. *Without paddle*: same as reference but without the electrode paddle.

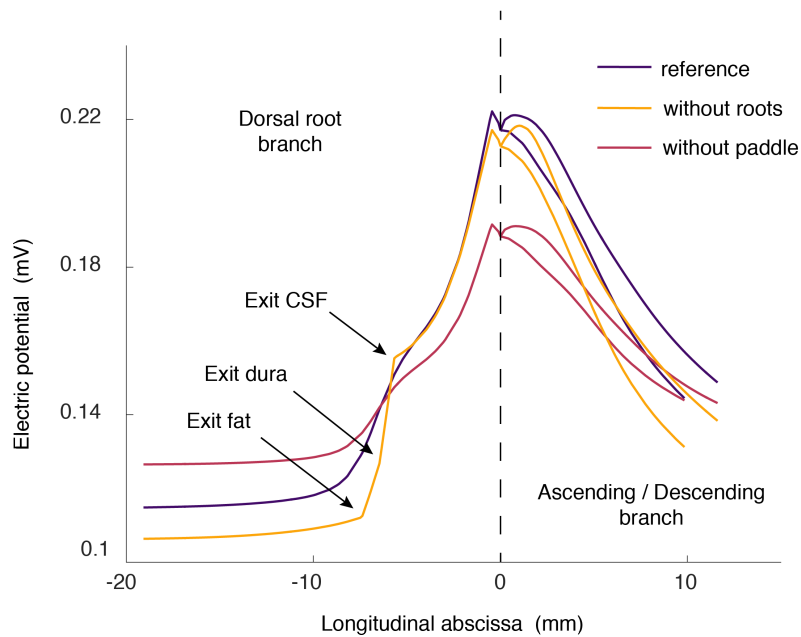


Figure 3.36 Same as Figure 3.35 but for a medially-positioned electrode (facing the dorsal columns).

accurate compensatory jumps of the electric potential from mesh node to mesh node in this model.

On the other hand, when delivering the stimulation from a medial electrode facing the dorsal columns, the discrepancy between the peak without roots and the reference peak virtually vanished. This is illustrated by Figure 3.36, which represents the potential profile along the same dorsal root fiber as in Figure 3.35. At the population level, the average peak reduction when the roots were not included was 1.5% with a standard deviation of 2%. This is coherent with the intuition that, as the distance between the stimulating electrode and the roots increases, the actual representation of the roots tends to be of lesser importance.

Conversely to the above, the peak potential obtained with the model without paddle was consistently and significantly lower than the reference peak, as illustrated by Figures 3.35 and 3.36. At the population level, for the lateral electrode, the peak potential was reduced by 18% (standard deviation 3%); for the medial electrode, the reduction was 13% (standard deviation 1%).

The first (and likely predominant) reason for this reduction is that in the model without paddle, the total impedance between the lateral stimulating electrode and the return electrode was reduced by 47%, and the total impedance between the medial stimulating electrode and the return electrode by 54%. The second reason, which is in fact related to the first, is that when it is included, the electrode paddle forces the injected current forward into the roots or the dorsal columns. When it is not included, the injected current has many more less resistive pathways to circumvent the roots and the spinal cord to reach the ground electrode, such that the electric potential does not build-up in the roots and the dorsal columns. Besides, this partly explains why the reduction was of lesser extent for the medial electrode: the second part of the explanation is that the layer of CSF separating the medial electrode from the dorsal columns was thicker than the CSF layer separating the lateral electrode from the root, the latter leaving even less room for the current to avoid the root.

Peak of $-\Delta^2V$: I then examined the influence of the different models on Δ^2V . First of all, the peaks of $-\Delta^2V$ were largest along the dorsal root branches of all fibers, for all models, and for both lateral and medial electrodes. In essence, this suggests that the excitation of dorsal root fibers is likelier to happen in the dorsal root branch, even when the electrode is facing the dorsal columns. This is examined more carefully in a later section, but for the purposes discussed here, the implications are that I restricted the analysis of Δ^2V to the dorsal root branches.

As was the case for the peak potential, the influence of the roots strongly varied across fibers. For both lateral and medial stimulations, when the roots were not included, the

peak of $-\Delta^2V$ increased for some fibers, and decreased for the others. For lateral stimulation, the maximal increase reached 270% (*ie* the peak of $-\Delta^2V$ was approximately 4 times higher without than with the roots) and the maximal decrease reached 43% (*ie* the peak was approximately divided by 2 without the roots). On average, the peak of $-\Delta^2V$ increased by 11%, with standard deviation 47%. For medial stimulation, the maximal increase reached 325%, the maximal decrease reached 50%, and the mean increase was 73% (standard deviation: 96%).

Interestingly, the maximal increase, which occurred in the same fiber F_0 for both lateral and medial stimulations, was due to a very high peak of $-\Delta^2V$ at the interface between the CSF and the dura (*ie* as the fiber exited the dural sac) which was paralleled by very low peaks of $-\Delta^2V$ near the electrode (see Figure 3.37). The peak at the CSF-dura interface was most likely due to the discontinuity of the electrical conductivity in the model without roots, which was absent in the model with roots because the root itself occupied the volume of space in which the fiber was running until after it exited the vertebral column, ensuring electrical conductivity continuity. However, the magnitude of this peak was lower than the peaks that occurred near the electrode for other fibers. For instance, the peak of $-\Delta^2V$ along the fiber whose potential profile is depicted in Figure 3.35 was approximately twice higher than the large peak along F_0 , as shown in Figure 3.38.

Regarding the model without paddle, the findings were similar to those obtained for the peak potential. For both the lateral and medial electrodes, the peak of $-\Delta^2V$ was consistently and significantly decreased when the paddle was not included. For the lateral electrode, the mean decrease was of 37% (standard deviation 5%); for the medial electrode, the mean decrease was of 36% (standard deviation 2%).

Dorsal column fibers The situation for the dorsal column fibers is illustrated by Figures 3.39 and 3.40, which represent the electric potential profiles along the same dorsal column fiber (selected at random among a collection of 50 such fibers) for lateral and medial stimulation respectively. The graphs for the 49 other fibers were similar to those of Figures 3.39 and 3.40.

In the model without roots, for lateral stimulation, the peak potential was decreased by an average 3% (standard deviation 0.5%). For medial stimulation, the mean decrease was 2% (standard deviation $\sim 0\%$). The latter is probably a mere reflection of the impedance decrease of 2% when the roots are not included, already noted when analyzing the dorsal root fibers. The slightly more pronounced effect seen for lateral stimulation is likely attributable to the intercalation of the roots between the lateral electrode and the dorsal columns. Overall, somewhat expectedly, the roots are shown to have little influence on the peak potential along dorsal column fibers.

In the model without paddle, as was the case for the dorsal root fibers, the peak potential

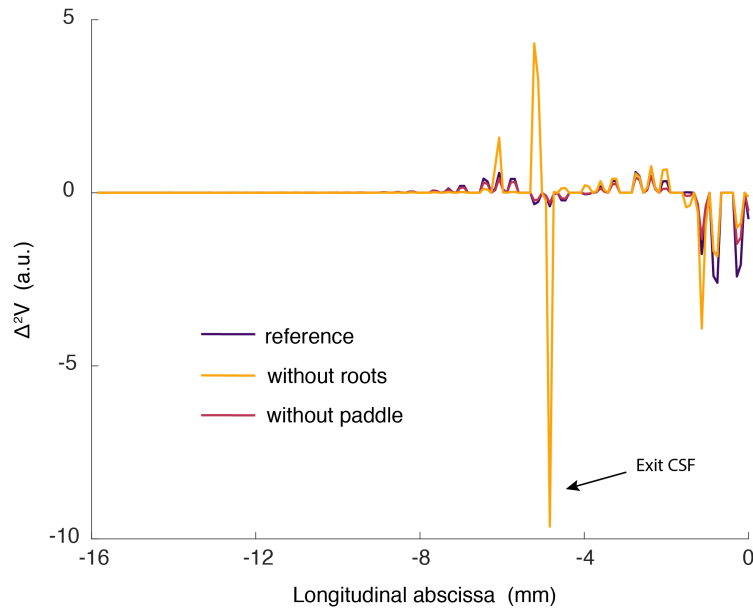


Figure 3.37 Profile of the second-order finite differences of the electric potential along the dorsal root branch of F_0 (see text) for a unitary stimulation current of $1\ \mu\text{A}$ delivered from the lateral electrode. The longitudinal abscissa starts at the tip of the dorsal root branch (on the left) and ends at the bifurcation point in the spinal cord (at abscissa 0 mm).

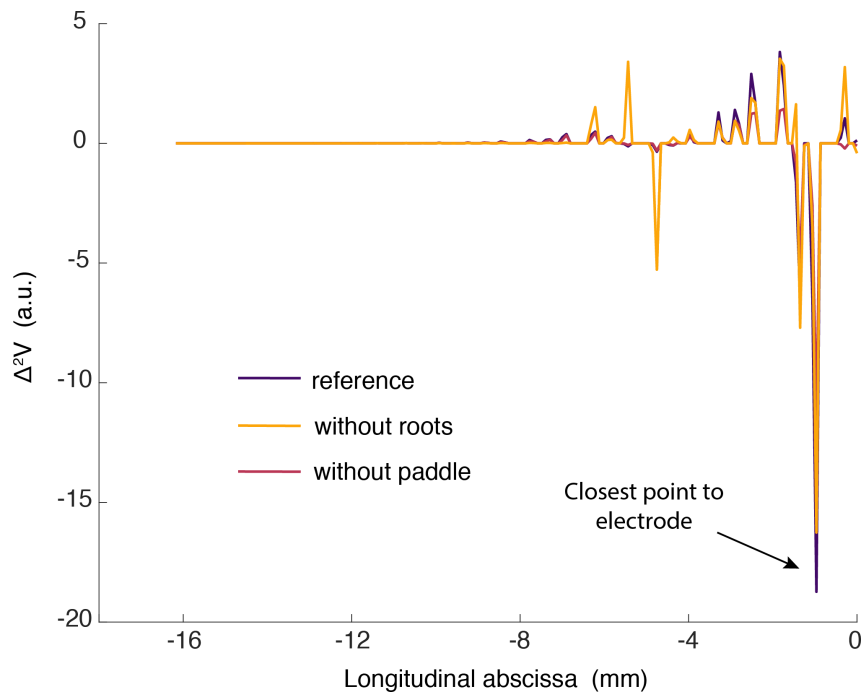


Figure 3.38 Same as in Figure 3.37 but for the fiber of Figure 3.35. The vertical axis scale is the same as in Figure 3.37.

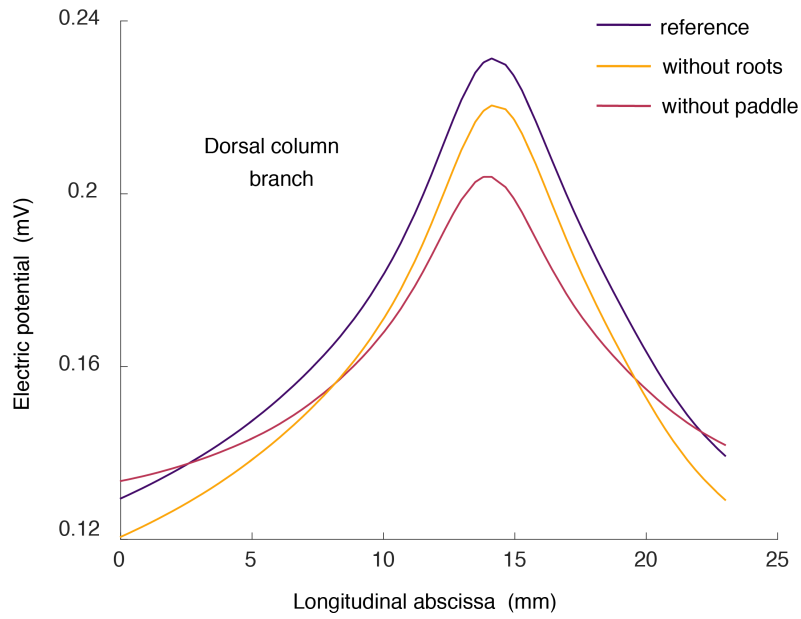


Figure 3.39 Electric potential profile along a dorsal column fiber for a unitary stimulation current of $1\text{ }\mu\text{A}$ delivered from a laterally-positioned electrode (as in Figure 3.35).

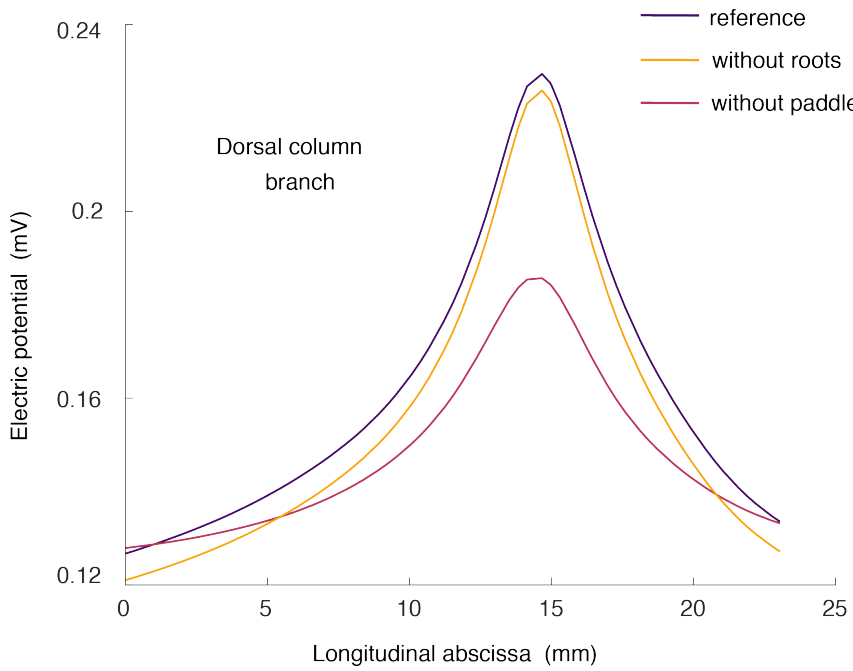


Figure 3.40 Same as Figure 3.39 but for a medially-positioned electrode (as in Figure 3.36).

along dorsal column fibers was significantly decreased. The average decrease was 10% for lateral stimulation (standard deviation $\sim 0\%$) and 20% for medial stimulation (standard deviation $\sim 0\%$). The same arguments to explain these peak reductions as those put forward in the case of the dorsal root fibers also prevail here.

The peak of $-\Delta^2V$ along dorsal column fibers was also significantly and somewhat uniformly reduced when the paddle was absent. The average decrease was 18% for lateral stimulation (standard deviation 3%) and 40% for medial stimulation (standard deviation 3%).

Surprisingly however, the absence of the roots increased the peak of $-\Delta^2V$ for almost all fibers for both lateral and medial stimulations. The average increase was 20% for lateral stimulation (standard deviation 10%) and 16% for medial stimulation (standard deviation 12%). This suggests that the presence of the roots does disrupt the electric potential in the dorsal columns in a non-trivial way.

Motor axons The situation for the motor axons is illustrated by Figures 3.41 to 3.43, which represent the electric potential profiles and the profile of Δ^2V along the same motor axon (selected at random among a collection of 50 such axons) for lateral and medial stimulations. As was the case of dorsal column fibers, the influence of the roots and paddle was quite similar across motor axons.

The peak potential was lowly affected by the removal of the roots: it was increased by an average $2\% \pm 1\%$ for lateral stimulation, and decreased by an average $3.5\% \pm 0\%$ for medial stimulation. Interestingly, the removal of the paddle also had a small influence, contrasting the situation of dorsal root and dorsal column fibers. In absence of paddle, the peak potential was decreased by an average $2.5\% \pm 0.5\%$ for lateral stimulation and by $5\% \pm 0.5\%$ for medial stimulation. This small influence is likely attributable to the distance separating motor axons from the stimulating electrodes: the effects of the large impedance reduction when the paddle is removed are more pregnant in the vicinity of the electrodes and get attenuated as one moves away from them.

On both Figures 3.41 and 3.42, it can be appreciated that the removal of the roots results in sharp variations of the potential profile at the interfaces between different media. As a matter of fact, while the removal of the roots had little effect on the peak potential, it had a very large influence on the peak of $-\Delta^2V$: the latter was increased by an average $760\% \pm 415\%$ for lateral stimulation and by $695\% \pm 370\%$ for medial stimulation. Despite the large variance, the peak was increased for all motor axons, with a minimum of 150%. This is again attributable to the discontinuities of the electric conductivity at the interface between two media, and in particular at the CSF-dura interface, as illustrated in Figure 3.43. Because these peaks are suppressed when including the roots in the volume conductor, this suggests that their inclusion is likely to cause an even smaller predicted

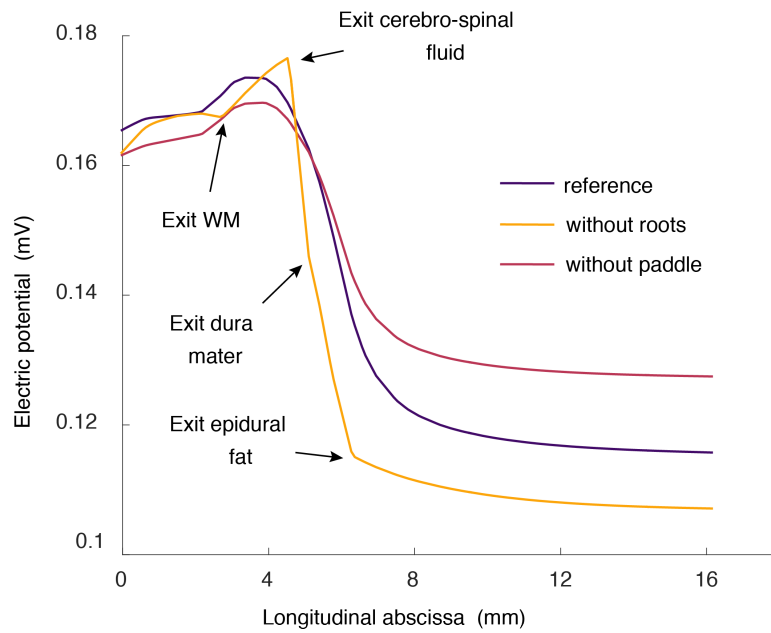


Figure 3.41 Electric potential profile along a motor axon running in the companion ventral root of the dorsal root used in Figure 3.35. The stimulation conditions are as in Figure 3.35. The longitudinal abscissa starts at the soma (0 mm) and ends at the tip of the ventral root.

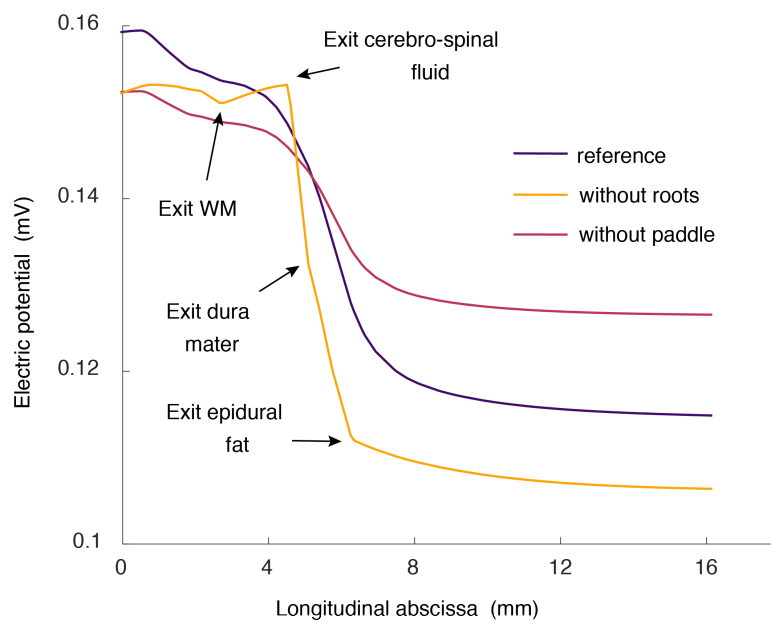


Figure 3.42 Same as Figure 3.41 but for medial stimulation.

recruitment of motor axons by hybrid models comparatively to dorsal root and dorsal column fibers.

On the other hand, the removal of the paddle had comparable influence on the peak of $-\Delta^2V$ along motor axons compared to dorsal root and dorsal column fibers: the peak was decreased by $23\% \pm 4\%$ for lateral stimulation and by $41\% \pm 2\%$ for medial stimulation.

Recruitment of nerve fiber populations

The second step was to assess whether and how the differences of electric potential described in the previous section translated into different recruitments of nerve fiber populations as predicted by neurophysical simulations. For this assessment, I used the same populations of dorsal root fibers, dorsal column fibers, and motor axons used in the previous section.

For each nerve fiber, I simulated the delivery of 200 μs -long cathodic square pulses of increasing amplitudes ($-25 \mu\text{A}$ to $-2000 \mu\text{A}$ with fixed increments of $-25 \mu\text{A}$) for each potential distribution described in the previous section. The motor axons were attached to motoneurons with realistic dendritic trees which were included in the neurophysical simulations (and along the branches of which the extracellular potential was also interpolated).

To obtain statistics on the obtained simulation results, I employed a bootstrap approach, whereby I re-sampled with replacement the initial populations of 50 fibers a number $N = 10\,000$ of times, thereby obtaining N bootstrapped populations of 50 individuals for each fiber type. The mean and standard deviations indicated in the curves and bar plots below are the mean and standard deviations across these bootstrapped populations.

Dorsal root fibers For each model (reference, without paddle, and without roots), and for each electrode position (lateral and medial), I plotted the percentage of recruited dorsal root fibers as a function of the stimulation amplitude. A fiber was considered recruited if an action potential was induced and propagated until the tips of its collateral branches during the simulation. The resulting curves are shown in Figure 3.44. The amplitudes are expressed in multiples of the *reference threshold*, which is the amplitude at which 10% of all fibers were recruited using the potential distribution of the reference model and for lateral stimulation.

As can be seen in Figure 3.44, higher stimulation amplitudes were required to recruit dorsal root fibers when using the potential distribution obtained with the model without paddle, especially for medial stimulation. This is also indicated by the bar plots of Figure 3.45, which represent the threshold and saturation amplitudes for the different models and lateral and medial stimulation (saturation was defined as the amplitude at which 90% of

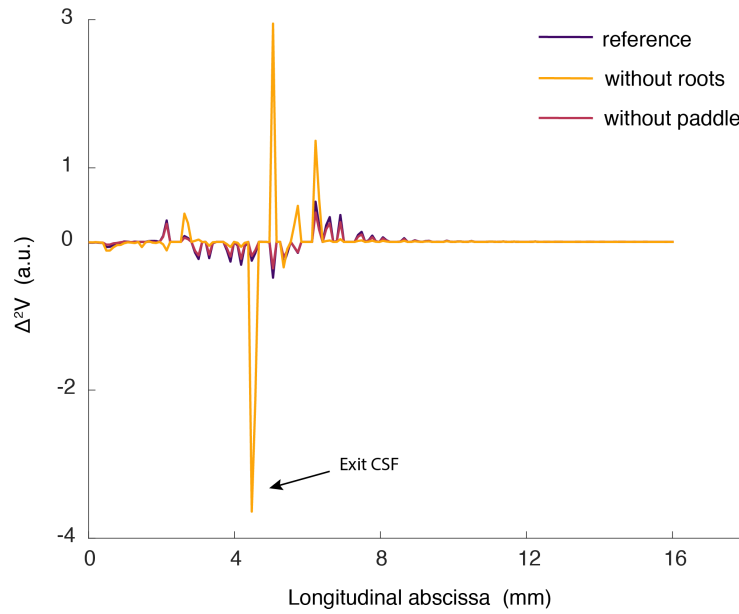


Figure 3.43 Profile of the potential's second-order finite differences along the motor axon of Figure 3.41, for lateral stimulation. The vertical axis scale is the same as in Figure 3.37.

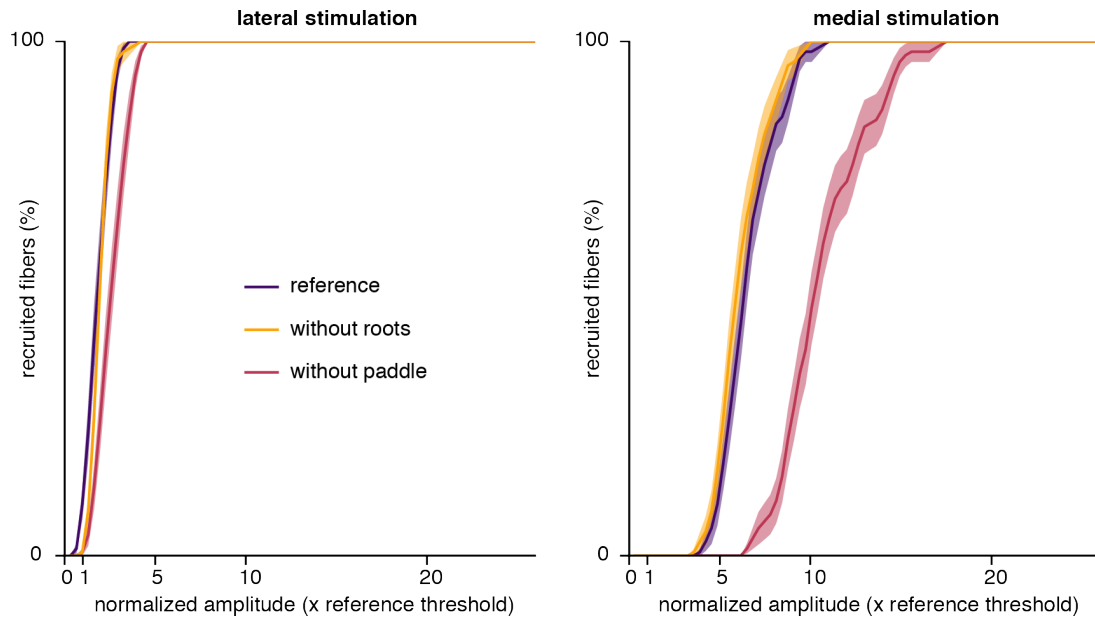


Figure 3.44 Recruitment curves of dorsal root fibers for the three models and for lateral and medial stimulations. *Reference threshold*: amplitude at which 10% of all fibers were recruited for the reference model and for lateral stimulation. *Solid lines and faint strips*: mean \pm standard deviation.

the fibers were recruited). This could have been expected, because the peak of $-\Delta^2V$ was consistently and significantly decreased for all dorsal root fibers in the model without paddle.

By contrast, the estimated recruitment is very similar for the models with and without roots. This is somewhat surprising, notably for medial stimulation, considering that the peak of $-\Delta^2V$ was increased by an average 73% when the roots were removed from the model. This goes to suggest that the relative variations of $-\Delta^2V$ alone do not suffice to predict the evolution of the excitation threshold of nerve fibers in hybrid models.

Dorsal column fibers The same analysis for dorsal column fibers resulted in Figures 3.46 and 3.47. The results are sensibly similar to those of the dorsal root fibers, except for the fact that the excitation threshold of dorsal column fibers were lower for medial stimulation, which was expected but which is not the object of analysis here. The similarity resides in a weak influence of the roots on the estimated recruitment and a more pronounced one of the paddle.

Motor axons For the motor axons, the situation is depicted in Figures 3.48 and 3.49. Examining Figure 3.48, it must be first pointed out that the range of amplitudes used, which was large enough to recruit all dorsal root and dorsal column fibers for all models, is largely insufficient to recruit all motor axons, especially for medial stimulation, though this is discussed in more detail in Chapter 4. An interesting finding is that the removal of the roots indeed caused a drastic reduction of excitation threshold of motor axons, especially for medial stimulation, as shown in Figure 3.49, and accordingly with the analysis of Δ^2V exposed in the previous section.

Recruitment selectivity I then assessed the influence of the modeling options on the selectivity of the recruitment of dorsal root fibers, dorsal column fibers, and motor axons.

Dorsal root fibers VS dorsal column fibers: For a given stimulation amplitude, I computed an index of the selectivity for dorsal root fibers over dorsal column fibers as $SI_{DR-DC} = N_{DR}/(N_{DR}+N_{DC})$ where N_{DR} and N_{DC} denote the numbers of recruited dorsal root and dorsal column fibers, respectively. The selectivity index for dorsal column fibers over dorsal root fibers was $SI_{DC-DR} = N_{DC}/(N_{DR}+N_{DC})$. A value of 1 for SI_{DR-DC} means a pure recruitment of dorsal root fibers; a value of 0, a pure recruitment of dorsal column fibers; and a value of 0.5, an even recruitment of dorsal root and dorsal column fibers (and conversely for SI_{DC-DR}). In Figure 3.50, I have plotted SI_{DR-DC} in function of the stimulation amplitude for lateral stimulation, and in Figure 3.51 I have plotted SI_{DC-DR} for medial stimulation.

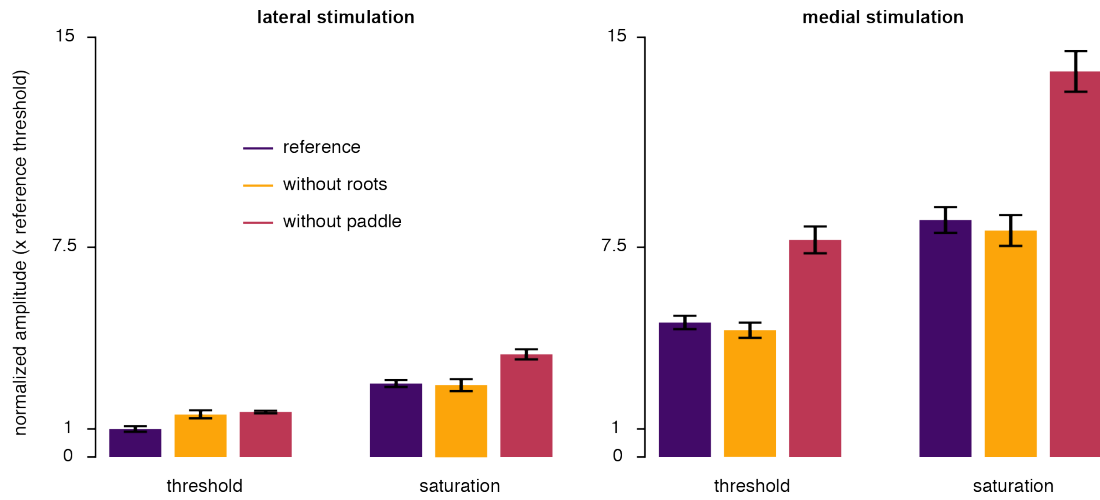


Figure 3.45 Threshold and saturation amplitudes of dorsal root fibers for the three models and for lateral and medial stimulations. *Reference threshold*: amplitude at which 10% of all fibers were recruited for the reference model and for lateral stimulation. *Threshold*: amplitude at which 10% of all fibers were recruited. *Saturation*: amplitude at which 90% of all fibers were recruited. *Bars and whiskers*: mean \pm standard deviation.

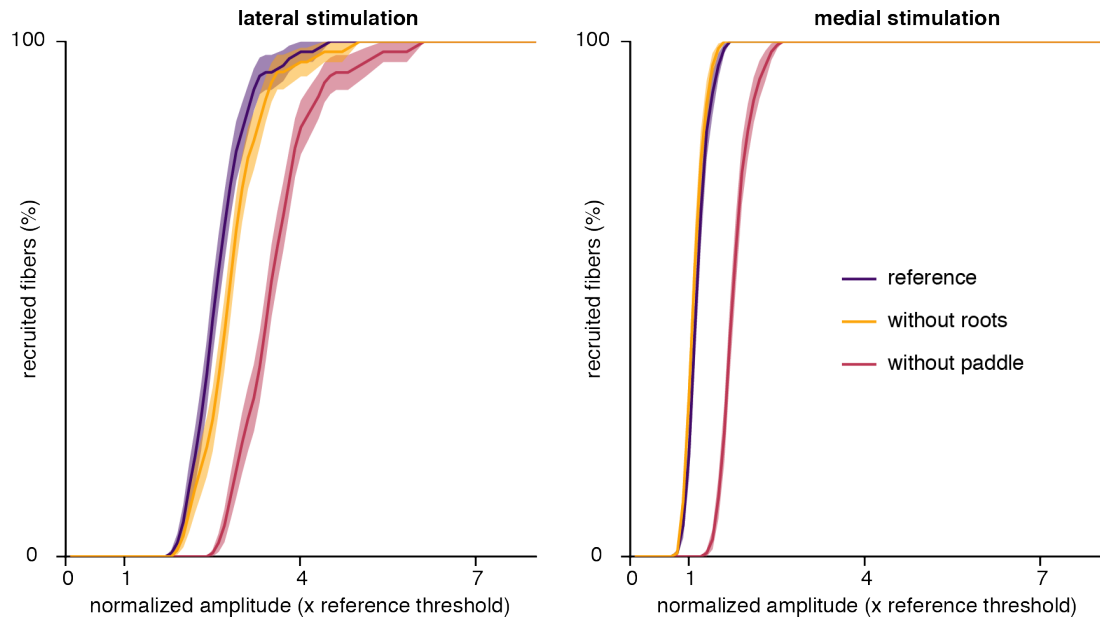


Figure 3.46 Recruitment curves of dorsal column fibers for the three models and for lateral and medial stimulations. *Reference threshold*: amplitude at which 10% of all fibers were recruited for the reference model and for medial stimulation. *Solid lines and faint strips*: mean \pm standard deviation.

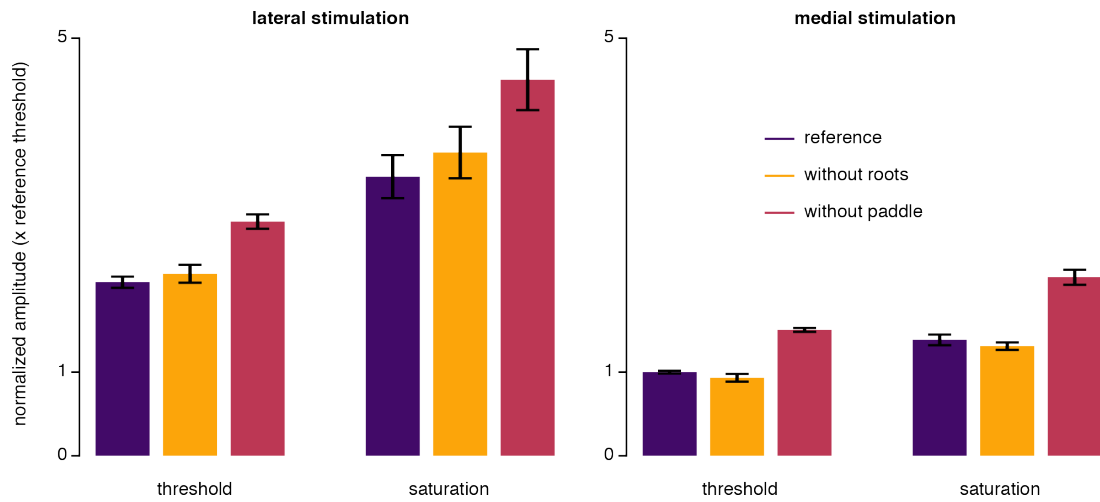


Figure 3.47 Threshold and saturation amplitudes of dorsal column fibers for the three models and for lateral and medial stimulations. *Reference threshold*: amplitude at which 10% of all fibers were recruited for the reference model and for medial stimulation. *Threshold*: amplitude at which 10% of all fibers were recruited. *Saturation*: amplitude at which 90% of all fibers were recruited. *Bars and whiskers*: mean \pm standard deviation.

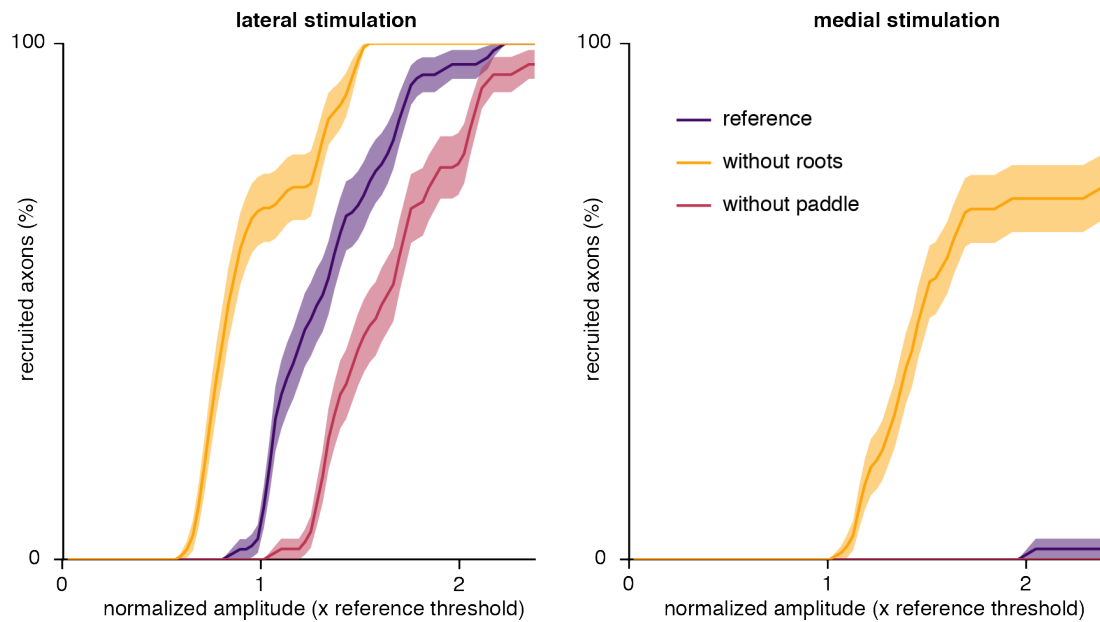


Figure 3.48 Recruitment curves of motor axons for the three models and for lateral and medial stimulations. *Reference threshold*: amplitude at which 10% of all axons were recruited for the reference model and for lateral stimulation. *Solid lines and faint strips*: mean \pm standard deviation.

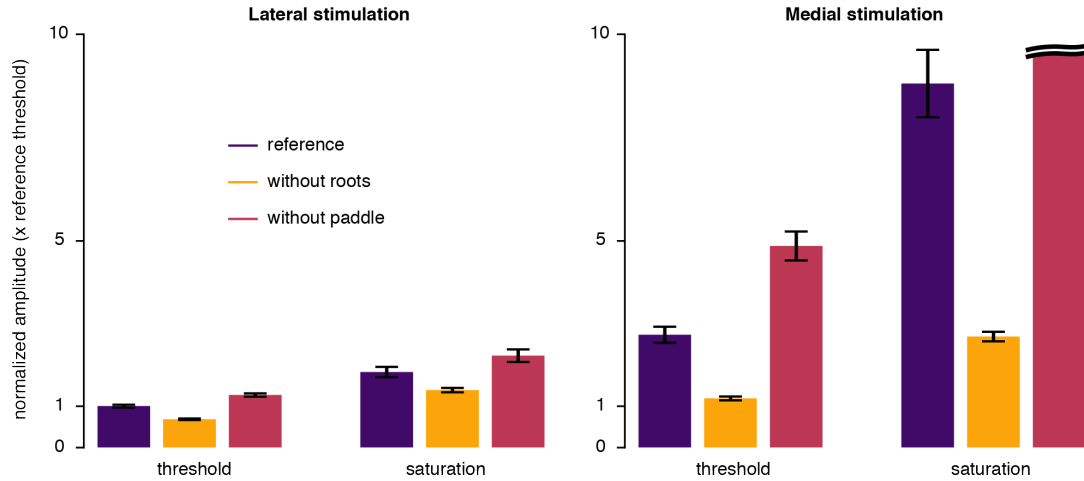


Figure 3.49 Threshold and saturation amplitudes of motor axons for the three models and for lateral and medial stimulations. The range of amplitudes used was $-25\mu\text{A}$ to $-8000\mu\text{A}$. Saturation for the model without paddle and medial stimulation was not reached. *Reference threshold*: amplitude at which 10% of all axons were recruited for the reference model and for lateral stimulation. *Threshold*: amplitude at which 10% of all axons were recruited. *Saturation*: amplitude at which 90% of all axons were recruited. *Bars and whiskers*: mean \pm standard deviation.

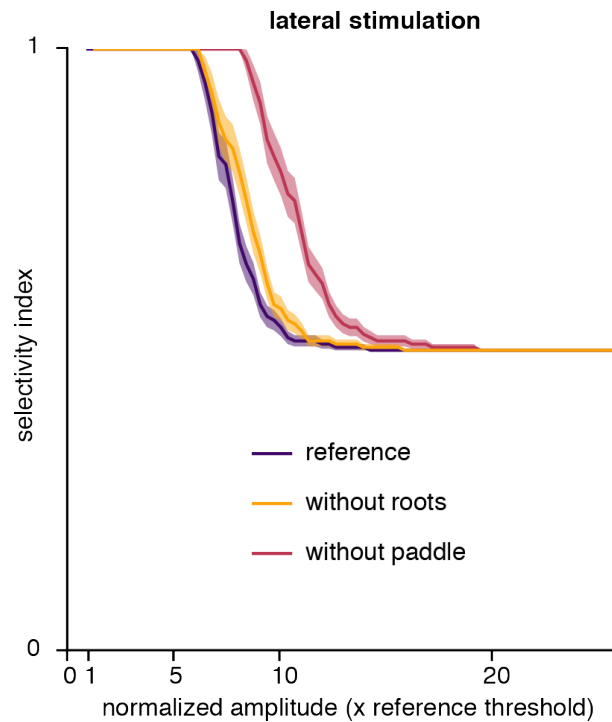


Figure 3.50 Selectivity curves of dorsal root fibers VS dorsal column fibers ($SI_{\text{DR-DC}}$) for the three models and for lateral stimulation. *Reference threshold*: amplitude at which 10% of all dorsal root fibers were recruited for the reference model. *Solid lines and faint strips*: mean \pm standard deviation.

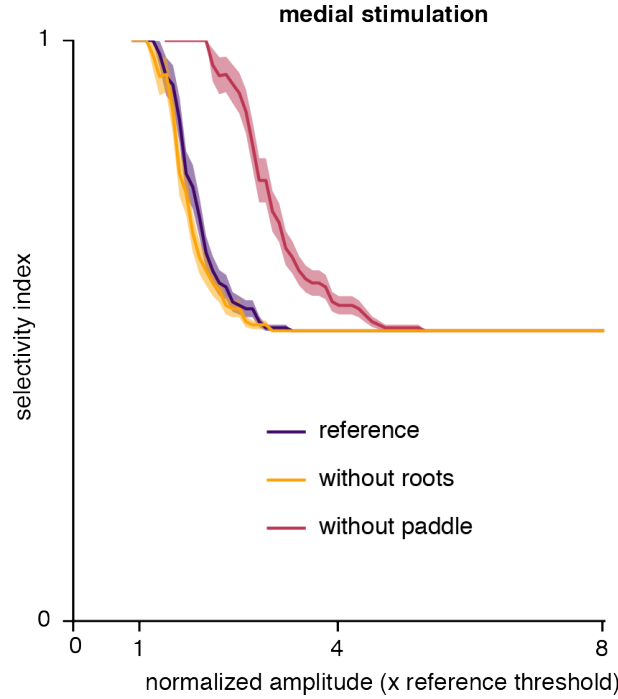


Figure 3.51 Selectivity curves of dorsal column fibers VS dorsal root fibers (SI_{DC-DR}) for the three models and for medial stimulation. *Reference threshold*: amplitude at which 10% of all dorsal column fibers were recruited for the reference model. *Solid lines and faint strips*: mean \pm standard deviation.

The resulting curves are in accordance with the recruitment curves exposed in the previous paragraphs. Namely, the removal of the roots from the model had little influence on the selectivity indices while the removal of the paddle had a more pronounced effect. The latter shifted the selectivity curves towards the right, reflecting the increased excitation threshold of both dorsal root and dorsal column fibers. Nonetheless, for lateral stimulation, the mean of SI_{DR-DC} over the *dynamic amplitude range* of dorsal root fibers (defined as the amplitude range from threshold to saturation, *ie* 10% recruitment to 90% recruitment) was of 1 for all models. Similarly, for medial stimulation, the mean of SI_{DC-DR} over the dynamic amplitude range of dorsal column fibers was almost of 1 for all models (0.98 ± 0.01 for the reference model, 0.99 ± 0.004 for the model without paddle, and 0.98 ± 0.01 for the model without roots). Analysis of the selectivity over the dynamic amplitude range of the targeted nerve fiber population is relevant, for in actual experimental or clinical settings, one would attempt to restrict the stimulation amplitude to this range. Thus, the paddle like the roots seemed to have no influence on the estimated selectivity neither for dorsal root fibers over dorsal column fibers for lateral stimulation, nor for dorsal column fibers over dorsal root fibers for medial stimulation.

Dorsal root fibers VS motor axons: Similarly to the above, I computed an index of the selectivity for dorsal root fibers over motor axons as $SI_{DR-MA} = N_{DR}/(N_{DR}+N_{MA})$, where N_{MA}

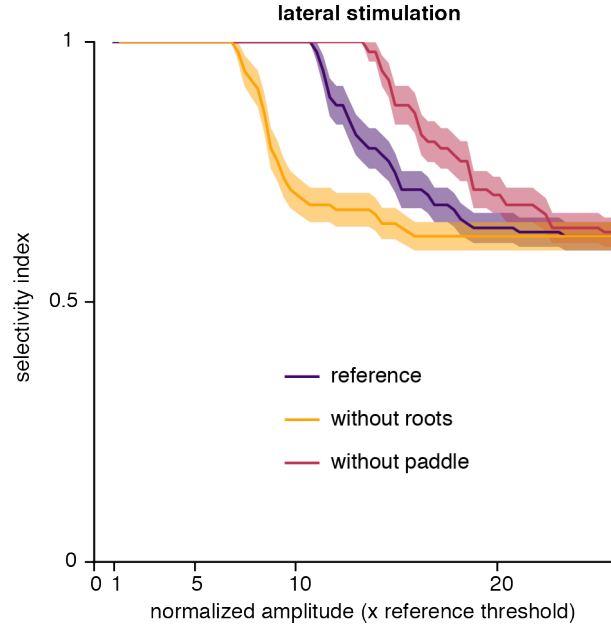


Figure 3.52 Selectivity curves of dorsal root fibers VS motor axons (SI_{DR-MA}) for the three models and for lateral stimulation. *Reference threshold*: amplitude at which 10% of all dorsal root fibers were recruited for the reference model. *Solid lines and faint strips*: mean \pm standard deviation.

denotes the number of motor axons that are recruited (for a given stimulation amplitude). The variations of SI_{DR-MA} in function of the stimulation amplitude for the three models are depicted in Figure 3.52. The reduction of excitation threshold of motor axons in the model without roots was clearly reflected by the shift of the curve towards the left, and inversely for the model without paddle. However, as was the case for the selectivity of dorsal root fibers over dorsal column fibers, the mean of SI_{DR-MA} over the dynamic amplitude range of dorsal root fibers was of 1 for all models, suggesting the little influence of the roots and the paddle in this estimation.

Summary and conclusions

The representation of the spinal roots and the silicone paddle of paddle electrode arrays in the volume conductor model have contrasted effects on the predictions of hybrid models. In the simulations reported here, removing the paddle led to a large decrease of the total impedance between the active and return electrodes (47% for the lateral electrode, 54% for the medial electrode). The electric potential was thus significantly and consistently reduced along dorsal root and dorsal column fibers, resulting in similarly significant and consistent reductions of the negative peaks of the second-order finite differences of V ($\Delta^2 V$) along these fibers. This translated into increased excitation thresholds for both fiber types and both electrode positions in the neurophysical simulations. However, the selectivity of the recruitment of one type over the other was largely unaffected by the

paddle removal, at least in the relevant ranges of stimulation amplitudes. On the other hand, removing the roots from the volume conductor had very little effect on the estimated recruitment of dorsal root and dorsal column fibers, despite large variations of the peaks of $-\Delta^2V$ with or without roots. The effect was more pronounced for motor axons, but was nonetheless inexistent regarding the estimated recruitment selectivity of dorsal root fibers over motor axons with lateral stimulation.

These findings indicate that representing the insulating paddle in hybrid models should significantly decrease the estimated power consumption required by paddle electrode arrays to target dorsal root and dorsal column fibers. This is a valuable insight because power consumption is an important criteria when comparing different electrode array designs or stimulation configurations using hybrid models [55]. The relevance of representing the roots with fully-fledged compartments is less evident. Nonetheless, the effort put into the faithful representation of the roots' geometry readily translate into realistic trajectories of dorsal root fibers in the dural sac, which instead is of prime influence on model predictions [38, 42]. For this reason, it should not be disregarded.

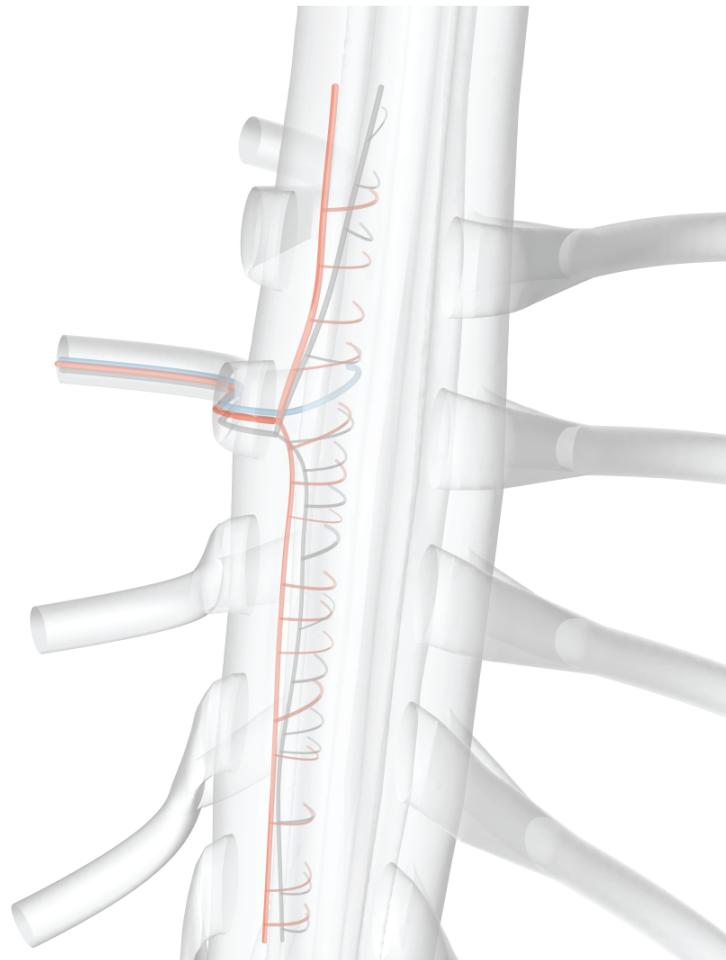
3.4.3 Nerve fiber geometry and segmental selectivity

I developed new realistic geometries of spinal nerve fibers, and notably of dorsal root primary afferents, for two main purposes:

1. I wanted to be able to estimate the selectivity of the recruitment of primary afferents of specific dorsal roots over primary afferents of the other roots. Two main approaches have been employed by previous investigators to address this problem: some have effectively represented dorsal root fibers of different roots and estimated the recruitment selectivity, but without representing the dorsal column bifurcations of the fibers [38, 42]; others have represented the dorsal column bifurcations, but they did not estimate the recruitment selectivity for specific dorsal roots over the other roots, and have instead estimated the selectivity for dorsal root fibers over abstract dorsal column fibers (abstract in the sense that they were not attributed to specific dorsal roots) [50, 58, 59, 88, 90]. The first approach is limited by the fact that medial stimulation is likely to recruit dorsal column bifurcations of fibers coming from many different roots (although this should depend on the depth at which the bifurcations run inside the dorsal columns [39, 59, 90]). The second approach is limited in that, when trying to evaluate the selectivity with which specific motor nuclei can be modulated by epidural stimulation, which was the object of the investigations presented in Chapter 4, it is important that the recruitment of the fibers from all the roots of interest be estimated: the information that dorsal column fibers are being recruited is insufficient: we need to know to which roots these fibers belong.
2. The realistic representation of the branching morphology of dorsal root fibers, notably of group-Ia fibers, and notably with regard to the innervation of motoneurons by their collateral branches, provides the most direct way to estimate the synaptic excitation of the motoneurons: the synapses which should be activated and the delay with which they should be activated for a given stimulation pulse constitute a direct result of the neurophysical simulations performed on the Ia-fibers.

In this section, I examine the influence of the geometry of dorsal root fibers on the recruitment selectivity of specific dorsal roots (segmental selectivity). I compare three different geometries:

- a *reference* geometry, which is the geometry described in Section 3.3.2;
- an *unbranching* geometry, whereby the dorsal root fibers did not bifurcate in the dorsal columns: their dorsal root branches projected directly towards the ventral horn of the gray matter;



— reference — OD₃
— unbranching

Figure 3.53 Representative trajectories of reference, unbranching and OD₃ fibers in the spinal cord.

- a geometry, here termed OD_3 , whereby the dorsal column bifurcations of the fibers were running close to the surface of the dorsal columns (specifically, in the compartment OD_3 of the dorsal columns, as defined in Section 3.2.5) instead of running in their normally dedicated DC compartment (as is the case for the reference geometry fibers).

These geometries are illustrated in Figure 3.53. To lead the analysis, I used the reference volume conductor model of the previous section, whose main specifications are summarized in Section 3.4.1, and are detailed in Section 4.2.4.

Targeted segment

I first sought to evaluate how the branching morphology impacted the recruitment of fibers of the dorsal root at the level of the stimulating electrode, referred to as the *targeted* root (its segment is referred to as the *targeted* segment). I considered populations of 50 fibers for each geometry model. The fibers were running in the C6 root, and I assessed their recruitment in response to 200 μ s-long stimulation pulses from both lateral and medial electrodes at the C6 level, and for amplitudes ranging from -25μ A to -2000μ A. Like in the previous section, I used a bootstrap approach ($N = 10\,000$ bootstrap samples) to obtain statistics from these populations.

The recruitment curves and the excitation and saturation thresholds for the three morphologies and for both lateral and medial stimulations are depicted in Figures 3.55 and 3.56. As can be observed, the absence of branching or the branching in the OD_3 compartment had very little influence on the recruitment of these fibers, either for lateral or for medial stimulation.

Non-targeted segments

I then assessed how the morphology impacted the recruitment of fibers of the non-targeted roots. For each fiber morphology, I considered populations of 50 fibers in each of the C5, C7, C8 and T1 roots (all but the targeted C6 root), *ie* a total of 200 fibers for each morphology, and I assessed the recruitment of these compound populations. The recruitment curves are shown in Figure 3.57. Expectedly, the branching morphology had a very strong influence on the recruitment of fibers of the non-targeted roots. The non-branching fibers are seen to be the least recruited by either lateral or medial stimulation, while the OD_3 fibers were far more recruited than the two other fiber populations. This is also apparent from the excitation and saturation thresholds depicted in Figure 3.58.

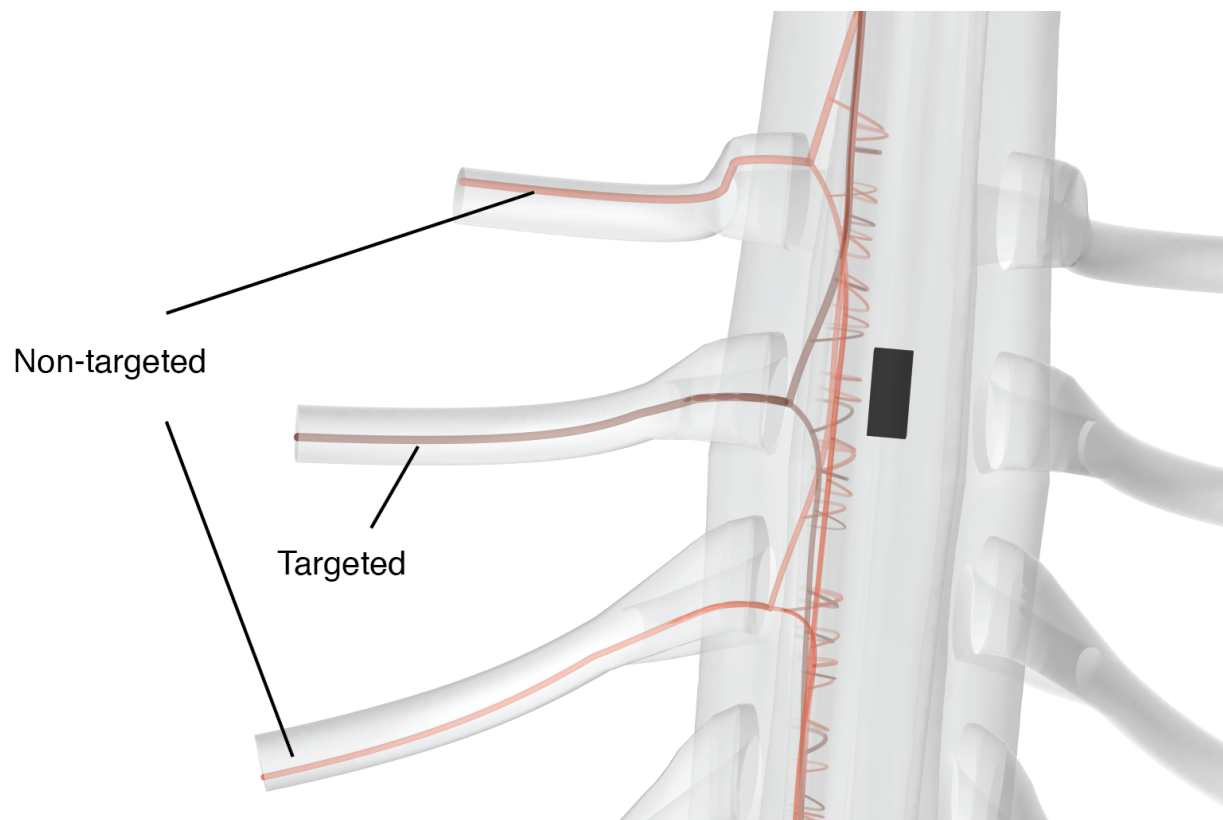


Figure 3.54 Example of targeted and non-targeted OD₃ fibers.

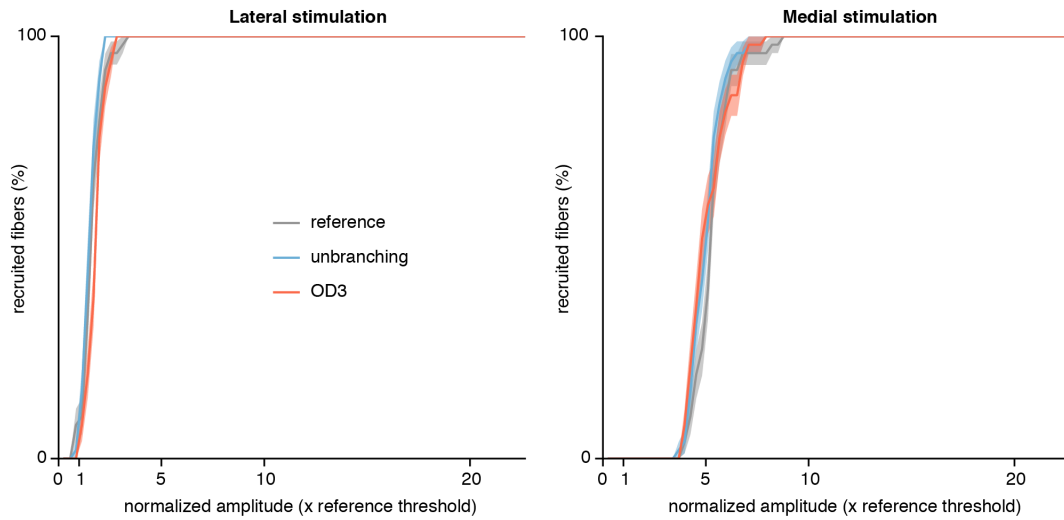


Figure 3.55 Recruitment curves of branching and unbranching fibers of the targeted segment for lateral and medial stimulations. *Reference threshold*: amplitude at which 10% of all branching fibers were recruited for lateral stimulation. *Solid lines and faint strips*: mean \pm standard deviation.

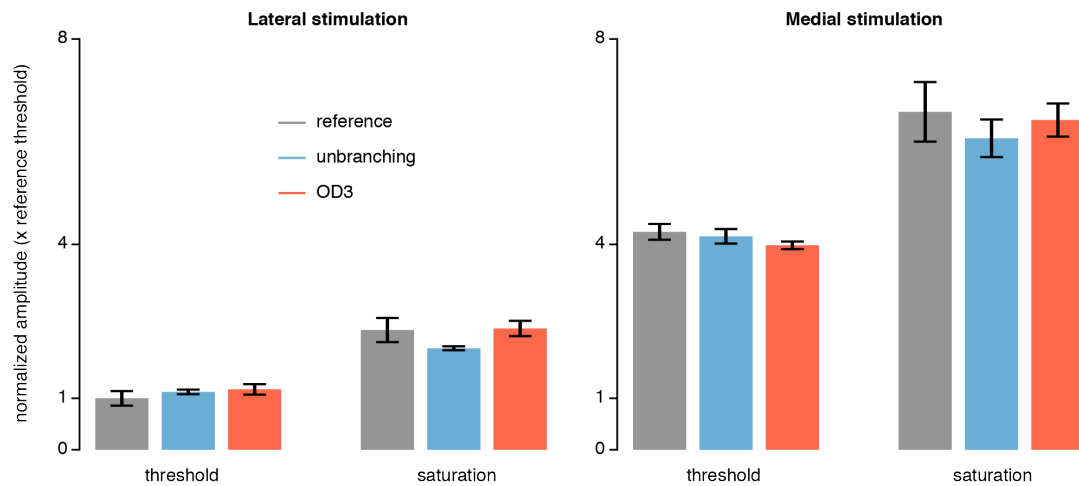


Figure 3.56 Threshold and saturation amplitudes of fibers of the targeted segment for lateral and medial stimulations. *Reference threshold*: amplitude at which 10% of all reference fibers were recruited for lateral stimulation. *Threshold*: amplitude at which 10% of all fibers were recruited. *Saturation*: amplitude at which 90% of all fibers were recruited. *Bars and whiskers*: mean \pm standard deviation.

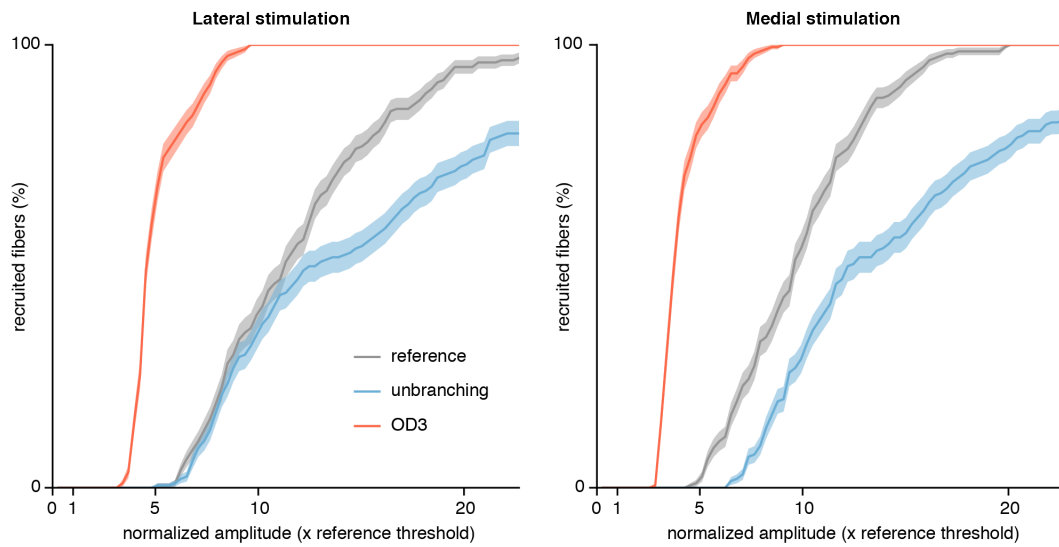


Figure 3.57 Recruitment curves of fibers of non-targeted segments for lateral and medial stimulations for the three morphologies. *Reference threshold*: amplitude at which 10% of all reference fibers of the targeted segment were recruited for lateral stimulation. *Solid lines and faint strips*: mean \pm standard deviation.

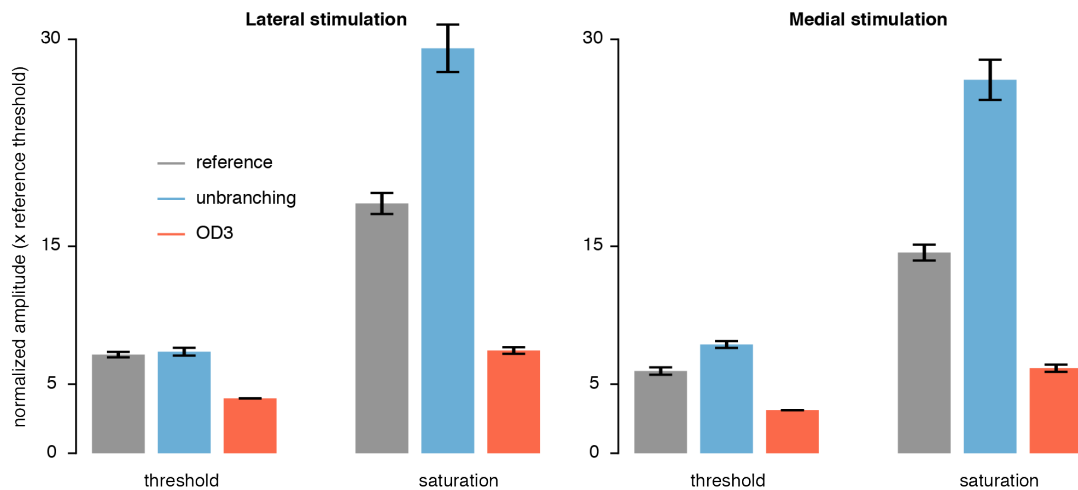


Figure 3.58 Threshold and saturation amplitudes of fibers of non-targeted segments for lateral and medial stimulations for the three morphologies. *Reference threshold*: amplitude at which 10% of all reference fibers of the targeted segment were recruited for lateral stimulation. *Threshold*: amplitude at which 10% of all fibers were recruited. *Saturation*: amplitude at which 90% of all fibers were recruited. *Bars and whiskers*: mean \pm standard deviation.

Segmental selectivity

Finally, I assessed the influence of the fiber morphology on the segmental selectivity. As was done in Section 3.4.2, for each stimulation amplitude and lateral or medial stimulation, I computed an index of the selectivity for the fibers of the targeted segment as $SI_t = R_t / (R_t + R_{nt})$ where R_t denotes the level of recruitment of the targeted fibers (*ie* the number of targeted fibers which were recruited divided by the total number of targeted fibers) and R_{nt} the level of recruitment of the non-targeted fibers. I then computed the mean of SI_t over the appropriate dynamic ranges of amplitudes for each fiber morphology (excitation threshold to saturation threshold for the fibers of the targeted segment). The resulting mean selectivity levels for the three morphologies and lateral and medial stimulation are depicted in Figure 3.59.

As can be seen, the selectivity for the targeted segment with lateral stimulation was unaffected by the fiber morphology (besides, the selectivity was perfect, which is further discussed in Chapter 4). By contrast, for medial stimulation, the selectivity greatly depended on the fiber morphology. For the unbranching fibers, the selectivity remained perfect, while for the other two, the selectivity dropped. For the OD₃ fibers, the selectivity was even poorer for the targeted than for the non-targeted segments due to the high recruitment of dorsal column bifurcations of the non-targeted fibers as they passed near the surface of the dorsal columns at the level of the electrode.

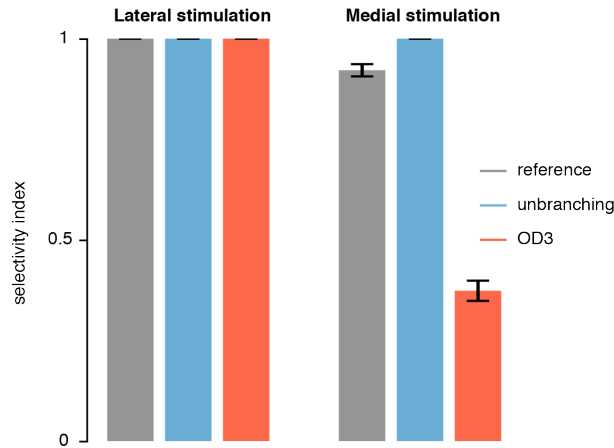


Figure 3.59 Mean selectivity indices for the fibers of the targeted segment \overline{SI}_t for lateral and medial stimulation and for the three fiber morphologies. *Bars and whiskers*: mean \pm standard deviation.

Summary and conclusions

To evaluate the selectivity of the recruitment of specific dorsal roots in hybrid models, the branching morphology of dorsal root fibers is essential, at least for some electrode positions. Moreover, the depth at which the fibers' rostro-caudal bifurcations run in the dorsal columns was observed to also be critical, which is coherent with previous computational findings [39, 59, 90]. From reconstructions of dorsal root afferent trajectories in the cat lumbosacral spinal cord [12, 13, 48, 49], it seems that the dorso-ventral and medio-lateral positions of the dorsal column bifurcations vary greatly from fiber to fiber. The bifurcations of one given fiber may even migrate in the transversal plane along their rostro-caudal course. Therefore, appropriately taking into account these trajectory characteristics, such as aimed for with the geometrical models developed here and exposed in Sections 3.2 and 3.3, is important to study the segmental selectivity of EES with hybrid models.

CHAPTER 4 EES OF THE CERVICAL SPINAL CORD IN MONKEYS AND HUMANS: COMPUTATIONAL AND EXPERIMENTAL ANALYSIS

In this chapter, I present the results of a collaborative investigation of EES of the cervical spinal cord in monkeys and humans.

This investigation eventually led to the elaboration of a scientific manuscript which has been submitted for publication to the fully open-access, peer-reviewed journal *Nature Communications*¹. Entitled *Recruitment of upper-limb motoneurons with epidural electrical stimulation of the primate cervical spinal cord*, it is referenced as item [99] in the bibliography of this dissertation.

The contents of the present chapter largely overlap with the contents of this manuscript, of which I am first author. I present here only those aspects of the study to which I have directly contributed. I have largely reorganized and rewritten the elements found in the original manuscript, but some passages are reproduced without modifications. I also included graphical illustrations produced by some of my collaborators, with the aim to facilitate the reader's understanding of the study, in which case I have systematically and explicitly mentioned their provenance.

The other investigators of the study, in the order as they appear on the manuscript, are:

- Beatrice BARRA, from the Department of Neuroscience and Movement Science (DNMS), Faculty of Science and Medicine, University of Fribourg, Fribourg, Switzerland;
- Giuseppe SCHIAVONE, from the Bertarelli Foundation Chair in Neuroprosthetic Technology, Laboratory for Soft Bioelectronics Interface (LSBI), Institute of Microengineering, Institute of Bioengineering, Centre for Neuroprosthetics, Ecole Polytechnique Fédérale de Lausanne, Geneva, Switzerland;
- Nicholas JAMES, from the Center for Neuroprosthetics and Brain Mind Institute (CNP-BMI), School of Life Sciences, École Polytechnique Fédérale de Lausanne, Geneva, Switzerland;
- Florian FALLEGER, from the LSBI;
- Simon BORGOGNON, affiliated to the DNMS and the CNP-BMI;
- Stéphanie LACOUR, from the LSBI;

¹*Nature Communications* ISSN 2041-1723 (online). <https://www.nature.com/ncomms/>.

- Jocelyne BLOCH, affiliated to the Neurosurgery Department, Centre Hospitalier Universitaire Vaudois (CHUV), Lausanne, Switzerland, and to the Defitech Center for Interventional Neurotherapies (NeuroRestore), EPFL and CHUV, Lausanne, Switzerland;
- Grégoire COURTINE, affiliated to the CNP-BMI, the CHUV, and NeuroRestore;
- Marco CAPOGROSSO, affiliated to the DNMS and the Department of Neurological Surgery, Rehabilitation and Neural Engineering Laboratories, University of Pittsburgh, Pittsburgh, PA.

Author contributions:

Marco CAPOGROSSO conceived the study.

I and Marco CAPOGROSSO are the main writers of the manuscript.

I have conceived and implemented the hybrid neurophysical volume conductor model, devised the simulations, and analyzed their results.

I and Simon BORGOGNON carried out the anatomical analysis described in Section 4.2.4. Beatrice BARRA, I, Marco CAPOGROSSO, Nicholas JAMES, Grégoire COURTINE and Jocelyne BLOCH performed the experiments discussed in Section 4.3.

Jocelyne BLOCH, Marco CAPOGROSSO, Grégoire COURTINE, I, Beatrice BARRA, Giuseppe SCHIAVONE, Florian FALLEGER and Stéphanie LACOUR designed the epidural arrays described in Section 4.3.1.

Giuseppe SCHIAVONE, Florian FALLEGER and Stéphanie LACOUR manufactured and tested the epidural arrays.

Etienne PRALONG provided the clinical data discussed in Section 4.4.

I, Beatrice BARRA, Giuseppe SCHIAVONE and Nicholas JAMES analyzed the in-house experimental data and the clinical data and created the figures of the manuscript.

Marco CAPOGROSSO and Grégoire COURTINE supervised the study.

4.1 Introduction

Two decades of preclinical and clinical studies have demonstrated that the delivery of EES to the lumbosacral spinal cord can reactivate spinal sensorimotor circuits after SCI. EES has mitigated a wide range of lower-limb motor deficits and promoted long-term recovery of voluntary motor control in various individuals with chronic SCI [23–31].

Computational and experimental studies conducted in animal models and humans [18, 38–42, 100] have provided evidence that EES applied over the lumbosacral spinal cord primarily engages large myelinated afferent fibers running in the posterior roots and dorsal columns of the spinal cord. These fibers form synaptic connections with spinal interneurons and motoneurons located in the gray matter, thereby constituting a gateway to the motor circuits controlling leg muscles [60, 101]. For instance, muscle spindle group-Ia fibers provide monosynaptic excitation to motoneurons [11, 16] and connect to various populations of interneurons located in the intermediate region of the gray matter [12, 102, 103]. Similarly, muscle spindle group-II fibers, force-sensitive group-Ib fibers (from Golgi tendon organs) and low-threshold cutaneous mechanoreceptor fibers all contact specific populations of interneurons that exert direct or indirect influences onto motoneurons [15]. Some also possess direct connections to motoneurons [47].

Due to their branching morphology [11, 12, 14], the artificial recruitment of these fibers is likely to supply synaptic inputs to circuits in many spinal segments. This divergence of excitatory inputs limits the ability to selectively engage skeletal muscles when stimulating the spinal cord. Nonetheless, the distribution of the sensory afferents in the posterior roots can be exploited to steer the modulation exerted by EES towards specific motor nuclei. Indeed, as early as in the first half of the last century, Lloyd [53] reported that selective stimulation of individual posterior roots evoked efferent volleys exclusively in the corresponding ventral roots (*ie* of the same spinal segment). This principle has recently been translated into stimulation protocols that target individual lumbosacral posterior roots independently, with timings corresponding to the natural dynamics of the motoneuronal activity in the spinal segments that they innervate [25, 30, 31]. These spatiotemporal patterns of targeted EES have proven more efficacious at mitigating lower-limb motor deficits compared to conventional EES protocols.

Sensorimotor circuits controlling upper-limb muscles, located in the cervical spinal cord, present a similar organization compared to their lumbosacral counterparts. This similarity suggests that EES could also be applied to cervical spinal segments to facilitate the execution and promote the recovery of arm and hand function in people with quadriplegia following high cervical SCI [32]. However, the ability of EES to selectively modulate specific cervical motor nuclei via pre-synaptic pathways remains unclear. In fact, studies on intraspinal microstimulation, which also engages motoneurons via pre-synaptic

pathways [104], have reported low reproducibility and limited specificity of arm muscle recruitment when applied to the cervical spinal cord of monkeys [79, 104–107]. Here, we hypothesized that the anatomy of the cervical spinal cord enables targeted EES to modulate specific motor nuclei involved in the production of upper-limb movements via the direct recruitment of sensory fibers in the posterior roots.

To address this question, we implemented a detailed hybrid neurophysical volume conductor model capable of estimating the relative recruitment of various populations of nerve fibers and neurons in response to single pulses of EES delivered over the cervical spinal cord. Numerical simulations suggested that cervical EES primarily recruits large myelinated afferent fibers in the posterior roots and in the dorsal columns, and is unlikely to recruit motor axons directly. Furthermore, the model predicted that the selective recruitment of individual posterior roots was contingent on the precise position of electrodes on the mediolateral and rostrocaudal axes. Electrophysiological experiments in monkeys and humans corroborated these predictions. These results provide a conceptual framework to design EES strategies to improve the recovery of upper-limb motor functions after cervical SCI.

4.2 EES of the macaque monkey cervical spinal cord: theoretical analysis

We sought to study the recruitment of nerve fibers and neurons in response to the application of EES over the cervical spinal cord. To this end, I constructed a hybrid neurophysical volume conductor model of the macaque monkey cervical spinal cord, which I used for three main purposes:

- determining which are the primary direct targets of the stimulation;
- evaluating the ability to selectively recruit individual cervical dorsal roots;
- assessing the plausibility of a purely mono-synaptic recruitment of motoneurons mediated by group-Ia fibers.

4.2.1 Model construction and anatomical findings

The first step of our study was to gather the necessary elements of anatomy and neurology of the macaque cervical spinal cord by means of in-house measurements and a review of the literature (see Section 4.2.4).

Some of these elements were also necessary for me to build the hybrid model, in particular those regarding the macro-anatomy of the spinal cord and the vertebral canal, the electrical conductivities of the tissues and materials represented in the volume conductor model, and the distributions of motoneurons and group-Ia fibers of a selection of upper-limb muscles in the segments and the dorsal roots of the macaque monkey cervical spinal cord.

Anatomical analysis of preserved spinal cord specimens revealed consistent cross-section widths of the cervical spinal segments (largest segments were C6 to C8, > 7.5 mm, see Figure 4.1). However, the length of the spinal segments exhibited a greater degree of variability, although our measurements suggested a trend of decreasing length from rostral to caudal segments.

Furthermore, examining the trajectories of the dorsal and ventral roots from their entrance in the spinal cord to their exit from the spine through the intervertebral foramina, we found that these trajectories were almost perpendicular to the rostro-caudal axis of the spine for spinal segments C2-C3, and that they became more and more downward-oriented for the more caudal segments, exiting the spine at rostro-caudal levels markedly more caudal than their segment of connection (Figure 4.1.a). Consequently, the T1 spinal segment was approximately located at the same rostro-caudal level as the C7 vertebra.

Computed tomography images acquired in a living animal enabled us to reconstruct in three dimensions the vertebral column of the macaque monkey (see Section 4.2.4). Notably, this allowed to extract the coordinates of the intervertebral foramina. I could thus

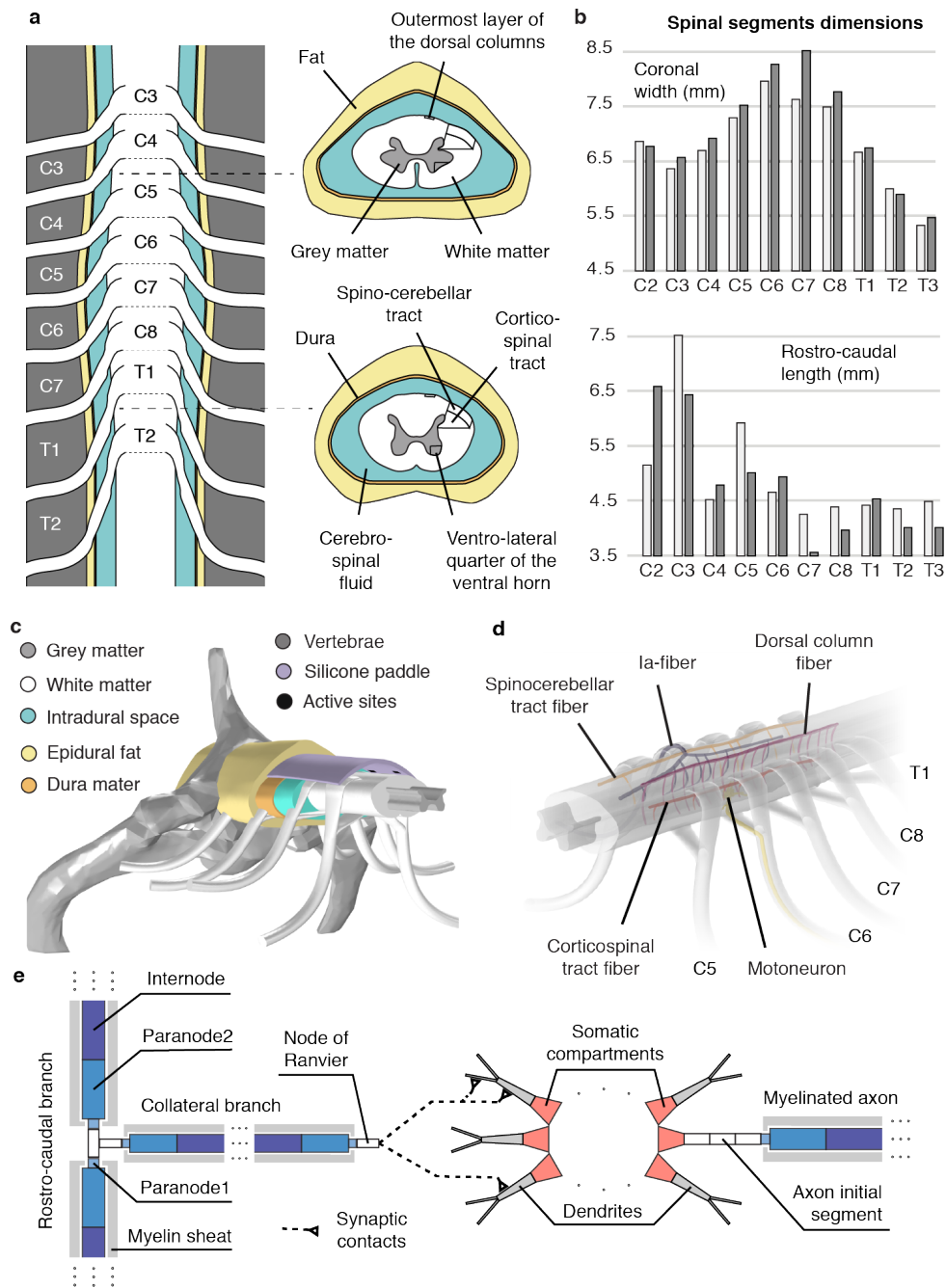


Figure 4.1 Morphology and hybrid model of EES of the macaque monkey cervical spinal cord. **a** Macroscopic organization of the cervical spinal cord. Left: relationships between spinal segments, spinal roots and vertebrae. Right: cross-sections at the C5 and T1 segmental levels showing the internal compartmentalization of the spinal cord. **b** Spinal segments dimensions. The two shades of gray indicate measurements coming from two different spinal cord dissections. **c** Tridimensional view of the volume conductor. **d** Trajectories of virtual nerve fibers and motoneurons. **e** Compartmentalization of myelinated nerve fibers and motoneurons [77, 79] used in neurophysical simulations.

construct the model using the algorithms presented in Chapter 3 and the specific data reported in Section 4.2.4 and Figure 4.1, which came for a large part from previously published works.

Furthermore, we estimated the distributions of motoneurons and group-Ia fibers of a selection of upper-limb muscles in the segments and the roots of the macaque monkey cervical spinal cord, which are reported in Tables 4.1 and 4.2.

4.2.2 Primary direct targets of EES of the cervical spinal cord

I first used the model to estimate the direct recruitment of neural entities induced by electrical stimuli delivered from lateral and medial positions of the epidural space.

Our hypothesis was that:

1. Laterally-positioned electrodes would primarily recruit large myelinated fibers running in the nearest dorsal roots.
2. Medially-located electrodes would primarily recruit dorsal column fibers.
3. Given the dimensions of the primate cervical spinal cord, recruitment of motor axons would not occur within the range of stimulation amplitudes that is necessary to recruit dorsal root afferent fibers.

Laterally-positioned electrodes

When placing electrodes laterally, facing a single dorsal root, the electrical current density was strongest directly next to and inside the roots (Figure 4.2.a). Furthermore, the current density was very weak in the spinal cord, and stronger in the highly conductive cerebrospinal fluid.

As a result, electric potentials and potential gradients were largest along the DR-fibers (Figure 4.2.a), which were recruited at the lowest stimulation amplitudes (Figure 4.2.b and c). DR-fibers were followed by longitudinal fibers running in the spinocerebellar tract (ST-fibers), in the dorsal columns (DC-fibers), and in the lateral corticospinal tract (CST-fibers).

Finally, the direct recruitment of motoneurons remained null at amplitudes as high as ~ 10 times the threshold for $A\alpha$ -DR-fibers and twice the saturation amplitude for both $A\alpha$ - and $A\beta$ -DR-fibers and DC-fibers (Figure 4.2.b).

Surprisingly, the larger diameter of the $A\alpha$ -DR-fibers did not seem to confer them a substantially lower excitation threshold compared to $A\beta$ -DR-fibers, as could have been expected [86]. This might have been due to the close proximity between the electrode and

Table 4.1 Distribution of upper-limb motoneurons in the cervical segments of the macaque monkey spinal cord. *[Extracted from [96].]* Data for the deltoid was assumed to be identical to that of the biceps, following observations made in humans [97].

Muscle	Spinal segment						Total
	C5	C6	C7	C8	T1	T2	
Deltoid	212	489	265	85	0	0	1051
Biceps	212	489	265	85	0	0	1051
Triceps	7	60	332	678	190	4	1271
Flexor Carpi Radialis	0	0	180	51	4	0	235
Extensor Carpi Radialis	129	506	205	38	8	0	886
Flexor Carpi Ulnaris	0	0	11	224	79	0	314
Extensor Carpi Ulnaris	0	4	10	113	89	0	216
Flexor Digitorum Superficialis	0	0	0	80	224	2	306
Extensor Digitorum Communis	0	0	9	178	86	0	273
Flexor Digitorum Profundus	0	0	10	209	241	15	475
Abductor and Flexor Pollicis Brevis	0	0	0	15	95	5	115

Table 4.2 Distribution of upper-limb Ia-fibers in the cervical dorsal roots of the macaque monkey spinal cord. *[Derived from [108]. See Section 4.2.4.]*

Muscle	Spinal segment						Total
	C5	C6	C7	C8	T1	T2	
Deltoid	14	32	17	5	0	0	68
Biceps	24	55	30	30	10	0	119
Triceps	1	9	50	103	29	1	193
Flexor Carpi Radialis	0	0	37	10	1	0	48
Extensor Carpi Radialis	9	37	15	3	1	0	65
Flexor Carpi Ulnaris	0	0	2	46	16	0	64
Extensor Carpi Ulnaris	0	1	3	30	24	0	58
Flexor Digitorum Superficialis	0	0	0	35	97	0	132
Extensor Digitorum Communis	0	0	3	53	26	0	82
Abductor and Flexor Pollicis Brevis	0	0	0	7	49	3	59

the root, resulting in such steep potential distributions that these diameter differences played a minor role in their excitability.

I then devised simulations to inquire whether DR-fibers of adjacent roots are mostly recruited via the spread of the electric potential towards the adjacent roots or via the recruitment of the dorsal column projections of these fibers. Specifically, I analyzed the recruitment order and action potential initiation sites of Ia-afferents of the C5, C6 and C7 roots in response to stimulation targeting the C6 root.

First of all, as expected, the Ia-afferents running in the targeted root (C6) were recruited at significantly lower stimulation amplitudes than those running in the adjacent or more distal roots (C5, C7, C8 and T1, see Figure 4.2.c). Additionally, action potentials were initiated exclusively within their dorsal root branches (Figure 4.2.d).

By contrast, action potential initiation sites for fibers belonging to the adjacent roots were partly found within their dorsal root branches and partly within their dorsal column projections. Specifically, recruitment of caudal afferents (C7) was mostly induced in their dorsal columns branches, while the situation was reversed for the fibers rostral to the stimulation site (C5). This can be explained by the fact that caudal branches of the modeled Ia-afferents had smaller diameters compared to the rostral branches (see Section 4.2.4), theoretically increasing their excitation threshold [86].

Medially-positioned electrodes

Medial location of the electrodes induced a markedly different recruitment profile. First, the electric current density was strongest in the CSF dorsal layer, just next to and oriented towards the dorsal columns (Figure 4.2.e), resulting in DC-fibers exhibiting the lowest recruitment threshold (Figure 4.2.f), followed by $A\alpha$ - and $A\beta$ -fibers in the dorsal roots, and finally by ST-fibers. The threshold for CST-fibers was ~ 5 times that of DC-fibers, while that for motor axons was as high as ~ 9 times this value (Figure 4.2.f).

Furthermore, the selective recruitment of individual roots was poorer with medial than with lateral stimulation, as indicated by the selectivity indices reported in Figure 4.2.h, which were computed for each root and lateral or medial stimulation respectively (see Section 4.2.4). Moreover, this poorer selectivity achieved by medial stimulation seemed to be mainly due to a less efficient recruitment of the Ia-fibers of the targeted segment, as suggested by the comparison between Figure 4.2.c and Figure 4.2.g.

Finally, analysis of the recruitment order and action potential initiation sites (data not shown) suggested similar recruitment characteristics for caudal and rostral afferents compared to lateral stimulation (Figure 4.2.d), though rostral fibers tended to be recruited via their dorsal column projections more often. For the Ia-fibers of the targeted spinal segment, the increase in excitation threshold was accompanied by the migration of the ac-

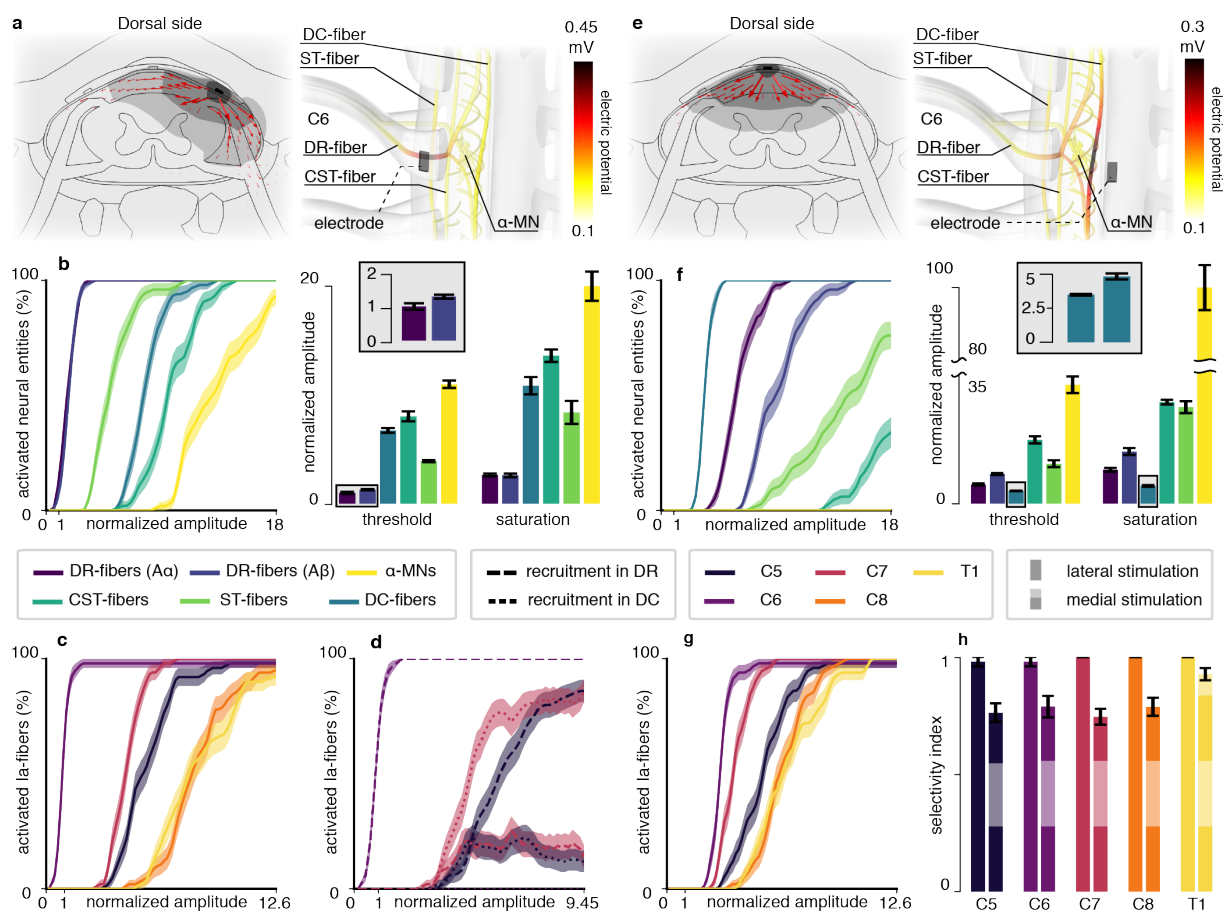


Figure 4.2 Caption on next page.

Figure 4.2 Computational analysis of the direct targets of cervical EES in macaque monkeys. **a** Electric currents and potential distribution(ϕ) generated by a lateral electrode contact at the C6 spinal level for a stimulation current of 1 μ A estimated with the finite element method. *Left*: transversal cross-section cutting the electrode contact in two halves. Red arrows: current density vectors. Dark gray surface: $\phi \geq 0.2$ mV. Mild gray: $\phi \geq 0.1$ mV. Light gray: $\phi \geq 0.08$ mV. *Right*: along trajectories of virtual nerve fibers and motoneurons. *DC*: dorsal columns. *ST*: spinocerebellar tract. *DR*: dorsal root. *CST*: corticospinal tract. *MN*: motoneuron. **b** Direct recruitment of nerve fibers and motoneurons estimated from neurophysical simulations using the potential distribution of **a**. *Left*: recruitment curves. *Right*: threshold amplitudes (10% recruitment) and saturation amplitudes (90% recruitment) for the different neural entities, expressed as multiples of the threshold for DR-A α -fibers. *Inset*: threshold for DR-A α -fibers and DR-A β -fibers. **c** Simulated recruitment of Ia-fibers of individual dorsal roots using the potential distribution of **a**. Amplitudes are expressed as multiples of the threshold for the Ia-fibers of the C6 root. **d** Detailed recruitment for the C5, C6 and C7 roots. Amplitudes are expressed as multiples of the threshold for the Ia-fibers of the C6 root. **e** Same as **a** for a medially-positioned electrode contact. **f** Same as **b** with the potential distribution of **e**. *Inset*: threshold and saturation amplitudes for the DC-fibers. Amplitudes are expressed as in **b**. **g** Same as **c** with the potential distribution of **e**. **h** Maximal selectivity indexes for each root using lateral or medial electrodes (see Section 4.2.4). *Recruitment curves*: curves are made of 80 data points (except for **d**, 60 data points) consisting in the mean and standard deviation of the recruitment computed across 10 000 bootstrapped populations (see Section 4.2.4). Lines and filled areas represent the moving average over 3 consecutive data points. *Bar-plots*: mean and standard deviation across 10 000 bootstrapped populations (see Section 4.2.4).

tion potential initiation sites from within the dorsal root branch to either the bifurcation point of the dorsal columns projections (for most fibers) or the dorsal column projections themselves.

4.2.3 Ia-mediated recruitment of upper-limb motoneurons

To summarize, the previous results indicated that appropriate (*ie* lateral) placement of epidural electrodes theoretically allows to recruit individual dorsal roots with very high selectivity, and that the direct recruitment of motor axons should require much higher stimulation amplitudes compared to dorsal sensory afferents.

I thus sought to investigate whether the mere recruitment of dorsal sensory afferents was amenable to induce the trans-synaptic recruitment of motoneurons, and in particular if this was the case of the mere recruitment of Ia-fibers. Indeed, though it is well-established that Ia-fibers can induce homonymous motoneuronal recruitment [109], variability in the Ia-to-motoneuron synaptic connectivity across muscles could influence this recruitment and make some muscles more prone to Ia-mediated activation than others. Moreover, the stimulation amplitudes necessary to recruit a sufficient amount of Ia-fibers to trigger the activation of motoneurons could be above the threshold for the direct recruitment of motor axons.

To that end, I used the model to assess the relative influence of several parameters affecting the Ia-to-motoneuron synaptic connectivity, namely:

- the number of Ia-fibers (N^{Iaf});
- the Ia-to-motoneurons connectivity ratio (r_{connec});
- the contact abundance (a_{contact}), *ie* the mean number of synapses per Ia-motoneuron pair;
- the synaptic conductance (g_{syn}).

As a preliminary result, I found that the somatic excitatory post-synaptic potential (EPSP) of a motoneuron was mainly determined by the product of the total number of synapses it receives (n_{syn}) by the synaptic conductance (g_{syn}) of individual synapses (Figure 4.3.a). This indicates that a low (resp. a high) number of active synapses can be compensated by an increased (resp. decreased) synaptic conductance to achieve a given motoneuronal excitation.

This suggested that the Ia-excitability of a motor nucleus innervated by a population of Ia-afferents can be characterized by the product $N^{\text{Iaf}} \times r_{\text{connec}} \times a_{\text{contact}} \times g_{\text{syn}}$, since in this case the mean total number of synapses received by each motoneuron can be estimated

as $n_{\text{syn}} = N^{\text{Iaf}} \times r_{\text{connec}} \times a_{\text{contact}}$. Keeping constant the mean number of synapses per Ia-motoneuron pair (a_{contact}), I found that the number of Ia-afferents (N^{Iaf}) that needs be recruited to induce the recruitment of a certain percentage of homonymous motoneurons is indeed dictated by the product $r_{\text{connec}} \times g_{\text{syn}}$ (Figure 4.3.c). Keeping constant the connectivity ratio (r_{connec}), a similar analysis revealed an equivalent dependence on the product $a_{\text{contact}} \times g_{\text{syn}}$ (data not shown).

Next, assuming uniform and realistic values for the connectivity ratio (r_{connec}) and the contact abundance (a_{contact}) across muscles [11, 14], and after estimating N^{Iaf} for eight monkey upper-limb muscles (see Section 4.2.4), I determined for each of them the minimum g_{syn} value enabling the recruitment of 100% of its motoneurons.

The resulting g_{syn} values ranged from 3.375 pS (triceps) to 28.5 pS (abductor pollicis brevis) (Table 4.3) which are of the same order of magnitude as the 5 pS value estimated experimentally by Finkel and Redman [110]. Thus, the model was able to produce a purely Ia-mediated recruitment of motoneurons within a range of synaptic connectivity parameters coherent with experimental findings.

Based on these preliminary results, I sought to evaluate whether such a purely Ia-mediated trans-synaptic recruitment of motoneurons was plausible during EES, where not all Ia-fibers of a given muscle are necessarily recruited by the stimulation. To that end, I evaluated the monosynaptic recruitment of motoneurons resulting from the direct activation of Ia-fibers following lateral stimulation targeting the C6 root.

For that, I either used the g_{syn} values of Table 4.3, implying a uniform Ia-excitability across muscles (hypothesis H1), or a uniform average g_{syn} value for all muscles, implying a higher excitability for muscles possessing higher numbers of Ia-fibers (hypothesis H2) (see Section 4.2.4). Both hypotheses yielded trans-synaptic recruitment of the motor nuclei located in the targeted segment at stimulation amplitudes that were supra-threshold only for DR-fibers (Figure 4.3.d,e,f and g). Moreover, full (under H1) or almost full (under H2) monosynaptic recruitment can be reached before direct motor axonal recruitment begins.

Finally, these results indicated that under H1, the motoneuronal recruitment is well predicted by the proportions of recruited Ia-fibers (Figure 4.3.c and d) while under H2, it is well predicted by the absolute number of recruited Ia-fibers (Figure 4.3.e and f).

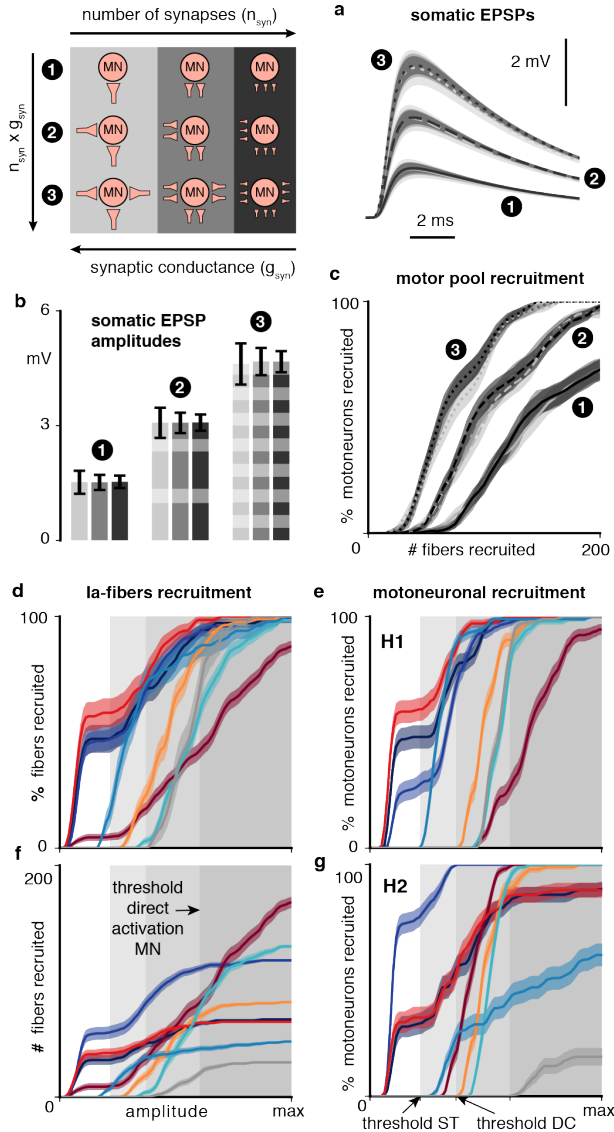


Figure 4.3 Computational analysis of the Ia-mediated recruitment of motoneurons. **a** Time course of the somatic excitatory post-synaptic potential (EPSP) induced in a motoneuron model by various populations of synapses, for different population sizes n_{syn} and synaptic conductances g_{syn} . Lines (solid, dashed and dotted) and filled areas represent the mean and standard deviation of the EPSPs obtained with 100 random synapse populations for each condition (9 conditions in total, see legend and Section 4.2.4). **b** Maximal amplitudes of the EPSPs of **a**. **c** Recruitment of a motor nucleus as a function of the number of simultaneously activated fibers innervating this motor nucleus, for different connectivity ratios and synaptic conductances. Higher connectivity ratios are indicated by higher numbers of synapses in the legend (see Section 4.2.4). **d** Recruitment of Ia-fibers of specific muscles following electrical stimulation from a lateral contact at the C6 spinal level (Figure 4.2.a). **e** Monosynaptic recruitment of motoneurons resulting from the Ia-fiber recruitment shown in **d** using muscle-specific synaptic conductances (see Table 4.3). **f** Same Ia-fiber recruitment as shown in **d** but represented in absolute numbers of recruited fibers. **g** Same as **e** but using a uniform synaptic conductance of 7.625 pS. Recruitment curves: curves are made of 80 data points (except for **c**, 40 data points) consisting of the mean and standard deviation of the recruitment computed across 10 000 bootstrapped populations (see Section 4.2.4). Lines and filled areas represent the moving average over 3 consecutive data points.

Table 4.3 Minimum synaptic conductances enabling the Ia-mediated recruitment of eight macaque monkey upper-limb muscles. See Section 4.2.4.

Muscle	Ia-fiber headcount	Mean number of synapses per motoneuron	Synaptic conductance [pS]	Total conductance per motoneuron [pS]
Deltoid	68	578	9.625	5560
Biceps	119	1036	5.0	5180
Triceps	193	1681	3.375	5675
Extensor Digitorum Communis	82	699	7.625	5330
Extensor Carpi Radialis	65	555	10.5	5830
Flexor Digitorum Superficialis	132	1157	5.75	6650
Flexor Carpi Radialis	48	408	15.375	6275
Abductor Pollicis Brevis	30	250	28.5	7125

4.2.4 Material and methods

Volume conductor model of the cervical spinal cord

Geometry Dimensions of the cervical segments were measured from $n = 2$ preserved spinal cords during dissections performed at the University of Fribourg, Switzerland. Preserved vertebral columns were cleared from connective tissue and the spinous processes removed. The dura mater was cut longitudinally and retracted laterally to expose the spinal cord with care to avoid damaging the spinal roots. Spinal roots were labeled according to the vertebral level at which they exited the spine and spinal segments were delimited as portions of the spinal cord extending from the caudal-most rootlet of one root to the caudal-most rootlet of the root directly rostral to it (Figure 4.1).

The segments' rostro-caudal lengths and coronal widths (at mid-segment-height) were measured independently by 3 experimenters and the average values were retained. I reconstructed cross-sectional contours of the gray matter (GM) and white matter (WM) from a spinal cord atlas [111] and scaled them using the previous measurements. I formed tridimensional volumes interpolating these cross-sectional contours using the free open-source software FreeCAD (<https://www.freecadweb.org/>).

We used OsiriX Lite (Pixmeo SARL) to reconstruct a tridimensional volume representing the cervical vertebrae obtained from CT-scan images (see imaging section for details). To do so, we first processed the acquired images to correct for the bending of the animal neck during the CT-scan acquisitions using custom Matlab routines (Matlab, The Mathworks, Inc.). I then used the free open-source software Blender (Blender Foundation) to split the reconstructed volume into individual vertebrae, and the free open-source software MeshLab (Visual Computing Laboratory) to smooth these vertebrae. In this process, their relative positions were preserved.

The GM and WM were positioned with respect to the vertebrae to be in the center of the vertebral canal and such that the C6 spinal root was perpendicular to the rostro-caudal axis of the spine. The roots were represented after the algorithms presented in Section 3.2 and after extraction of the coordinates of the intervertebral foramina from the reconstructed vertebrae.

To build the volumes representing the dural sac, dura mater and epidural tissue, I extracted the vertebrae inner contours which I smoothed and symmetrized using custom Matlab routines. I then scaled them to match the coronal and sagittal widths respectively of the dural sac, dura mater and epidural tissue (determined according to the local spinal cord dimensions), and interpolated them using FreeCAD similarly to the GM and WM. The dura mater thickness was set to 0.15 mm [112]. The dimensions chosen for the dural sac were such that both the dural sac and dura mater were completely enclosed in

the vertebral canal and did not overlap with the vertebrae. The epidural electrode array was represented by metallic active contacts and a large tridimensional strip embedding the contacts (the paddle) in contact with the dura. The dimensions and layout of this array were similar to the design-1 electrode array presented in Section 4.3.1. It displayed two parallel columns of 5 active contacts, one along the midline of the spinal cord, and one shifted by ~ 3 mm on the left side. By design, each row of active contacts was approximately at the rostro-caudal level of one spinal segment among C5 to T1. The active surface of the contacts had a geometric area of $1.0 \times 0.5 \text{ mm}^2$.

Finally, a large cylinder representing the tissues surrounding the spine wrapped all the previous volumes and allowed to apply boundary conditions on its surface $\partial\Omega$.

Physics Each represented tissue was assigned with an electrical conductivity tensor. I used values previously used in literature [113] for the GM, WM and spinal roots, CSF, epidural tissue, electrode contacts, bone and surrounding saline bath (wrapping cylinder). I used the Curvilinear Coordinates toolbox of COMSOL (COMSOL, Burlington MA) to generate curvilinear coordinates in the WM and spinal roots and orient their anisotropic conductivity tensor. Specifically, I used the diffusion method with the inlet set on the top surface of the WM, the outlet set on the surfaces at the tip of each root and the bottom surface of the WM, and the wall set on the remaining lateral surfaces. Isotropic conductivities of $3 \times 10^{-2} \text{ S m}^{-1}$ [90] and 10^{-13} S m (typical conductivity for silicone rubbers) were respectively assigned to the dura mater and the electrode paddle. The capacitive and inductive effects of the materials were neglected, and the quasi-static approximation was employed (see Section 2.1.5).

I modeled the delivery of a unitary electric current through the active surface S of a contact by imposing a Neumann condition on S with current density $j_s = 1$ (see Section 2.2.2). The resulting potential distributions (expressed in volts) were then divided by A_S (the area of S) and by 10^3 , and by considering that they were expressed in millivolts instead of volts, they thus corresponded to a total injected current of $1 \mu\text{A}$. I assigned a zero-flux condition at the border, and I inserted a ground point in the ventral region of the wrapping cylinder, playing the role of a virtual return electrode placed there.

The Finite Element Method was employed to compute an approximation for the electric potential V . To this end, the geometry was discretized into a tridimensional mesh of approximately 10 million tetrahedral elements which was denser where high electric potential gradients were expected (near the electrode contacts). The equations' linearity allowed to estimate the electric potential distributions resulting from arbitrary amounts of injected current as scaled versions of the corresponding unitary distributions.

Neurophysical models of motoneurons and nerve fibers

The neurophysical models of motoneurons and nerve fibers were implemented in Python 3.7.4 (The Python Software Foundation), using NEURON v7.5 [114] to solve the membrane potential dynamics. Computer code is available at https://bitbucket.org/ngreiner/biophy_smc_ees/src/master/.

Motoneurons (MNs) MNs were modeled with a multi-compartmental soma, a realistic dendritic tree, an explicit axon initial segment, and a myelinated axon.

Dendritic trees were derived from digital reconstructions of cat spinal MNs established by Cullheim and colleagues [80] freely available from the online open-access library NeuroMorpho.org (cell references NMO_00604 to NMO_00609). These specify the geometry of dendritic trees as binary trees of frusta (tapered cylinders) originating at the soma. The axon initial segments comprised 3 linearly-connected identical cylindrical compartments [79]. These were prolonged by a myelinated axon compartmentalized according to the MRG model specifications [77]. The somata were modeled with multiple interconnected frusta following the developments of [79]. For a given MN, the soma included one frustum for each dendrite stem, and one for the axon initial segment. The dimensions of the frusta were adjusted to preserve the total area of the soma, imposed by the MN diameter. The MN diameters were sampled uniformly in the range [44 μm , 71 μm] [115]. Lengths and diameters of their dendritic compartments were linearly scaled accordingly. Axon diameters were linearly scaled to fall in the range [10 μm , 18 μm]. This last range was an arbitrary estimation for the class A α fibers in monkeys, which I assumed to be intermediate between that of humans [6] and that of rats [116]. The dimensions of axon and initial segment compartments were derived from the axon diameters using piecewise linear interpolants established from the data of Table 1 of [77] and Table 1 of [79].

The somata centers of MNs were uniformly distributed in the ventro-lateral quarter of the GM ventral horn of their host segments. Their dendritic trees, selected uniformly at random among the 6 available templates, were rotated (at random) around their somata centers and partially verticalized to ensure they stayed in the GM or exited it only by short extents. Motor axon trajectories were generated as cubic splines running through the appropriate ventral spinal roots. They kept fixed relative positions along their paths in the spinal roots, reflecting the fact that nerve fibers do not jump from side to sides in nerve bundles.

The neurophysical properties of MN compartments were the same as in [79]. In addition, the FLUT compartments of the motor axons comprised a K⁺ conductance as in [78] (see Section 2.3.1).

Motoneuron headcounts and their rostro-caudal distributions for specific motor nuclei

were extracted from [96]. For the deltoid (data unavailable) I used the same distribution as for the biceps, following observations made in humans [97].

Group-Ia fibers, dorsal root proprioceptive A α -fibers The geometry of group-Ia fibers was as described in Section 3.3.2.

Each branch was compartmentalized according to the MRG model specifications [77]. The last node of Ranvier of the dorsal root branch was connected by its extremity to the extremities of the initial nodes of the ascending and descending branches. The initial nodes of the collateral branches were connected to the center of their branching node on the dorsal column branches.

The diameters of the dorsal root branches were distributed log-normally with mean $\mu = 14\mu\text{m}$ and standard deviation $\sigma = 3\mu\text{m}$. The diameters of the ascending and descending branches were derived by weighing the dorsal root branch diameter by $\sqrt{4/5}$ and $\sqrt{1/5}$ respectively. These factors ensured that ascending branches had diameters twice as large as descending branches [11], and that the total cross-sectional area was preserved upon bifurcation. The diameters of the collaterals were log-normally distributed with mean $\mu = 2.5\mu\text{m}$ and standard deviation $\sigma = 1\mu\text{m}$ [14].

The dimensions of the compartments of the fiber branches were derived from the branch diameters using piecewise linear interpolants established from the data of Table 1 of [77]. The neurophysical properties of Ia-fiber compartments were the same as reported in [77]. In addition, the FLUT compartments contained a fast potassium channel as described in [79] which was adjusted to a resting potential of -80mV instead of -70mV , as was the case of the other compartments.

Ia-fiber headcounts of the monkey upper-limb muscles were derived from [108]. First, the spindle headcount sp_i^{mon} of muscle M_i was derived from the spindle headcount sp_i^{hum} of the homologous human muscle as $\text{sp}_i^{\text{mon}} = \text{sp}_i^{\text{hum}} \times (m^{\text{mon}}/m^{\text{hum}})^{1/3}$ where m^{mon} and m^{hum} are typical masses of monkey specimens and human individuals respectively. Ia-fiber headcounts were obtained by assuming a 1:1 ratio between Ia-fibers and muscle spindles [6].

Their distribution in the spinal roots was assumed to be identical to that of their homonymous MNs, as discussed in Section 3.3.2. The resulting distributions, assuming $m^{\text{mon}} = 3.5\text{kg}$ and $m^{\text{hum}} = 70\text{kg}$, are reported in Table 4.2.

Dorsal root proprioceptive A β -fibers Class A β dorsal root proprioceptive fibers were modeled identically to A α -DR-fibers, but their diameters were log-normally distributed with mean $\mu = 9\mu\text{m}$ and standard deviation $\sigma = 2\mu\text{m}$.

Dorsal columns fibers, spinocerebellar tract fibers, corticospinal tract fibers

These fibers were modeled similarly to DR-A β -fibers but they didn't possess a dorsal root branch. They possessed a rostral-caudal branch running in the dorsal columns, spinocerebellar tract and corticospinal tract respectively. They also possessed a series of collateral branches. The dorsal branches of the dorsal column fibers were restricted to the outermost layer of the dorsal columns, where likelihood of recruitment is highest [51]. Corticospinal tract fibers were meant to represent the large-diameter axons directly connecting to spinal motoneurons and originating from large Layer V cells in the primary motor cortex. Smaller diameter fibers were not represented. Spinocerebellar tract fibers represented A β sensory fibers originating from caudal spinal segments.

Extracellular stimulation 200 μ s-long square pulses of extracellular stimulation were modeled by transiently driving the extracellular batteries of NEURON's extracellular mechanism to the voltage appropriate for each modeled compartment. The rise and fall of the voltage transients were linear, lasting 2 μ s.

Synapses Synapses contacting MNs were modeled as transient conductances inserted in the membrane of dendritic compartments. The temporal profile of these transients was described by the same function for every synapse, namely $\alpha(t) = (t - t_{\text{onset}})_+ \cdot \exp\left(-(t - t_{\text{onset}})/\tau\right)$ where t_{onset} is the time onset of the transient (synapse-dependent), τ is the time-to-peak of the transient (synapse-independent), t denotes the running time of the simulation, and $(t - t_{\text{onset}})_+$ is null if $t < t_{\text{onset}}$ and is equal to $t - t_{\text{onset}}$ otherwise. τ was set equal to 0.2 ms [81].

Synapses were distributed on the dendritic trees of the contacted MNs using the electrotonic-distance-based distribution reported in Figure 16 of [11].

The synaptic currents were implemented as $i_{\text{syn}}(t) = g_{\text{syn}} \cdot \alpha(t) \cdot V(t)$ where g_{syn} is the peak synaptic conductance and $V(t)$ denotes the membrane potential at the synapse.

For synapses supplied by Ia-fibers, the delay between electrical stimulation and the onset of the conductance transient was the sum of the action potential propagation delay through the Ia-fiber and a log-normally distributed stochastic jitter with mean 1 ms and standard deviation 0.5 ms accounting for synaptic transmission. Otherwise, the delay reduced to the previous stochastic jitter.

Somatic EPSP analysis I used a motoneuron model with somatic diameter of 55 μ m, 10 dendrites, and a total membrane area of $\sim 475\,000\,\mu\text{m}^2$. I performed $3 \times 3 \times 100$ simulations where each series of 100 simulations was characterized by a $(n_{\text{syn}}, g_{\text{syn}})$ pair of values. These series were grouped by 3, where each group was characterized by a constant $n_{\text{syn}} \times g_{\text{syn}}$ product.

Group 1: $n_{\text{syn}} \times g_{\text{syn}} = 500 \text{ pS}$

($n_{\text{syn}} = 50, g_{\text{syn}} = 10 \text{ pS}$ / $n_{\text{syn}} = 100, g_{\text{syn}} = 5 \text{ pS}$ / $n_{\text{syn}} = 150, g_{\text{syn}} = 3.3 \text{ pS}$)

Group 2: $n_{\text{syn}} \times g_{\text{syn}} = 1000 \text{ pS}$

($n_{\text{syn}} = 100, g_{\text{syn}} = 10 \text{ pS}$ / $n_{\text{syn}} = 200, g_{\text{syn}} = 5 \text{ pS}$ / $n_{\text{syn}} = 300, g_{\text{syn}} = 3.3 \text{ pS}$)

Group 3: $n_{\text{syn}} \times g_{\text{syn}} = 1500 \text{ pS}$

($n_{\text{syn}} = 150, g_{\text{syn}} = 10 \text{ pS}$ / $n_{\text{syn}} = 300, g_{\text{syn}} = 5 \text{ pS}$ / $n_{\text{syn}} = 450, g_{\text{syn}} = 3.3 \text{ pS}$)

Ia-mediated monosynaptic recruitment of motoneurons I assessed the recruitment of a population of 100 motoneurons following the monosynaptic excitation provided by increasing numbers of Ia-fibers (fixed increment of 5 fibers). I assumed a fixed contact abundance of 9.6 synapses per Ia-motoneuron pair, and used 3×3 different ($r_{\text{connec}}, g_{\text{syn}}$) combinations. They were respectively characterized by a product $r_{\text{connec}} \times g_{\text{syn}}$ of:

- 3 pS ($r_{\text{connec}}=0.3, g_{\text{syn}}=10 \text{ pS}$ / $r_{\text{connec}}=0.6, g_{\text{syn}}=5 \text{ pS}$ / $r_{\text{connec}}=0.9, g_{\text{syn}}=3.3 \text{ pS}$);
- 5 pS ($r_{\text{connec}}=0.3, g_{\text{syn}}=15 \text{ pS}$ / $r_{\text{connec}}=0.6, g_{\text{syn}}=7.5 \text{ pS}$ / $r_{\text{connec}}=0.9, g_{\text{syn}}=5 \text{ pS}$);
- 6.75 pS ($r_{\text{connec}}=0.3, g_{\text{syn}}=22.5 \text{ pS}$ / $r_{\text{connec}}=0.6, g_{\text{syn}}=12.25 \text{ pS}$ / $r_{\text{connec}}=0.9, g_{\text{syn}}=7.5 \text{ pS}$).

The actual number of synapses of a given Ia-motoneuron pair was drawn from a Poisson distribution, and the motoneurons contacted by a given Ia-fiber were drawn uniformly at random.

To evaluate the muscle-specific g_{syn} values of Table 4.3, I assumed a connectivity ratio of 0.9 [14], a contact abundance of 9.6 [11], and I set N^{Iaf} appropriately for each muscle (see Section 4.2.4). The g_{syn} values were determined via a binary search with a resolution of 0.125 pS. The uniform g_{syn} value used under H2 was set to 7.625 pS, which is the value estimated for the extensor digitorum communis muscle, possessing an average number of Ia-fibers among the eight studied muscles.

Recruitment curves

Figure 4.2. Populations of $N = 50$ nerve fibers or motoneurons were simulated for stimulation with multiple electrode contacts and stimulus amplitudes. A nerve fiber or motoneuron was considered recruited when an action potential was elicited and traveled along its entire length.

The recruitment level (between 0 and 1) of a population of nerve fibers or motoneurons X at stimulation amplitude amp with either a lateral or medial electrode contact located at the rostro-caudal level of segment S was estimated as:

$$R_X(amp, E_S^{\text{lat/med}}) = \frac{N_{\text{recr}}}{N}$$

where N_{recr} denotes the number of recruited nerve fibers or motoneurons of population X . Threshold and saturation amplitudes of a population were defined as inducing recruitments respectively of 10% and 90% of the population (Figure 4.2.b and f). Standard deviations were obtained using a bootstrapping approach (see Section 4.2.4).

Figure 4.3. Same as above but populations of $N = 100$ motoneurons were simulated for each muscle, and the sizes of the Ia-fiber populations were muscle-specific (see Table 4.2).

Selectivity indices The selectivity indices of Figure 4.2.h were computed as:

$$SI_S^{\text{lat/med}} = \max_{\text{amp}} \left\{ R_S(\text{amp}, E_S^{\text{lat/med}}) - \frac{1}{N_{\text{seg}} - 1} \sum_{S' \neq S} R_{S'}(\text{amp}, E_S^{\text{lat/med}}) \right\}$$

where $R_S(\text{amp}, E_S^{\text{lat/med}})$ denotes the recruitment level (between 0 and 1) of the population of Ia-fibers of segment S at stimulation amplitude amp for either the lateral or medial electrode contact located at the rostro-caudal level of segment S .

Bootstrapping For each simulated recruitment curve, the initial population of N simulated nerve fibers or motoneurons was re-sampled with replacement to obtain $K = 10\,000$ fictive populations of N individuals. The means and standard deviations across these fictive populations were used to construct the recruitment curves of Figure 4.2 and Figure 4.3, the threshold and saturation amplitudes and the selectivity indices of Figure 4.2, and the comparisons between the two sets of simulated recruitment curves of Figure 4.3.h.

4.3 EES of the macaque monkey cervical spinal cord: experimental analysis

The theoretical results of Section 4.2 indicated that:

1. the direct recruitment of motor axons with EES of the macaque monkey cervical spinal cord should require much higher stimulation amplitudes compared to dorsal sensory afferents;
2. laterally-positioned epidural electrodes should enable to recruit the large myelinated fibers of a single root without recruiting fibers of other tracts or roots but marginally;
3. this selectivity is likely to be lost with medially-positioned electrodes, which primarily recruit dorsal column fibers;
4. a pure Ia-mediated trans-synaptic recruitment of motoneurons induced by EES is plausible.

Assuming that group-Ia fibers form direct excitatory synaptic contacts predominantly with homonymous motoneurons and that they are distributed in the dorsal roots similarly to their homonymous motoneurons in the spinal segments (see Sections 3.3.2 and 4.3.5), we hypothesized that targeting the stimulation towards individual roots should allow to selectively recruit the motoneurons located in the corresponding segments.

As a corollary, since dorsal column fibers are likely to convey neural inputs to widespread motor nuclei, we expected medial stimulation to induce muscular recruitment profiles which would correlate less well with the rostro-caudal distribution of motor nuclei in the spinal cord.

4.3.1 Design of tailored cervical epidural electrode arrays

To obtain experimental evidence supporting these hypotheses, we designed two types of multi-electrode spinal implants that were tailored to the dimensions of the spinal cord of macaque monkeys.

The first design (design-1) allowed the delivery of electrical stimuli from both medial and lateral locations of the epidural space. It comprised 2 columns of 5 stimulation active sites, one of which was intended to be positioned along the midline of the spinal cord, facing the dorsal columns, and the other to be laterally-positioned, with one active site facing each of the C5 to T1 spinal roots (Figure 4.4). The second design (design-2) comprised a single, laterally-positioned column of seven stimulation contacts, and one medial stimulation contact spanning three active sites connected together (Figure 4.5).

Spinal implants of the two types were manufactured by the Laboratory for Soft Bioelectronics Interface (LSBI), Ecole Polytechnique Fédérale de Lausanne, Geneva, Switzerland.

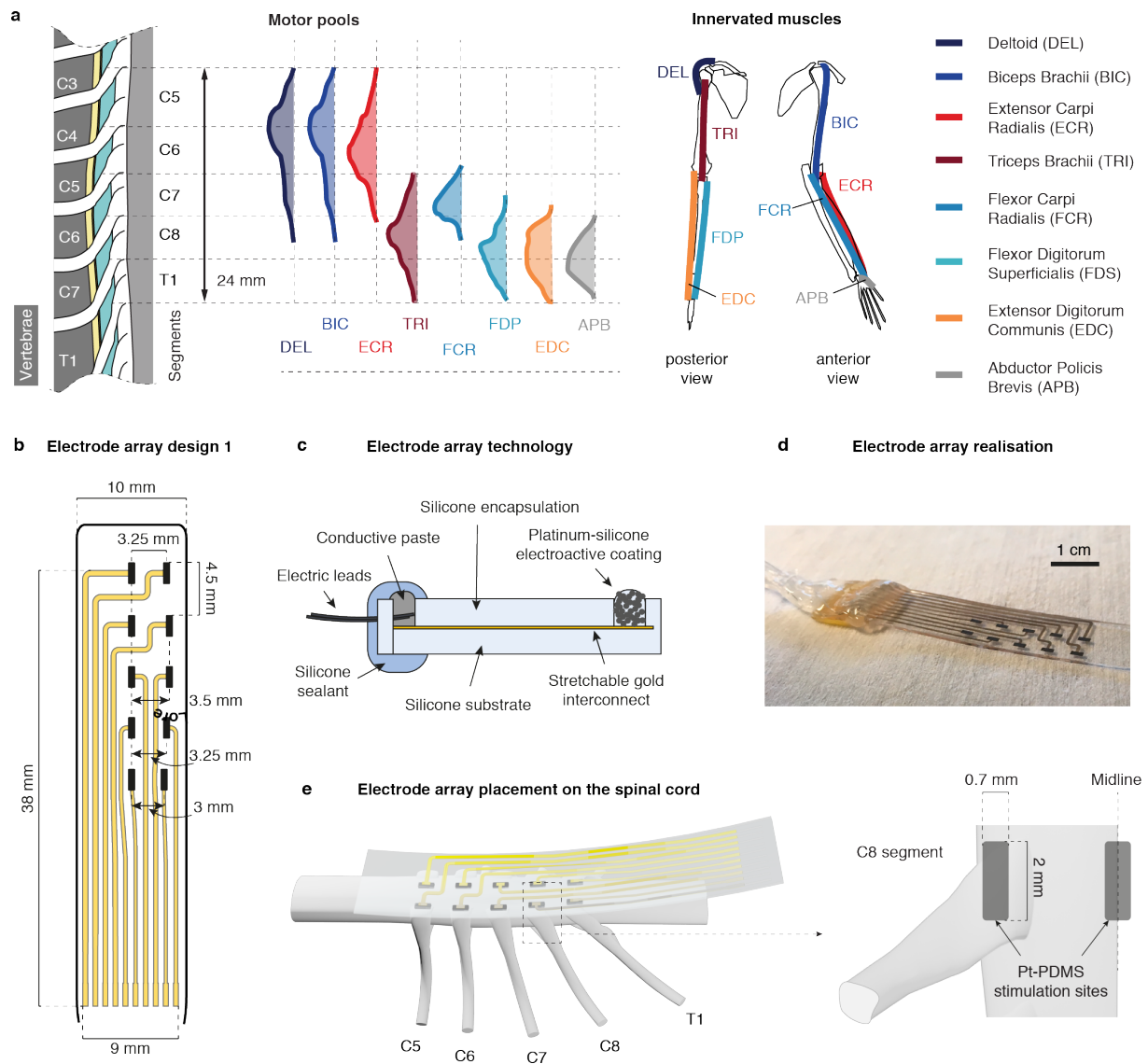
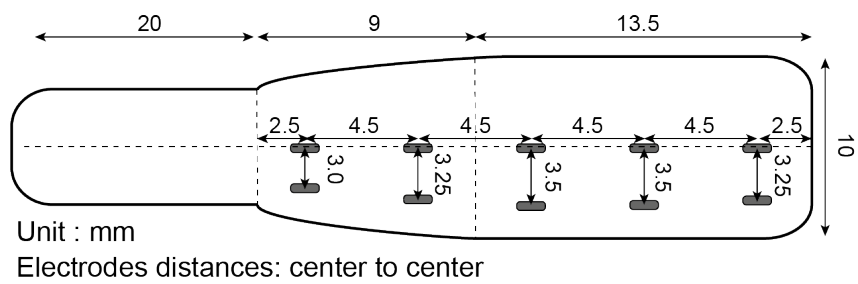


Figure 4.4 Organization of the monkey cervical spinal cord and soft electrode array tailored to the epidural space of the cervical spinal cord. **a** Distribution of the motor pools of eight upper-limb muscles in the monkey cervical spinal cord [96] and skeletal positions of these upper-limb muscles. **b** Custom layout of an electrode array with 5 lateral and 5 medial electrode contacts (design-1) tailored to the monkey cervical spinal cord. **c** Cross-section diagram of a soft electrode array with the components labeled. **d** Photograph of a fabricated soft electrode array. Scale bar: 1 cm. **e** Placement of the electrode array relative to the cervical spinal cord. Lateral electrode contacts were made to face individual dorsal roots while medial contacts were made to be along the dorsal columns midline. [Credits: the motor nuclei of **a** were sketched by Beatrice BARRA. The arm skeletons of **a** were sketched by Pierre KIBLEUR. **b** and **c** were sketched by Giuseppe SCHIAVONE. The picture in **d** was provided by Giuseppe SCHIAVONE. **e** was co-realized with Giuseppe SCHIAVONE.]

Cervical array design-1



Cervical array design-2

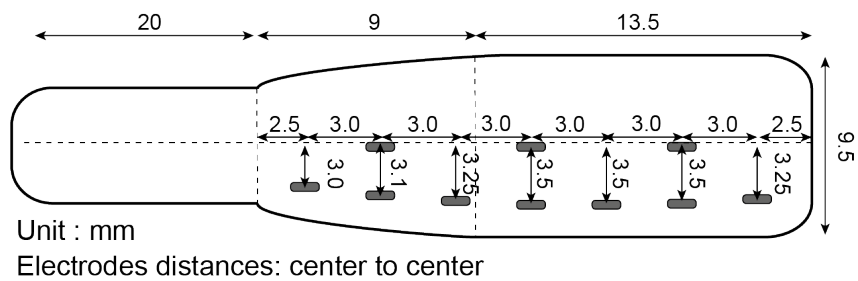


Figure 4.5 Layouts of the design-1 and design-2 epidural electrode arrays. *[Credits: the layouts and sketches were co-invented and co-realized with Beatrice BARRA.]*

4.3.2 Recruitment of upper-limb motoneurons with cervical EES

We then proceeded to conduct electrophysiological experiments in $n = 5$ anesthetized monkeys (see Section 4.3.6). Two animals were implanted with the design-1 implant, and three with the design-2 implant.

Laterally-positioned electrodes

In a first series of electrophysiological tests, we delivered single pulses of EES at increasing amplitudes from each lateral contact of the electrode array. In parallel we recorded electromyographic activity from the same eight muscles of the left arm and hand that were studied in Section 4.2 (see Section 4.3.6). From the EMG recordings, we formed *muscular recruitment curves*, whereby an indicator of the intensity of the recorded compound muscle action potentials (CMAPs) is plotted against the stimulus intensity (see Section 4.3.6).

Muscular recruitment curves from monkey Mk-Li (Figure 4.6.b) indicated that rostral stimulation (approximately at the C5 and C6 spinal levels) induced activation predominantly of the deltoid, biceps, and extensor carpi radialis muscles (Figure 4.6.b, top panel), all of which are innervated in the C5 and C6 segments (see Figure 4.4.a). Caudal stimulation (C8-T1 level) mainly recruited the extensor digitorum communis, flexor digitorum profundus, flexor carpi radialis and abductor pollicis brevis muscles (Figure 4.6.b, bottom panel), innervated in the C8 and T1 segments (except for the flexor carpi radialis, mostly innervated in C7). Finally, stimulating from an intermediary rostro-caudal level (around C7 level) yielded a recruitment almost purely restricted to the triceps muscle (Figure 4.6.b, middle panel), innervated from C7 to T1. Importantly, this rostro-caudal recruitment pattern was obtained with every animal involved in the study, as illustrated by the mean muscular activation levels of Figure 4.6.c and the maximal selectivity indexes of Figure 4.6.d (see Section 4.3.6).

Medially-positioned electrodes

We then performed the same analysis with the medially-positioned electrodes in the two animals that were implanted with the design-1 electrode array.

Compared to lateral stimulation, we observed that medial stimulation induced a recruitment pattern strongly biased towards the caudally-innervated muscles (Figure 4.7.a and e). In particular, medial stimulation failed to recruit the deltoid and biceps muscles altogether. Moreover, when computing the correlation between muscular recruitment profiles and rostro-caudal distributions of motor nuclei (Figure 4.7.d, and see Section 4.3.6), we observed that lateral stimulation outperformed medial stimulation for all muscles except for the flexor carpi radialis. The maximum level of muscle recruitment (Figure 4.7.e) and

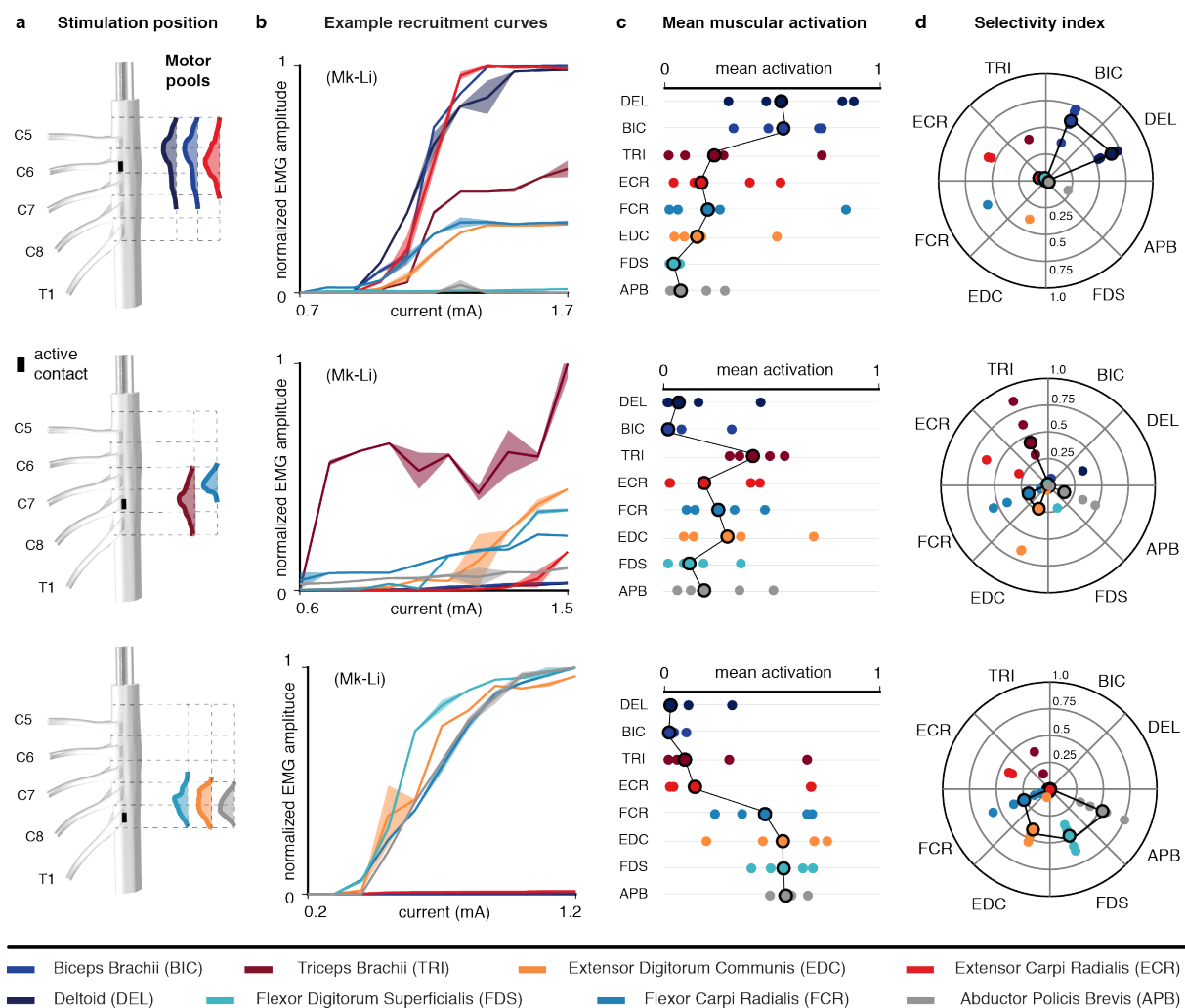


Figure 4.6 Muscular recruitment induced by laterally-positioned cervical epidural electrodes in macaque monkeys. **a** Approximate positions of the electrode contacts used to obtain the results in **b**, **c** and **d** and underlying motoneuronal distributions. Electrode contacts are magnified for better visualization (scale factor = 2). **b** Examples of muscular recruitment curves observed in monkey Mk-Li using one rostral, one intermediate, and one caudal active contacts. Curves are made of 11 data points consisting of the mean and standard deviation of the normalized peak-to-peak EMG amplitude across 4 responses induced at the same stimulation current. **c** Mean muscular activations observed in 5 monkeys. One rostral, one intermediate and one caudal active contacts were chosen for each animal, and the observed mean muscular activations (see Section 4.3.6) reported as individual bullets (for Mk-Li, the same active contacts as in **b** were used). **d** Maximal selectivity indexes (see Section 4.3.6) obtained for each muscle and each animal with the same active contacts as in **c**. *Circled bullets*: medians across the five animals.

the maximum muscle recruitment specificity (Figure 4.7.f) were also higher with lateral stimulation compared to medial stimulation.

Furthermore, we measured the latency of the responses evoked in caudally innervated muscles following stimulation from rostral or caudal electrode contacts. We found that rostral stimulation induced responses with latencies that were consistently higher (Figure 4.7.f and g). Specifically, the observed differences ranged from 0.2 ms to 1.1 ms (25th and 75th percentiles respectively) with a median of 0.3 ms. Considering the length separating the rostral and caudal electrodes used (approximately 2.5 cm), these additional delays corresponded to action potentials propagation velocities ranging from 23 m s^{-1} to 122 m s^{-1} (25th and 75th percentiles respectively) with a median of 71 m s^{-1} , which happen to be compatible with diameter-class A β -A α nerve fibers.

4.3.3 Electrophysiological assessment of the nature of the motoneuronal recruitment

We conducted a second series of electrophysiological tests, with the aim to gain further evidence of the trans-synaptic nature of the motoneuronal recruitment induced by EES. These were based on the well-established experimental finding that repetitive stimulation of primary sensory afferents produces characteristic patterns of muscular responses, such as frequency-dependent suppression [35, 42] or alternation of different reflex responses [117].

We thus delivered supra-threshold stimuli from various electrode contacts at frequencies of 10, 20, 50 and 100 Hz in $n = 4$ monkeys. As expected, muscular responses were modulated by repetitive stimulation. We observed various modulation modalities of the recorded CMAPs as consecutive stimuli were delivered:

1. attenuation of the CMAPs' amplitude (Figure 4.8.a);
2. quasi-suppression of the CMAPs (Figure 4.8.b);
3. alternation, often irregular, of two or three stereotypical CMAP waveforms (Figure 4.8.c);
4. erratic adaptation to the pulse trains, wherein the first 5 to 10 CMAP waveforms didn't comply to the pattern respected by the subsequent CMAPs of the train (Figure 4.8.d).

Overall these behaviors were more likely to happen at high frequencies than at low frequencies (Figure 4.8.f). Absence of frequency-dependent modulation such as reported in Figure 4.8.e was observed only rarely.

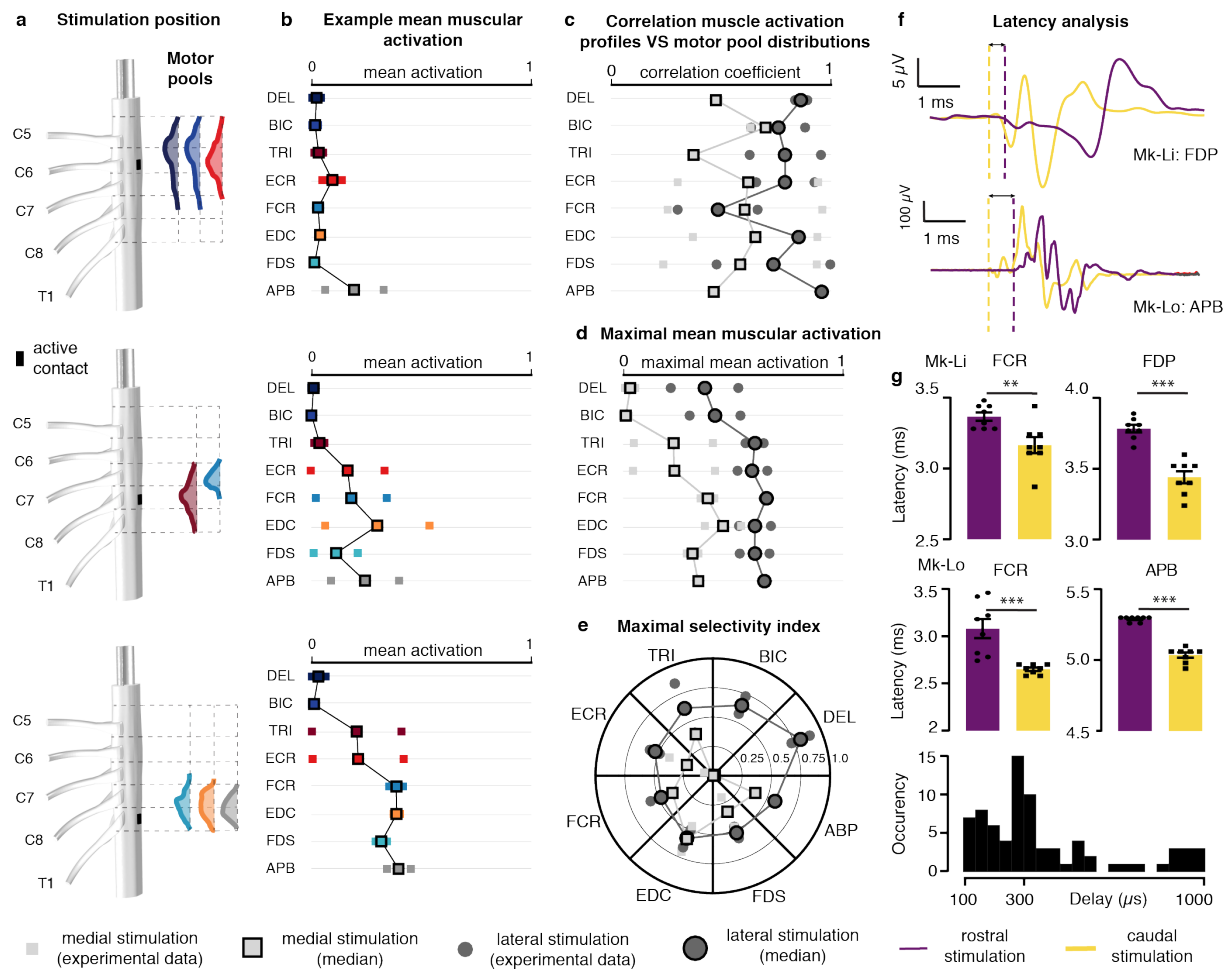


Figure 4.7 Caption on next page.

Figure 4.7 Muscular recruitment induced by medially-positioned cervical epidural electrodes in macaque monkeys and comparison with lateral electrodes. **a** Approximate positions of the medial electrode contacts used to obtain the results in **b** and underlying motoneuronal distributions. Electrode contacts are magnified for better visualization (scale factor = 2). **b** Mean muscular activations obtained with the medial electrode contacts at the same rostro-caudal levels than the lateral contacts of Figure 4.6.c for the two monkeys implanted with the design-1 array (see Section 4.3.6). **c** Correlation coefficients between muscular recruitment profiles and motor nuclei distributions (see Section 4.3.6) for lateral and medial electrode contacts. **d** Maximal mean muscular activations achieved with lateral or with medial electrode contacts. **e** Maximal selectivity indexes (see Section 4.3.6) achieved with lateral or medial electrode contacts. **f** Examples of muscular response latencies following stimulation from rostral medial or caudal medial electrode contacts. *Top*: muscular responses recorded in the flexor digitorum profundis of monkey Mk-Li. *Bottom*: muscular responses recorded in the abductor pollicis brevis of monkey Mk-Lo. Onsets of responses are indicated by the vertical dashed lines. **g** Statistical analysis of the differences in onset latencies between rostrally-induced responses and caudally-induced responses. For each muscle, eight responses induced at amplitudes near motor threshold with one rostral (purple) and one caudal (yellow) active sites were retained. *Statistics*: ** $p < 0.01$; *** $p < 0.001$. *Bottom histogram*: distribution of the delay of rostrally-induced responses compared to caudally-induced responses. [*Credits: **f** and **g** were sketched by Nicholas JAMES.*]

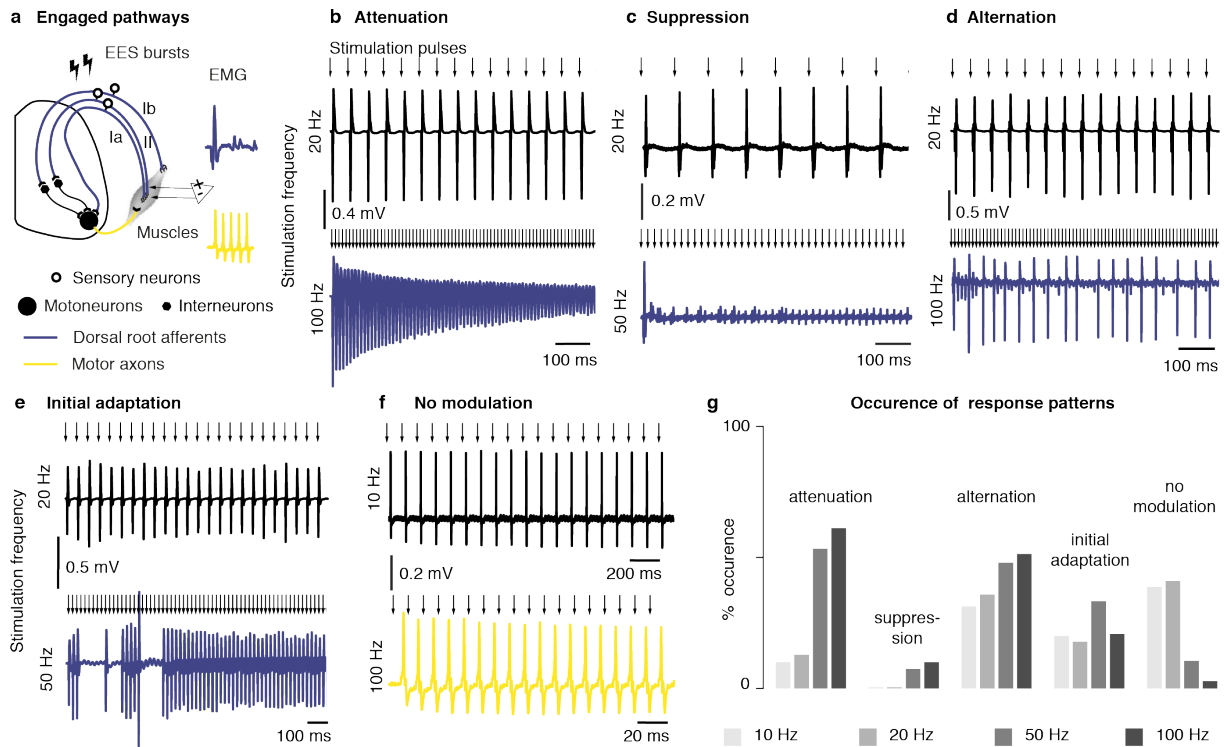


Figure 4.8 Patterns of muscular responses elicited during high-frequency stimulation of the cervical spinal cord of monkeys. **a** Diagram of the presumed engaged pathways during high-frequency stimulation when muscular responses are modulated and unmodulated, respectively. **b, c, d, e** Examples of frequency-dependent modulation of muscular responses. In each panel, the top and bottom EMG traces were recorded in the same muscle and using the same stimulation amplitude (near motor threshold) but different frequencies. **f** Example of absence of frequency-dependent modulation. **g** Frequency of occurrence of muscular response patterns during high-frequency stimulation. All the patterns recorded in all the muscles of the four animals in which high-frequency stimulation was tested were included in the analysis ($n = 80$ patterns at 10 Hz, $n = 39$ patterns at 20 Hz, $n = 75$ patterns at 50 Hz, $n = 72$ patterns at 100 Hz).

4.3.4 Direct comparison between experimental and simulation results

Finally, I sought to investigate whether our experimental data could shed light on the question of the connectivity between Ia-afferents and motoneurons. For this, I devised metrics to compare a representative subset of experimental and simulated recruitment curves (Section 4.3.6). In particular, I sought to assess whether either of the hypotheses H1 or H2 (Section 4.2.3) could better explain the experimental data. Unfortunately, this comparison was not conclusive (Figure 4.9).

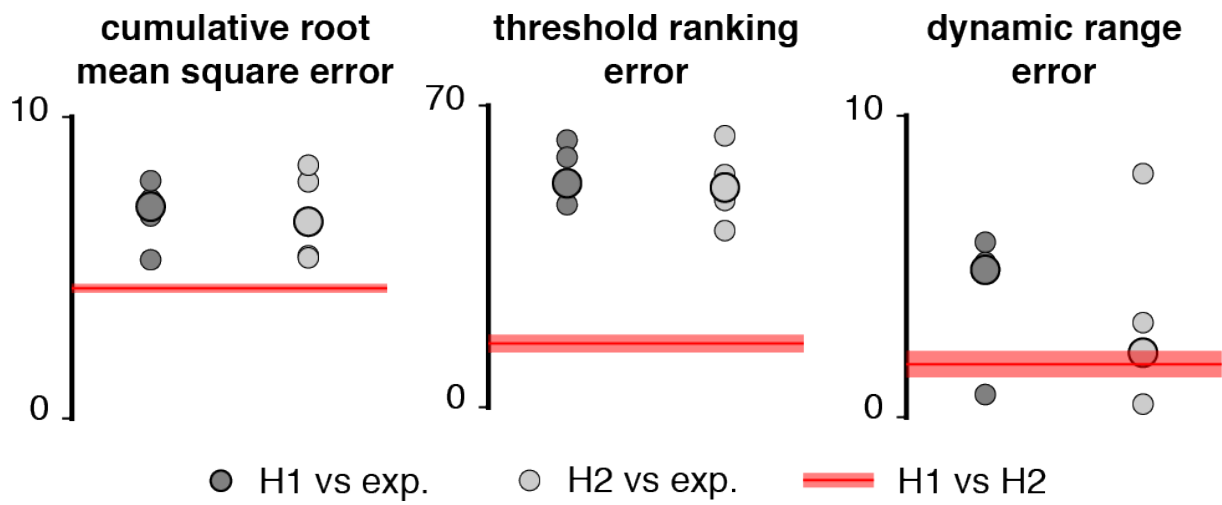


Figure 4.9 Comparison between experimental muscular recruitment curves and simulated motoneuronal recruitment curves with H1 or H2 (see Section 4.3.6). Each bullet represents the comparison score for one animal (5 animals in total). *Large circled bullets*: medians across the 5 animals.

4.3.5 Discussion

Trans-synaptic recruitment of motoneurons

We have found that delivering trains of electrical stimuli at high frequency (10 Hz to 100 Hz) modulated the stimulation-induced muscular responses, suggesting the trans-synaptic nature of the underlying motoneuronal recruitment. However, in the case of attenuation, alternation, or initial adaptation, the fact that a baseline muscular activity was preserved despite the observed modulation prevented us from completely discarding the hypothesis that some direct recruitment of motor axons was involved. Nonetheless, the hypothesis of a marginal (if existent at all) direct motor axon recruitment was in line with the simulation results of Section 4.2. These indeed predicted that this recruitment is unlikely when using dorsal epidural electrodes, notably due to the size of the monkey cervical spinal cord (implying low potential and potential gradients at the level of the ventral roots, Figure 4.2), and they also indicated that a purely Ia-mediated recruitment of motoneurons is plausible at moderately-high stimulation amplitudes (Figure 4.3.e and g). Thus, while we couldn't fully exclude that direct motor axonal recruitment was involved during our electrophysiological experiments, we concluded that our results constituted a strong indicator that the upper-limb motor responses evoked by cervical EES are predominantly of mono-/poly-synaptic origin, corroborating and extending the experimental findings of [35].

Stimulation specificity and lead design

The recruitment profiles of arm and hand muscles induced by lateral contacts correlated well with the rostro-caudal distribution of their motor nuclei in the spinal cord (Figure 4.6 and Figure 4.7.c). This is in accordance with a selective recruitment of individual dorsal roots under the assumptions that:

- Ia-afferents are distributed in the dorsal roots similarly to their homonymous motoneurons in the spinal segments;
- the motoneurons they directly innervate with excitatory synapses are predominantly homonymous [11, 16].

Indeed, in this case, if fibers coming from different roots had been recruited all at once, stimulation *eg* from rostral active sites would not necessarily have induced recruitment of rostrally innervated muscles.

The validity of these two assumptions is not firmly established. For instance, Ia-afferents are known to form connections with heteronymous motoneurons. However, previous works seem to indicate that these are indeed minority [11, 14, 16]. In that case, if Ia-afferents

innervate predominantly homonymous motoneurons, it seems logical that they enter the spinal cord at the location where these motoneurons are located, and the first assumption above is likely to be valid. Still, it is important to point out that the distribution of Ia-afferents in the posterior roots in monkeys and humans remains largely unknown to date.

Stimulation from medial contacts elicited markedly distinct muscular recruitment profiles. These correlated less well with motor nuclei distributions and showed substantially lower levels of muscle recruitment compared to those obtained with lateral contacts Figure 4.7. Moreover, recruitment of caudally innervated muscles induced by rostral contacts occurred with latencies that were significantly higher than those measured when stimulating with caudal contacts. The differences in latency were compatible with propagation delays through $A\beta$ and $A\beta$ fibers between the rostral and caudal sites, which suggested that rostrally-induced responses in caudally innervated muscles may result from the antidromic recruitment of dorsal column projections of caudal sensory afferents. Overall, this corroborated our hypothesis that stimulation from medially-positioned electrode contacts primarily recruit dorsal column fibers, conveying neural inputs to widespread motor nuclei via their rostro-caudal branches, including in spinal segments far remote from the stimulation contacts.

Impact of sensorimotor connectivity on muscle recruitments

The trans-synaptic nature of the motoneuronal recruitment during epidural stimulation implies that the connectivity between sensory afferents and motoneurons is of primary importance for the induced muscle recruitment. However, to date, even for the intensively studied Ia-to-motoneuron pathway [11,12,14,16,81,110,118], the properties characterizing the strength of the connection between Ia-afferents and motoneurons remain unknown for most if not all muscles of the monkey. Yet, this pathway in particular might critically affect the specificity, order and magnitude of the recruitment of muscles during epidural stimulation, as indicated by the simulation results of Section 4.2.3.

Attempting to confront our experimental data to simulation results obtained for different hypotheses for this connectivity did not allow to discriminate between them (Figure 4.9). However, while we simulated the recruitment of motoneurons, the experimental data consisted in normalized EMG peak-to-peak amplitudes, which is only qualitatively related to the total number of recruited motoneurons (Section 1.1.3). In fact, as long as direct experimental measurements readily comparable to simulation results are missing, the lack of precise information on afferent-to-motoneuron connectivity limits the use of computer simulations to quantitatively accurately predict EES-induced muscle recruitment.

Summary and conclusions

In summary, these findings led us to conclude that:

- Cervical epidural stimulation can engage upper-limb muscles consistently and reproducibly across subjects.
- The recruitment of motoneurons induced by EES is likely predominantly trans-synaptic.
- Lateral electrode placement increases the stimulation specificity, but the latter is limited by the macro- and micro-anatomical organizations of the dorsal roots.

Specifically, the wide spatial separations between adjacent dorsal roots at the cervical level (several millimeters), which is consistent across subjects, allows robust selective recruitment of individual roots by using lateral electrodes, but the intermingling of different fiber populations within individual roots may limit the ability to engage specific motor nuclei.

To further increase the stimulation specificity, a possible strategy could be to target individual rootlets, thereby recruiting more restricted populations of sensory fibers. For that, high-density electrode arrays and multipolar stimulation configurations may be required.

4.3.6 Material and methods

Experimental procedures

Animals involved in the study Four adult female and one male *Macaca Fascicularis* monkeys were involved in the study. Animal identification and information are summarized in Table 4.4. All procedures were carried out in accordance to the Guide for Care and Use of Laboratory Animals [119] and the principle of the 3Rs. Protocols were approved by local veterinary authorities of the Canton of Fribourg (authorization numbers reported in Table 4.4) including the ethical assessment by the local (cantonal) Survey Committee on Animal Experimentation and acceptance by the Federal Veterinary Office (BVET, Bern, Switzerland).

Monkeys were housed in collective rooms designed according to European guidelines (45 m³ for maximum five animals). They had free access to water and were not food deprived. Environmental enrichment was provided in the form of food puzzles, toys, tree branches and devices to climb and hide.

Imaging We performed MRI- and CT-scans on all animals involved in the study. All procedures were performed at the Cantonal Hospital of Fribourg, Switzerland. The animals were sedated with a combination of ketamine and medetomidine and transported to the imaging facilities where anatomical T1-weighted and T2-weighted images were acquired with a 3 T General Electric scanner at a resolution of 0.7 mm. CT-scan procedures were analogue to MRI with a spatial resolution of 0.5 mm.

Surgical procedures and electromyography We performed two types of surgical procedures, terminal in $n = 3$ animals, and acute tests under deep anesthesia in $n = 2$ animals.

Table 4.4 Identification information, characteristics, type of procedure performed, and license numbers of the monkeys involved in the study.

Animal ID	Authorization number	Sex	Age	Weight	Procedure
Mk-Ca	2014_42E_FR	Female	11 years	5.8 kg	Terminal
Mk-Li	2017_03_FR	Male	12 years	5.8 kg	Terminal
Mk-Cs	2017_04E_FR	Female	9 years	5.8 kg	Survival
Mk-Lo	2014_42E_FR	Female	9 years	5.8 kg	Terminal
Mk-Sa	2017_04E_FR	Female	7 years	5.8 kg	Survival

Both procedures were performed under full anesthesia induced with midazolam (0.1 mg kg^{-1}) and ketamine (10 mg kg^{-1} , intramuscular injection) and maintained under continuous intravenous infusion of propofol ($5 \text{ ml kg}^{-1} \text{ h}^{-1}$) and fentanyl ($0.2 \text{ ml kg}^{-1} \text{ h}^{-1}$ to $1.7 \text{ ml kg}^{-1} \text{ h}^{-1}$) using standard aseptic techniques. Animals involved in the terminal procedures were injected with pentobarbital (60 mg kg^{-1}) and euthanized at the end of the experiments following the protocols described in the authorizations mentioned in Table 4.4.

During the surgical procedures, the monkeys were implanted with bipolar stainless-steel electrodes to record electromyographic signals (sampling rate = 24 kHz) from the following upper-limb muscles: deltoid (DEL), biceps brachii (BIC), triceps brachii (TRI), flexor carpi radialis (FCR), flexor digitorum superficialis (FDS), extensor carpi radialis (ECR), extensor digitorum communis (EDC), and abductor pollicis brevis (APB). In one monkey (Mk-Ca), the flexor carpi ulnaris (FCU) and extensor carpi ulnaris (ECU) were recorded in place of FCR and ECR respectively. Details on muscle implantation can be found in [54].

Laminectomies were performed at the T1/T2 and C3/C4 junctions to provide access to the cord and allow insertion of the spinal implants. The custom-made spinal implants were inserted into the epidural space and pulled with the help of a custom-made polyamide inserter. Electrophysiological testing was performed intra-operatively to adjust the position of the electrodes. Specifically, we verified that a single pulse of stimulation delivered through a rostro-caudally median electrode induced motor responses in the triceps muscle. Detailed protocols for the implantation and placement of the spinal implant are provided in [54].

Electrophysiology Trains of biphasic square electrical pulses (charge-balanced, cathodic phase first lasting $200 \mu\text{s}$) were delivered at low frequency (0.67 Hz) through a single active site at a time. Within a train, square pulses were grouped by 4 using the same stimulation amplitude, and the amplitude was increased by fixed increments for 11 groups [54]. The first stimulation amplitude was chosen to be the lowest amplitude eliciting a response in any of the recorded muscles, while the last amplitude was chosen by the experimenters upon consensual judgment that some muscle was maximally recruited, either by inspection of the EMG responses or by direct observation of the movements induced in the limbs of the animals.

Additional trains of stimuli were delivered from multiple contacts (at least 2 per animal) at motor threshold stimulation amplitudes and at frequencies ranging from 10 Hz to 100 Hz to test for frequency-dependent modulation of muscular responses [35].

Data Analysis

Muscle recruitment and recruitment curves From the electromyographic recordings of low-frequency stimulation protocols (0.67 Hz), we extracted 50 ms-long snippets of data following each stimulation pulse. For each data snippet, we measured the peak-to-peak amplitude of the recorded signal, P2P(snippet) (or 0 V when the signal was purely noisy). Then, for each animal (A), electrode contact (E), muscle (M) and stimulation amplitude (amp), we computed the mean and standard deviation across the 4 P2P(snippet) values corresponding to the configuration (A, E, M, amp) , respectively noted $P2P_{E,M}^A(amp)$ and $sP2P_{E,M}^A(amp)$. We defined the muscle recruitment $R_{E,M}^A(amp)$ and associated standard deviation $sR_{E,M}^A(amp)$ as:

$$R_{E,M}^A(amp) = \frac{P2P_{E,M}^A(amp)}{\max_{E', amp'} \{P2P_{E',M}^A(amp')\}}$$

$$sR_{E,M}^A(amp) = \frac{sP2P_{E,M}^A(amp)}{\max_{E', amp'} \{P2P_{E',M}^A(amp')\}}$$

and thereby obtained normalized muscular recruitment curves (as represented in Figure 4.6.b).

Mean muscle activation and selectivity index For a given animal (A) and electrode active contact (E), the mean activation of muscle M was estimated as:

$$\overline{R_{E,M}^A} = \frac{1}{N_{\text{amps}}} \sum_{amp \in DR} R_{E,M}^A(amp)$$

where DR denotes the dynamic range of stimulation amplitudes of electrode contact E and was defined as the range from threshold amplitude (defined as inducing a muscular recruitment higher than 10% in at least one muscle) to saturation amplitude (defined either as inducing a muscular recruitment higher than 90% in every muscle, or as the highest amplitude used).

The selectivity index of muscle M was computed as:

$$SI_{E,M}^A = \max_{amp \in DR} \left\{ R_{E,M}^A(amp) - \frac{1}{N_{\text{musc}} - 1} \sum_{M' \neq M} R_{E,M'}^A(amp) \right\}.$$

Correlation between muscular recruitment pattern and motor nucleus rostro-caudal distribution For each animal (A) implanted with the design-1 array ($n = 2$), for each muscle (M), I formed the vector $(\overline{R_{E_1,M}^{A,S}}, \overline{R_{E_2,M}^{A,S}}, \overline{R_{E_3,M}^{A,S}}, \overline{R_{E_4,M}^{A,S}}, \overline{R_{E_5,M}^{A,S}})$ where E_1, E_2, E_3, E_4 and E_5 denote the electrodes at the C5, C6, C7, C8 and T1 levels for each

side (S) either lateral or medial, respectively. I then estimated the correlation between muscular recruitment pattern and motor nucleus rostro-caudal distribution as:

$$CC_M^{A,S} = \frac{\left(\overline{R_{E_1,M}^{A,S}}, \overline{R_{E_2,M}^{A,S}}, \overline{R_{E_3,M}^{A,S}}, \overline{R_{E_4,M}^{A,S}}, \overline{R_{E_5,M}^{A,S}} \right) \cdot \left(p_{1,M}, p_{2,M}, p_{3,M}, p_{4,M}, p_{5,M} \right)}{\left\| \overline{R_{E_1,M}^{A,S}}, \overline{R_{E_2,M}^{A,S}}, \overline{R_{E_3,M}^{A,S}}, \overline{R_{E_4,M}^{A,S}}, \overline{R_{E_5,M}^{A,S}} \right\| \times \left\| p_{1,M}, p_{2,M}, p_{3,M}, p_{4,M}, p_{5,M} \right\|}$$

Where $p_{1,M}$, $p_{2,M}$, $p_{3,M}$, $p_{4,M}$ and $p_{5,M}$ are the proportions of motoneurons of muscle M in each of C5, C6, C7, C8 and T1, respectively.

Comparison between simulated and experimental recruitment curves

Representative subset of experimental recruitment curves: for each animal ($n = 5$), I selected 3 recruitment curves respectively obtained with a rostral, a caudal, and an intermediate lateral active contact.

Simulated recruitment curves: the simulated motoneuronal recruitment curves corresponding to the previous 3 active contacts and obtained with each of the two synaptic conductance hypotheses (H1 and H2) were retained for comparison.

Dynamic range: here, the saturation amplitude of the simulated and experimental recruitment curves was defined as the amplitude at which any motor nucleus/muscle was recruited above 90%, incremented by two amplitude steps.

Cumulative root mean square error (CRMSE): I restricted the simulated and experimental recruitment curves to their respective dynamic ranges and re-sampled them over a normalized amplitude vector. The root mean square error ($RMSE$) between the simulated curve with hypothesis H , electrode E and muscle M , and the corresponding experimental curve for animal A was estimated as:

$$RMSE_{H,A}(E, M) = \sqrt{\frac{1}{N_{\text{amps}}} \sum_{amp \in DR} \left(R_{E,M}^H(amp) - R_{E,M}^A(amp) \right)^2}.$$

The $CRMSE$ between the simulated recruitment curves with hypothesis H and the experimental curves of animal A was defined as:

$$CRMSE_{H,A} = \sum_{E,M} RMSE_{H,A}(E, M).$$

Threshold ranking error (TRE): I extracted from the simulated and experimental recruitment curves the recruitment order of the different muscles as lists $[M_1, M_2, \dots, M_8]_E^{A/H}$ where each M_i denotes a distinct muscle. I then compared the simulated recruitment order under hypothesis H with the experimental recruitment order obtained with animal A by counting the number of inversions (in the sense of permutations) between the lists $[M_1, M_2, \dots, M_8]_E^H$ and $[M_1, M_2, \dots, M_8]_E^A$, and summing the obtained values for each of the 3 electrode contact positions.

Dynamic range error (DRE): I extracted from the simulated and experimental recruitment curves the normalized length of the dynamic range $L_E^{A/H}$ as the length of the absolute dynamic range divided by its first amplitude. The dynamic range error between the simulated recruitment curves under hypothesis H and the experimental recruitment curves of animal A was computed as:

$$DRE_{H,A} = \sum_E \left(\frac{L_E^A}{L_E^H} + \frac{L_E^H}{L_E^A} - 2 \right).$$

The two sets of simulated recruitment curves were compared with respect to the same 3 metrics. Standard deviations were obtained using a bootstrapping approach (see Section 4.2.4).

Analysis of frequency-dependent modulation of muscular responses The recordings of high-frequency (10, 20, 50 and 100 Hz) stimulation protocols from all animals, muscles and electrode contacts were visually inspected and characterized according to 5 criteria: *attenuation*, *suppression*, *alternation*, *initial adaptation* and *no modulation*. *Attenuation* and *suppression* applied to those patterns of muscular responses where the amplitude of subsequent responses was progressively reduced and abruptly canceled, respectively (Figure 4.8.a and b). *Alternation* applied to patterns where subsequent responses alternated between low amplitude and high amplitude (Figure 4.8.c) [117]. *Initial adaptation* applied to patterns in which the evoked responses became steady only after several (5 to 20) initial pulses (Figure 4.8.d). Finally, *no modulation* applied to patterns in which no observable modulation or change in the evoked responses occurred. Multiple criteria could apply to a single pattern, except for the *no modulation* criteria.

Analysis of latencies of muscular responses Latencies of evoked muscular responses were measured as the duration between stimulation onset and onset of evoked EMG waveform. For every animal and every muscle where applicable, the difference in latency between the responses evoked by a rostral and a caudal stimulation site was computed (candidate muscles were such that a response could be evoked from both a rostral and

a caudal site). In this case, for both the rostral and caudal sites, the latencies of eight individual responses evoked at stimulation amplitudes near motor threshold were retained to analyze the difference.

For each comparison between rostrally-evoked and caudally-evoked response latencies of Figure 4.7.g, the performed statistical tests were unpaired two-sided t -tests.

4.4 EES of the human cervical spinal cord: applicability and limitations

Our team gained access to electrophysiological measurements acquired during standard clinical procedures involving EES in three human patients (see Section 4.4.4). The three patients were implanted with a commercial epidural electrode array for the treatment of chronic neuropathic upper-arm pain, approximately positioned between the spinal segments C6 and T1.

During the clinical procedures, electrophysiological tests similar to those we conducted in monkeys were performed in the three patients. The muscular activity evoked in $n = 8$ muscles was recorded using percutaneous EMG electrodes.

4.4.1 Nature of the motoneuronal recruitment

First, supra-threshold electrical stimuli were delivered from individual contacts of the epidural array at frequencies of 10, 20, 60 and 100 Hz. The EMG recordings we analyzed showed muscular responses modulated in a similar way as in monkeys. Specifically, we noted:

- attenuation of the CMAPs' amplitude;
- alternation, often irregular, of two or three stereotypical CMAP waveforms;
- suppression of muscle responses within the first 3 to 5 stimuli (Figure 4.10.e).

Also as observed in monkeys, modulation occurrences were overall more frequent at high frequencies (Figure 4.10.e). In fact, there were no instance of unmodulated responses following stimulation at 60 or 100 Hz.

As discussed in Section 4.3.5, these findings are indicative of a trans-synaptic recruitment of motoneurons. Moreover, the arguments developed in Section 4.3.5 regarding the unlikelihood of a direct motor axonal recruitment in relation to the size of the macaque monkey cervical spinal cord apply even more in the case of humans. Indeed, while the human spinal cord and vertebral canal are even larger (Figure 4.10.b), fiber diameters are relatively similar between humans and monkeys. Thus, similar potential distributions should be necessary to excite their motor axons, but the increased distance of human motor axons from dorsal epidural electrodes will presumably require higher stimulation amplitudes to induce their recruitment. Furthermore, although dorsal afferents should also be further away from epidural electrodes in humans compared to monkeys, this distance increase should be of lesser importance than that affecting the motor axons, suggesting that the gap in recruitment threshold between the two classes of fibers may be wider in humans.

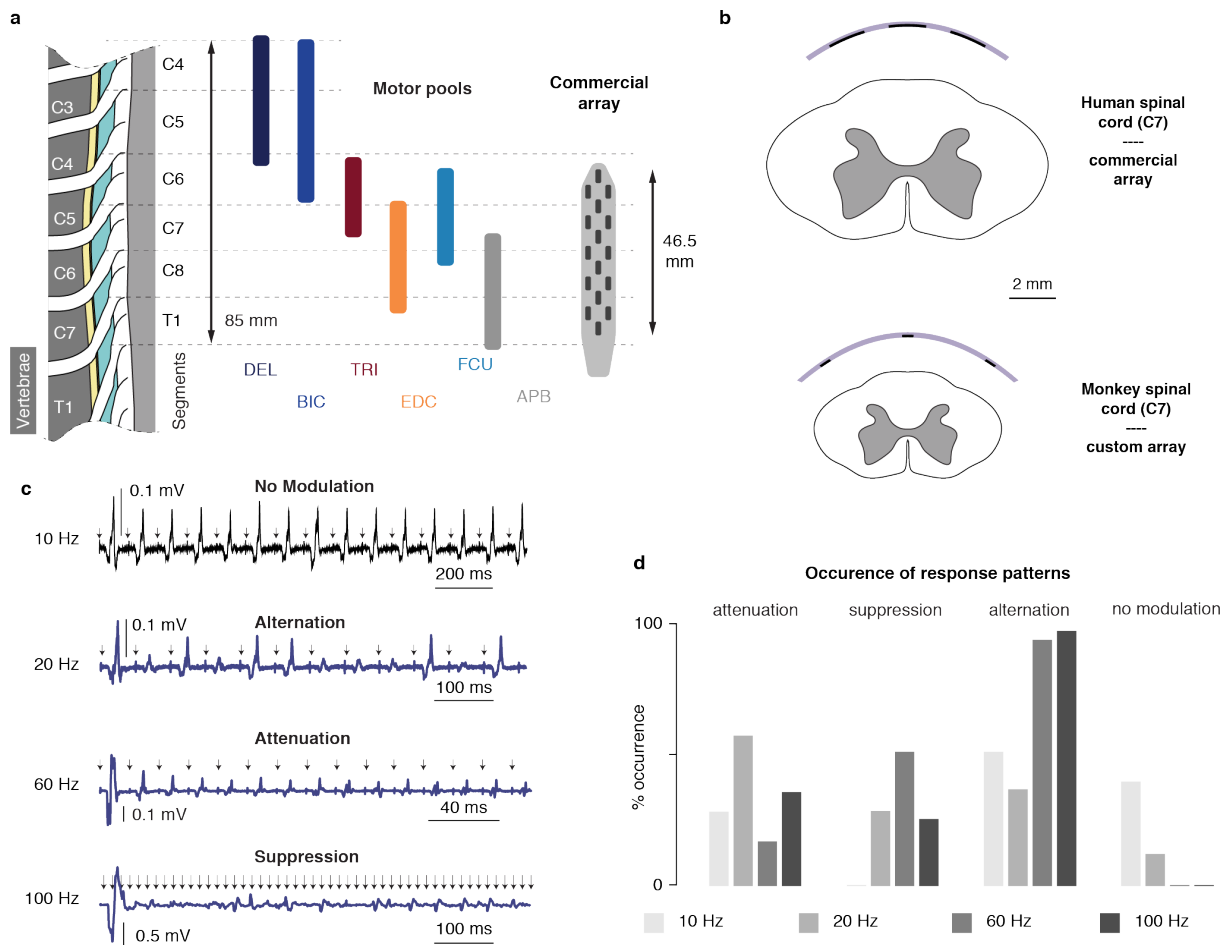


Figure 4.10 Analysis of EES of the cervical spinal cord in humans. **a** Dimensions of the human cervical spinal segments, heuristic distribution of the motor pools of six upper-limb muscles [97], and sketch of the commercial paddle epidural electrode array used to obtain the data reported in **c** and **d**. **b** Comparison between the relative dimensions of the monkey cervical spinal cord and our custom implant, and the human cervical spinal cord and the commercial epidural implant of **a**. **c** Examples of frequency-dependent modulation of muscular responses. The 4 EMG traces were obtained in the same muscle, using the same stimulation amplitude (near motor threshold) but different frequencies. *Arrows*: timestamps of stimulation pulses. **d** Frequency of occurrence of muscular response patterns during high-frequency stimulation. All the patterns recorded in all the muscles of the three subjects were included in the analysis ($n = 24$ patterns at 10 Hz, $n = 32$ patterns at 20 Hz, $n = 32$ patterns at 60 Hz, $n = 24$ patterns at 100 Hz). [Credits: the motor pools of **a** were sketched by Beatrice BARRA. The electrode diagram of **a** was co-realized with Beatrice BARRA. **c** and **d** were sketched by Beatrice BARRA.]

4.4.2 Recruitment selectivity

Analysis of recruitment selectivity in the clinical data was limited by the nature of the clinical procedures, which were not experimentally-oriented. In particular, we could not reference the muscular activation levels to the maximal EMG amplitudes. Consequently, it was not possible to normalize the recruitment curves of each muscle in a relevant way, and thus to compare the recruitment of different muscles. This limitation prevented us from evaluating the muscular specificity of the stimulation in function of the electrode position.

However, comparison between the dimensions of the implanted epidural electrode array and the dimensions of the cervical segments of the human spinal cord [92] indicated that the array might have spanned only few spinal segments (Figure 4.10.a) and that even its lateral electrodes were facing the dorsal columns, due to its small width (Figure 4.10.b). In fact, existing clinical implants are purposely designed to target dorsal column fibers [90]. This suggests that new implants with lateralized electrodes are required to target individual posterior roots and thus achieve the level of motoneuronal recruitment selectivity that we obtained in monkeys with tailored implants.

4.4.3 Summary and conclusions

Collectively, these results indicate that EES can be applied to the human cervical spinal cord to recruit upper-limb motoneurons, and that this recruitment is also predominantly mediated by mono- or poly-synaptic pathways. However, they also suggest that current clinically-compliant epidural electrode arrays may not be suited to selectively engage individual dorsal roots, and therefore not specific upper-limb motor nuclei either. To reach a selectivity such as obtained in monkeys, it will be necessary to design human-compatible epidural implants with electrode contacts that are more laterally-offset than in currently available technologies.

4.4.4 Material and methods

Clinical data Clinical data were obtained from the Centre Hospitalier Universitaire Vaudois (CHUV, Lausanne, Switzerland). The data were collected during standard clinical practice and under the CHUV’s general ethical approval for clinical procedures and use of data for scientific purposes.

Current-controlled electrical stimulation was delivered at frequencies ranging from 1 Hz to 100 Hz and amplitudes ranging from 0 mA to 5 mA to test for correct surgical placement of Medtronic SPECIFY™ 5-6-5 lead interfaces in patients with upper-arm neuropathic pain. Percutaneous needles were placed in upper-limb muscles and EMG signals were recorded (sampling rate = 10 kHz) using a clinical monitoring interface. Exported data were made anonymous and provided to our team with no reference to patient identity.

Data analysis We re-structured the clinical data provided by the CHUV to analyze it using the same methods as described in Section 4.3.6. In particular, we examined individual muscular responses recorded during high-frequency (10 Hz to 100 Hz) stimulation protocols to assess the occurrence of frequency-dependent modulation of muscular responses.

CHAPTER 5 REPRESENTATION OF MULTIPOLAR STIMULATION CONFIGURATIONS IN HYBRID NEUROPHYSICAL VOLUME CONDUCTOR MODELS

Multipolar stimulation configurations are employed in numerous applications of electrical stimulation of the nervous system, such as deep brain stimulation [55, 120], cochlear stimulation [121], or spinal cord stimulation [30].

Contrary to monopolar stimulation—where electrical current flows between one electrode located in the targeted region and one electrode far remote from it—, multipolar stimulation makes use of multiple electrodes located in the targeted region, withdrawing with some of them the current injected by the others. This allows to sculpt the electric potential distribution in the targeted region and may increase the selectivity with which specific neural populations can be stimulated [61]. However, the possibilities for combining different electrodes of an electrode array are theoretically countless and practically very numerous, such that finding optimal multipolar configurations to achieve a desired functional outcome in clinical or experimental settings is generally a tedious process.

The computational scheme of hybrid models enables particularly efficient exploration of the space of multipolar configurations accessible to any given set of electrodes. Using appropriate boundary conditions in the volume conductor model, only a small, finite number N of FEM calculations need be performed to estimate the electric potential distribution elicited by any combination of current or voltage sources. In turn, to estimate the induced recruitment of a given neuron or nerve fiber population with subsequent neurophysical simulations, the interpolation of the electric potential along the neuron or nerve fiber trajectories also needs be performed only N times.

In this chapter, after having exposed the problematic of the representation of multipolar configurations in hybrid models, I start by reviewing a number of approaches that have been employed by previous investigators. In particular, I indicate the current limitations of state-of-the-art approaches, which are notably focused at representing multipolar current sources—and not voltage sources—and which restricts the treatment of the volume conductor border $\partial\Omega$.

I then present an alternative approach, whereby a single set of basis potential distributions can be used to estimate the potential distribution arising from arbitrary multipolar current or voltage sources, or any mixture of the two. The border $\partial\Omega$ or specific patches of it can be treated in several ways, allowing to represent a distributed return electrode or an insulating border with eventual localized voltage or current sources (as desirable *eg* in hybrid models of transcutaneous electrical stimulation).

Moreover, this approach readily allows to compute a solution for the potential distribution when only current sources are specified and $\partial\Omega$ is assigned with a zero-flux condition—normally constituting an ill-defined boundary value problem—and I demonstrate the equivalence between the computed solution and any other solution of the same problem with regard to neurophysical simulations.

5.1 Position of the problem

In Chapter 2, we have seen that the computational scheme of hybrid neurophysical volume conductor models relies on three steps:

1. Computing the electric potential distribution throughout a volume conductor under quasi-stationary conditions.
2. Interpolating the potential distribution along trajectories of neurons and nerve fibers putatively populating the volume conductor.
3. Simulating the electrical response of these neurons and nerve fibers by means of neurophysical models using these interpolated potentials.

We have also seen that current or voltage sources are represented by means of boundary conditions in the volume conductor model (see Section 2.2.2). At first sight, it would thus seem that each multipolar stimulation configuration requires its own set of representative boundary conditions, and consequently, that the three steps of the computational scheme need be carried out for all of them.

5.1.1 Computational cost

In Table 5.1, I have reported typical time complexities for the three main computational tasks involved in the calculation chain. As one can see, FEM computations are much more computationally costly than individual interpolation operations, which are themselves much more costly than individual neurophysical simulations. However, to assess the response of a population of N neurons or nerve fibers, N interpolation operations are required for any FEM computation (one per neuron or nerve fiber), and multiple neurophysical simulations are required for any interpolation operation (multiple amplitudes and/or stimulation waveforms per neuron or nerve fiber). Thus, as N grows, the computational cost of the FEM computation is likely to get dwarfed by that of the other two steps of the computational scheme, but the respective costs of the interpolation operations and neurophysical simulations should remain in fixed proportion. Moreover, as long as the number of neurophysical simulations per interpolation operation remains below a few tens, the interpolation operations are likely to represent no less than 50% of the total computational cost.

Incidentally, this is often the case of applications that seek to determine optimal multipolar stimulation configurations. These typically involve testing only a few stimulus amplitudes and stimulation waveforms to determine the threshold level for each neuron or nerve fiber. Furthermore, when making use of automatized optimization algorithms, the number of configurations to be tested may be very large (the number of all possible configurations

Table 5.1 Typical computational costs of the different steps of the computational scheme of hybrid models. Computational cost is given as the *elapsed time* of computational task execution. The different computational tasks were carried out on a MacBook Pro (Retina, Mid 2012) with 2,6 GHz Intel Core i7 processor and 16 GB 1600 MHz DDR3 RAM running macOS High Sierra. The FEM computation was performed with COMSOL v5.2a on the volume conductor model of Section 4.2 which comprised $\sim 10 \times 10^6$ elements. The interpolation operations were performed using Matlab R2015b along the trajectory of the same group-Ia fiber which was used in the neurophysical simulations and which comprised 2757 compartments—of which 765 contained active mechanisms (ion channels). The refined interpolation fetched one value per compartment from the solution of the FEM computation. The poor interpolation fetched one value for a fraction of $3/11$ -th of all compartments. The neurophysical simulations were ran with NEURON v7.7 and lasted 10 ms, with a square pulse of electrical stimulation lasting 200 μ s starting after 5 ms of simulation (*AP*: action potential).

Computational task	Duration (s)
FEM computation of electric potential	~ 4000
Interpolation along fiber (refined)	~ 500
Interpolation along fiber (poor)	~ 140
Neurophysical simulation with fixed time step (0.01 ms)	~ 4.5
Neurophysical simulation with variable time step (with AP)	~ 9
Neurophysical simulation with variable time step (without AP)	~ 1.75

grows as $N!$ where N is the number of electrodes). In this case, strategies allowing to minimize the number of times the first two steps of the computational scheme need be performed become very relevant.

5.1.2 Superposition principle

To this end, when the superposition principle applies (see Section 2.1.4), it is possible to *superpose* the solutions satisfying different—though compatible—boundary conditions to obtain the solution satisfying the *superposed boundary conditions*.

Consider the generic computational domain Ω sketched in Figure 5.1. The T_i 's in Ω are the *terminals*: they will be assigned with boundary conditions to represent current or voltage sources. For simplicity, I have sketched Ω as a two-dimensional domain, but the following considerations apply equally to tridimensional computational domains. Likewise, I have sketched the T_i 's as unidimensional geometric objects—equivalent to the two-dimensional surfaces of the three-dimensional space—, but the T_i 's may as well be points. (Some of the following equations would be written differently, but the underlying principles being the same, I will omit these distinctions.)

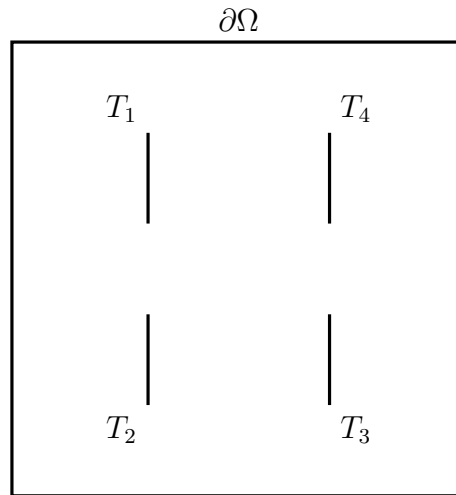


Figure 5.1 Generic computational domain Ω with its frontier $\partial\Omega$ and four internal terminals T_1 , T_2 , T_3 and T_4 .

Dirichlet conditions Let us first consider a problem \mathcal{P} characterized by the following system of equations:

$$\mathcal{S} \left\{ \begin{array}{ll} \nabla \cdot (\sigma \nabla V) & = 0 & \forall \mathbf{x} \in \Omega \\ V(\mathbf{x}) & = v_0 & \forall \mathbf{x} \in \partial\Omega \\ V(\mathbf{x}) & = v_1 & \forall \mathbf{x} \in T_1 \\ V(\mathbf{x}) & = v_2 & \forall \mathbf{x} \in T_2 \\ V(\mathbf{x}) & = v_3 & \forall \mathbf{x} \in T_3 \\ V(\mathbf{x}) & = v_4 & \forall \mathbf{x} \in T_4 \end{array} \right.$$

The theory of boundary value problems ensures that there exists a distribution V that is twice differentiable over Ω and which satisfies the system \mathcal{S} [72].

Replacing v_i by v'_i , $0 \leq i \leq 4$, one similarly obtains a unique solution V' to the corresponding problem \mathcal{P}' .

Now forming $V'' := V + V'$, and due to the linearity of Poisson's equation, one finds that V'' is solution of the problem \mathcal{P}'' characterized by:

$$\mathcal{S}'' \left\{ \begin{array}{ll} \nabla \cdot (\sigma \nabla V) & = 0 & \forall \mathbf{x} \in \Omega \\ V(\mathbf{x}) & = v_0 + v'_0 & \forall \mathbf{x} \in \partial\Omega \\ V(\mathbf{x}) & = v_1 + v'_1 & \forall \mathbf{x} \in T_1 \\ V(\mathbf{x}) & = v_2 + v'_2 & \forall \mathbf{x} \in T_2 \\ V(\mathbf{x}) & = v_3 + v'_3 & \forall \mathbf{x} \in T_3 \\ V(\mathbf{x}) & = v_4 + v'_4 & \forall \mathbf{x} \in T_4 \end{array} \right.$$

The second to sixth equations of \mathcal{S}'' constitute superposed boundary conditions, and the fact that V'' is solution of \mathcal{P}'' is a manifestation of the superposition principle.

Uniqueness If the boundary value problem specifies only Dirichlet boundary conditions, the potential is uniquely defined. Indeed, if there were two solutions, the difference between the two (let us call it V_d) would satisfy a combination of null-Dirichlet boundary conditions. If V_d was non-trivial, *ie* non-identically null over Ω , V_d would have a non-zero extremum either within the interior of Ω or at its boundary. A non-zero extremum in the interior of Ω would violate Poisson's homogeneous equation and the divergence theorem, and is thus excluded, while a non-zero extremum on a null-Dirichlet boundary condition is clearly nonsensical. Hence, V_d must be identically null, and the initial boundary value problem admits an unique solution.

In fact, if the boundary value problem specifies an insulating boundary condition (*ie* null-

Neumann condition) in addition to Dirichlet boundary conditions, the uniqueness of the solution still holds, because the insulating condition also forbids a non-zero extremum to exist on the boundary where it is applied.

Neumann conditions The previous example exhibited only Dirichlet boundary conditions, but the superposition principle also prevails in case of Neumann conditions.

If V is a solution of the problem \mathcal{P} characterized by:

$$\mathcal{S} \left\{ \begin{array}{ll} \nabla \cdot (\sigma \nabla V) & = 0 & \forall \mathbf{x} \in \Omega \\ \sigma \nabla V(\mathbf{x}) \cdot \mathbf{n}(\mathbf{x}) & = j_0 & \forall \mathbf{x} \in \partial\Omega \\ (\sigma_b \nabla V_b(\mathbf{x}) - \sigma_a \nabla V_a(\mathbf{x})) \cdot \mathbf{n}_{a,b}(\mathbf{x}) & = j_1 & \forall \mathbf{x} \in T_1 \\ (\sigma_b \nabla V_b(\mathbf{x}) - \sigma_a \nabla V_a(\mathbf{x})) \cdot \mathbf{n}_{a,b}(\mathbf{x}) & = j_2 & \forall \mathbf{x} \in T_2 \\ (\sigma_b \nabla V_b(\mathbf{x}) - \sigma_a \nabla V_a(\mathbf{x})) \cdot \mathbf{n}_{a,b}(\mathbf{x}) & = j_3 & \forall \mathbf{x} \in T_3 \\ (\sigma_b \nabla V_b(\mathbf{x}) - \sigma_a \nabla V_a(\mathbf{x})) \cdot \mathbf{n}_{a,b}(\mathbf{x}) & = j_4 & \forall \mathbf{x} \in T_4 \end{array} \right.$$

and if V' is a solution of the same problem but where j_i is changed to j'_i , $0 \leq i \leq 4$, then $V'' := V + V'$ is a solution of the problem where the second terms of the second to sixth equations of \mathcal{S} are $j_i + j'_i$. (In each equation above, a and b denote the two sides of terminal T_i and play the same role as in Section 2.2.2.)

Integrated current condition Another frequently encountered boundary condition assumes constant potential, but instead of prescribing the potential value v_i on T_i , it prescribes the total current flowing through T_i :

$$I_i := \int_{T_i} (\sigma_b \nabla V_b(\mathbf{x}) - \sigma_a \nabla V_a(\mathbf{x})) \cdot \mathbf{n}_{a,b}(\mathbf{x}) \, ds$$

It will be hereafter referred to as *integrated current condition* (ICC). It should be noted, that ICCs are not equivalent to Neumann conditions, as they do not assume that the normal component of the current density is uniform on T_i . Nonetheless, by prescribing a uniform potential, they result in a zero-tangential current density component. The ICC is of high practical relevance, as metals or other highly conductive materials are frequently used for electrode active contacts (which ascertains a uniform potential over the terminal surface), and stimulation systems (*ie* IPGs or extra-corporal stimulators) often impose a total current flux between electrodes, rather than voltage differences. Moreover, boundary value problems that prescribe the same total current flux through a terminal via an ICC or via a Neumann condition have very similar solutions, except possibly in the direct vicinity of the terminal (differences should be most pronounced for sharp terminal geometries).

ICCs must be complemented by at least one Dirichlet condition imposed in Ω or on

its boundary, as otherwise the potential would be left undetermined. Once a Dirichlet condition has been prescribed, the boundary value problem again admits of a unique solution, which can be proved similarly to the case of pure Dirichlet boundary conditions: if there were two solutions, their difference V_d would satisfy null-ICCs everywhere, except at the boundary where the Dirichlet condition is imposed, where V_d now satisfies a null-Dirichlet condition. We already know that extrema of V_d can neither occur in the interior of Ω , nor on the boundary where the null-Dirichlet condition prevails. If there was a non-zero extremum in a point of the boundaries where a null-ICC prevails (let us denote it P_0 , and the terminal to which it belongs T_i), the gradient of V_d would need to be non-zero in P_0 . Due to the uniformity of the potential on a boundary where an ICC prevails, this gradient would be purely normal. Without loss of generality, let's assume that the extremum is a maximum (otherwise we simply flip the sign of V_d). Then, the gradient must be pointing outwards of Ω . To ensure that a net zero-current (null-ICC) flows through T_i , some gradients elsewhere on T_i must be pointing inwards of Ω . As the potential is uniform on T_i , this contradicts the assumption that the potential in P_0 is a maximum. Thus, no extrema can occur on the boundaries where null-ICCs are imposed, and we are again led to conclude that V_d is identically null over Ω , implying the uniqueness of the solution of the initial boundary value problem.

Mixed conditions The superposition principle also applies when Dirichlet conditions are imposed on some of the T_i 's, Neumann conditions on some others, and ICCs on the remaining ones.

However, it is in general not possible to formulate any prediction regarding the superposition of two solutions satisfying different types of conditions on the same T_i .

Basis solutions Importantly, the superposition principle allows to express all the solutions of boundary value problems such as depicted above as linear combinations formed from small finite sets of solutions satisfying *unitary* boundary conditions, often called *basis solutions*.

To illustrate this, let us consider the problem \mathcal{P} characterized by:

$$\mathcal{S} \left\{ \begin{array}{ll} \nabla \cdot (\sigma \nabla V) & = 0 \quad \forall \mathbf{x} \in \Omega \\ \sigma \nabla V(\mathbf{x}) \cdot \mathbf{n}(\mathbf{x}) & = 0 \quad \forall \mathbf{x} \in \partial\Omega \\ (\sigma_b \nabla V_b(\mathbf{x}) - \sigma_a \nabla V_a(\mathbf{x})) \cdot \mathbf{n}_{a,b}(\mathbf{x}) & = j_1 \quad \forall \mathbf{x} \in T_1 \\ V(\mathbf{x}) & = v_2 \quad \forall \mathbf{x} \in T_2 \\ \int_{T_3} (\sigma_b \nabla V_b(\mathbf{x}) - \sigma_a \nabla V_a(\mathbf{x})) \cdot \mathbf{n}_{a,b}(\mathbf{x}) \, ds & = I_3 \\ (\sigma_b \nabla V_b(\mathbf{x}) - \sigma_a \nabla V_a(\mathbf{x})) \cdot \mathbf{n}_{a,b}(\mathbf{x}) & = j_4 \quad \forall \mathbf{x} \in T_4 \end{array} \right.$$

If we denote:

- V_1 the solution of \mathcal{S} for $(j_1, v_2, I_3, j_4) := (1, 0, 0, 0)$;
- V_2 the solution of \mathcal{S} for $(j_1, v_2, I_3, j_4) := (0, 1, 0, 0)$;
- V_3 the solution of \mathcal{S} for $(j_1, v_2, I_3, j_4) := (0, 0, 1, 0)$;
- V_4 the solution of \mathcal{S} for $(j_1, v_2, I_3, j_4) := (0, 0, 0, 1)$;

then, the general solution of \mathcal{S} is given by $V := j_1 \cdot V_1 + v_2 \cdot V_2 + I_3 \cdot V_3 + j_4 \cdot V_4$.

Thus in this example, four basis solutions allow us to estimate the electric potential distribution arising from any voltage source at T_2 , and any current sources at T_1 , T_3 and T_4 (should they be described by ICCs or Neumann conditions), which thus requires performing only four FEM computations. In turn, to estimate the potential along any given neuron or nerve fiber trajectory, it suffice to interpolate the potential once for each of these four FEM computations, and to superpose the interpolated potentials using the appropriate multiplicative factors.

5.1.3 Stimulation paradigms and boundary conditions

Before reviewing a number of approaches that have been employed by previous investigators to represent and search for optimal multipolar configurations using hybrid models, I wish to insist on the physical interpretation of different boundary conditions used in volume conductor models in terms of actual stimulation paradigms.

Ideal physical representation and implications for hybrid models

Let us first consider the situation where only two electrodes are implanted in the body of a vertebrate. There is no additional return electrode, such that electric current can only flow between the two electrodes.

This situation is faithfully depicted by the diagram of Figure 5.2. The border $\partial\Omega$ represents the surface of the skin and is considered to be perfectly insulating, which is a pretty good reflection of the electrical insulation occurring at the skin-air interface. As is conventionally done, the value of the electric potential distribution in the body is considered to be 0 V, which is legitimate since:

1. the potential distribution in the body is relatively uniform at the macroscopic scale (at least in comparison with what it will be during electrical stimulation);
2. the reference level of the electric potential can be set arbitrarily.

Lastly, the potential in the bulk of the two metallic electrodes slightly deviate from the potential of the biological tissue, which is due to an electro-chemical equilibrium between the bulk metallic phase and the dissolved ionic phase of the chemical species composing the electrodes [17].

During electrical stimulation, as the circuit is being closed, the potentials of both electrodes drift away from their resting equilibrium levels—one positively, the other negatively—establishing a non-uniform potential distribution throughout the body, as depicted in Figure 5.3. In particular, due to the continuity of the electric potential, we know that there is a region of the geometry (theoretically—an infinitely thin surface), lying between the two electrodes, where the electric potential is 0 V. In this region (let us call it Ω_0), the electric potential is thus *unaffected* by the stimulation: it is continuously equal to 0 V just before and just after the stimulation onset. Therefore, if a neuron or a nerve fiber lies entirely in Ω_0 , it is guaranteed that the stimulation will have no effect on it.

This observation has practical implications for the calculation chain of hybrid models. Recall from Section 2.3 that in absence of externally applied stimulation, neurophysical models assume that neurons and nerve fibers are plunged in a uniform electric potential of 0 V. This is in accordance with the conventions we have adopted here, namely that the potential distribution in the body is assumed to be uniformly equal to 0 V before the stimulation onset. This means that for a neuron or nerve fiber whose trajectory lie in Ω_0 , the interpolation of the potential distribution along its trajectory should yield null values, so as to guarantee that neurophysical simulations will predict a total absence of stimulation effects on this neuron or nerve fiber. More succinctly: ideally, the boundary conditions used in the volume conductor model should allow to obtain precisely the electric potential distribution depicted in Figure 5.3.

To achieve this, one strategy would be to simply assign the following boundary conditions:

$$\left\{ \begin{array}{ll} \sigma \nabla V(\mathbf{x}) \cdot \mathbf{n}(\mathbf{x}) & = 0 & \forall \mathbf{x} \in \partial\Omega \\ V(\mathbf{x}) & = v_1 & \forall \mathbf{x} \in T_1 \\ V(\mathbf{x}) & = v_2 & \forall \mathbf{x} \in T_2 \end{array} \right.$$

Unfortunately, the potentials v_1 and v_2 can not be known in advance. This requires that surrogate strategies be employed, possibly guaranteeing that the computed potential distribution is equivalent to the “true” potential distribution (defined by the above conditions) with respect to subsequent neurophysical simulations.

Voltage-controlled stimulation

When representing voltage-controlled stimulation conditions, although v_1 and v_2 are not known, their difference $v_0 := v_1 - v_2$ is. Moreover, the solution V obtained with the

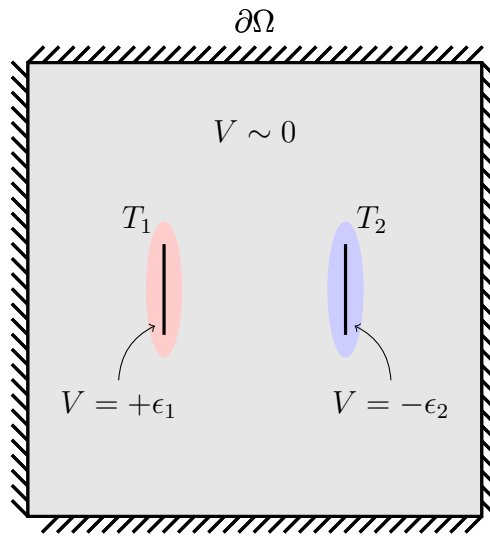


Figure 5.2 Implanted stimulation system with two electrodes: open-circuit situation.

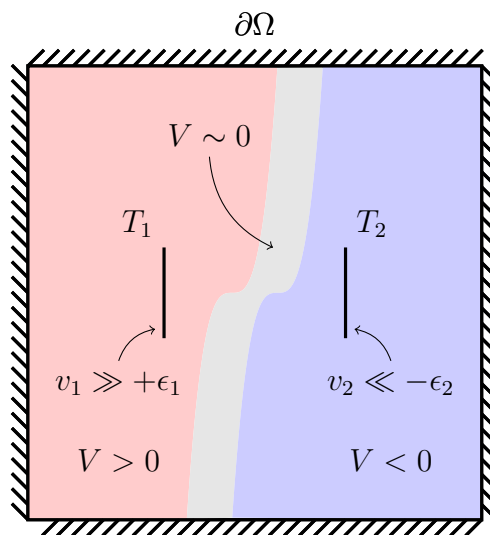


Figure 5.3 Implanted stimulation system with two electrodes: closed-circuit situation.

boundary conditions:

$$\left\{ \begin{array}{ll} \sigma \nabla V(\mathbf{x}) \cdot \mathbf{n}(\mathbf{x}) & = 0 & \forall \mathbf{x} \in \partial\Omega \\ V(\mathbf{x}) & = v_0 & \forall \mathbf{x} \in T_1 \\ V(\mathbf{x}) & = 0 & \forall \mathbf{x} \in T_2 \end{array} \right.$$

only differs from the “true” distribution (with v_1 and v_2 assigned on T_1 and T_2 instead of v_0 and 0) by a spatially-uniform shift of magnitude v_2 .

As will be demonstrated in Section 5.3.2, it turns out that two such potential distributions are equivalent with respect to neurophysical simulations. Thus, although the solution satisfying the above conditions is not precisely that depicted in Figure 5.3, it should yield the exact same simulation results.

Furthermore, thanks to the superposition principle, it is possible to merely compute the solution V_1 satisfying the conditions:

$$\left\{ \begin{array}{ll} \sigma \nabla V(\mathbf{x}) \cdot \mathbf{n}(\mathbf{x}) & = 0 & \forall \mathbf{x} \in \partial\Omega \\ V(\mathbf{x}) & = 1 & \forall \mathbf{x} \in T_1 \\ V(\mathbf{x}) & = 0 & \forall \mathbf{x} \in T_2 \end{array} \right.$$

to obtain that for any voltage difference v_0 as $V := v_0 \cdot V_1$.

Finally, as shown in Section 5.3, this strategy can easily be generalized to an arbitrary number of terminals. Moreover, it is possible to represent the situation where the enclosure of an IPG serves as a return electrode by treating it like any other electrode. Similarly, it is also possible to represent surface cutaneous electrodes by replacing the insulating condition on some parts of $\partial\Omega$ by Dirichlet conditions (see Section 5.3).

Current-controlled stimulation

When representing current-controlled stimulation conditions, neither v_1 and v_2 nor v_0 are *a priori* known. Instead, the total current I_0 flowing between T_1 and T_2 is known.

A natural way to represent this situation would be to specify the following conditions:

$$\left\{ \begin{array}{llll} \sigma \nabla V(\mathbf{x}) \cdot \mathbf{n}(\mathbf{x}) & = & 0 & \forall \mathbf{x} \in \partial\Omega \\ \left(\sigma_b \nabla V_b(\mathbf{x}) - \sigma_a \nabla V_a(\mathbf{x}) \right) \cdot \mathbf{n}_{a,b}(\mathbf{x}) & = & j_1 & := \frac{I_0}{A_1} \quad \forall \mathbf{x} \in T_1 \\ \left(\sigma_b \nabla V_b(\mathbf{x}) - \sigma_a \nabla V_a(\mathbf{x}) \right) \cdot \mathbf{n}_{a,b}(\mathbf{x}) & = & j_2 & := -\frac{I_0}{A_2} \quad \forall \mathbf{x} \in T_2 \end{array} \right.$$

where A_1 and A_2 are the areas respectively of T_1 and T_2 (which ensures that $A_1 \cdot j_1 = -A_2 \cdot j_2 = I_0$).

However, doing so results in an ill-defined boundary value problem: all the conditions bear on the gradient of V ; none on V itself.

A common approach to eliminate the indetermination bearing on V is to replace the insulation condition at the border by a ground condition, although this requires that we also change our interpretation for $\partial\Omega$. Under the new interpretation, $\partial\Omega$ does no longer represent the surface of the skin but represents a *distributed* or *indifferent return electrode* surrounding the stimulated region. This representation is based on the assumption that a return electrode is placed in a body region far remote from the stimulated region, and is justified by the following reasoning: if an excess current is delivered through the stimulating electrodes (corresponding to $A_1 \cdot j_1 + A_2 \cdot j_2 \neq 0$ in our example), it will be withdrawn at the return electrode, and it will first have to escape the stimulated region, somewhat in every possible direction, to do so. Thus, instead of representing the whole body and a remote return electrode, it suffice to represent a volume of unspecified biological tissue surrounding the stimulated tissue, and to consider that the excess current is withdrawn at the frontier of this volume (in reality, the current is not *withdrawn* at this frontier, but it does indeed *flow* through it in the outwards direction). For instance, for an implanted stimulation system, the role of the remote return electrode would be played by the enclosure of the IPG, and the ground condition imposed on $\partial\Omega$ would *reflect* the return of eventual excess currents to the IPG enclosure.

The specification precisely of 0 V on $\partial\Omega$ is of no consequences on the calculation chain of hybrid models (due to the equivalence of distributions differing by spatially-uniform shifts with respect to neurophysical simulations, as mentioned previously and demonstrated in Section 5.3). However, the assumption of iso-potentiality of $\partial\Omega$ does compromise the theoretical equivalence of the computed solution with the “true” potential distribution of Figure 5.3 (recall that this equivalence is instead guaranteed for the solutions satisfying the boundary conditions of Section 5.1.3). In practice (*ie* in actual volume conductor model applications), the size of the surrounding volume of unspecified tissue is increased until the computed solution stops varying perceptibly in the region of interest, and this representation is thought to be a faithful reflection of the physical reality.

When resorting to it, one can again make use of the superposition principle and define basis solutions V_i satisfying the conditions:

$$\left\{ \begin{array}{ll} V(\mathbf{x}) &= 0 & \forall \mathbf{x} \in \partial\Omega \\ (\sigma_b \nabla V_b(\mathbf{x}) - \sigma_a \nabla V_a(\mathbf{x})) \cdot \mathbf{n}_{a,b}(\mathbf{x}) &= 1 & \forall \mathbf{x} \in T_i \end{array} \right.$$

to obtain the potential distribution V arising from current sources j_1 and j_2 at T_1 and T_2 as $V := j_1 \cdot V_1 + j_2 \cdot V_2$. Furthermore, this approach can straightforwardly be generalized to an arbitrary number of electrodes.

However, it should be pointed out that it can not be applied to volume conductor models where $\partial\Omega$ should represent an insulating border, as would be desirable *eg* in volume conductor models of transcutaneous electrical stimulation paradigms.

5.2 State-of-the-art

In the preceding section, I have presented important elements of the problematic of the search for optimal multipolar configurations using hybrid models, namely:

- the need for strategies minimizing the number of FEM computations and subsequent interpolation operations that need be carried out;
- the physical interpretation of different sets of boundary conditions in volume conductor models.

In this section, I review a number of approaches that have been employed by previous investigators to address this problem.

5.2.1 Butson and McIntyre, 2008 [61]

Butson and McIntyre have searched for optimal multipolar configurations in the context of deep brain stimulation. They constructed a volume conductor model of the thalamus and subthalamic nucleus with multiple cylindrical electrodes T_i with surfaces Σ_i , and a surrounding unspecified tissue whose boundaries constituted the border $\partial\Omega$ of the volume conductor.

They sought for bipolar stimulation configurations achieving the best selectivity for neurons of the subthalamic nucleus. The boundary conditions they used were as follows:

$$\mathcal{S} \quad \left\{ \begin{array}{ll} V(\mathbf{x}) & = 0 \quad \forall \mathbf{x} \in \partial\Omega \\ (\sigma_b \nabla V_b(\mathbf{x}) - \sigma_a \nabla V_a(\mathbf{x})) \cdot \mathbf{n}_{a,b}(\mathbf{x}) & = x \quad \forall \mathbf{x} \in \Sigma_i \\ (\sigma_b \nabla V_b(\mathbf{x}) - \sigma_a \nabla V_a(\mathbf{x})) \cdot \mathbf{n}_{a,b}(\mathbf{x}) & = 1 - x \quad \forall \mathbf{x} \in \Sigma_j \end{array} \right.$$

ie a ground condition at the border and Neumann conditions on two distinct electrodes. The apportionment x of the injected current between the two electrodes was chosen among a small finite collection $\{0, 0.2, 0.4, 0.6, 0.8, 1\}$. For a given apportionment, the potential distributions corresponding to different total amounts of injected current were obtained by multiplying the solution satisfying the above conditions by the desired amount I_0 . The different apportionments were then evaluated with respect to their ability to sculpt the *volume of tissue activated* as closely as possible to a desired shape.

5.2.2 Capogrosso et al., 2011 [62]

Capogrosso and colleagues have searched for optimal multipolar configurations in the context of peripheral nerve stimulation. Specifically, they employed a genetic algorithm (which is a particular type of optimization algorithm) in combination with a hybrid model

of a transverse multi-electrode array in the rat sciatic nerve to find multipolar configurations targeting at best specific nerve fascicles (N disk-like electrode contacts T_i , with respective surfaces Σ_i).

They represented multipolar current-controlled stimulation configurations with a distributed return electrode using the approach discussed in Section 5.1.3. Specifically, they first computed a series of basis solutions V_i satisfying the following boundary conditions:

$$\mathcal{S} \quad \left\{ \begin{array}{ll} V(\mathbf{x}) & = 0 \quad \forall \mathbf{x} \in \partial\Omega \\ (\sigma_b \nabla V_b(\mathbf{x}) - \sigma_a \nabla V_a(\mathbf{x})) \cdot \mathbf{n}_{a,b}(\mathbf{x}) & = 1 \quad \forall \mathbf{x} \in \Sigma_i \end{array} \right.$$

ie an insulating condition at the border and a unitary Neumann condition at T_i .

Their genetic algorithm generated random sequences $(\omega_1, \omega_2, \dots, \omega_N)$ with $-1 < \omega_k < 1 \quad \forall k$ which were used to form linear combinations $V := j_0 \cdot \sum_i \omega_i \cdot V_i$ where j_0 was set to 400 μA .

The recruitment of nerve fiber populations induced by those distributions was assessed by means of neurophysical simulations, and scores were attributed to the sequences $(\omega_1, \omega_2, \dots, \omega_N)$ with respect to their efficiency at selectively recruiting specific groups of nerve fibers.

The genetic algorithm looked for sequences maximizing the previous scores, and thus indicated multipolar stimulation configurations optimally targeting specific fascicles.

5.2.3 Howell et al., 2015 [55]

Howell and colleagues also employed a genetic algorithm combined with a hybrid model to optimize a number of parameters for deep brain stimulation. The parameters subjected to optimization included the voltages applied on the active surface of three cylindrical electrodes, as well as geometrical parameters such as the length, inter-spacing, and radius of the electrodes.

From their paper, it can be understood that they performed FEM computations and subsequent interpolation operations for each tested multipolar configuration, and that this was required by the fact that the random sequences generated by their genetic algorithm represented simultaneously parameters for the multipolar configurations and geometrical parameters (since distinct multipolar configurations were associated with distinct volume conductor geometries, and since distinct geometries imply distinct computational meshes and thus separate FEM computations).

They represented multipolar voltage-controlled stimulation configurations with the following boundary conditions:

$$\mathcal{S} \quad \left\{ \begin{array}{ll} V(\mathbf{x}) &= 0 \\ V(\mathbf{x}) &= v_1 \\ V(\mathbf{x}) &= v_2 \\ V(\mathbf{x}) &= v_3 \end{array} \right. \quad \begin{array}{l} \forall \mathbf{x} \in \partial\Omega \\ \forall \mathbf{x} \in \Sigma_1 \\ \forall \mathbf{x} \in \Sigma_2 \\ \forall \mathbf{x} \in \Sigma_3 \end{array}$$

ie a ground condition at the border and specific Dirichlet conditions on each electrode.

Note that with these conditions, $\partial\Omega$ acted as a distributed return electrode.

5.2.4 Xiao et al., 2016 [63]

Xiao and colleagues also looked for optimal multipolar configurations for deep brain stimulation. They used a volume conductor model of the non-human primate thalamic nuclei together with a custom algorithm to find multipolar configurations maximizing the likelihood of neural recruitment in specific thalamic areas. The latter did not rely on neurophysical simulations, but on the evaluation of the spatial second-order finite differences of the electric potential along the trajectories of nerve fibers. This is a common technique to estimate the likelihood of nerve fiber recruitment without having to perform neurophysical simulations. It is based on the *activating function* concept [37], and it nonetheless requires to perform the FEM computations and interpolation operations along the nerve fiber trajectories.

To compute the potential distributions arising from arbitrary multipolar current-controlled stimulation configurations, they employed the same boundary conditions and basis solutions as Capogrosso and colleagues in [62] .

5.2.5 Pelot et al., 2018 [122]

Recently, Pelot and colleagues have reviewed a number of options for representing multipolar current-controlled stimulation configurations in volume conductor models. The scope of their study was wider than multipolar configurations: it included a detailed assessment of other parameters concerning the representation of metallic electrode contacts and current sources in general. Furthermore, they did not actually attempt to find optimal multipolar stimulation configurations in any particular context. Nonetheless, I think it is worth to include their study in this short review, having regard to the developments presented in this chapter.

The reason is that they formulated recommendations for the approach employed by Capogrosso and colleagues [62] and Xiao and colleagues [63], of which I have emphasized the limitations in Section 5.1.3.

Recall once more that if N denotes the number of represented electrodes, this approach

consists in computing the solutions V_i satisfying:

$$\mathcal{S} \quad \left\{ \begin{array}{ll} V(\mathbf{x}) & = 0 \quad \forall \mathbf{x} \in \partial\Omega \\ (\sigma_b \nabla V_b(\mathbf{x}) - \sigma_a \nabla V_a(\mathbf{x})) \cdot \mathbf{n}_{a,b}(\mathbf{x}) & = 1 \quad \forall \mathbf{x} \in \Sigma_i \end{array} \right.$$

and to estimate the distribution resulting from current source densities j_1, j_2, \dots, j_N at T_1, T_2, \dots, T_N as $V := \sum_i j_i \cdot V_i$.

It implies that $\partial\Omega$ acts as a distributed return electrode, and it can not readily be applied *eg* to volume conductor models where $\partial\Omega$ is meant to represent an insulating border.

Note: in the above equations, the T_i 's are implicitly assumed to be surface electrodes with surfaces Σ_i 's, but the equations could be adapted in case of punctual current sources.

5.2.6 Summary and conclusions

This brief review highlights three important findings:

- attempts to find optimal multipolar *voltage-controlled* stimulation configurations with hybrid models are seldom in the literature, and no recommendations can be found for the basis solutions to search for such configurations;
- the state-of-the-art representation of multipolar *current-controlled* stimulation configurations, which is often used to search for optimal such configurations, is based on a representation of the physical reality which could be improved (distributed return electrode);
- none of the strategies that have been employed to represent either *voltage-* or *current-controlled* multipolar configurations can readily be applied to represent voltage or current sources on parts of $\partial\Omega$, as required to represent *eg* transcutaneous stimulation paradigms.

This review is not exhaustive, and other strategies may have been proposed by previous investigators for the search of optimal multipolar configurations using hybrid models in the context of spinal cord stimulation, deep brain stimulation, or peripheral nerve stimulation, but not to my knowledge.

5.3 New versatile approach

In this section I present an approach to represent multipolar stimulation configurations in hybrid models which has the following characteristics:

- If T_i , $0 \leq i \leq N$, are $N + 1$ *terminals* of the volume conductor (surfaces, lines or points), the solutions to N boundary value problems suffice to represent the potential distribution arising from any combination of electrical sources (either voltage or current sources) at the T_i 's.
- The border $\partial\Omega$ can either represent a distributed return electrode, or the skin-air interface. In the latter case it is assumed to be perfectly insulating except on eventual subparts of $\partial\Omega$, allowing to represent surface cutaneous electrodes.
- When only current sources are prescribed, a solution for the potential distribution is readily obtained, despite the ill-definition of the boundary value problem.

In Section 5.3.2, I demonstrate the equivalence of potential distributions differing by spatially-uniform shifts with regard to neurophysical simulations, thereby demonstrating the theoretical validity of the presented approach.

This approach has probably already been used in hybrid models of cochlear stimulation [56, 123] to represent what the authors of the mentioned publications called *phased array stimulation*. It is attributed to VAN COMPERNOLLE [124] who would have developed it and exposed it in his PhD dissertation at the Stanford University in 1985. However, his PhD dissertation is not in the public domain, such that I am unable to say whether and to what extent the developments which I present in this chapter overlap with the developments of VAN COMPERNOLLE. The developments presented here are in any case quite close to the experimental developments of VAN DEN HONERT [19] which are referenced by the authors of [123], and they somewhat constitute a computational parallel to them. Finally, I should mention that the idea for the basis solutions presented hereafter is originally coming from Dr. Esra NEUFELD.

5.3.1 Problem definition, basis solutions, and superposition

We consider a computational domain Ω , representing part or all of a vertebrate body, and:

- $(\hat{T}_j)_j$: a collection of points, lines or surfaces such that \hat{T}_j is in the interior of $\Omega \ \forall j$, and which do not overlap (ie $\hat{T}_j \cap \hat{T}_{j'} = \emptyset \ \forall j \neq j'$).
- $(\tilde{T}_k)_k$: a collection of points, lines or surfaces such that $\tilde{T}_k \subset \partial\Omega \ \forall k$, and which do not overlap.
- $\Gamma_{\mathcal{N}} := \partial\Omega \setminus \left(\bigcup_k \tilde{T}_k\right)$, ie $\Gamma_{\mathcal{N}}$ and $\left(\bigcup_k \tilde{T}_k\right)$ form a partition of $\partial\Omega$.

We denote $(T_i)_{i=0\dots N}$ the combined collection of \hat{T}_j 's and \tilde{T}_k 's, which is of cardinality $N + 1$. An example domain with a boundary such partitioned is depicted on Figure 5.4.

The typical situations covered by this partitioning scheme, and the role of the \hat{T}_j 's, \tilde{T}_k 's and $\Gamma_{\mathcal{N}}$ in each of them, are the following:

1. $\partial\Omega$ represents a distributed return electrode surrounding the stimulated region: in this case, $\Gamma_{\mathcal{N}} = \emptyset$ and there is only one element in the family $(\tilde{T}_k)_k$, $\partial\Omega$ itself, assigned with a null-Dirichlet condition.
2. $\partial\Omega$ represents the skin-air interface *without any* surface cutaneous electrodes: in this case, the family $(\tilde{T}_k)_k$ is empty, and $\Gamma_{\mathcal{N}} = \partial\Omega$ and is assigned with a null-Neumann (insulating) condition.
3. $\partial\Omega$ represents the skin-air interface *with* surface cutaneous electrodes: in this case, the \tilde{T}_k 's represent the surface cutaneous electrodes and $\Gamma_{\mathcal{N}}$ represents the part of the skin free of electrodes.

In each case, the \hat{T}_j 's represent electrical terminals that are strictly in the interior of the studied system.

Possibly, other situations may be covered by this partitioning scheme and by the following approach to represent multipolar configurations. Also, the following mathematical developments assume that the T_i 's are surfaces, but the equations could be adapted in case of unidimensional or punctual terminals.

Basis solutions

Without further ado, let us define V_i (for $1 \leq i \leq N$) the solution of the boundary value problem \mathcal{P}_i , illustrated by Figure 5.5, and characterized by:

$$\mathcal{S}_i \left\{ \begin{array}{ll} \nabla \cdot (\sigma \nabla V) &= 0 & \forall \mathbf{x} \in \Omega \\ \sigma \nabla V(\mathbf{x}) \cdot \mathbf{n}(\mathbf{x}) &= 0 & \forall \mathbf{x} \in \Gamma_{\mathcal{N}} \\ V(\mathbf{x}) &= 1 & \forall \mathbf{x} \in T_i \\ V(\mathbf{x}) &= 0 & \forall \mathbf{x} \in T_j \quad \forall j \neq i \end{array} \right.$$

The V_i 's ($1 \leq i \leq N$) constitute the basis solutions from which one can obtain the potential distributions arising from any voltage or current sources at the T_i 's ($0 \leq i \leq N$), as we shall now see.

Note that we define only N solutions: we do not define a solution V_0 with a unitary Dirichlet condition on T_0 and null-Dirichlet conditions on the other T_i 's, which would be superfluous, as will be shown in the following.

Voltage-controlled multipolar configurations

Considering $V := \sum_i v_i \cdot V_i$ where (v_1, v_2, \dots, v_N) is any sequence of N scalar values, one finds immediately that V is solution of the problem \mathcal{P} characterized by:

$$\mathcal{S} \left\{ \begin{array}{ll} \nabla \cdot (\sigma \nabla V) &= 0 & \forall \mathbf{x} \in \Omega \\ \sigma \nabla V(\mathbf{x}) \cdot \mathbf{n}(\mathbf{x}) &= 0 & \forall \mathbf{x} \in \Gamma_{\mathcal{N}} \\ V(\mathbf{x}) &= 0 & \forall \mathbf{x} \in T_0 \\ V(\mathbf{x}) &= v_i & \forall \mathbf{x} \in T_i \quad \forall i \neq 0 \end{array} \right.$$

Thus, the potential distributions arising from multipolar voltage-controlled configurations involving all of the T_i 's are readily obtained by direct linear combination of the V_i 's. The imposition of 0 V on T_0 does not represent a restriction, since potential distributions differing by spatially-uniform shifts are equivalent with regard to neurophysical simulations (demonstrated in Section 5.3.2).

Current-controlled multipolar configurations

Let us now introduce I_{ij} ($0 \leq j \leq N$) the total amount of current flowing outwards of T_j under the potential distribution V_i . As discussed in Section 2.2.2, when T_j is a surface, I_{ij} is given by:

$$I_{ij} := \int_{T_j} (\sigma_b \nabla V_{i,b}(\mathbf{x}) - \sigma_a \nabla V_{i,a}(\mathbf{x})) \cdot \mathbf{n}_{a,b}(\mathbf{x}) \, ds$$

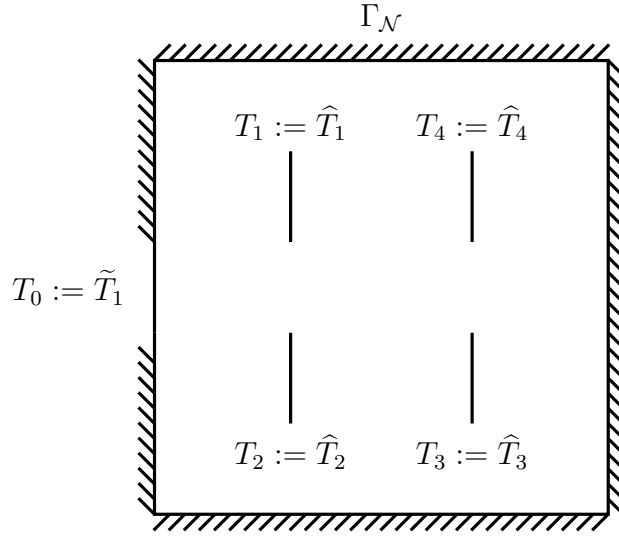


Figure 5.4 Example of domain boundary partition. In this example, the family $(\hat{T}_j)_j$ contains four elements: T_1, T_2, T_3, T_4 . The family $(\tilde{T}_k)_k$ contains one element: T_0 .

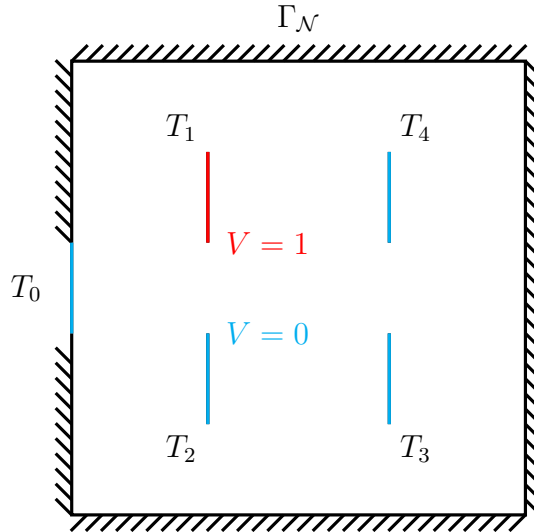


Figure 5.5 Schematic of the boundary conditions defining the basis solutions. The unitary Dirichlet condition is applied on T_1 , and the null Dirichlet conditions on T_0, T_2, T_3 and T_4 .

with the understanding that if $T_j \subset \partial\Omega$, σ on the outside of Ω is null.

Using the divergence theorem, it can be proven that $\sum_{j \geq 0} I_{ij} := 0 \quad \forall i$, which expresses the fact that the net current that is injected through some of the T_j 's is precisely withdrawn by the others. The I_{ij} 's are illustrated in Figure 5.6.

Suppose now that we wish to get a solution V for the potential distribution arising from prescribed current sources at the T_i 's. Here, prescribed current sources refer to prescribed total amounts of current flowing outwards of the T_i 's, not to prescribed current densities imposed at the T_i 's. Furthermore, the prescribed currents have to sum up to 0 A, otherwise the divergence theorem guarantees that the boundary value problem has no solution, regardless of which boundary conditions are used to represent the sources. It is thus only possible to prescribe the amounts of current I_1, I_2, \dots, I_N flowing outwards of T_1, T_2, \dots, T_N , and we obtain as a consequence that the amount of current flowing outwards of T_0 is $I_0 := -\sum_{i \geq 1} I_i$.

Let us search for a linear combination $V := \sum_{i \geq 1} v_i \cdot V_i$ which satisfies these prescriptions. By linearity of the gradient operator and of the integral, we have:

$$\int_{T_j} (\sigma_b \nabla V_b(\mathbf{x}) - \sigma_a \nabla V_a(\mathbf{x})) \cdot \mathbf{n}_{a,b}(\mathbf{x}) \, ds = \sum_{i \geq 1} v_i \int_{T_j} (\sigma_b \nabla V_{i,b}(\mathbf{x}) - \sigma_a \nabla V_{i,a}(\mathbf{x})) \cdot \mathbf{n}_{a,b}(\mathbf{x}) \, ds$$

which yields:

$$I_j = \sum_{i \geq 1} v_i \cdot I_{ij} \quad \forall j = 1 \dots N \quad (5.1)$$

Introducing matrix \mathbf{J} and vectors \mathbf{I} and \mathbf{V} defined as:

$$\mathbf{J} := (I_{ij})_{1 \leq i, j \leq N}^T := \begin{pmatrix} I_{11} & I_{21} & \dots & \dots & I_{N1} \\ I_{12} & I_{22} & \dots & \dots & I_{N2} \\ \vdots & \vdots & \ddots & & \vdots \\ \vdots & \vdots & & \ddots & \vdots \\ I_{1N} & I_{2N} & \dots & \dots & I_{NN} \end{pmatrix} \quad \mathbf{I} := \begin{pmatrix} I_1 \\ I_2 \\ \vdots \\ \vdots \\ I_N \end{pmatrix} \quad \mathbf{V} := \begin{pmatrix} v_1 \\ v_2 \\ \vdots \\ \vdots \\ v_N \end{pmatrix}$$

the linear system summarized by Equation (5.1) can be written in matricial form:

$$\mathbf{I} = \mathbf{J} \cdot \mathbf{V} \quad (5.2)$$

Note that due to the definition of the V_i 's, \mathbf{J} is invertible. To prove it, it suffice to show that if \mathbf{I} is the null-vector, then so must be \mathbf{V} . But if \mathbf{I} is null, this means that the flux of the current density associated to $V := \sum_{i=1}^N v_i \cdot V_i$ is null through every T_j for $1 \leq j \leq N$. Furthermore, V being a linear combination of the V_i 's, it has uniform potential on each of the T_i 's. Thus, V satisfies null-ICCs on every T_i for $1 \leq i \leq N$, a null-Dirichlet condition on T_0 , and an insulating condition anywhere else (on $\Gamma_{\mathcal{N}}$). We can thus conclude that V

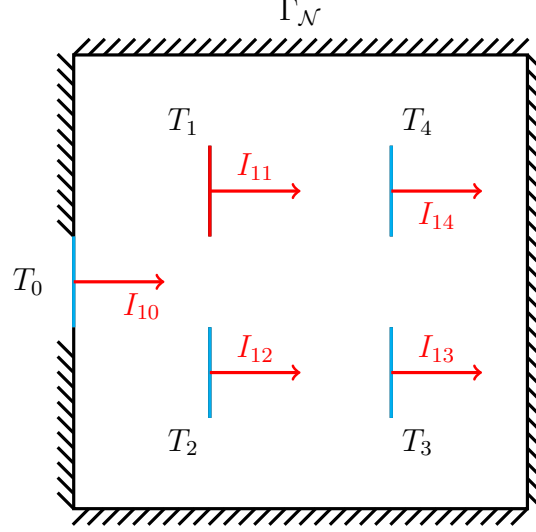


Figure 5.6 Schematic of the currents flowing outwards of the T_i 's. The conditions are the same as in Figure 5.5. The direction of the arrows for I_{10} , I_{12} , I_{13} , I_{14} remind that the latter are outwards current fluxes, although given the conditions of Figure 5.5, the current would in reality be directed towards T_0 , T_2 , T_3 and T_4 .

is identically null by invoking the same arguments as in Section 5.1.2. In particular, V is identically null on the T_i 's, which requires that all the v_i 's be null, *ie* that \mathbf{V} be null.

Therefore \mathbf{J} is invertible, and we can readily obtain the coefficients for a linear combination of the V_i 's satisfying any prescribed currents I_i 's as:

$$\mathbf{V} = \mathbf{J}^{-1} \cdot \mathbf{I}$$

This is nonetheless at the expense of accepting an alternative definition of *current source*, where the latter doesn't designate a uniform current density applied on a surface, but rather an iso-potential source globally delivering a desired amount of current.

Also, note that to prescribe the current flowing out of T_0 , it suffice to adjust the currents flowing out of the other terminals.

Mixed multipolar configurations

Finally, it is also possible to obtain a solution for the potential distribution satisfying a voltage prescription on some T_i 's, and a current prescription on the others. For that, denote $X := \{i_1, i_2, \dots, i_k\}$ the set of indices of the terminals for which the voltage is prescribed instead of the current, and permute the lines of \mathbf{J} and \mathbf{I} such that $i_1 \rightarrow 1$, $i_2 \rightarrow 2$, \dots , $i_k \rightarrow k$. In the equation $\mathbf{I} = \mathbf{J} \cdot \mathbf{V}$ the unknowns are the first k entries of \mathbf{I} and the last $N - k$ entries of \mathbf{V} . If we reflect that split by denoting $\mathbf{I} = (\mathbf{I}_a | \mathbf{I}_b)$, $\mathbf{V} = (\mathbf{V}_a | \mathbf{V}_b)$, and the sub-blocks of \mathbf{J} as $\mathbf{J}_{a,a}$, $\mathbf{J}_{a,b}$, $\mathbf{J}_{b,a}$, and $\mathbf{J}_{b,b}$, we obtain a system of

matricial equations:

$$\begin{cases} \mathbf{I}_a &= \mathbf{J}_{a,a} \cdot \mathbf{V}_a + \mathbf{J}_{a,b} \cdot \mathbf{V}_b \\ \mathbf{I}_b &= \mathbf{J}_{b,a} \cdot \mathbf{V}_a + \mathbf{J}_{b,b} \cdot \mathbf{V}_b \end{cases}$$

This can be solved by computing $\mathbf{V}_b = \mathbf{J}_{b,b}^{-1} \cdot (\mathbf{I}_b - \mathbf{J}_{b,a} \cdot \mathbf{V}_a)$ using the second equation (inversion), and then evaluating the first equation (forward multiplication).

Note With the approach just presented, representing voltage-controlled, current-controlled, or mixed electrical sources involving $N + 1$ terminals only require N basis solutions. For current-controlled configurations, this is a mere reflection of the current conservation ensuing from the assumption of stationarity of the problem, which implies that the current flowing through the $(N + 1)$ -th terminal amounts to the negative sum of the current flows through the N others. For voltage-controlled configurations, it results from the physical equivalence of potential distributions differing by spatially-uniform offsets, which permits to arbitrarily set the potential of one of the terminals to zero, and which is without consequences for subsequent neurophysical simulations, as shall be demonstrated now.

5.3.2 Neurophysical models and equivalent potential distributions

In order to prove the theoretical validity of the previous approach for its use in hybrid neurophysical volume conductor models, we need to prove that potential distributions differing by spatially-uniform shifts are equivalent with respect to neurophysical simulations.

Indeed, although two such potential distributions are theoretically equivalent from the physics point of view (see Section 2.1), the computational scheme of neurophysical simulators may *a priori* not treat them equivalently.

I demonstrate this equivalence in the case of the open-source simulator NEURON [114], when the application of an external electrical stimulation is represented via the batteries of the second layer of the **extracellular** mechanism.

Electrical circuit

To represent externally applied voltages, NEURON uses the **extracellular** mechanism, which can also be used to represent a myelin sheath wrapping an axon. For instance, the electrical circuit of the MRG model presented in Section 2.3.1 corresponds exactly to its implementation in NEURON with the **extracellular** mechanism used. Specifically, in Figure 2.1, the second and third horizontal levels (from bottom to top), as well as the vertical components joining the second to third and third to fourth levels are all part of the **extracellular** mechanism.

Here I will consider an abstract portion of neurite made of three linearly-connected compartments with the **extracellular** mechanism included, as depicted in Figure 5.7. I will assume that the vertical components joining the second and third levels represent an eventual myelin sheath, and that the conductances $G_{x,X}^2$ are numerically infinite (making them act as short-circuits), and the conductances $G_{xr,X}^2$ and capacitances $C_{x,X}^2$ are null (making them act as open-circuits). I will nonetheless keep on representing them to show their role in the numerical integration scheme of NEURON.

In the membrane of each compartment, I included a single serial arrangement comprising a voltage-dependent conductance and battery in parallel to the capacitance, thus representing a single ion channel with its associated reversal potential. This is to avoid writing unnecessarily heavy equations, but the following developments would be valid for any number of parallel such serial arrangements.

State variables and differential equations

For NEURON, the variables to be solved for are the voltage drops $U_{K_i}^0$, $U_{K_i}^1$ and $U_{K_i}^2$, and their equivalents for the other compartments. The potentials at the nodes K_i^0 , K_i^1 and

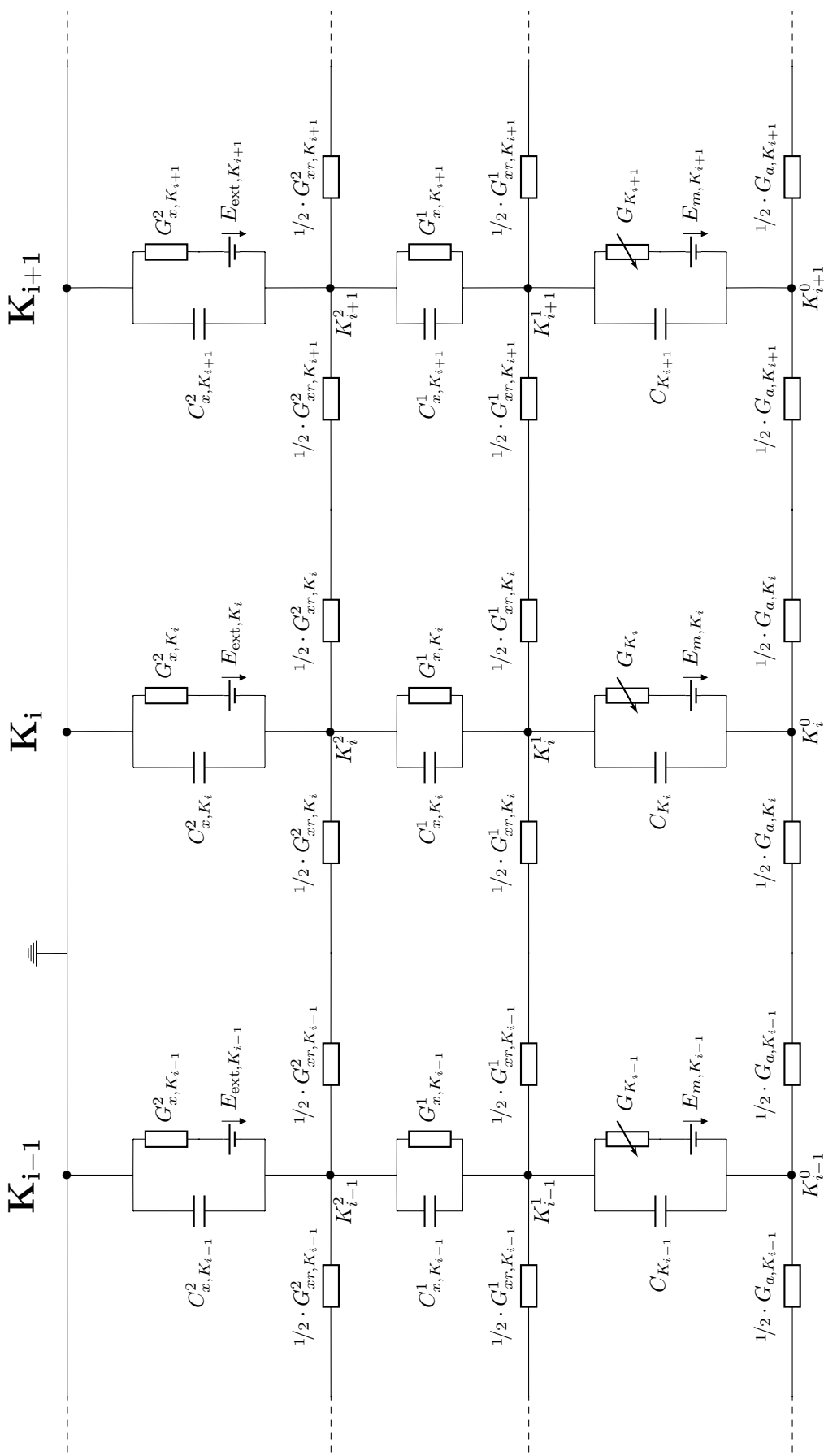


Figure 5.7 Electrical circuit of a generic compartmental neuron model including the extracellular mechanism in NEURON.

K_i^2 are estimated via simple algebraic relations:

$$\left\{ \begin{array}{lcl} V_{K_i}^2 & = & U_{K_i}^2 \\ V_{K_i}^1 & = & V_{K_i}^2 + U_{K_i}^1 \\ V_{K_i}^0 & = & V_{K_i}^1 + U_{K_i}^0 \end{array} \right. = \left\{ \begin{array}{lcl} U_{K_i}^2 & = & U_{K_i}^2 \\ U_{K_i}^2 + U_{K_i}^1 & = & U_{K_i}^2 + U_{K_i}^1 \\ U_{K_i}^2 + U_{K_i}^1 + U_{K_i}^0 & = & U_{K_i}^2 + U_{K_i}^1 + U_{K_i}^0 \end{array} \right.$$

Applying Kirschhoff's law at K_i^0 , K_i^1 and K_i^2 we obtain three ordinary differential equations coupling the voltage drops of the three compartments.

At K_i^0 :

$$\begin{aligned} C_{K_i} \frac{dU_{K_i}^0}{dt} &= - G_{K_i} \left\{ U_{K_i}^0 \right\} \cdot \left(U_{K_i}^0 - E_{m,K_i} \right) \\ &+ G_{a,K_i K_{i-1}} \cdot \left(U_{K_{i-1}}^0 + U_{K_{i-1}}^1 + U_{K_{i-1}}^2 - U_{K_i}^0 - U_{K_i}^1 - U_{K_i}^2 \right) \\ &+ G_{a,K_i K_{i+1}} \cdot \left(U_{K_{i+1}}^0 + U_{K_{i+1}}^1 + U_{K_{i+1}}^2 - U_{K_i}^0 - U_{K_i}^1 - U_{K_i}^2 \right) \end{aligned} \quad (5.3)$$

At K_i^1 :

$$\begin{aligned} C_{x,K_i}^1 \frac{dU_{K_i}^1}{dt} &= C_{K_i} \frac{dU_{K_i}^0}{dt} + G_{K_i} \left\{ U_{K_i}^0 \right\} \cdot \left(U_{K_i}^0 - E_{m,K_i} \right) - G_{x,K_i}^1 \cdot U_{K_i}^1 \\ &+ G_{xr,K_i K_{i-1}}^1 \cdot \left(U_{K_{i-1}}^1 + U_{K_{i-1}}^2 - U_{K_i}^1 - U_{K_i}^2 \right) \\ &+ G_{xr,K_i K_{i+1}}^1 \cdot \left(U_{K_{i+1}}^1 + U_{K_{i+1}}^2 - U_{K_i}^1 - U_{K_i}^2 \right) \end{aligned} \quad (5.4)$$

At K_i^2 :

$$\begin{aligned} C_{x,K_i}^2 \frac{dU_{K_i}^2}{dt} &= C_{x,K_i}^1 \frac{dU_{K_i}^1}{dt} + G_{x,K_i}^1 \cdot U_{K_i}^1 - G_{x,K_i}^2 \cdot \left(U_{K_i}^2 - E_{\text{ext},K_i} \right) \\ &+ G_{xr,K_i K_{i-1}}^2 \cdot \left(U_{K_{i-1}}^2 - U_{K_i}^2 \right) \\ &+ G_{xr,K_i K_{i+1}}^2 \cdot \left(U_{K_{i+1}}^2 - U_{K_i}^2 \right) \end{aligned} \quad (5.5)$$

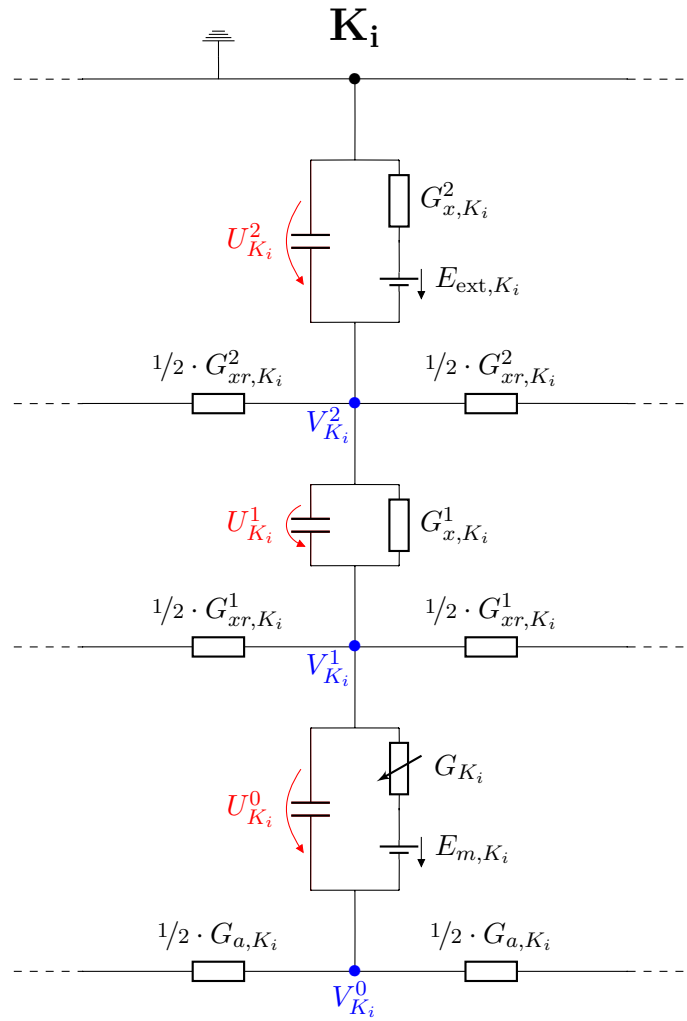


Figure 5.8 In NEURON, the state variables subjected to numerical integration are the voltage drops (in red). Node potentials (in blue) can be deduced from the latter by algebraic relationships.

In the above equations, we have noted:

$$\left\{ \begin{array}{lcl} G_{a,K_i K_{i-1}} & = & 1/2 \cdot G_{a,K_i} + 1/2 \cdot G_{a,K_{i-1}} \\ G_{a,K_i K_{i+1}} & = & 1/2 \cdot G_{a,K_i} + 1/2 \cdot G_{a,K_{i+1}} \\ G_{xr,K_i K_{i-1}}^1 & = & 1/2 \cdot G_{xr,K_i}^1 + 1/2 \cdot G_{xr,K_{i-1}}^1 \\ G_{xr,K_i K_{i+1}}^1 & = & 1/2 \cdot G_{xr,K_i}^1 + 1/2 \cdot G_{xr,K_{i+1}}^1 \\ G_{xr,K_i K_{i-1}}^2 & = & 1/2 \cdot G_{xr,K_i}^2 + 1/2 \cdot G_{xr,K_{i-1}}^2 \\ G_{xr,K_i K_{i+1}}^2 & = & 1/2 \cdot G_{xr,K_i}^2 + 1/2 \cdot G_{xr,K_{i+1}}^2 \end{array} \right.$$

Numerical integration

By default, NEURON employs a numerical integration scheme which is equivalent to the Crank-Nicholson or central difference method. It consists in splitting the integration steps into two steps: the first using the backward Euler method, and the second being a linear forward projection.

Denoting Δt the time-step of the simulation, the second step simply boils down to estimating:

$$X(t + \Delta t) := 2 \cdot X\left(t + \frac{\Delta t}{2}\right) - X(t)$$

where X denotes any state variable solved for by the numerical solver.

Thus, the effort resides in estimating $X\left(t + \frac{\Delta t}{2}\right)$ using the backward Euler method.

In backward Euler, Equations (5.3) to (5.5) are written at time $t + \Delta t/2$, and the time derivatives are evaluated as finite differences between time t and time $t + \Delta t/2$. The only exception is the evaluation of $G_{K_i}\{U_{K_i}^0\}$, which is done using $U_{K_i}^0(t)$ instead of $U_{K_i}^0(t + \Delta t/2)$.

Discretizing the equations in this way, one can form a linear system writing $\mathbf{A}(t) \cdot \mathbf{U}(t + \Delta t/2) = \mathbf{U}(t)$, where $\mathbf{U}(t + \Delta t/2)$ regroups the unknown values of the state variables at time $t + \Delta t/2$, which can thus be obtained via a matrix inversion and multiplication.

In the following, I will denote $t_k := k \cdot \Delta t$, and I will abbreviate $X(t_k)$ into $X(k)$ for any time-dependent variable X .

Cancellation of uniform potential distributions

Applying the mentioned discretization to Equation (5.5) yields:

$$\begin{aligned}
C_{x,K_i}^2 \frac{U_{K_i}^2(k+1/2) - U_{K_i}^2(k)}{\Delta t/2} &= C_{x,K_i}^1 \frac{U_{K_i}^1(k+1/2) - U_{K_i}^1(k)}{\Delta t/2} \\
&+ G_{x,K_i}^1 \cdot U_{K_i}^1(k+1/2) - G_{x,K_i}^2 \cdot \left(U_{K_i}^2(k+1/2) - E_{\text{ext},K_i} \right) \\
&+ G_{xr,K_i K_{i-1}}^2 \cdot \left(U_{K_{i-1}}^2(k+1/2) - U_{K_i}^2(k+1/2) \right) \quad (5.6) \\
&+ G_{xr,K_i K_{i+1}}^2 \cdot \left(U_{K_{i+1}}^2(k+1/2) - U_{K_i}^2(k+1/2) \right)
\end{aligned}$$

We now suppose that we impose a uniform extracellular potential distribution V_0 to our model. That is, at the end of the integration step leading to time t_k , and before starting the integration step leading to time $t_{k+1/2}$, we set $E_{\text{ext},K_i} = E_{\text{ext},K_{i-1}} = E_{\text{ext},K_{i+1}} = V_0$.

Thus, in Equation (5.6), we actually have $E_{\text{ext},K_i} = V_0$. Moreover, since G_{x,K_i}^2 is assumed to be numerically infinite, Equation (5.6) reduces to:

$$U_{K_i}^2(k+1/2) = V_0 \quad (5.7)$$

For the same reason, we also have $U_{K_{i-1}}^2(k+1/2) = V_0$ and $U_{K_{i+1}}^2(k+1/2) = V_0$.

Let us now examine the discretized version of Equation (5.4):

$$\begin{aligned}
C_{x,K_i}^1 \frac{U_{K_i}^1(k+1/2) - U_{K_i}^1(k)}{\Delta t/2} &= C_{K_i} \frac{U_{K_i}^0(k+1/2) - U_{K_i}^0(k)}{\Delta t/2} \\
&+ G_{K_i} \left\{ U_{K_i}^0(k) \right\} \cdot \left(U_{K_i}^0(k+1/2) - E_{m,K_i} \right) - G_{x,K_i}^1 \cdot U_{K_i}^1(k+1/2) \quad (5.8) \\
&+ G_{xr,K_i K_{i-1}}^1 \cdot \left(U_{K_{i-1}}^1(k+1/2) + U_{K_{i-1}}^2(k+1/2) - U_{K_i}^1(k+1/2) - U_{K_i}^2(k+1/2) \right) \\
&+ G_{xr,K_i K_{i+1}}^1 \cdot \left(U_{K_{i+1}}^1(k+1/2) + U_{K_{i+1}}^2(k+1/2) - U_{K_i}^1(k+1/2) - U_{K_i}^2(k+1/2) \right)
\end{aligned}$$

Since we have $U_{K_i}^2(k+1/2) = U_{K_{i-1}}^2(k+1/2) = U_{K_{i+1}}^2(k+1/2) = V_0$, Equation (5.8) can be written:

$$\begin{aligned}
 C_{x,K_i}^1 \frac{U_{K_i}^1(k+1/2) - U_{K_i}^1(k)}{\Delta t/2} &= C_{K_i} \frac{U_{K_i}^0(k+1/2) - U_{K_i}^0(k)}{\Delta t/2} \\
 &+ G_{K_i} \left\{ U_{K_i}^0(k) \right\} \cdot \left(U_{K_i}^0(k+1/2) - E_{m,K_i} \right) - G_{x,K_i}^1 \cdot U_{K_i}^1(k+1/2) \\
 &+ G_{xr,K_i K_{i-1}}^1 \cdot \left(U_{K_{i-1}}^1(k+1/2) + \mathbf{V}_0 - U_{K_i}^1(k+1/2) - \mathbf{V}_0 \right) \\
 &+ G_{xr,K_i K_{i+1}}^1 \cdot \left(U_{K_{i+1}}^1(k+1/2) + \mathbf{V}_0 - U_{K_i}^1(k+1/2) - \mathbf{V}_0 \right)
 \end{aligned}$$

which is equivalent to:

$$\begin{aligned}
 C_{x,K_i}^1 \frac{U_{K_i}^1(k+1/2) - U_{K_i}^1(k)}{\Delta t/2} &= C_{K_i} \frac{U_{K_i}^0(k+1/2) - U_{K_i}^0(k)}{\Delta t/2} \\
 &+ G_{K_i} \left\{ U_{K_i}^0(k) \right\} \cdot \left(U_{K_i}^0(k+1/2) - E_{m,K_i} \right) - G_{x,K_i}^1 \cdot U_{K_i}^1(k+1/2) \\
 &+ G_{xr,K_i K_{i-1}}^1 \cdot \left(U_{K_{i-1}}^1(k+1/2) + \mathbf{0} - U_{K_i}^1(k+1/2) - \mathbf{0} \right) \\
 &+ G_{xr,K_i K_{i+1}}^1 \cdot \left(U_{K_{i+1}}^1(k+1/2) + \mathbf{0} - U_{K_i}^1(k+1/2) - \mathbf{0} \right)
 \end{aligned}$$

which is the very equation that we would have, had we not imposed V_0 to each compartment, but let the $E_{\text{ext},X}$'s equal to 0 V instead.

Similarly, the discretized Kirschhoff equations written at nodes K_{i-1}^1 and K_{i+1}^1 are *unaffected* by the applied uniform potential V_0 . And this is also the case of the discretized equations written at nodes K_{i-1}^0 , K_i^0 and K_{i+1}^0 .

Consequently, the integration step will yield the exact same values for each of $U_{K_{i-1}}^1$, $U_{K_i}^1$, $U_{K_{i+1}}^1$, $U_{K_{i-1}}^0$, $U_{K_i}^0$ and $U_{K_{i+1}}^0$ at time $k+1/2$ than if the $E_{\text{ext},X}$'s had been kept equal to 0 V. And this will propagate to the subsequent time-steps.

Conclusion

The previous developments could as well have been led by considering an extracellular potential distribution of the form $V + V_0$ where V were non-uniform and V_0 were uniform: we would have concluded that the presence or absence of V_0 would yield the same results for $U_{K_{i-1}}^1$, $U_{K_i}^1$, $U_{K_{i+1}}^1$, $U_{K_{i-1}}^0$, $U_{K_i}^0$ and $U_{K_{i+1}}^0$.

The only state variables that would be affected are $U_{K_{i-1}}^2$, $U_{K_i}^2$ and $U_{K_{i+1}}^2$, which would be shifted by the amount V_0 . In consequence, the node potentials would also be shifted by V_0 , but the membrane potential, represented by $U_{K_{i-1}}^0$, $U_{K_i}^0$ and $U_{K_{i+1}}^0$, would be unaffected.

This holds true in the case of a model comprising an arbitrary number of compartments, including when connected non-linearly.

Therefore, potential distributions differing by spatially-uniform shifts are equivalent with respect to neurophysical simulations involving nerve fiber and neuron models such as implemented in NEURON with the `extracellular` mechanism.

CHAPTER 6 CONCLUSION

This thesis has been driven by one main objective: developing a conceptual framework to study and develop applications of EES of the cervical spinal cord for the restoration of motor function in the upper-limb. This research subject was inspired by the success met by a similar framework, developed to study EES of the lumbo-sacral spinal cord, which has proved very valuable for the development of clinical applications for the restoration of lower-limb function.

I mostly set myself to develop a realistic hybrid model of EES of the cervical spinal cord, with the aim to assess the selectivity with which cervical EES can modulate specific upper-limb motor nuclei, and to identify the anatomical elements conditioning this selectivity. My developments and investigations led me to implement refinements in these models whose scope extend beyond the specific case of EES and the cervical spinal cord.

6.1 Summary of works

I have conceived an abstract geometrical model of the spinal cord and the surrounding tissues of the vertebral canal, which can be used to represent any portion of the spinal cord, of any species, and for any given dimensions and shapes of the represented structures (within reasonable limits). This model notably includes a representation of the spinal roots and a detailed compartmentalization of the white and gray matters, allowing the definition of realistic trajectories of spinal nerve fibers and motoneurons. Accordingly, I also conceived new geometrical models for the latter.

I implemented these models in an open-source software suite, freely accessible from an online repository. This suite, relying on Matlab and COMSOL, constitutes an integrated tool to build volume conductor models of electrical stimulation of the spinal cord. I have complemented it by another software suite allowing to perform neurophysical simulations on the very neurons and nerve fibers represented in the previous volume conductor models. This one, written in Python and relying on the neuro-simulator NEURON, is also available from an open-access online repository.

I have then used these tools to build a realistic hybrid model of EES of the macaque monkey cervical spinal cord. I first used it to assess the influence of novelties introduced in the volume conductor model, namely: the spinal roots, the silicone paddle of an epidural electrode array, and realistic trajectories of dorsal root primary afferents. The representation of the spinal roots with fully-fledged compartments in the volume conductor was shown to have very little influence on hybrid model predictions. By contrast, representing the paddle led to a 2-fold increase of the volume conductor impedance between the active

and return electrodes, and significantly decreased the excitation thresholds of dorsal root and dorsal column fibers. The morphology and trajectories of dorsal root afferents were also shown to be of importance to estimate the segmental selectivity of EES, justifying the developments undertaken to refine their representation.

I then used the model to investigate the proper specificities of cervical EES. In line with previous findings, simulations indicated that dorsal root and dorsal column fibers constitute the primary targets of cervical EES, the direct recruitment of motor axons requiring significantly higher stimulation amplitudes. Placing electrodes laterally in the epidural space, facing individual roots, resulted in perfect segmental selectivity. With medially-positioned electrodes, the segmental selectivity dropped. Furthermore, assessment of the Ia-mediated synaptic excitation of motoneurons suggested that a purely trans-synaptic, Ia-driven recruitment of motoneurons is plausible during cervical EES.

Electrophysiological experiments conducted in macaque monkeys corroborated these insights. EES delivered from lateral electrodes using custom epidural implants tailored to the cervical spinal cord of the macaque monkey induced muscular responses in a segmental-selective way. However, the specificity of the recruitment was limited, which could be explained by the intermingling of different populations of afferent fibers in the dorsal roots. By contrast, medial stimulation induced more chaotic muscular responses, in line with a recruitment of dorsal column fibers conveying excitatory synaptic inputs to widespread populations of motoneurons. High-frequency trains of stimulation pulses led to modulations of evoked compound muscle action potentials characteristic of a pre-synaptic recruitment of motoneurons, strengthening this hypothesis regarding the nature of the recruitment.

Analysis of intra-operative clinical data suggested that recruitment of upper-limb motoneurons with cervical EES in humans is also mediated by pre-synaptic pathways. Furthermore, comparative analysis of the dimensions of spinal cord and epidural electrode arrays in monkeys and humans indicated that current clinical epidural implants may be unfit to achieve selective modulation of upper-limb motoneurons with cervical EES, providing indications for the design of epidural arrays tailored for the restoration of upper-limb function.

Finally, I have reviewed the strategies employed to represent multipolar stimulation configurations in hybrid models and I have developed a new general, economic approach that is justified on the theoretical ground. This approach can be employed to efficiently explore the wide spaces of stimulation configurations of multi-electrode arrays and find optimal configurations to target specific neural structures. In particular, it could be used to find multipolar configurations targeting specific cervical dorsal rootlets to refine the modulation exerted by EES on upper-limb motoneurons.

6.2 Limitations and future research

This work, and the study of cervical EES with hybrid models in general, are subjected to limitations. In the following paragraphs, I discuss those limitations which seem most important to me.

6.2.1 Intrinsic limitations of hybrid models

By essence, the computational scheme of hybrid models entails a fundamental assumption, already discussed in Section 2.1: it assumes that biological electrical current sources are negligible compared to artificial current sources (by setting the volumetric current source to zero in Poisson's equation, Equation (2.11)), such that the eventual activity induced in one neuron or nerve fiber during electrical stimulation is without effect on the fate of the others. In short, it neglects any *ephaptic coupling* between neighboring neurons [125].

The validity of this assumption has recently been challenged by a study by Tveito and colleagues [126], which revealed via an integrated computational scheme the potentially large influence of this coupling on simulation predictions. Tveito and colleagues used a very simple two-dimensional model, featuring two parallel and close-by unmyelinated nerve fibers plunged in a small rectangular box. In particular, due to the absence of myelin sheath, activity in any part of the two fibers induced fluctuations of the potential in the neighboring extracellular space, and thus all along the fibers. In the case of fiber tracts like the dorsal columns or spinal roots, and in the range of stimulation amplitudes used *eg* with EES, the fibers whose activity is involved are myelinated, and the influence of their activity on the extracellular milieu should be localized at the sparsely distributed nodes of Ranvier. Therefore, ephaptic coupling might be of smaller influence in this context. Besides, the difficulty of implementing integrated computational schemes with realistic tridimensional geometries, but also the colossal computational cost of the latter, acknowledged by Tveito and colleagues themselves, imply that hybrid models remain valuable computational tools to study electrical stimulation of the nervous system.

Nonetheless, the influence of ephaptic coupling between myelinated nerve fibers in tridimensional geometries, such as involved in EES of the spinal cord, should be assessed in future works.

6.2.2 Geometry meshing

One limitation in building realistic tridimensional volume conductor models resides in the difficulty to build and mesh the geometrical volumes representing the different compartments of the model. In this work, I have represented complex structures defined by surfaces interpolating cross-sectional contours which sometimes had very different shapes

(*eg* for the gray matter) or were not lying in parallel planes (*eg* for the spinal roots). Modern computer-aided design programs (such as COMSOL and FreeCAD, used in this work) are capable of handling many various types of geometric objects and many geometric file formats, and they allow to perform boolean operations like unions, intersections or differences on multiple objects, enabling to assemble complex geometries almost automatically. Moreover, COMSOL also allows automatic meshing of these geometries. However, this process is very error-prone and requires many manual fine-tunings of the geometrical parameters onto which the model is based.

This was the case for the construction of the volume conductor of the macaque monkey cervical spinal cord presented in Section 4.2. In particular, I couldn't assess the influence of the fineness of the mesh on the computed electric potential distributions. Usually, the geometry mesh is refined until the variations of the computed solutions in the regions of interest become insignificant [42, 127]. However, the number of elements in the mesh of the model used here was very high (~ 10 millions), especially near the electrodes, in the spinal roots and dorsal columns, and in the region of space between the two. Thus I expect that refining the mesh would not have yielded substantially different results. Nonetheless, future works should be dedicated to finding appropriate computer representations of the modeled compartments, to limit the errors in the geometry and mesh construction processes.

6.2.3 Micro-anatomy of the cervical spinal cord

At present, many unknowns remain regarding the micro-anatomy of the cervical spinal cord. First and of prime importance to cervical EES, the precise distribution of primary afferents from upper-limb muscles in the cervical spinal roots remain largely unknown. Yet, although the results of Chapter 4 tend to confirm the assumption that primary afferents are distributed similarly to their homonymous motoneurons in the spinal segments, a more reliable information is crucial to the theoretical study of EES, but also practically for the design of electrode arrays and for the positioning of these arrays in the spinal epidural space. Moreover, analysis of the Ia-mediated excitation of motoneurons (Section 4.2.3) revealed that the Ia-fiber headcount of a muscle may also play a significant role in the excitability of its motor nucleus via cervical EES, which may limit the applicability of EES to engage certain muscles, and ought to be known. Heteronymous connections between Ia-fibers and motoneurons, which can straightforwardly be included in the hybrid model which I have developed, and which are also likely to be of great importance in the engagement of cervical motoneurons with EES, are also largely undocumented. Establishing the quantitative anatomical libraries describing these distributions and connections in the non-human primate, phylogenetically very close to humans [57], would be of prominent value to any future research in cervical EES and seems a priority research objective to me.

6.2.4 Experimental validation of simulation results

Finally, one tricky issue is the confrontation of hybrid model predictions to experimental data. The output of hybrid models often consists in estimations of the direct recruitment of neurons and nerve fibers, and sometimes of the trans-synaptic recruitment of motoneurons via additional assumptions regarding the connectivity between nerve fibers and motoneurons [60, 79]. Ideally, intracellular recordings of neurons and nerve fibers would be needed to verify these predictions. However, direct recordings of afferent activity in humans is limited to few individual fibers [128], and not directly in the spinal cord [129]. In animal models, intra- or extracellular recordings of dorsal root ganglia neurons or spinal motoneurons could be achieved, but simultaneously stimulating the spinal cord from the epidural space makes it a delicate and challenging experiment. Moreover the recording apparatus may interfere with the stimulation, compromising the relevance of the recorded signals.

In the work presented here, the only source of experimental validation was provided by the EMG recordings of upper-limb muscles of macaque monkeys. I tried to use them for comparison with simulated motoneuronal recruitments, but such comparisons were limited by two important factors: (i) the transfer function between motoneuronal recruitment and compound muscle action potential amplitude is unknown and is dependent on the recording system (notably the type and placement of the recording electrodes), and (ii) whether or not the maximal EMG signals which we recorded corresponded to maximal muscular activations was also unknown. Yet, this second piece of information would already improve our interpretation of recorded EMG signals, and future investigations should include measures to acquire the EMG signals corresponding to maximal muscle contractions (*eg* via direct electrical stimulation of muscles until saturation) in their experimental protocols.

REFERENCES

- [1] B. B. Lee *et al.*, “The global map for traumatic spinal cord injury epidemiology: update 2011, global incidence rate,” *Spinal Cord*, vol. 52, no. 2, pp. 110–116, Feb. 2014. [Online]. Available: <http://www.nature.com/articles/sc2012158>
- [2] N. S. C. I. S. Center, “Facts and Figures at a Glance,” 2019.
- [3] S. Hou and A. G. Rabchevsky, “Autonomic consequences of spinal cord injury,” *Comprehensive Physiology*, vol. 4, no. 4, pp. 1419–1453, Oct. 2014.
- [4] A. S. Burns *et al.*, “Clinical diagnosis and prognosis following spinal cord injury,” *Handbook of Clinical Neurology*, vol. 109, pp. 47–62, 2012.
- [5] K. D. Anderson, “Targeting Recovery: Priorities of the Spinal Cord-Injured Population,” *Journal of Neurotrauma*, vol. 21, no. 10, pp. 1371–1383, Oct. 2004. [Online]. Available: <http://www.liebertpub.com/doi/10.1089/neu.2004.21.1371>
- [6] E. R. Kandel, Ed., *Principles of neural science*, 5th ed. New York: McGraw-Hill, 2013.
- [7] C. Fabricius, C. H. Berthold, and M. Rydmark, “Dimensions of individual alpha and gamma motor fibres in the ventral funiculus of the cat spinal cord,” *Journal of Anatomy*, vol. 184 (Pt 2), pp. 319–333, Apr. 1994.
- [8] W. H. Organization and I. S. C. Society, Eds., *International perspectives on spinal cord injury*. Geneva, Switzerland: World Health Organization, 2013, oCLC: ocn871342223.
- [9] M. Pérez Rubiralta, “Intradural and extradural dorsal spinal pediatric lesions,” p. 3664 words, 2015. [Online]. Available: <http://epos.myesr.org/poster/ecr2015/C-2520>
- [10] B. Solmaz *et al.*, “Intradural communication between dorsal rootlets of spinal nerves: their clinical significance,” *Acta Neurochirurgica*, vol. 157, no. 6, pp. 1069–1076; discussion 1076, Jun. 2015.
- [11] R. E. Burke and L. L. Glenn, “Horseradish peroxidase study of the spatial and electrotonic distribution of group Ia synapses on type-identified ankle extensor motoneurons in the cat,” *The Journal of Comparative Neurology*, vol. 372, no. 3, pp. 465–485, Aug. 1996.

- [12] A. G. Brown and R. E. Fyffe, "The morphology of group Ia afferent fibre collaterals in the spinal cord of the cat," *The Journal of Physiology*, vol. 274, pp. 111–127, Jan. 1978.
- [13] R. E. Fyffe, "The morphology of group II muscle afferent fibre collaterals [proceedings]," *The Journal of Physiology*, vol. 296, pp. 39P–40P, Nov. 1979.
- [14] J. F. Iles, "Central terminations of muscle afferents on motoneurons in the cat spinal cord." *The Journal of Physiology*, vol. 262, no. 1, pp. 91–117, Oct. 1976. [Online]. Available: <http://doi.wiley.com/10.1113/jphysiol.1976.sp011587>
- [15] E. Jankowska, "Interneuronal relay in spinal pathways from proprioceptors," *Progress in Neurobiology*, vol. 38, no. 4, pp. 335–378, Apr. 1992. [Online]. Available: <https://linkinghub.elsevier.com/retrieve/pii/0301008292900249>
- [16] J. C. Eccles, R. M. Eccles, and A. Lundberg, "The convergence of monosynaptic excitatory afferents on to many different species of alpha motoneurons," *The Journal of Physiology*, vol. 137, no. 1, pp. 22–50, Jun. 1957.
- [17] D. R. Merrill, M. Bikson, and J. G. R. Jefferys, "Electrical stimulation of excitable tissue: design of efficacious and safe protocols," *Journal of Neuroscience Methods*, vol. 141, no. 2, pp. 171–198, Feb. 2005.
- [18] J. Ladenbauer *et al.*, "Stimulation of the human lumbar spinal cord with implanted and surface electrodes: a computer simulation study," *IEEE transactions on neural systems and rehabilitation engineering: a publication of the IEEE Engineering in Medicine and Biology Society*, vol. 18, no. 6, pp. 637–645, Dec. 2010.
- [19] C. van den Honert and D. C. Kelsall, "Focused intracochlear electric stimulation with phased array channels," *The Journal of the Acoustical Society of America*, vol. 121, no. 6, p. 3703, 2007. [Online]. Available: <http://scitation.aip.org/content/asa/journal/jasa/121/6/10.1121/1.2722047>
- [20] S. F. Lempka and P. G. Patil, "Innovations in spinal cord stimulation for pain," *Current Opinion in Biomedical Engineering*, vol. 8, pp. 51–60, Dec. 2018.
- [21] J. L. Collinger *et al.*, "Neuroprosthetic technology for individuals with spinal cord injury," *The Journal of Spinal Cord Medicine*, vol. 36, no. 4, pp. 258–272, Jul. 2013.
- [22] M. O. Krucoff *et al.*, "Enhancing Nervous System Recovery through Neurobiologics, Neural Interface Training, and Neurorehabilitation," *Frontiers in Neuroscience*, vol. 10, Dec. 2016. [Online]. Available: <http://journal.frontiersin.org/article/10.3389/fnins.2016.00584/full>

- [23] C. A. Angeli *et al.*, “Recovery of Over-Ground Walking after Chronic Motor Complete Spinal Cord Injury,” *The New England Journal of Medicine*, vol. 379, no. 13, pp. 1244–1250, 2018.
- [24] R. van den Brand *et al.*, “Restoring voluntary control of locomotion after paralyzing spinal cord injury,” *Science (New York, N.Y.)*, vol. 336, no. 6085, pp. 1182–1185, Jun. 2012.
- [25] M. Capogrosso *et al.*, “A brain-spine interface alleviating gait deficits after spinal cord injury in primates,” *Nature*, vol. 539, no. 7628, pp. 284–288, 2016.
- [26] G. Courtine *et al.*, “Transformation of nonfunctional spinal circuits into functional states after the loss of brain input,” *Nature Neuroscience*, vol. 12, no. 10, pp. 1333–1342, Oct. 2009.
- [27] M. L. Gill *et al.*, “Neuromodulation of lumbosacral spinal networks enables independent stepping after complete paraplegia,” *Nature Medicine*, vol. 24, no. 11, pp. 1677–1682, 2018.
- [28] S. Harkema *et al.*, “Effect of epidural stimulation of the lumbosacral spinal cord on voluntary movement, standing, and assisted stepping after motor complete paraplegia: a case study,” *The Lancet*, vol. 377, no. 9781, pp. 1938–1947, Jun. 2011. [Online]. Available: <https://linkinghub.elsevier.com/retrieve/pii/S0140673611605473>
- [29] R. M. Ichiyama *et al.*, “Hindlimb stepping movements in complete spinal rats induced by epidural spinal cord stimulation,” *Neuroscience Letters*, vol. 383, no. 3, pp. 339–344, Aug. 2005.
- [30] F. B. Wagner *et al.*, “Targeted neurotechnology restores walking in humans with spinal cord injury,” *Nature*, vol. 563, no. 7729, pp. 65–71, Nov. 2018. [Online]. Available: <http://www.nature.com/articles/s41586-018-0649-2>
- [31] N. Wenger *et al.*, “Spatiotemporal neuromodulation therapies engaging muscle synergies improve motor control after spinal cord injury,” *Nature Medicine*, vol. 22, no. 2, pp. 138–145, Feb. 2016. [Online]. Available: <http://www.nature.com/articles/nm.4025>
- [32] D. C. Lu *et al.*, “Engaging Cervical Spinal Cord Networks to Reenable Volitional Control of Hand Function in Tetraplegic Patients,” *Neurorehabilitation and Neural Repair*, vol. 30, no. 10, pp. 951–962, 2016.

- [33] M. Alam *et al.*, “Evaluation of optimal electrode configurations for epidural spinal cord stimulation in cervical spinal cord injured rats,” *Journal of Neuroscience Methods*, vol. 247, pp. 50–57, May 2015.
- [34] —, “Electrical neuromodulation of the cervical spinal cord facilitates forelimb skilled function recovery in spinal cord injured rats,” *Experimental Neurology*, vol. 291, pp. 141–150, 2017.
- [35] A. N. Sharpe and A. Jackson, “Upper-limb muscle responses to epidural, subdural and intraspinal stimulation of the cervical spinal cord,” *Journal of Neural Engineering*, vol. 11, no. 1, p. 016005, Feb. 2014. [Online]. Available: <http://stacks.iop.org/1741-2552/11/i=1/a=016005?key=crossref.23e0f65ec9bd6cd8f68c732be0aaf9de>
- [36] G. Taccola *et al.*, “And yet it moves: Recovery of volitional control after spinal cord injury,” *Progress in Neurobiology*, vol. 160, pp. 64–81, 2018.
- [37] F. Rattay, “Analysis of models for external stimulation of axons,” *IEEE transactions on bio-medical engineering*, vol. 33, no. 10, pp. 974–977, Oct. 1986.
- [38] F. Rattay, K. Minassian, and M. R. Dimitrijevic, “Epidural electrical stimulation of posterior structures of the human lumbosacral cord: 2. quantitative analysis by computer modeling,” *Spinal Cord*, vol. 38, no. 8, pp. 473–489, Aug. 2000.
- [39] J. Holsheimer, “Which Neuronal Elements are Activated Directly by Spinal Cord Stimulation,” *Neuromodulation: Journal of the International Neuromodulation Society*, vol. 5, no. 1, pp. 25–31, Jan. 2002.
- [40] Y. P. Gerasimenko *et al.*, “Spinal cord reflexes induced by epidural spinal cord stimulation in normal awake rats,” *Journal of Neuroscience Methods*, vol. 157, no. 2, pp. 253–263, Oct. 2006.
- [41] K. Minassian *et al.*, “Posterior root-muscle reflexes elicited by transcutaneous stimulation of the human lumbosacral cord,” *Muscle & Nerve*, vol. 35, no. 3, pp. 327–336, Mar. 2007.
- [42] M. Capogrosso *et al.*, “A Computational Model for Epidural Electrical Stimulation of Spinal Sensorimotor Circuits,” *Journal of Neuroscience*, vol. 33, no. 49, pp. 19 326–19 340, Dec. 2013. [Online]. Available: <http://www.jneurosci.org/cgi/doi/10.1523/JNEUROSCI.1688-13.2013>
- [43] K. Minassian *et al.*, “Stepping-like movements in humans with complete spinal cord injury induced by epidural stimulation of the lumbar cord: electromyographic study of compound muscle action potentials,” *Spinal Cord*, vol. 42, no. 7, pp. 401–416, Jul. 2004. [Online]. Available: <http://www.nature.com/articles/3101615>

- [44] P. H. Peckham and J. S. Knutson, "Functional Electrical Stimulation for Neuromuscular Applications," *Annual Review of Biomedical Engineering*, vol. 7, no. 1, pp. 327–360, Aug. 2005. [Online]. Available: <http://www.annualreviews.org/doi/10.1146/annurev.bioeng.6.040803.140103>
- [45] A. Jackson and J. B. Zimmermann, "Neural interfaces for the brain and spinal cord—restoring motor function," *Nature Reviews Neurology*, vol. 8, no. 12, pp. 690–699, Dec. 2012. [Online]. Available: <http://www.nature.com/articles/nrneurol.2012.219>
- [46] X. Navarro *et al.*, "A critical review of interfaces with the peripheral nervous system for the control of neuroprostheses and hybrid bionic systems," *Journal of the peripheral nervous system: JPNS*, vol. 10, no. 3, pp. 229–258, Sep. 2005.
- [47] P. A. Kirkwood and T. A. Sears, "Monosynaptic excitation of motoneurons from secondary endings of muscle spindles," *Nature*, vol. 252, no. 5480, pp. 243–244, Nov. 1974.
- [48] A. G. Brown and R. E. Fyffe, "The morphology of group Ib afferent fibre collaterals in the spinal cord of the cat," *The Journal of Physiology*, vol. 296, pp. 215–226, Nov. 1979.
- [49] A. G. Brown, "Cutaneous axons and sensory neurones in the spinal cord," *British Medical Bulletin*, vol. 33, no. 2, pp. 109–112, May 1977.
- [50] J. Struijk *et al.*, "Recruitment of dorsal column fibers in spinal cord stimulation: influence of collateral branching," *IEEE Transactions on Biomedical Engineering*, vol. 39, no. 9, pp. 903–912, Sep. 1992. [Online]. Available: <http://ieeexplore.ieee.org/document/256423/>
- [51] H. K. P. Feirabend *et al.*, "Morphometry of human superficial dorsal and dorso-lateral column fibres: significance to spinal cord stimulation," *Brain: A Journal of Neurology*, vol. 125, no. Pt 5, pp. 1137–1149, May 2002.
- [52] J. Niu *et al.*, "Modality-based organization of ascending somatosensory axons in the direct dorsal column pathway," *The Journal of Neuroscience: The Official Journal of the Society for Neuroscience*, vol. 33, no. 45, pp. 17 691–17 709, Nov. 2013.
- [53] D. P. C. Lloyd, "REFLEX ACTION IN RELATION TO PATTERN AND PERIPHERAL SOURCE OF AFFERENT STIMULATION," *Journal of Neurophysiology*, vol. 6, no. 2, pp. 111–119, Mar. 1943. [Online]. Available: <http://www.physiology.org/doi/10.1152/jn.1943.6.2.111>

- [54] M. Capogrosso *et al.*, “Configuration of electrical spinal cord stimulation through real-time processing of gait kinematics,” *Nature Protocols*, vol. 13, no. 9, pp. 2031–2061, Sep. 2018. [Online]. Available: <http://www.nature.com/articles/s41596-018-0030-9>
- [55] B. Howell, B. Huynh, and W. M. Grill, “Design and in vivo evaluation of more efficient and selective deep brain stimulation electrodes,” *Journal of Neural Engineering*, vol. 12, no. 4, p. 046030, Aug. 2015.
- [56] R. K. Kalkman, J. J. Briaire, and J. H. M. Frijns, “Current focussing in cochlear implants: an analysis of neural recruitment in a computational model,” *Hearing Research*, vol. 322, pp. 89–98, Apr. 2015.
- [57] G. Courtine *et al.*, “Can experiments in nonhuman primates expedite the translation of treatments for spinal cord injury in humans?” *Nature Medicine*, vol. 13, no. 5, pp. 561–566, May 2007. [Online]. Available: <http://www.nature.com/articles/nm1595>
- [58] B. Coburn and W. K. Sin, “A theoretical study of epidural electrical stimulation of the spinal cord—Part I: Finite element analysis of stimulus fields,” *IEEE transactions on bio-medical engineering*, vol. 32, no. 11, pp. 971–977, Nov. 1985.
- [59] S. F. Lempka *et al.*, “Computational Analysis of Kilohertz Frequency Spinal Cord Stimulation for Chronic Pain Management:,” *Anesthesiology*, vol. 122, no. 6, pp. 1362–1376, Jun. 2015. [Online]. Available: <http://Insights.ovid.com/crossref?an=00000542-201506000-00029>
- [60] E. M. Moraud *et al.*, “Mechanisms Underlying the Neuromodulation of Spinal Circuits for Correcting Gait and Balance Deficits after Spinal Cord Injury,” *Neuron*, vol. 89, no. 4, pp. 814–828, Feb. 2016.
- [61] C. R. Butson and C. C. McIntyre, “Current steering to control the volume of tissue activated during deep brain stimulation,” *Brain Stimulation*, vol. 1, no. 1, pp. 7–15, Jan. 2008.
- [62] M. Capogrosso, S. Raspopovic, and S. Micera, “Does multipolar stimulation enhance selectivity of the TIME electrode? A simulation study using a genetic algorithm,” in *2011 5th International IEEE/EMBS Conference on Neural Engineering*. Cancun: IEEE, Apr. 2011, pp. 124–127. [Online]. Available: <http://ieeexplore.ieee.org/document/5910504/>
- [63] Y. Xiao, E. Peña, and M. D. Johnson, “Theoretical Optimization of Stimulation Strategies for a Directionally Segmented Deep Brain Stimulation Electrode Array,” *IEEE transactions on bio-medical engineering*, vol. 63, no. 2, pp. 359–371, Feb. 2016.

- [64] R. Fitzpatrick, *Classical Electromagnetism: an intermediate level course*, 2006. [Online]. Available: <https://farside.ph.utexas.edu/teaching/jk1/Electromagnetism.pdf>
- [65] C. A. Balanis, *Advanced engineering electromagnetics*, 2nd ed. Hoboken, N.J: John Wiley & Sons, 2012.
- [66] T. Lemaire, “Biocompatibility and specificity of a novel peripheral interface: a modelling study,” Master’s thesis, EPFL, 2015.
- [67] C. A. Bossetti, M. J. Birdno, and W. M. Grill, “Analysis of the quasi-static approximation for calculating potentials generated by neural stimulation,” *Journal of Neural Engineering*, vol. 5, no. 1, pp. 44–53, Mar. 2008. [Online]. Available: <http://stacks.iop.org/1741-2552/5/i=1/a=005?key=crossref.70ba51d686f7f13f0eaa9d6d6ba284ff>
- [68] R. Plonsey and D. B. Heppner, “Considerations of quasi-stationarity in electrophysiological systems,” *The Bulletin of Mathematical Biophysics*, vol. 29, no. 4, pp. 657–664, Dec. 1967.
- [69] H. P. Schwan and C. F. Kay, “The conductivity of living tissues,” *Annals of the New York Academy of Sciences*, vol. 65, no. 6, pp. 1007–1013, Aug. 1957.
- [70] L. A. Geddes and L. E. Baker, “The specific resistance of biological material—a compendium of data for the biomedical engineer and physiologist,” *Medical & Biological Engineering*, vol. 5, no. 3, pp. 271–293, May 1967.
- [71] S. Gabriel, R. W. Lau, and C. Gabriel, “The dielectric properties of biological tissues: III. Parametric models for the dielectric spectrum of tissues,” *Physics in Medicine and Biology*, vol. 41, no. 11, pp. 2271–2293, Nov. 1996. [Online]. Available: <http://stacks.iop.org/0031-9155/41/i=11/a=003?key=crossref.53515b64cc0754a65706d6adbf3981b2>
- [72] A. Fortin and A. Garon, *Les éléments finis : de la théorie à la pratique*, 2011. [Online]. Available: https://moodle.polymtl.ca/pluginfile.php/357690/mod_resource/content/2/Fortin-Garon-elements-finis.pdf
- [73] S. Gabriel, R. W. Lau, and C. Gabriel, “The dielectric properties of biological tissues: II. Measurements in the frequency range 10 Hz to 20 GHz,” *Physics in Medicine and Biology*, vol. 41, no. 11, pp. 2251–2269, Nov. 1996. [Online]. Available: <http://stacks.iop.org/0031-9155/41/i=11/a=002?key=crossref.bd742e03921dc87fd9ca8755d988111c>

- [74] C. R. Butson and C. C. McIntyre, "Tissue and electrode capacitance reduce neural activation volumes during deep brain stimulation," *Clinical Neurophysiology: Official Journal of the International Federation of Clinical Neurophysiology*, vol. 116, no. 10, pp. 2490–2500, Oct. 2005.
- [75] C. Koch, *Biophysics of computation: information processing in single neurons*, 1st ed., ser. Computational neuroscience. New York: Oxford Univ. Press, 2004, oCLC: 254577920.
- [76] P. Dayan and L. F. Abbott, *Theoretical neuroscience: computational and mathematical modeling of neural systems*, ser. Computational neuroscience. Cambridge, Mass: Massachusetts Institute of Technology Press, 2001.
- [77] C. C. McIntyre, A. G. Richardson, and W. M. Grill, "Modeling the excitability of mammalian nerve fibers: influence of afterpotentials on the recovery cycle," *Journal of Neurophysiology*, vol. 87, no. 2, pp. 995–1006, Feb. 2002.
- [78] C. C. McIntyre *et al.*, "Cellular effects of deep brain stimulation: model-based analysis of activation and inhibition," *Journal of Neurophysiology*, vol. 91, no. 4, pp. 1457–1469, Apr. 2004.
- [79] C. C. McIntyre and W. M. Grill, "Extracellular Stimulation of Central Neurons: Influence of Stimulus Waveform and Frequency on Neuronal Output," *Journal of Neurophysiology*, vol. 88, no. 4, pp. 1592–1604, Oct. 2002. [Online]. Available: <http://www.physiology.org/doi/10.1152/jn.2002.88.4.1592>
- [80] S. Cullheim *et al.*, "Membrane area and dendritic structure in type-identified triceps surae alpha motoneurons," *The Journal of Comparative Neurology*, vol. 255, no. 1, pp. 68–81, Jan. 1987.
- [81] I. Segev, J. W. Fleshman, and R. E. Burke, "Computer simulation of group Ia EPSPs using morphologically realistic models of cat alpha-motoneurons," *Journal of Neurophysiology*, vol. 64, no. 2, pp. 648–660, Aug. 1990. [Online]. Available: <http://www.physiology.org/doi/10.1152/jn.1990.64.2.648>
- [82] W. Rall, "Core Conductor Theory and Cable Properties of Neurons," in *Comprehensive Physiology*, R. Terjung, Ed. Hoboken, NJ, USA: John Wiley & Sons, Inc., Jan. 2011, p. cp010103. [Online]. Available: <http://doi.wiley.com/10.1002/cphy.cp010103>
- [83] B. Coburn, "Electrical stimulation of the spinal cord: two-dimensional finite element analysis with particular reference to epidural electrodes," *Medical & Biological Engineering & Computing*, vol. 18, no. 5, pp. 573–584, Sep. 1980.

- [84] —, “A theoretical study of epidural electrical stimulation of the spinal cord—Part II: Effects on long myelinated fibers,” *IEEE transactions on bio-medical engineering*, vol. 32, no. 11, pp. 978–986, Nov. 1985.
- [85] W. K. Sin and B. Coburn, “Electrical stimulation of the spinal cord: a further analysis relating to anatomical factors and tissue properties,” *Medical & Biological Engineering & Computing*, vol. 21, no. 3, pp. 264–269, May 1983. [Online]. Available: <http://link.springer.com/10.1007/BF02478492>
- [86] D. R. McNeal, “Analysis of a model for excitation of myelinated nerve,” *IEEE transactions on bio-medical engineering*, vol. 23, no. 4, pp. 329–337, Jul. 1976.
- [87] J. Struijk *et al.*, “Epidural spinal cord stimulation: calculation of field potentials with special reference to dorsal column nerve fibers,” *IEEE Transactions on Biomedical Engineering*, vol. 38, no. 1, pp. 104–110, Jan. 1991. [Online]. Available: <http://ieeexplore.ieee.org/document/68217/>
- [88] J. J. Struijk, J. Holsheimer, and H. B. Boom, “Excitation of dorsal root fibers in spinal cord stimulation: a theoretical study,” *IEEE transactions on bio-medical engineering*, vol. 40, no. 7, pp. 632–639, Jul. 1993.
- [89] F. Rattay, “The basic mechanism for the electrical stimulation of the nervous system,” *Neuroscience*, vol. 89, no. 2, pp. 335–346, Mar. 1999.
- [90] B. Howell, S. P. Lad, and W. M. Grill, “Evaluation of Intradural Stimulation Efficiency and Selectivity in a Computational Model of Spinal Cord Stimulation,” *PLoS ONE*, vol. 9, no. 12, p. e114938, Dec. 2014. [Online]. Available: <https://dx.plos.org/10.1371/journal.pone.0114938>
- [91] M. Arslan *et al.*, “Lumbosacral intrathecal nerve roots: an anatomical study,” *Acta Neurochirurgica*, vol. 153, no. 7, pp. 1435–1442, Jul. 2011.
- [92] H.-Y. Ko *et al.*, “Gross quantitative measurements of spinal cord segments in human,” *Spinal Cord*, vol. 42, no. 1, pp. 35–40, Jan. 2004.
- [93] J. D’Errico, “interparc,” MATLAB Central File Exchange, 2019. [Online]. Available: <https://www.mathworks.com/matlabcentral/fileexchange/34874-interparc>
- [94] N. A. Smith and R. W. Tromble, “Sampling Uniformly from the Unit Simplex,” 2004. [Online]. Available: <http://www.cs.cmu.edu/~nasmith/papers/smith+tromble.tr04.pdf>

- [95] N. Ishizuka *et al.*, “Trajectory of group Ia afferent fibers stained with horseradish peroxidase in the lumbosacral spinal cord of the cat: three dimensional reconstructions from serial sections,” *The Journal of Comparative Neurology*, vol. 186, no. 2, pp. 189–211, Jul. 1979.
- [96] A. B. Jenny and J. Inukai, “Principles of motor organization of the monkey cervical spinal cord,” *The Journal of Neuroscience: The Official Journal of the Society for Neuroscience*, vol. 3, no. 3, pp. 567–575, Mar. 1983.
- [97] C. M. Schirmer *et al.*, “Heuristic map of myotomal innervation in humans using direct intraoperative nerve root stimulation,” *Journal of Neurosurgery. Spine*, vol. 15, no. 1, pp. 64–70, Jul. 2011.
- [98] T. Futami, Y. Shinoda, and J. Yokota, “Spinal axon collaterals of corticospinal neurons identified by intracellular injection of horseradish peroxidase,” *Brain Research*, vol. 164, pp. 279–284, Mar. 1979.
- [99] N. Greiner *et al.*, “Recruitment of Upper-Limb Motoneurons with Epidural Electrical Stimulation of the Primate Cervical Spinal Cord,” Bioengineering, preprint, Feb. 2020. [Online]. Available: <http://biorxiv.org/lookup/doi/10.1101/2020.02.17.952796>
- [100] E. Formento *et al.*, “Electrical spinal cord stimulation must preserve proprioception to enable locomotion in humans with spinal cord injury,” *Nature Neuroscience*, vol. 21, no. 12, pp. 1728–1741, Dec. 2018. [Online]. Available: <http://www.nature.com/articles/s41593-018-0262-6>
- [101] V. R. Edgerton *et al.*, “Training locomotor networks,” *Brain Research Reviews*, vol. 57, no. 1, pp. 241–254, Jan. 2008.
- [102] M. Tripodi, A. E. Stepien, and S. Arber, “Motor antagonism exposed by spatial segregation and timing of neurogenesis,” *Nature*, vol. 479, no. 7371, pp. 61–66, Oct. 2011.
- [103] S. Grillner and T. M. Jessell, “Measured motion: searching for simplicity in spinal locomotor networks,” *Current Opinion in Neurobiology*, vol. 19, no. 6, pp. 572–586, Dec. 2009.
- [104] R. A. Gaunt *et al.*, “Intraspinal microstimulation excites multisegmental sensory afferents at lower stimulus levels than local alpha-motoneuron responses,” *Journal of Neurophysiology*, vol. 96, no. 6, pp. 2995–3005, Dec. 2006.
- [105] B. J. Holinski *et al.*, “Intraspinal microstimulation produces over-ground walking in anesthetized cats,” *Journal of Neural Engineering*, vol. 13, no. 5, p. 056016, 2016.

- [106] C. T. Moritz *et al.*, “Forelimb movements and muscle responses evoked by microstimulation of cervical spinal cord in sedated monkeys,” *Journal of Neurophysiology*, vol. 97, no. 1, pp. 110–120, Jan. 2007.
- [107] J. B. Zimmermann, K. Seki, and A. Jackson, “Reanimating the arm and hand with intraspinal microstimulation,” *Journal of Neural Engineering*, vol. 8, no. 5, p. 054001, Oct. 2011.
- [108] R. W. Banks, “An allometric analysis of the number of muscle spindles in mammalian skeletal muscles,” *Journal of Anatomy*, vol. 208, no. 6, pp. 753–768, Jun. 2006.
- [109] T. A. Miller, I. Mogyoros, and D. Burke, “Homonymous and heteronymous monosynaptic reflexes in biceps brachii,” *Muscle & Nerve*, vol. 18, no. 6, pp. 585–592, Jun. 1995. [Online]. Available: <http://doi.wiley.com/10.1002/mus.880180604>
- [110] A. S. Finkel and S. J. Redman, “The synaptic current evoked in cat spinal motoneurons by impulses in single group 1a axons,” *The Journal of Physiology*, vol. 342, pp. 615–632, Sep. 1983.
- [111] G. Sengul, Ed., *Atlas of the spinal cord of the rat, mouse, marmoset, rhesus, and human*, 1st ed. London ; Boston: Elsevier Academic Press, 2013, oCLC: ocn798062279.
- [112] E. Zarzur, “Mechanical properties of the human lumbar dura mater,” *Arquivos De Neuro-Psiquiatria*, vol. 54, no. 3, pp. 455–460, Sep. 1996.
- [113] M. Capogrosso *et al.*, “Advantages of soft subdural implants for the delivery of electrochemical neuromodulation therapies to the spinal cord,” *Journal of Neural Engineering*, vol. 15, no. 2, p. 026024, 2018.
- [114] M. L. Hines and N. T. Carnevale, “The NEURON Simulation Environment,” *Neural Computation*, vol. 9, no. 6, pp. 1179–1209, Aug. 1997. [Online]. Available: <http://www.mitpressjournals.org/doi/10.1162/neco.1997.9.6.1179>
- [115] S. Cullheim, “Relations between cell body size, axon diameter and axon conduction velocity of cat sciatic alpha-motoneurons stained with horseradish peroxidase,” *Neuroscience Letters*, vol. 8, no. 1, pp. 17–20, Apr. 1978.
- [116] C. L. A. M. Vleggeert-Lankamp *et al.*, “Electrophysiology and morphometry of the Aalpha- and Abeta-fiber populations in the normal and regenerating rat sciatic nerve,” *Experimental Neurology*, vol. 187, no. 2, pp. 337–349, Jun. 2004.

- [117] U. S. Hofstoetter *et al.*, “Periodic modulation of repetitively elicited monosynaptic reflexes of the human lumbosacral spinal cord,” *Journal of Neurophysiology*, vol. 114, no. 1, pp. 400–410, Jul. 2015. [Online]. Available: <http://www.physiology.org/doi/10.1152/jn.00136.2015>
- [118] L. M. Mendell and E. Henneman, “Terminals of single Ia fibers: location, density, and distribution within a pool of 300 homonymous motoneurons,” *Journal of Neurophysiology*, vol. 34, no. 1, pp. 171–187, Jan. 1971.
- [119] National Research Council (US) Institute for Laboratory Animal Research, *Guide for the Care and Use of Laboratory Animals*. Washington (DC): National Academies Press (US), 1996. [Online]. Available: <http://www.ncbi.nlm.nih.gov/books/NBK232589/>
- [120] A. L. Benabid *et al.*, “Deep brain stimulation of the subthalamic nucleus for the treatment of Parkinson’s disease,” *The Lancet. Neurology*, vol. 8, no. 1, pp. 67–81, Jan. 2009.
- [121] R. V. Shannon, “Advances in auditory prostheses,” *Current Opinion in Neurology*, vol. 25, no. 1, pp. 61–66, Feb. 2012.
- [122] N. A. Pelot, B. J. Thio, and W. M. Grill, “Modeling Current Sources for Neural Stimulation in COMSOL,” *Frontiers in Computational Neuroscience*, vol. 12, p. 40, Jun. 2018. [Online]. Available: <https://www.frontiersin.org/article/10.3389/fncom.2018.00040/full>
- [123] J. H. M. Frijns, D. M. T. Dekker, and J. J. Briaire, “Neural excitation patterns induced by phased-array stimulation in the implanted human cochlea,” *Acta Otolaryngologica*, vol. 131, no. 4, pp. 362–370, Apr. 2011.
- [124] D. Van Compernelle, “Speech processing strategies for a multichannel cochlear prosthesis,” Ph.D. dissertation, Stanford University, Department of Electrical Engineering, 1985.
- [125] C. A. Anastassiou *et al.*, “Ephaptic coupling of cortical neurons,” *Nature Neuroscience*, vol. 14, no. 2, pp. 217–223, Feb. 2011. [Online]. Available: <http://www.nature.com/articles/nn.2727>
- [126] A. Tveito *et al.*, “An Evaluation of the Accuracy of Classical Models for Computing the Membrane Potential and Extracellular Potential for Neurons,” *Frontiers in Computational Neuroscience*, vol. 11, p. 27, Apr. 2017. [Online]. Available: <http://journal.frontiersin.org/article/10.3389/fncom.2017.00027/full>

- [127] S. Raspopovic, M. Capogrosso, and S. Micera, “A computational model for the stimulation of rat sciatic nerve using a transverse intrafascicular multichannel electrode,” *IEEE transactions on neural systems and rehabilitation engineering: a publication of the IEEE Engineering in Medicine and Biology Society*, vol. 19, no. 4, pp. 333–344, Aug. 2011.
- [128] P. Kibleur *et al.*, “Spatiotemporal Maps of Proprioceptive Inputs to the Cervical Spinal Cord During Three-Dimensional Reaching and Grasping,” *Bioengineering*, preprint, Oct. 2019. [Online]. Available: <http://biorxiv.org/lookup/doi/10.1101/790816>
- [129] T. Mano, S. Iwase, and S. Toma, “Microneurography as a tool in clinical neurophysiology to investigate peripheral neural traffic in humans,” *Clinical Neurophysiology: Official Journal of the International Federation of Clinical Neurophysiology*, vol. 117, no. 11, pp. 2357–2384, Nov. 2006.

CURRICULUM VITAE

Personal Data

NAME: Nathan, Antoine GREINER
NATIONALITY: French
DATE OF BIRTH: 14 December 1990
ADDRESS: 64 rue du chateau des rentiers, 75013, Paris, France
PHONE: +33 7 81 80 22 44
EMAIL: nathan.greiner@m4x.org

Education

2016 - *Curr.* **Ph. D.** Neurosciences
École Polytechnique Fédérale de Lausanne, Switzerland
“Refinements of hybrid neurophysical volume conductor models and application to study epidural electrical stimulation of the cervical spinal cord”
Director: Prof. Grégoire COURTINE | Co-director: Prof. Marco CAPOGROSSO

2014 - 2015 **M. Sc. A.** Nuclear reactor physics
École Polytechnique de Montréal, Canada
“Fine coupling between thermics and neutronics in lattice calculations for pressurized water reactors” | Director: Prof. Alain HÉBERT
http://www.polymtl.ca/merlin/downloads/NGreiner_memoire.pdf

2010 - 2014 Engineering Diploma | **École Polytechnique**, Palaiseau, France

Publications in peer-reviewed journals

M. Capogrosso*, J. Gandar*, N. Greiner *et al.*, “Advantages of soft subdural implants for the delivery of electro- chemical neuromodulation therapies to the spinal cord,” *Journal of Neural Engineering*, vol. 15, no. 2, p. 026024, 2018.

Conference papers

N. Greiner and M. Capogrosso, “Anatomically Realistic Computational Model to Assess

the Specificity of Epidural Electrical Stimulation of the Cervical Spinal Cord,” in Converging Clinical and Engineering Research on Neurorehabilitation III, L. Masia et al., Eds. Cham: Springer International Publishing, 2019, vol. 21, pp. 44–48. [Online]. Available: http://link.springer.com/10.1007/978-3-030-01845-0_9

Preprints

P. Kibleur, S. R. Tata*, N. Greiner* *et al.*, “Spatiotemporal Maps of Proprioceptive Inputs to the Cervical Spinal Cord During Three-Dimensional Reaching and Grasping,” *Bioengineering*, preprint, Oct. 2019. [Online]. Available: <http://biorxiv.org/lookup/doi/10.1101/790816>

N. Greiner *et al.*, “Recruitment of Upper-Limb Motoneurons with Epidural Electrical Stimulation of the Primate Cervical Spinal Cord,” *Bioengineering*, preprint, Feb. 2020. [Online]. Available: <http://biorxiv.org/lookup/doi/10.1101/2020.02.17.952796>

Work Experience

- 2014 Sep. - 2015 Feb. **Internship** industrial research
 EDF R&D, SINETICS department, Clamart, France
 Development of a computational scheme coupling the APOLLO2
 lattice code and the C3THER thermomechanics code
 Supervisor: Enrico GIRARDI | Co-supervisor: Hadrien LEROYER
- 2013 Sep. - 2013 Dec. **Internship** nuclear safety engineering
 EDF CNEN, SNE department, Montrouge, France
 Design basis analysis (PTR cooling system, cask-loading pit) for the
 Generic Design Assessment of the HPC EPR project
 Supervisor: Mathieu ALCHOURROUN

Languages

ENGLISH: Fluent

FRENCH: Mothertongue

Computer Skills

Advanced Knowledge: UNIX, Python, Matlab, COMSOL Multiphysics

Intermediate Knowledge: C++, Java

Basic Knowledge: DRAGON, APOLLO2, C3THER

Authored repositories:

https://bitbucket.org/ngreiner/fem_smc_ees/src/master/

https://bitbucket.org/ngreiner/biophy_smc_ees/src/master/